



Master's Thesis
in Nuclear, Particle and Astrophysics

Characterization of a TRISTAN Silicon Drift Detector Array with a Laser System

Charakterisierung einer TRISTAN Silizium-Drift-Detektor-Matrix
mit einem Lasersystem

Christian Georg Anton Forstner
03695552

14 March 2023

Primary Reviewer: Prof. Dr. Susanne Mertens
Secondary Reviewer: Prof. Dr. Stefan Schönert
Supervisor: Korbinian Urban

Introduction

Sterile neutrinos are a minimal extension to the [Standard Model \(SM\)](#) of particle physics. The existence of these particles could resolve several open questions in neutrino physics and cosmology. With a mass on the keV-scale, they are a promising [Dark Matter \(DM\)](#) candidate. Despite their right-handed nature which prevents them from interacting weakly, the active-sterile mixing amplitude $\sin^2(\theta_s)$ gives access to sterile neutrinos in the decay of unstable isotopes such as tritium.

The [Karlsruhe Tritium Neutrino \(KATRIN\)](#) experiment is designed to measure the effective electron antineutrino mass using the tritium β -decay with an unprecedented precision. After the completion of the neutrino mass measurements, the [KATRIN](#) experiment will be modified to search sterile neutrinos on the keV-mass scale. In contrast to the neutrino mass, which manifests itself in the very endpoint region of the tritium β -decay spectrum, the imprint of the additional sterile mass eigenstate is a kink-like distortion that could be located anywhere in the energy spectrum. Therefore, a novel detector system is required that is capable of handling the high count rates of the strong tritium source. The [TRISTAN](#) detector and readout system, which is currently under development, fulfills this requirement and at the same time provides an excellent energy resolution of less than 300 eV ([FWHM](#)) at 20 keV. The [TRISTAN](#) detectors make use of the [Silicon Drift Detector](#) technology which features an extremely low anode capacitance and allows for high-precision electron spectroscopy. The integration of a [Junction-gate Field-Effect Transistor \(JFET\)](#) directly into every detector pixel enables to take advantage of this property and achieve the ultimate noise performance.

One of the key elements to search for sterile neutrinos is to precisely understand the detector response to incident radiation. In the scope of this thesis, a dedicated experimental laser setup was designed to study a 7 pixel [TRISTAN SDD](#) with a monochromatic photon beam and investigate the properties of the detector with respect to three main effects: 1) By studying timing effects of the incident radiation in the detector, it was observed that the geometry of the detector pixels has substantial influence on the drift of the electron charge cloud. Reconstructing the drift times of the electron charge clouds has shown that their distribution resembles the hexagonal structure of [SDD](#) pixels. Since a linear relation could be

obtained between the drift time and the distance to the detector anode, the drift time was found to be a well-suited parameter to describe the radial dependence of the charge cloud drift in the **TRISTAN SDD** pixels. 2) By investigating the charge collection in the region of the integrated **JFET**, the effectiveness of the **Inner Guard Ring (IGR)** to shield the **JFET** from the bulk was presented. By having applied a too positive voltage to the **IGR** electrode prior to the investigations in the scope of this thesis, $\sim 4\%$ of the charge in the center region of the **SDD** pixels was lost to the most positive electrode, the drain contact of the transistor. Decreasing the **IGR** voltage and thus increasing the strength of the potential barrier fully restored the charge collection. This defines a new operating point for the **TRISTAN** detectors. 3) By analyzing the effect of charge sharing at the boundary between adjacent pixels, an upper limit on the size of the charge cloud of $(16.3 \pm 0.2) \mu\text{m}$ was obtained. In addition, comparing the rise time of regular and charge sharing events has verified earlier studies on the shape of signal pulses.

The experimental investigations were complemented by dedicated detector simulations. In particular, the field configuration and the drift of the charge carriers were simulated and showed very good agreement with the experimental results. The observed charge loss in the transistor region could be reproduced with high accuracy and the size of the charge cloud was determined to be $(15.1 \pm 0.1) \mu\text{m}$, in overall agreement with the measurement. Moreover, the drift of the electron charge cloud showed the same distribution of the drift time. By varying the detector bias voltages in the simulation, it was demonstrated that applying proper bias voltages is indispensable to ensure optimal working conditions for the **TRISTAN SDDs**.

This thesis is structured as described in the following: Chapter 1 gives a general overview on neutrino physics with a focus on sterile neutrinos. In chapter 2, the **KATRIN** experiment is introduced and the measurement principle as well as the technical realization are discussed. The **TRISTAN** detector and readout system is presented in chapter 3 with a special emphasis on the detailed description of the **SDD** technology. In chapter 4, preparatory measurements are performed and the dedicated experimental laser setup is introduced. The characterization measurements of a 7 pixel **TRISTAN** detector are described in chapter 5. Finally, the results of dedicated simulations are compared to the experimental results in chapter 6.

Contents

Introduction	iii
Contents	v
1 Neutrino Physics	1
1.1 Neutrino Discovery	2
1.2 Neutrino Mixing and Oscillations	3
1.3 Sterile Neutrinos	5
1.4 Neutrino Mass	7
1.5 Current Neutrino Mass Limits	10
1.5.1 Limits from Cosmological Observations	10
1.5.2 Search for the Neutrinoless Double Beta Decay	11
1.5.3 Limits from Direct Measurements	12
2 The KATRIN Experiment	13
2.1 Measurement Principle	14
2.2 Technical Realization	17
2.2.1 Rear Section	18
2.2.2 Windowless Gaseous Tritium Source	18
2.2.3 Transport Section	18
2.2.4 Spectrometer Section	19
2.2.5 Focal Plane Detector	19
2.2.6 Monitoring Devices	20
2.3 keV-scale sterile Neutrino Search with the KATRIN Experiment	20
3 The TRISTAN Detector and Readout System	25
3.1 Basics of Semiconductors	25
3.2 Working Principle of Silicon Drift Detectors	31
3.3 TRISTAN Detectors	34
3.4 Charge Motion and Signal Formation	36
3.4.1 Statistical Movement	36
3.4.2 Self-Repulsion	37

3.4.3	Drift	37
3.4.4	Diffusion	38
3.4.5	Signal Formation	38
3.5	TRISTAN Readout System	40
4	Preparatory Measurements	45
4.1	Reference Calibration with an ^{55}Fe Source	45
4.2	Optimization of the Laser System	51
5	Detector Characterization	57
5.1	Experimental Setup	57
5.2	Modelling the Signal Shape	61
5.3	Results of the Laser Characterization	70
5.3.1	Amplitude	70
5.3.2	Drift Time	75
5.3.3	Gaussian Width	80
5.3.4	Exponential Rise Time	83
5.3.5	Rise Time	86
6	Simulations	89
6.1	Simulation of the Field Configuration in a TRISTAN SDD Pixel	89
6.2	Simulation of the Drift of the Charge Carriers	96
6.3	Comparison of Experiment and Simulation	105
6.4	Variation of Simulation Parameters	115
6.4.1	Variation of the Energy of the Incident Radiation	115
6.4.2	Variation of the Back Contact (BC) Voltage	118
6.4.3	Variation of the Inner Guard Ring (IGR) Voltage	121
6.4.4	Variation of the Innermost Drift Ring (R1) Voltage	124
6.4.5	Variation of the Outermost Drift Ring (RX) Voltage	127
7	Conclusions	131
A	Appendix	135
A.1	Laser Stability	135
	Acronyms	137
	List of Figures	141
	List of Tables	145
	Bibliography	147

Neutrino Physics

The [Standard Model \(SM\)](#) of particle physics describes our current knowledge of the theory of fundamental forces (electromagnetic, weak, and strong interaction - excluding gravity) and gives an overview of all known elementary particles. The [SM](#) unites bosons and fermions, particles with integer and half-integer spin, respectively. While bosons are exchange particles mediating the fundamental forces, so-called interaction/force carriers, fermions are sub-atomic particles that are fundamental constituents of all known matter. Specifically, matter is composed of quarks forming hadrons, i. e. baryons and mesons, and of charged and neutral leptons, each in three particle generations. Neutrinos, the subject of this thesis, belong to the latter group of particles and are the only particles in the [SM](#) that do not carry any electric charge. All the above also applies to antiparticles, which - with opposite charge - form the antimatter.

Until today not all neutrino mysteries could be solved, e. g. the origin of the neutrino mass or whether the neutrino is its own antiparticle. Hence, this chapter starts with section [1.1](#) giving an overview over the extensive search for neutrinos that has been conducted over decades. This is followed by an introduction to neutrino mixing in section [1.2](#) and sterile neutrinos in section [1.3](#). In section [1.4](#), different ways of introducing the neutrino mass are presented. The review of current neutrino mass limits completes this chapter with section [1.5](#).

1.1 Neutrino Discovery

In 1914, Chadwick observed continuous energy spectra in the β -decay of ^{214}Po and ^{214}Bi , which are two of the daughter nuclei in the decay chain of ^{226}Ra [47]. This was in contradiction to the well-established concept of β -decays producing discrete, monoenergetic lines in the electron energy spectrum. Energy conservation was questioned as in two-body decays each of the emitted particles should have a well-defined energy. In 1934, Fermi proposed a theory to explain the β -decay preserving energy, momentum, and spin [64]. Following Pauli's postulation, a fraction of the released energy is used to create a new type of particle, the neutrino ν . The decay of a nucleus with atomic number Z and mass number A can be described by

$$(Z, A) \rightarrow (Z + 1, A) + e^- + \bar{\nu}_e, \quad (1.1)$$

where e^- denotes the electron and $\bar{\nu}_e$ the electron antineutrino. The first direct measurement of neutrinos was conducted by Cowan and Reines within the project Poltergeist in 1956. The Savannah River Power Plant acted as an electron antineutrino source for the [Inverse Beta Decay \(IBD\)](#) on protons p producing neutrons n and positrons e^+ :

$$\bar{\nu}_e + p \rightarrow n + e^+. \quad (1.2)$$

Large water tanks with dissolved cadmium chloride (CdCl_2) served as target material. An instant emission of two gamma rays from the electron-positron annihilation was observed, directly followed by another one originating from the capture of the neutron on the cadmium several microseconds later, proving the existence of the electron (anti)neutrino $\bar{\nu}_e$ [51].

In 1962, Ledermann, Schwartz, and Steinberg observed muon neutrinos ν_μ at the [Alternating Gradient Synchrotron \(AGS\)](#) at Brookhaven National Laboratory [52]. A 15 GeV proton beam was shot onto a beryllium target. Charged pions were generated which consequently decayed producing neutrinos. In front of the spark chamber, that acted as detector, a steel shield stopped all particles except the neutrinos. By the observation of long muon tracks, which were created in the charged current interactions of the muon neutrinos, the existence of a second neutrino flavor was deduced.

After the discovery of the τ lepton in 1975 [103], the tau neutrino ν_τ was the last one to be found by the [DONUT](#) collaboration at Fermilab in 2001 [88]. This completes the exploration of the leptonic part of the [SM](#) as studies of the decay width of the Z boson at the [Large Electron-Positron \(LEP\)](#) collider limit the total number of light active neutrinos to $N = 2.9840 \pm 0.0082$ [50].

1.2 Neutrino Mixing and Oscillations

After the discovery of the electron neutrino, Davis designed the Homestake experiment in the late 1960s [53]. The goal of the experiment was to measure neutrinos originating from the nuclear fusion in the Sun by counting the number of ^{37}Ar atoms produced in the [IBD](#) reaction



It turned out that the detected neutrino flux was only one-third of the theoretical predictions of the [Standard Solar Model \(SSM\)](#) calculated by Bahcall [33]. This discrepancy was referred to as the solar neutrino problem and was confirmed by several other experiments like [GALLEX](#) [28], [GNO](#) [26], [SAGE](#) [4, 5], and [Borexino](#) [30, 23, 38].

A possible solution was proposed by Montecorvo in 1957, now known as neutrino oscillations [104]. This phenomenon arises from the mixing of the three neutrino flavor eigenstates (ν_e, ν_μ, ν_τ) and the corresponding mass eigenstates (ν_1, ν_2, ν_3). While the flavor eigenstates are the projection onto the interaction state, the mass eigenstates are the eigenvalues of the Hamiltonian for free propagation in vacuum. In other words, neutrinos propagate in a quantum-mechanical superposition of mass eigenstates but interact in flavor eigenstates. Both states are related via the [Pontecorvo-Maki-Nakagawa-Sakata \(PMNS\)](#) matrix:

$$\begin{pmatrix} \nu_e \\ \nu_\mu \\ \nu_\tau \end{pmatrix} = \begin{pmatrix} U_{e1} & U_{e2} & U_{e3} \\ U_{\mu1} & U_{\mu2} & U_{\mu3} \\ U_{\tau1} & U_{\tau2} & U_{\tau3} \end{pmatrix} \cdot \begin{pmatrix} \nu_1 \\ \nu_2 \\ \nu_3 \end{pmatrix}. \quad (1.4)$$

The [PMNS](#) matrix can be depicted as a rotation-matrix in three dimensions. It depends on three mixing angles ($\theta_{12}, \theta_{13}, \theta_{23}$), which determine the mixing amplitudes, and a complex Dirac phase δ_{CP} , which introduces [Charge conjugation Parity \(CP\)](#) violation. If neutrinos are Majorana particles, two Majorana phases α and β are added additionally.

For simplicity, relation (1.4) is reduced to a two neutrino mixing to show an exemplary neutrino oscillation for two hypothetical flavor eigenstates (ν_α, ν_β) and a single mixing angle Θ . The probability to oscillate from an initial state $|\nu_\alpha\rangle$ to the measured, final state $|\nu_\beta\rangle$ is described by

$$P(|\nu_\alpha\rangle \rightarrow |\nu_\beta\rangle) = \sin^2(2\Theta) \cdot \sin^2\left(1.27 \cdot \Delta m^2 [\text{eV}^2] \frac{L [\text{km}]}{E [\text{GeV}]}\right), \quad (1.5)$$

with Δm^2 the mass squared difference between the two mass eigenstates, L the baseline length of the oscillation, and E the neutrino energy. For neutrino flavor transitions to occur, the mass squared difference Δm^2 must be non-zero. In the case of three neutrino flavors this implies that at least two mass eigenstates must be non-zero. Depending on which mass eigenstates are non-zero, two different configurations arise:

Normal Ordering (NO) and **Inverted Ordering (IO)**. The normal ordering describes the case in which $m_1 < m_2 < m_3$ with m_1 being the mass of the lightest mass eigenstate, while in inverted ordering $m_3 < m_1 < m_2$ with m_3 being the mass of the lightest mass eigenstate. The **NO** regime is currently slightly preferred over the **IO** regime in the global fit of neutrino oscillation data [61]. However, more detailed future studies are needed to resolve the neutrino mass ordering issue [1].

In 1998, the Super-Kamiokande collaboration was the first to report evidence for the oscillation of atmospheric neutrinos [67]. These neutrinos are produced in the decay of charged kaons (K^\pm) and pions (π^\pm) which are created in the interaction of cosmic rays with air molecules in the upper atmosphere. A large underground tank filled with ultra-pure water and equipped with thousands of **Photo Multiplier Tubes (PMTs)** served as detection volume. The experiment was sensitive to charged current interactions of electron and muon neutrinos producing the associated charged leptons. The leptons were detected via Cherenkov light they emitted in the water. Studying their direction of interaction and comparing it to the neutrino flux for different zenith angles it was found that the measured neutrino flux was in agreement with two-flavor $\nu_\mu \leftrightarrow \nu_\tau$ oscillations.

In 2001, the **Sudbury Neutrino Observatory (SNO)** experiment was trying to finally solve the solar neutrino problem [17]. The experiment was designed to probe all three neutrino flavors at the same time using charged and neutral current interactions as well as electron elastic scattering. Heavy water with dissolved NaCl served as detection material and the light which was produced by the interactions was captured by Cherenkov detectors. They observed a deficit in the solar neutrino flux, similar to the Homestake experiment. However, the total neutrino flux was consistent with the **SSM** predictions and could be explained by electron neutrinos emitted from the sun changing their flavor on the way to earth.

Historically, solar neutrino oscillation experiments were the first being sensitive to the mass squared difference Δm_{21}^2 and the angle θ_{12} [7], atmospheric neutrino oscillation experiments to Δm_{31}^2 , Δm_{32}^2 , θ_{23} , and δ_{CP} [2]. Nowadays, most of the oscillation parameters are also measured in reactor [69] and accelerator [8] neutrino experiments. Table 1.1 gives an overview of the most recent neutrino oscillation parameters.

Table 1.1: **Overview of most recent Neutrino Oscillation Parameters**

For the three-flavor neutrino oscillations, the mixing angles and the squared mass differences are listed for the normal (NO, $l = 1$) and inverted ordering (IO, $l = 2$) regimes. The parameters are obtained from the global analysis NuFIT 5.2 and present best fit values without the inclusion of the tabulated χ^2 data on atmospheric neutrinos provided by the Super-Kamiokande collaboration [61].

Parameter	Best fit ($\pm 1\sigma$)	
	NO	IO
θ_{12} ($^\circ$)	33.41 $^{+0.75}_{-0.72}$	
θ_{13} ($^\circ$)	8.54 $^{+0.11}_{-0.12}$	8.57 $^{+0.12}_{-0.11}$
θ_{23} ($^\circ$)	49.1 $^{+1.0}_{-1.3}$	49.5 $^{+0.9}_{-1.2}$
δ_{CP} ($^\circ$)	197 $^{+42}_{-25}$	286 $^{+27}_{-32}$
Δm_{21}^2 (1×10^{-5} eV 2)	7.41 $^{+0.21}_{-0.20}$	
Δm_{3l}^2 (1×10^{-3} eV 2)	2.511 $^{+0.028}_{-0.027}$	-2.498 $^{+0.032}_{-0.025}$

1.3 Sterile Neutrinos

In the SM, only neutrinos with left-handed helicity (ν_L) exist. However, introducing neutrinos with right-handed helicity (ν_R) would be a natural extension to the SM, since all other fermions exist in both, left- and right-handed helicity as well. The introduction of these particles is in accordance to existing theories, because they would not participate in the electroweak interaction [76]. These neutrinos would be in a 'sterile' state and only have an impact on the mass mixing [3]. Figure 1.1 illustrates this extended, so-called **Neutrino Minimal Standard Model** (νMSM) proposed by Asaka and Shaposhnikov [31]. With neutrino masses smaller than the electroweak scale, i. e. $< \mathcal{O}(100 \text{ GeV})$, this model aims to explain the observed baryon asymmetry of the universe as well as the existence of **Dark Matter** (DM), and is consistent with neutrino oscillation experiments. As the mass of sterile neutrinos is not constrained from particle physics, it covers several orders of magnitude. Depending on the mass, mixing angle, and production mechanism three different mass scales can be distinguished:

eV-scale Anomalies in short-baseline oscillations experiments motivated the introduction of eV-scale sterile neutrinos. The first hint was found in the **Liquid Scintillator Neutrino Detector** (LSND) experiment [15] as well as later confirmed in the **Mini Booster Neutrino Experiment** (MiniBooNE) [16]. Both experiments found an excess of $\bar{\nu}_e$ in a $\bar{\nu}_\mu$ -beam which could be explained by introducing a light sterile neutrino. The **Gallium Experiment** (GALLEX) [81] and the **Soviet–American Gallium Experiment** (SAGE) [6] observed a decreased ν_e -rate during their calibration phases using strong ^{51}Ce and ^{37}Ar ν_e -sources yielding a combined significance of 2.8σ in favor of a eV-scale sterile neutrino. Most recently,

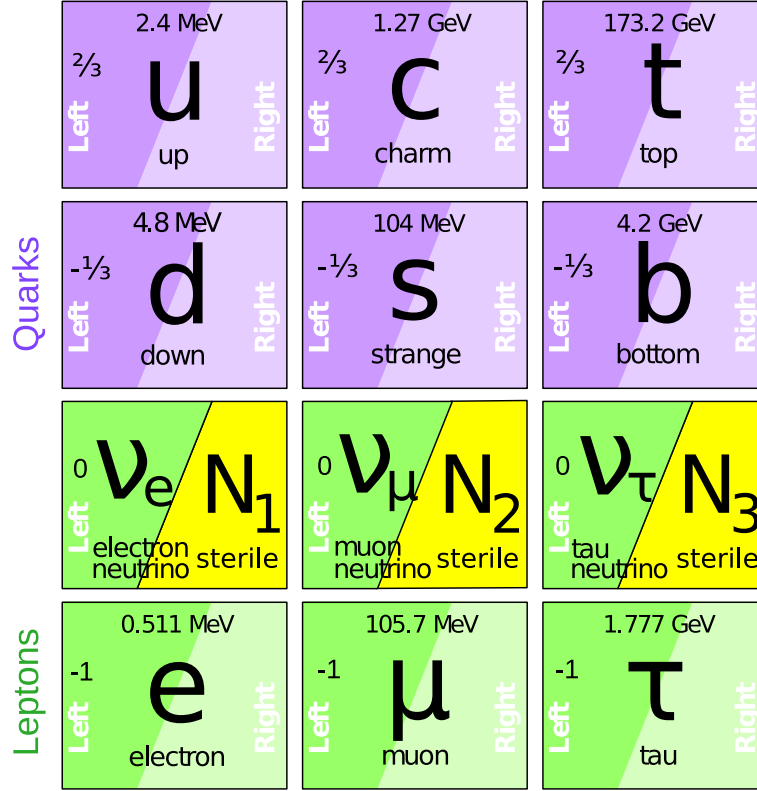


Figure 1.1: **Three Generations of Matter in the ν MSM**

The particle content of the ν MSM is illustrated for fermions. In the lepton sector, the ν MSM extends the SM by right-handed, sterile neutrinos. Therefore, all fermions have both left and right-handed components. The figure is adapted from [74].

the [Baksan Experiment on Sterile Transitions \(BEST\)](#) collaboration, that probes the gallium anomaly observed in [GALLEX](#) and [SAGE](#), claims a deficit in the ^{51}Ce production rate with 4σ significance being consistent with a sterile neutrino in the eV-scale [34]. In contrast to mentioned oscillation based experiments, the [KATRIN](#) experiment (see chapter 2) provides the possibility of a direct measurement of a light sterile neutrino [21]. However, until now, no sterile neutrino signal was observed.

keV-scale Aside [Weakly Interacting Massive Particles \(WIMPs\)](#), axions and primordial black holes, sterile neutrinos in the keV-mass range are a potential candidate for DM. Depending on the production mechanism, they either belong to [Cold Dark Matter \(CDM\)](#) or [Hot Dark Matter \(HDM\)](#) [35]. While [HDM-only](#) scenarios are disfavored by observations of small cosmological structures, whose formation would have been suppressed by [HDM](#) [35], [CDM](#) was favored over decades as it reproduces these structures in N -body simulations quite accurately. However, [Warm Dark Matter \(WDM\)](#) is even more robust in recreating the abundance, kinematics, and properties of dwarf galaxies as well [96]. The space observatory

X-ray Multi-Mirror (XMM)-Newton found a hint for the existence of a keV-scale sterile neutrino in observations of multiple galaxy clusters [41, 46]. A mono-energetic X-ray line at 3.5 keV originating from the decay of a sterile neutrino $N \rightarrow \nu + \gamma$ indicates a hypothetical sterile neutrino with a mass of 7 keV. This result is however rather controversial, as unconsidered systematics or incomplete knowledge of all astrophysical lines could produce a similar signal [83]. Laboratory-based sterile neutrino searches, first proposed by Shrock in 1980 [115], are independent of astrophysical or cosmological models. The decay of unstable isotopes (e.g. T_2) is studied with a wide variety of detection techniques [57]. Section 2.3 illustrates, how the **KATRIN** experiment will search for keV-scale sterile neutrinos.

GeV-scale As mentioned before, the ν **MSM** introduces sterile neutrinos in the GeV-scale. In the frame of this model, the lightness of the active neutrinos is explained through the Seesaw mechanism (see section 1.4). Moreover, the baryon asymmetry in the universe could be resolved via leptogenesis in case of the existence of a heavy sterile neutrino. However, GeV-scale sterile neutrinos could only be searched for in accelerator experiments today, since the observed abundance of light elements in the universe requires that they have decayed before the **Big Bang Nucleosynthesis (BBN)** [39].

1.4 Neutrino Mass

To explain the mechanism that gives mass to the active neutrinos, a "3+1" active-sterile neutrino mixing scheme is assumed with a new sterile flavor eigenstate ν_s and corresponding mass eigenstate ν_4 , that relate in a 4×4 **PMNS** matrix [11]:

$$\begin{pmatrix} \nu_e \\ \nu_\mu \\ \nu_\tau \\ \nu_s \end{pmatrix} = \begin{pmatrix} U_{e1} & U_{e2} & U_{e3} & U_{e4} \\ U_{\mu1} & U_{\mu2} & U_{\mu3} & U_{\mu4} \\ U_{\tau1} & U_{\tau2} & U_{\tau3} & U_{\tau4} \\ U_{s1} & U_{s2} & U_{s3} & U_{s4} \end{pmatrix} \cdot \begin{pmatrix} \nu_1 \\ \nu_2 \\ \nu_3 \\ \nu_4 \end{pmatrix} \quad (1.6)$$

Due to the mixing, the active and sterile components are a quantum-mechanical superposition. This makes sterile neutrinos experimentally accessible, as discussed in section 2.3, and also offers an elegant way to introduce mass to the normal, active neutrinos.

Figure 1.2 shows a comparison of the absolute mass scale of **SM** fermions. The mass of the electron as the lightest charged lepton differs by at least five orders of magnitude relative to the current upper limits on the neutrino mass (see section 1.5). This gives neutrinos a special position in the **SM** and raises the question of why the neutrino mass is so small. As of today, the origin of the neutrino mass is still unclear. Hence, various theories exist that try to explain the mass-giving mechanism.

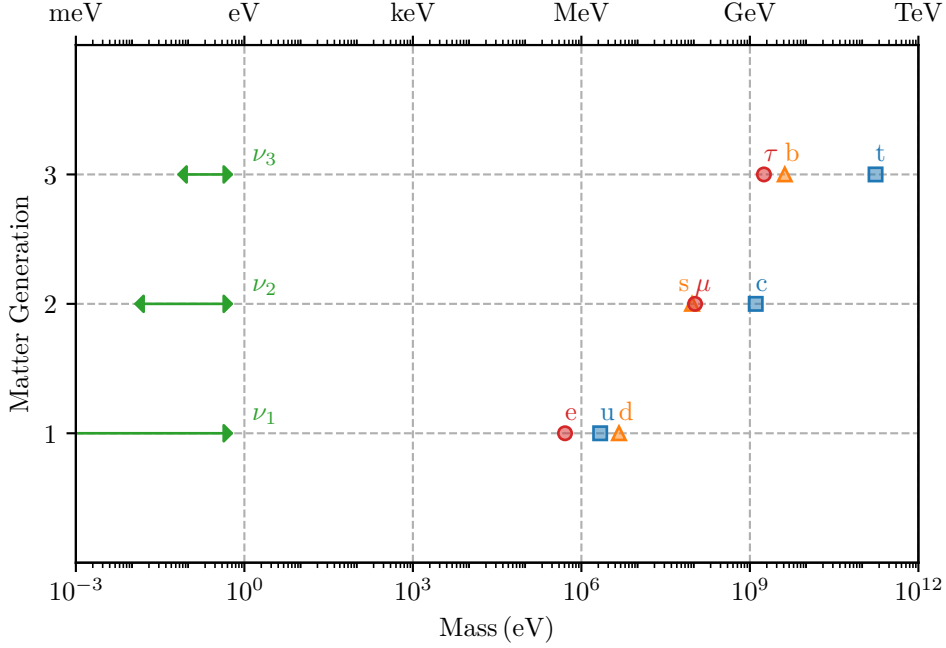


Figure 1.2: **Comparison of the Fermion Masses**

The mass distribution of the three generations of matter is displayed. Compared to the charged fermions, neutrinos have a mass at least five orders of magnitude smaller. The data is taken from [132].

Similar to Yukawa coupling, it would be intuitive to extend the Higgs mechanism also to neutrinos. This can be achieved by adding a **Dirac** mass term in the form of

$$\mathcal{L}^D = - \underbrace{\frac{h_\nu v}{\sqrt{2}}}_{m_D} (\bar{\nu}_L \nu_R + \bar{\nu}_R \nu_L) \quad (1.7)$$

to the SM Lagrangian, where m_D denotes the Dirac neutrino mass. This mass depends on the Yukawa coupling h_ν and the Vacuum Expectation Value (VEV) v of the Higgs field. It turns out, that the coupling has to be of the order of $h_\nu \approx 10^{-12}$ to match current upper limits of the neutrino mass of $\mathcal{O}(1 \text{ eV})$ [19]. This value seems unnaturally small compared to other particles gaining their mass via the same mechanism. Hence, the necessity of such fine-tuning disfavors a SM origin for the neutrino mass.

Another mass creation mechanism arises if we assume that neutrinos are **Majorana** particles, i. e. their own antiparticles. In this case, Majorana mass terms of the form

$$\mathcal{L}_L^M = -\frac{m_L}{2} \left(\bar{\nu}_L^C \nu_L + \bar{\nu}_L \nu_L^C \right) \quad (1.8)$$

and

$$\mathcal{L}_R^M = -\frac{m_R}{2} \left(\bar{\nu}_R^C \nu_R + \bar{\nu}_R \nu_R^C \right) \quad (1.9)$$

can be constructed with the superscript C denoting charge conjugation. These terms couple the antineutrino ($L = -1$) to the neutrino ($L = +1$) components violating lepton number L conservation by $\Delta L = \pm 2$. In the **SM**, a left-handed mass term like (1.8) hence does not seem to be possible [42]. The **Seesaw mechanism** tries to overcome this challenge [100, 133]. The most general mass term contains both left- and right-handed Dirac as well as Majorana fields and can be written as

$$\begin{aligned} \mathcal{L} &= \frac{1}{2} \left(\mathcal{L}_L^D + \mathcal{L}_R^D + \mathcal{L}_L^M + \mathcal{L}_R^M \right) + \text{h.c.} \\ &= \frac{1}{2} \left(m_D \bar{\nu}_R \nu_L + m_D \bar{\nu}_L^C \nu_R^C + m_L \bar{\nu}_L^C \nu_L + m_R \bar{\nu}_R^C \nu_R \right) + \text{h.c.} \end{aligned} \quad (1.10)$$

or equivalently in matrix form

$$\mathcal{L} = \frac{1}{2} \begin{pmatrix} \bar{\nu}_L^C & \bar{\nu}_R \end{pmatrix} \underbrace{\begin{pmatrix} m_L & m_D \\ m_D & m_R \end{pmatrix}}_{\mathcal{M}} \begin{pmatrix} \nu_L \\ \nu_R^C \end{pmatrix} + \text{h.c.} \quad (1.11)$$

By diagonalizing the mass matrix \mathcal{M} we get the eigenvalues m_1 and m_2 and the corresponding eigenvectors ν_1 and ν_2 :

$$\begin{aligned} m_1 &= \frac{m_D^2}{m_R}, \\ m_2 &= m_R \left(1 + \frac{m_D^2}{m_R^2} \right) \approx m_R. \end{aligned} \quad (1.12)$$

We identify ν_1 as the left-handed light active neutrino with mass m_1 and ν_2 as the right-handed heavy sterile neutrino with mass m_2 . This neutrino is supposed to be a Majorana particle and would have a mass up to the **Grand Unified Theory (GUT)** scale on the order of $\mathcal{O}(10^{15} \text{ GeV})$. It can be seen that m_1 is lighter, the heavier m_2 . Therefore, this mechanism is named after a seesaw as it explains the lightness of the active neutrino states very elegantly.

1.5 Current Neutrino Mass Limits

As pointed out in section 1.2, neutrino oscillation experiments are only sensitive to the mass squared differences of the mass eigenstates. Hence, another method is required to probe for the absolute neutrino mass scale. Currently, there are three different approaches to determine the neutrino mass.

1.5.1 Limits from Cosmological Observations

The structure formation of the universe was heavily influenced by neutrinos that decoupled from the early universe plasma about 1 s after the Big Bang. For a long period of time, these so-called relic neutrinos were still relativistic particles with a large free streaming length. Traces of these neutrinos are still visible today. Density fluctuations, which grew due to gravitational clustering of matter, formed the cosmological structures we observe nowadays. Relic neutrinos diminished their growth by washing-out over-densities smaller than their free streaming length. This effect results in a suppression of the matter power spectrum on small scale structures. Observations of the [Cosmic Microwave Background \(CMB\)](#) combined with measurements of the Lyman-alpha forest and large scale structure information from [Baryonic Acoustic Oscillations \(BAO\)](#) provide an upper limit on the sum over all neutrino mass eigenstates of [102]

$$m_\nu = \sum_{i=1}^3 m_i < 0.12 \text{ eV}. \quad (1.13)$$

However, a major limitation of this approach is the strong model dependence of the results. Cosmological models like the Λ CDM model aim to describe the evolution of the universe since the Big Bang. Although the Λ CDM model provides reasonably good agreement with observations [10], its validity gets tensioned by discrepancies most notably in direct estimates of the Hubble constant [108].

1.5.2 Search for the Neutrinoless Double Beta Decay

Another experimental approach to measure the neutrino mass is the search for the [neutrinoless double \$\beta\$ -decay \(\$0\nu\beta\beta\$ \)](#). In some nuclei, e. g. ^{76}Ge , the single beta decay is suppressed or forbidden in the SM when the nucleus will be in an energetically higher state than before the decay. Then, the only allowed decay mode is the [two-neutrino double \$\beta\$ -decay \(\$2\nu\beta\beta\$ \)](#). It was proposed by Goeppert-Mayer in 1935 [75] and experimentally observed in various isotopes yielding half-lives of $T_{1/2}^{2\nu} > 10^{18}$ yr (90 % CL) [128]. In this decay, two neutrons in the parent nuclei are converted into two protons via the weak interaction resulting in the emission of two electrons and two electron antineutrinos:



The experimental signature of $2\nu\beta\beta$ is a continuous energy spectrum with an endpoint value of $Q_{\beta\beta}$. For $0\nu\beta\beta$, however, one assumes that neutrinos are Majorana fermions [68]. As a consequence, the neutrinos released in the decay are emitted as virtual particles from the first vertex and absorbed by the second vertex as antineutrinos, hence being identical particles. The experimental signature for this decay is a Gaussian peak at $Q_{\beta\beta}$, whose width depends on the energy resolution of the detectors. The [Germanium Detector Array \(GERDA\)](#) experiment utilized high-purity germanium detectors on the search for $0\nu\beta\beta$ in the isotope ^{76}Ge [14]. The detectors were made from above 87 % isotopically enriched ^{76}Ge . This approach maximized the detection efficiency as source and detector coincide. The combined analysis of Phase I and II data provides a lower limit on the decay half-life of $T_{1/2}^{0\nu} > 1.8 \times 10^{26}$ yr (90 % CL) [14]. This limit can be converted into an upper limit on the effective Majorana neutrino mass of

$$m_{\beta\beta} = \left| \sum_{i=1}^3 U_{ei}^2 m_i \right| < (79 - 180) \text{ meV} \quad (1.15)$$

at 90 % CL, which is the coherent sum of the different neutrino mass eigenstates m_i weighted with the neutrino mixing elements U_{ei} of the [PMNS](#) matrix. The next generation experiment [LEGEND](#) will probe with an improved sensitivity beyond 10^{28} yr on the decay half-life of $0\nu\beta\beta$ [9]. For this project, [LEGEND](#) requires a detector in the tonne-scale. The collaboration aims to cover the inverted ordering region, which requires extremely low background despite a large exposure. The background levels have to be lowered by a factor of 5 compared to [GERDA](#) and [MAJORANA](#). In [LEGEND-200](#), the existing [GERDA](#) infrastructure at the [Laboratori Nazionali del Gran Sasso \(LNGS\)](#) in Italy is used to operate 200 kg of germanium detectors for an exposure of $1 \text{ t} \cdot \text{yr}$. In the following phase, [LEGEND-1000](#), 1000 kg of detectors will be operated for an exposure of $10 \text{ t} \cdot \text{yr}$. Compared to [LEGEND-200](#), the background needs to be reduced by another factor of 6 to remain in the background-free regime.

1.5.3 Limits from Direct Measurements

The most model-independent laboratory method to determine the neutrino mass is the direct measurement of the kinematics of the single β -decay or of [Electron Capture \(EC\)](#). In both cases, the effective mass m_β of the electron (anti)neutrino

$$m_\beta = \sqrt{\sum_{i=1}^3 |U_{ei}|^2 m_i^2} \quad (1.16)$$

is measured. This is the incoherent sum of the neutrino mass eigenstates.

The [KATRIN](#) experiment, which is described in detail in chapter 2, studies the single beta decay of molecular tritium T_2 . Tritium is an isotope of hydrogen and has the advantages of a short half-life of $T_{1/2} = 12.3$ yr and a low Q -value of 18.6 keV [101]. In this decay, a positive charged helium-tritium ion ${}^3\text{HeT}^+$, an electron as well as an electron antineutrino are produced:



The energy spectrum of the electron gives access to the effective mass of the neutrino. Figure 2.1 illustrates the impact of a non-zero neutrino mass on the spectral shape in the endpoint region. Most recently, the [KATRIN](#) collaboration could provide an upper limit of

$$m_\beta < 0.8 \text{ eV} \quad (1.18)$$

at 90 % CL being the first experiment reaching sub-eV sensitivity in a direct measurement [19].

The experiments [ECHO](#) [70] and [HOLMES](#) [63] on the other hand, investigate the [EC](#) reaction in the nuclide ${}^{163}\text{Ho}$. There, the imprint of a non-vanishing neutrino mass on the energy spectrum is similar to the [KATRIN](#) experiment. The energy released in the [EC](#) reaction causes a temperature rise in the absorber material. This change of temperature is read out by a sensitive thermal sensor. The experiments use [Metallic Magnetic Calorimeters \(MMCs\)](#) and [Transition-Edge Sensors \(TESs\)](#), respectively.

The Project 8 Experiment [60] takes a completely different approach compared to the [KATRIN](#) experiment, even though tritium gas is used there, too. Instead of measuring the kinetic energy of the β -decay electrons directly, it uses [Cyclotron Radiation Emission Spectroscopy \(CRES\)](#) to determine the cyclotron frequencies emitted from the electrons which are trapped inside a magnet field. Since the electron's cyclotron frequency depends on its kinetic energy, the neutrino mass can be derived identically as in the [KATRIN](#) experiment.

The KATRIN Experiment

The [Karlsruhe Tritium Neutrino \(KATRIN\)](#) experiment is designed to determine the effective electron antineutrino mass m_β in a direct measurement with a sensitivity of close to 0.2 eV (90 % CL) in a total measurement time of about 1000 days [49]. It is supplied by the [Tritium Laboratory Karlsruhe \(TLK\)](#) and located on the Campus North site of the [Karlsruhe Institute of Technology \(KIT\)](#). The experiment is the successor of the previous neutrino mass experiments in Mainz [89] and Troitsk [32] which were able to set an combined upper limit on $m_\beta < 2.2$ eV (95 % CL). Starting operation with calibration sources in 2016 [29] and measurements with tritium in 2018 [20], the [KATRIN](#) collaboration could improve the previous neutrino mass limit by a factor of two to $m_\beta < 1.1$ eV (90 % CL) [18] in 2019 after a measurement period of only four weeks. In 2022, the [KATRIN](#) experiment reached an unprecedented sub-eV sensitivity and could further improve the neutrino mass limit to $m_\beta < 0.8$ eV (90 % CL) [19] by combining the results from its first and second neutrino mass campaigns. If the neutrino mass was $m_\beta > 0.35$ eV, a 5σ discovery would be possible [49].

In the following, a brief overview of the measurement principle of the experiment is given in section 2.1 combined with the technical realization in section 2.2. After the neutrino mass measurement campaign is completed, the [KATRIN](#) experiment will be equipped with a novel detector system to search for a hypothetical sterile neutrino in the keV-mass range. This upgrade will be discussed in section 2.3.

2.1 Measurement Principle

The **KATRIN** experiment is investigating the kinematics of the tritium β -decay described in eq. (1.17). From this, the neutrino mass m_β can be derived. The differential decay rate can be calculated according to Fermi's theory [64] by

$$\frac{d\Gamma(E, m_\beta)}{dE} \propto C \cdot F(Z, E) \cdot (E + m_e) \cdot p \cdot (E_0 - E) \cdot \sqrt{(E_0 - E)^2 - m_\beta^2}. \quad (2.1)$$

It depends on the Fermi function $F(Z, E)$ [117] and the kinetic energy E , momentum p and mass m_e of the electron. The maximum kinetic energy E_0 defines the spectral endpoint in case $m_\beta = 0$. The constant

$$C = \frac{G_f^2}{2\pi^3 \hbar^7 c^5} \cdot \cos^2 \theta_c \cdot |M_{\text{nuc}}|^2 \quad (2.2)$$

is composed of the Fermi constant G_f , the Cabibbo angle θ_c as well as the nuclear transition matrix element M_{nuc} . A visual representation of equation 2.1 is given in figure 2.1.

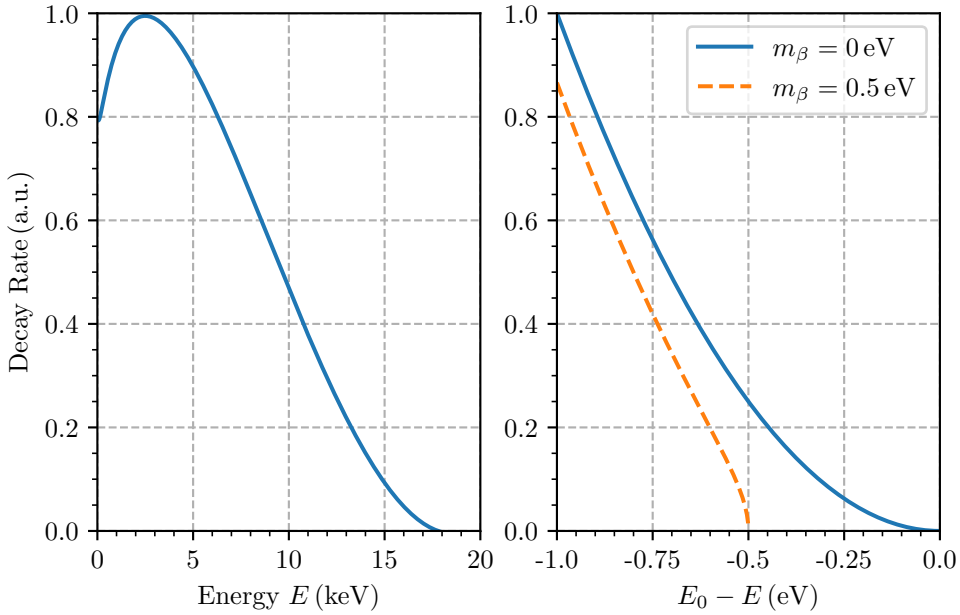


Figure 2.1: **Tritium β -Decay Spectrum and Endpoint Region**

In the left graph, the energy spectrum of the tritium β -decay is illustrated for a massless neutrino. The decay rate is normalized to its maximum value. The right plot depicts the endpoint region of the spectrum located at $E_0 = 18.574$ keV [19]. The orange dashed line demonstrates the impact of a massive neutrino of $m_\beta = 0.5$ eV on the spectral shape.

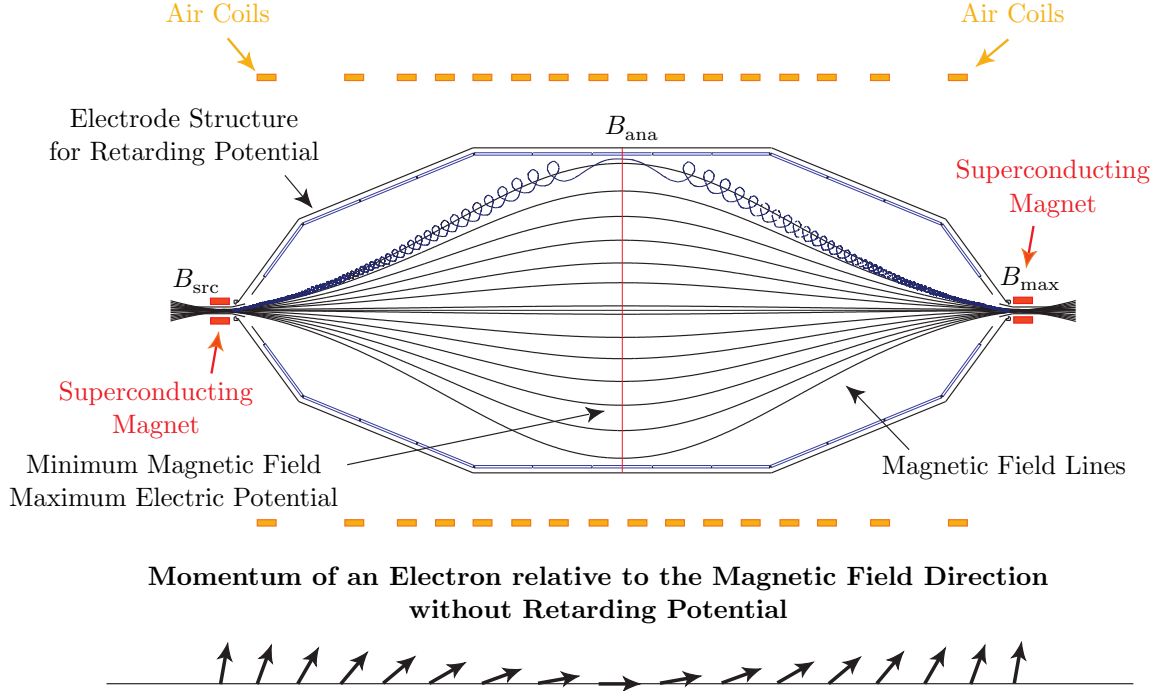


Figure 2.2: **Schematic Drawing of the KATRIN Main Spectrometer**

The **KATRIN** main spectrometer makes use of the **MAC-E** filter principle. Superconducting magnets are positioned at the front and rear end of the spectrometer vessel and create a magnetic field. The magnetic field lines guide the electrons in cyclotronic motion (blue example trajectory) from the source magnet field B_{src} to the maximum magnetic field B_{max} . At the analyzing plane, the minimal magnetic field B_{ana} and the maximum electric retarding potential are located. The retarding potential is generated by the electrode structure inside the vessel and forms a negative electrostatic barrier, which reflects the electrons below a certain energy threshold. The adiabatic transformation of the transversal momentum of the electron motion into longitudinal momentum is illustrated by the black arrows. The figure is adapted from [82].

A non-zero neutrino mass manifests itself at the spectral endpoint, where the term $(E_0 - E)$ vanishes. The maximum kinetic energy of the electron is reduced by the effective rest mass of the neutrino. This shifts the endpoint towards lower energies leading to a local spectral distortion. Conventional particle detectors are not capable of resolving this shift as an energy resolution in the order of 1 eV is required. Hence, the **Magnetic Adiabatic Collimation combined with an Electrostatic filter (MAC-E)** principle is applied in the **KATRIN** experiment. Proposed by Kruit and Read in 1983 [90] and adapted for neutrino mass measurements by Lobashev and Spivak in 1985 [95], this technology has already been deployed in the Mainz and Troitsk neutrino mass experiments. The working principle of a **MAC-E** spectrometer is depicted in figure 2.2. Superconducting solenoid magnets at the up- and downstream end of the spectrometer vessel create a magnetic field which guides the β -electrons on a cyclotron motion (caused by the Lorentz force) from the tritium source from one end towards the detector on the other

end. The magnetic field B is strong at both ends and drops by four orders of magnitude towards the center. By applying a retarding potential U to the electrodes, the spectrometer acts as a high-pass filter. Only electrons carrying an energy $E = E_{\parallel} + E_{\perp}$ larger than the retarding energy eU can overcome this electrostatic barrier. As the electric potential is perpendicular to the magnetic field, this filter is only sensitive to the longitudinal component E_{\parallel} of the electron energy. Hence, E_{\perp} has to be reduced significantly. This is achieved by magnetic adiabatic collimation: The transversal momentum p_{\perp} of the electron motion is adiabatically transformed into a longitudinal one keeping the electron magnetic moment μ constant:

$$\mu = \frac{E_{\perp}}{B} \propto \frac{p_{\perp}^2}{B} = \text{const.} \quad (2.3)$$

The parallel beam of electrons is filtered at the so-called analyzing plane, where the weakest magnetic field B_{ana} and the highest retarding energy eU are present. While electrons with enough energy to surpass the electrostatic barrier are re-accelerated and collimated onto a detector, those with lower energies than the retarding energy are reflected. The energy resolution ΔE of the spectrometer is determined by the remaining transversal component of the electron kinetic energy:

$$\Delta E = E \cdot \frac{B_{\text{ana}}}{B_{\text{max}}}. \quad (2.4)$$

Thus, minimizing the ratio of the minimal B_{ana} and maximal B_{max} magnetic fields leads to better energy resolution. For the [KATRIN](#) experiment, the design value of the spectrometer resolution is $\Delta E = 0.93$ eV ([Full Width at Half Maximum \(FWHM\)](#))¹ at $E = 18.574$ keV, $B_{\text{ana}} = 3 \times 10^{-4}$ T, and $B_{\text{max}} = 6$ T.

The variation of the retarding energy eU allows the acquisition of an integral tritium spectrum

$$\Gamma(eU, m_{\beta}) = \int_{eU}^{E_0} dE \frac{d\Gamma(eU, m_{\beta})}{dE}. \quad (2.5)$$

During each so-called run, the count rate is measured for a fixed retarding energy with a silicon [Positive-Intrinsic-Negative \(PIN\)](#) diode positioned at the downstream end of the spectrometer. A more detailed description of the detector and other individual components of the [KATRIN](#) experiment is given in section 2.2.

¹The energy resolution is always stated in [FWHM](#) in this thesis.

2.2 Technical Realization

This section provides an overview of the setup of the **KATRIN** experiment. The 70 m-long beam line of the experiment is shown in figure 2.3. It is divided into multiple components, the **Rear Section** (section 2.2.1), the **Windowless Gaseous Tritium Source** (section 2.2.2), the Transport Section (section 2.2.3), the Spectrometer Section (section 2.2.4), and the **Focal Plane Detector** (section 2.2.5). In addition, several Monitoring Devices (section 2.2.6) are installed which supervise the operation. The **KATRIN** Design Report [49] is the primary source of information unless otherwise stated.

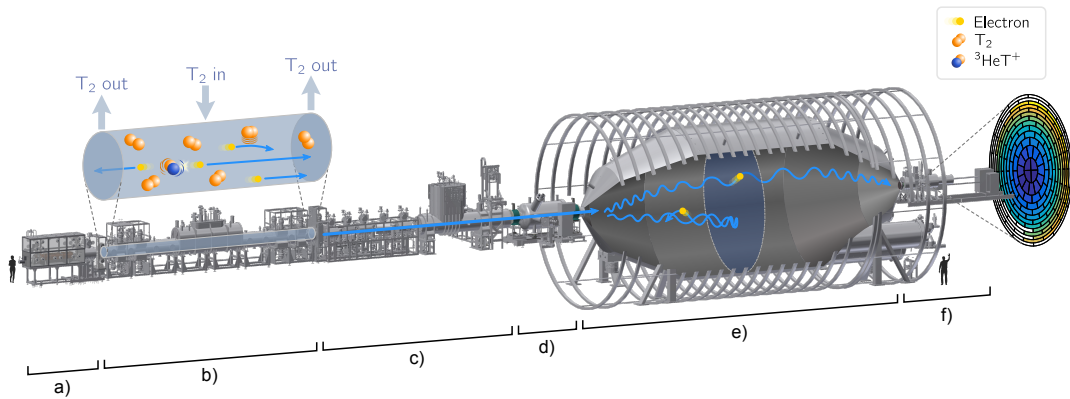


Figure 2.3: **Experimental Setup of the **KATRIN** Experiment**

- a): The **Rear Section** terminates the **KATRIN** beam line at the rear end and houses the **Rear Wall** as well as multiple calibration and monitoring devices.
 - b): Molecular tritium is injected into the **Windowless Gaseous Tritium Source** and decays.
 - c): The β -electrons are guided in the Transport Section to the Spectrometer Section. At the same time, the tritium flow is reduced by 14 orders of magnitude by a series of pumping sections.
 - d): The pre-spectrometer reflects low-energetic electrons that cannot be utilized for the neutrino mass determination.
 - e): By applying a large negative potential on the electrode structure of the main spectrometer, only electrons close to the endpoint of the tritium spectrum are transmitted.
 - f): The β -electrons, which could surpass the retarding potential, are counted on the **Focal Plane Detector** at the front end.
- The figure is adapted from [19].

2.2.1 Rear Section

The **Rear Section (RS)** is located at the rear end of the **KATRIN** beam line and terminates the setup. It consists of a **Differential Pumping Section (DPS)** and the **Calibration and Monitoring System (CMS)**. The pumps of the **DPS** have to reduce the tritium pressure to protect the **CMS** which houses a photoelectric **Electron Gun (e-gun)** and the **Rear Wall (RW)**. The **e-gun** is used for calibration purposes and measurements of the source activity as well as of the electron transmission properties. The **RW** is a gold-coated stainless steel disk with a diameter of 14.6 cm that defines the electric ground potential of the tritium source relative to the spectrometer voltage. All low-energy electrons reflected by the spectrometers are guided back to the rear wall. The gold coating lowers the probability of backscattering of these electrons and therefore reduces systematic uncertainties.

2.2.2 Windowless Gaseous Tritium Source

Attached to the **RS**, the **Windowless Gaseous Tritium Source (WGTS)** acts as a source for molecular tritium gas T_2 . The tritium is injected in the center of the 10 m-long stainless steel tube of 90 mm diameter and streams towards both sides while undergoing β -decay. The gas is removed by a series of pumps of a **DPS** located at the ends and re-injected into the **WGTS** [105]. Hence, it circulates in a closed loop system with a throughput of 40 g per day. To maintain the extremely high (1.7×10^{11} Bq) and stable ($\pm 0.1\%$) tritium decay rate, the gas is refurbished to ensure a constant and high tritium purity of $\epsilon_T > 95\%$. In addition, the **WGTS** is situated in **Liquid Neon (LNe)** and **Liquid Helium (LHe)** cryostats to provide a low source temperature of $T = 30$ K preserving a column density of $\rho d = 5 \times 10^{17}$ molecules/cm² which is monitored by a **Laser Raman (LARA)** system [113]. Moreover, a set of superconducting solenoid magnets surrounds the central beam tube. Since electrons are emitted isotropically in the decay, the source magnetic field is set to $B_{\text{src}} = 2.5$ T to maximize the number of electrons that can be directed in the downstream path.

2.2.3 Transport Section

The transport section of the beam line guides the electrons emitted in the β -decay from the tritium source to the spectrometer section. At the same time, the tritium flow is reduced by 14 orders of magnitude from $1.8 \text{ mbar} \cdot \text{l/s}$ to $10^{-14} \text{ mbar} \cdot \text{l/s}$, as the main spectrometer is required to be quasi tritium-free. This is achieved by a series of pumping sections. The **DPS** is operated at a temperature of $T = 77$ K and equipped with **Turbo Molecular Pumps (TMPs)**. The **TMPs** recover the residual tritium gas which is re-injected back into the **WGTS**. Following the **DPS**, any remaining traces of tritium will be trapped onto the argon-covered tube surface of the **Cryogenic Pumping Section (CPS)**. This surface layer is sustained

at a temperature of $T = 3\text{ K}$ and has to be purged with helium after 60 days of operation to remove the collected tritium molecules. Similar to the [DPS](#), the [CPS](#) is also surrounded by superconducting solenoid magnets which guide the electrons with magnetic fields up to 5.6 T. The individual transport elements are tilted by 20° to each other to prevent a direct line of sight.

2.2.4 Spectrometer Section

The spectrometer section consists of two separate components: the pre- and the main spectrometer. Both make use of the [MAC-E](#) principle, explained in section 2.1. Attached to the [CPS](#), the pre-spectrometer is a 3.4 m-long vessel with a diameter of 1.7 m. Its design purpose was to reduce the β -electron flow by operating it about 300 eV below the endpoint of the tritium β -spectrum, i.e. at -18.3 kV . This reflects all low-energy electrons, which do not carry information on the neutrino mass. However, a penning trap formed between the pre- and main spectrometer, resulting in time-dependent background effects. Therefore, the pre-spectrometer was switched off in later neutrino mass campaigns. The main spectrometer is the centerpiece of the [KATRIN](#) experiment. It sustains a vacuum of 10^{-11} mbar inside its vessel volume of 1240 m^3 . The spectrometer is 23.3 m long and has a maximal diameter of 9.8 m. This guarantees adiabatic motion of the electrons and ensures the conservation of the magnetic flux tube in the analyzing plane. There, the magnetic field has its minimum value of $B_{\text{ana}} = 6.3 \times 10^{-4}\text{ T}$, resulting in a spectrometer energy resolution of $\Delta E = 2.8\text{ eV}$ ([FWHM](#)). The wire electrode system installed at the inner walls of the spectrometer allows for a precise shaping of the electric field and also reduce the impact of background originating from cosmic muons, ambient or intrinsic radioactivity [[131](#)]. In addition, a magnetic air coil system surrounding the spectrometer also enables accurate shaping of the magnetic field and compensates for the earth magnetic field [[73](#)]. The pinch magnet at the downstream end of the vessel restricts electrons being transmitted to the detector above a certain polar angle. Combing the source magnetic field with the pinch magnetic field $B_{\text{max}} = 4.2\text{ T}$, the polar acceptance angle yields [[19](#)]

$$\theta_{\text{max}} = \arcsin\left(\sqrt{\frac{B_{\text{src}}}{B_{\text{max}}}}\right) = 50.4^\circ. \quad (2.6)$$

All electrons with emission angles below θ_{max} will be detected.

2.2.5 Focal Plane Detector

The [Focal Plane Detector](#) ([FPD](#)) is a silicon [PIN](#) diode segmented into 148 pixels of equal area. It is located at the front end of the beam line and counts the electrons at different retarding potentials, from which the integral tritium spectrum is obtained. The detector is arranged in a ring-wise structure allowing to map and investigate the radial and azimuthal dependence of the electron trajectories through

the beam line. In total, there are twelve rings with twelve pixels each and four pixels in the center. The detector is operated inside a vacuum of $< 10^{-9}$ mbar as it is coupled to the main spectrometer. To achieve an average energy resolution of 1.52 keV (FWHM) for photoelectrons with an energy of 18.6 keV [27], the detector is cooled with Liquid Nitrogen (LN₂) to reduce the leakage current and electronic noise. Furthermore, a Post Acceleration Electrode (PAE) accelerates the electrons with additional 12 kV since the intrinsic detector background is reduced at higher energies.

2.2.6 Monitoring Devices

In addition to the components required for the operation of the KATRIN experiment, there are several monitoring devices in the KATRIN facility, two of which are briefly highlighted. The Forward Beam Monitor (FBM) is a silicon detector placed inside the CPS. It can be moved into the flux tube to directly monitor the rate of the β -electrons and therefore the stability of the tritium source [59]. Another monitoring device is the Monitor Spectrometer (MoS). It was originally used as for the MAC-E principle in the Mainz neutrino mass experiment and was repurposed to monitor the long-term High Voltage (HV) stability of the main spectrometer [118]. The MoS also serves as test stand for characterization measurements since it is equipped with an e-gun and a ^{83m}Kr source.

2.3 keV-scale sterile Neutrino Search with the KATRIN Experiment

The search for a hypothetical sterile neutrino in the keV-mass range will succeed the neutrino mass measurement campaign of the KATRIN experiment. Although the KATRIN experiment is not able to resolve the individual neutrino mass eigenstates but only the effective neutrino mass of the electron antineutrino, a sterile neutrino would manifest itself as a kink and broad distortion in the continuous electron energy spectrum of the tritium β -decay, see figure 2.4. The total differential decay rate can be written as a superposition of active and sterile components [11]

$$\frac{d\Gamma_{\text{tot}}}{dE} = \underbrace{\cos^2(\theta_s) \frac{d\Gamma(m_\beta)}{dE}}_{\text{Active Term}} + \underbrace{\sin^2(\theta_s) \frac{d\Gamma(m_4)}{dE}}_{\text{Sterile Term}}, \quad (2.7)$$

which are related via the active-sterile mixing angle θ_s . The mixing amplitude $\sin^2(\theta_s)$ determines the strength of the distortion of the spectrum and is approximately equal to the matrix element $|U_{e4}|^2$ of equation 1.6. In contrast, the position of the kink depends on the mass m_4 of the sterile neutrino. This set of parameters opens up the parameter space for the sterile neutrino search.

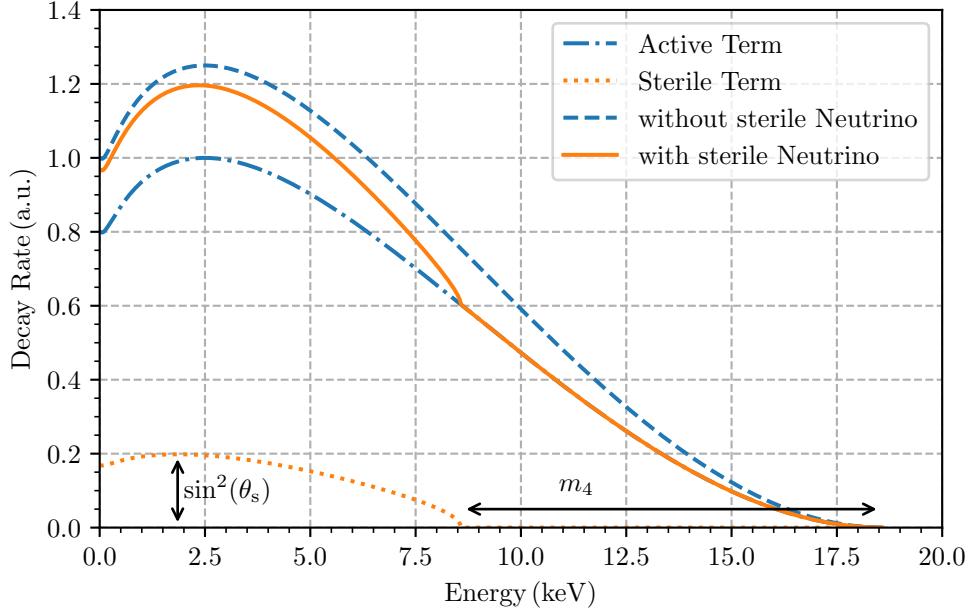


Figure 2.4: **Tritium β -decay Spectrum with Sterile Neutrino Admixture**

The tritium spectrum is illustrated for a sterile neutrino with mass $m_4 = 10$ keV and exaggerated mixing amplitude of $\sin^2(\theta_s) = 0.2$. The active and sterile terms of equation 2.7 demonstrate the influence of the individual components on the total decay rate.

The combination of the strong tritium source and the high resolution spectrometer of the **KATRIN** beam line offers the ideal conditions for this challenging operation. Based on a measurement time of three years, the **KATRIN** experiment can probe for the existence of a sterile neutrino down to $\sin^2(\theta_s) < 10^{-6}$ in its most sensitive mass region at about 12 keV [98]. However, since the mass of the sterile neutrino is unknown, the entire range of the tritium β -decay spectrum must be scanned. This requires lowering the retarding potential of the main spectrometer and results in an increased signal rate at the detector. Compared to the standard **KATRIN** operation, the rate will be several orders of magnitude higher. These high count rates exceed the capabilities of the current **KATRIN** detector system.

The **Tritium Investigations on Sterile to Active Neutrino mixing (TRISTAN)** detector and readout system is currently being developed and will replace the **KATRIN FPD** system. Both, the integral and differential, measurement modes are considered, such that a potential positive signal on a sterile neutrino can be verified independently. Consequently, several requirements are placed on this system to measure a keV-scale sterile neutrino at the ppm-level.

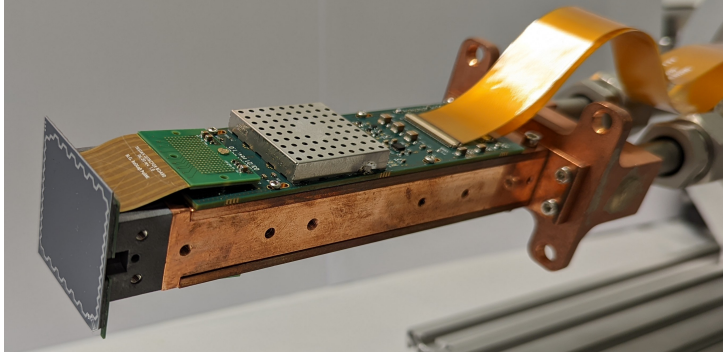


Figure 2.5: **TRISTAN Detector Module with 166 Pixels**

A single TRISTAN detector module is equipped with a monolithic silicon wafer of 166 pixels utilizing the [SDD](#) technology (see section 3.2). The Kapton cables connect the detector chip with the detector [Printed Circuit Boards \(PCBs\)](#), which houses the [ETTORE ASICs](#) (see section 3.5) and the components required for the operation of the detector. Due to the large number of pixels, two [PCBs](#) are placed on the copper cooling structure, one at the top and one at the bottom. The metal shield covers the [ASICs](#) and protects them from [Electromagnetic Interference \(EMI\)](#). The flexible flat cables supply the detector with the bias voltages and transmit the signals to the outside world. Since the detector modules are operated in [Ultra-High Vacuum \(UHV\)](#), all components must be vacuum-compatible.

Detector Requirements The detector must be able to handle high count rates of $\mathcal{O}(10^8 \text{ cps})$. To reduce the rate to a manageable level and minimize the pile-up probability, the detector is segmented into ~ 3500 pixels to distribute the rate to $\mathcal{O}(10^5 \text{ cps/pixel})$ [98]. The pixels are of hexagonal shape to minimize the uncovered detection area. Figure 2.5 shows a single [TRISTAN](#) detector module with 166 pixels. In 2022, one of these modules was installed in the [MoS](#) and characterized with electrons as well as a $^{83\text{m}}\text{Kr}$ source [44]. For the first keV-scale sterile neutrino measurement phase, called Phase 1, nine modules will be combined and installed in the [KATRIN](#) beam line to replace the current detector. A schematic drawing of the detector system of Phase 1 is shown in figure 2.6. In Phase 2, the detector will be upgraded to its full potential of 21 modules. The energy resolution of the detector is targeted to be less than 300 eV at 20 keV for electrons [99]. This is necessary to resolve the small kink-like distortion in the electron spectrum. A small detector capacitance as well as cooling the detector to lower the leakage current reduces the overall electronic noise. An entrance window with a thickness of only $\mathcal{O}(50 \text{ nm})$ further improves the energy resolution [99]. The entrance window is an insensitive area on the detector surface, where the generated charge is not fully collected. As a result, not all of the deposited energy can be reconstructed, which results in a systematic uncertainty in the model. In order to overcome the challenge of pile-up, a post acceleration of (10 – 20) kV is considered. At the same time, the energy loss in the entrance window is reduced as well as the effect of electron backscattering of the detector surface due to lower incident angles [18]. The electron backscattering was investigated for a [TRISTAN](#) detector module with a custom-designed [e-gun](#) [120].

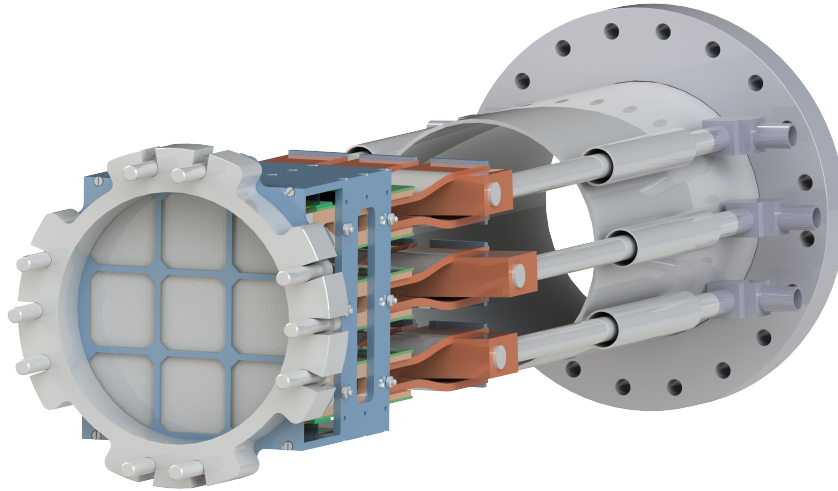


Figure 2.6: **Experimental Setup of the TRISTAN Detector for Phase 1**

For Phase 1 of the keV-scale sterile neutrino search, the TRISTAN detector is composed of nine detector modules, which are mounted inside a metal housing. The detector system is positioned at the front end of the KATRIN beam line inside UHV. A vacuum shield is placed in front of the detector to minimize the impact on the Extreme-High Vacuum (XHV) in the main spectrometer due to outgassing of the PCB and its components. The detector modules are connected to pipes that supply coolant and keep the detector at a stable operating temperature.

Courtesy to S. Lichter.

Readout Electronics For the detector readout, components with minimal noise contribution are required. An Application-Specific Integrated Circuit (ASIC) is part of the Charge Sensitive Pre-Amplifier (CSA) circuit and needs to provide high Bandwidth (BW) for short signal rise times. The ETTORÉ ASIC was developed for the TRISTAN detector and readout system and fulfills these requirements [129]. A detailed description of this ASIC is given in section 3.5.

Data Acquisition System High resolution Analog-to-Digital Converters (ADCs) of $\sigma_{\text{ADC}} = (14 - 16)$ bit and sampling rates of $\mathcal{O}(100 \text{ MHz})$ are preferred for accurate event discrimination, e. g. pile-up and charge sharing. The non-linearities of the ADCs must be well understood as they could resemble a sterile neutrino signature [56]. The Field-Programmable Gate Array (FPGA) used inside of the Digital Pulse Processor (DPP) must be capable of handling different signal types (e. g. the full signal waveform, histograms, etc.) and also pre-processing the data to reduce the amount of computation time and storage required for subsequent analysis. Furthermore, the DPP is needed to be HV compatible keeping readout lines short and thus avoiding unwanted additional noise components in the signal. The Institute for Data Processing and Electronics (IPE) at the KIT currently develops a Data Acquisition System (DAQ) which meets these requirements.

The TRISTAN Detector and Readout System

The TRISTAN detectors make use of the so-called Silicon Drift Detector (SDD) technology because it is well suited for the search of a sterile neutrino in the keV-range. This chapter focuses on the physical aspects of the TRISTAN detectors and the signal readout. An introduction to semiconductors and SDDs is given in sections 3.1 and 3.2. The TRISTAN detectors are presented in section 3.3. Section 3.4 provides a detailed description of the signal formation inside the SDDs. Concluding this chapter, section 3.5 describes the signal readout from the detector.

3.1 Basics of Semiconductors

Silicon (Si) is the most widely used semiconductor material in the world today [85]. Unlike in conductors, in which electrons can move freely between the valence and conduction band, and in insulators, in which electrons cannot move into the conduction band at all, the gap between valence and conduction band in semiconductors is small enough that a valence electron can be elevated into the conduction band if it gains sufficient thermal energy. The concept of valence and conduction bands is shown in figure 3.1a. The valence band is the highest occupied energy level inside a solid whereas the conduction band is the next higher-positioned non-populated energy level. The energy difference between both levels is called band gap E_g . When an electron is lifted into the conduction band, a hole is created in the valence band, indicated by filled and non-filled circles, respectively. The number of free electrons in the conduction band [123]

$$n = \int_{E_c}^{\infty} N(E)F(E) dE \quad (3.1)$$

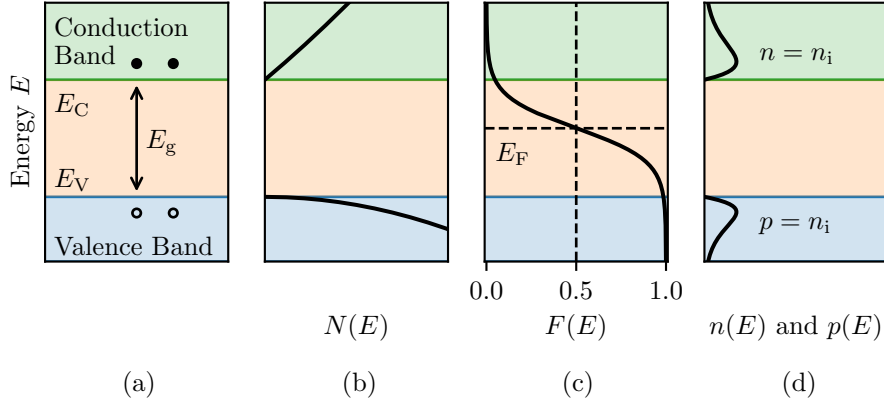


Figure 3.1: **Concept of Valence and Conduction Band in Semiconductors**

(a): The difference between the lower edge of the conduction band, E_C , and the upper edge of the valence band, E_V , defines the band gap E_g . When an electron (filled circle) has enough energy to overcome E_g , it is lifted into the conduction band, and leaves a hole (non-filled circle) in the valence band.

(b): For electrons, the density of states $N(E)$ describes the number of free states available for occupation at a certain energy. Increasing the energy of an electron in the conduction band makes more states available. The opposite holds in the valence band. Within the band gap, however, no states can be occupied.

(c): The Fermi-Dirac distribution $F(E)$ gives the probability of a certain energy level E being occupied by an electron for a specific temperature T . The point of symmetry, i. e. the Fermi level E_F , has a probability of 50% of being occupied and is located close to the center of the band gap. Hence, semiconductors are electrically neutral. With increasing energy, the probability of electrons occupying higher energy states decreases. While all states in the valence band are occupied, almost none in the valence band are taken.

(d): The concentration of free electrons $n(E)$ and holes $p(E)$ present in the conduction and valence band of an intrinsic semiconductor.

The figure is adapted from [110].

depends on its lower energy bound E_C , the density of states $N(E)$, and the Fermi-Dirac distribution $F(E)$. Figure 3.1b illustrates $N(E)$, which itself calculates as [123]

$$N(E) dE = 4\pi \left(\frac{2m_n}{h^2} \right)^{2/3} \sqrt{E} dE . \quad (3.2)$$

Here, m_n denotes the effective mass of the electron. It describes the apparent mass of the electron that it seems to have during movements inside a crystal and is related to the effective mass of the hole via $m_n = -m_p$. The Fermi-Dirac distribution can be approximated in the conduction band by [110]

$$F(E) = \frac{1}{1 + \exp\left(\frac{E-E_F}{k_B T}\right)} \approx \exp\left(-\frac{E-E_F}{k_B T}\right), \quad (3.3)$$

as the Fermi level E_F is close to the center of the band gap. This is depicted in figure 3.1c. The concentration of free electrons n and holes p is obtained by substituting equations 3.2 and 3.3 into equation 3.1 and calculating the integral [110]:

$$n = 2 \underbrace{\left(\frac{2\pi m_n k_B T}{h^2} \right)^{3/2}}_{N_C} \exp\left(-\frac{E_C - E_F}{k_B T} \right), \quad (3.4)$$

$$p = 2 \underbrace{\left(\frac{2\pi m_p k_B T}{h^2} \right)^{3/2}}_{N_V} \exp\left(-\frac{E_F - E_V}{k_B T} \right). \quad (3.5)$$

The concentrations of the free charge carriers are shown in figure 3.1d. The lower edge of the conduction band E_C and the upper edge of the valence band E_V define the band gap $E_g = E_C - E_V$ and restrict the charge carriers to their corresponding bands. For silicon, the band gap is $E_g = 1.12$ eV at room temperature $T = 300$ K [87]. The effective density of states in the conduction and valence band, N_C and N_V , are related to the effective electron and hole masses, m_n and m_p , and have values of $N_C = 2.8 \times 10^{19} \text{ cm}^{-3}$ and $N_V = 1.04 \times 10^{19} \text{ cm}^{-3}$ [122]. From the product of the electron and hole concentrations the intrinsic carrier concentration can be derived for silicon at $T = 300$ K [110]:

$$n_i = \sqrt{np} = \sqrt{N_C N_V \exp\left(-\frac{E_g}{k_B T} \right)} = 1.45 \times 10^{10} \text{ cm}^{-3}. \quad (3.6)$$

Semiconductors are called intrinsic when the concentration of impurities is negligible compared to the thermally generated free electrons and holes. However, in most cases the material used for semiconductor devices is not purely intrinsic. Instead, small fractions of other materials are placed into the crystal structure of the semiconductor to alter its conductivity. This process is called doping. Doping can be achieved e. g. by ion implantation, by diffusion of dopants or by epitaxy. The most commonly used silicon dopants include phosphorus as electron donor for negative n-type and boron as electron acceptor for positive p-type doping. Donors release an extra electron into the conduction band of the semiconductor, whereas acceptors produce a hole in the valence band due to a missing electron in their outer shell. The donors introduce shallow energy levels very close to the conduction band in the forbidden energy region of the band gap. For acceptors, the energy levels are very close to the valence band. At room temperature, the electron concentration n is equal to the doping concentration of the donor atoms N_D as all donor states are ionized, assuming no other doping is present. The same holds for the hole concentration p and the acceptor concentration N_A as all acceptor atoms are ionized. Since the electron concentration is increased in n-type material, they are called majority carriers while holes are named minority carriers. In p-type material, holes are the majority carriers while electrons are the minority carriers. In practise, an effective doping concentration

$$N_{\text{eff}} = |N_D - N_A| \quad (3.7)$$

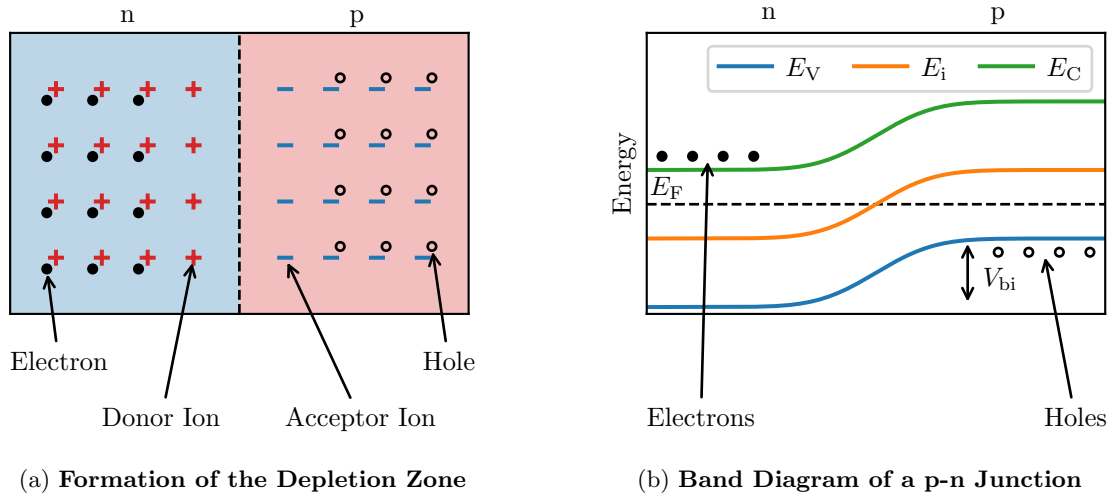


Figure 3.2: **Processes at a p-n Junction**

(a): When n-type and p-type doped semiconductor materials are combined, the majority carriers of the n-type materials, the electrons, diffuse into the p-type material and recombine with its majority carriers, the holes, in the region close to the junction. Vice versa, the holes from the p-type material diffuse into the n-type material and recombine with the electrons. The remaining donor and acceptor ions of the dopants are electrically charged and create an electric field, the space charge region, which counteracts the diffusion processes. In thermal equilibrium, the diffusion and drift current cancel each other and a volume without free charge carriers is formed: the depletion zone.

(b): The band diagram illustrates the energy states at a p-n junction. The valence band edge E_V , the intrinsic Fermi level E_i and the conduction band edge E_C vary continuously due to the sparse distribution of the dopants. This effect is known as band bending and describes the curving of energy states near a junction. The Fermi level E_F of the p-n junction is depicted by the horizontal dashed line. The built-in voltage V_{bi} is the result of the different Fermi potentials of the n-type and p-type doped materials.

is defined as semiconductors can contain several dopings and electrically active defects. It can be determined from the full depletion voltage in equation 3.13.

Semiconductors find their application in many devices, e.g. diodes, transistors, and particle detectors. These devices are based on Russell's discovery of the p-n junction in Si in 1940 [109]. A p-n junction is the transition between a p-type and n-type doped semiconductor material inside a single crystal. When p- and n-typed doped materials are brought together, some of the majority charge carriers diffuse into the opposite doped side due to the concentration difference. They recombine with the majority carriers located there and produce a region close to the junction which is depleted from free charge carriers. Figure 3.2a visualizes this depletion zone which only contains donor and acceptor ions without their reversely charged free carriers. Hence, this region is electrically charged, giving it also the name space charge region. This space charge region creates an electric field, which counteracts the diffusion process

and is characterized by the built-in voltage V_{bi} . When the thermal equilibrium is reached, the diffusion and drift current cancel each other. The built-in voltage for an abrupt p-n junction with constant doping concentrations on both sides is

$$V_{\text{bi}} = \frac{k_{\text{B}}T}{e} \ln\left(\frac{n_{0,\text{n}}p_{0,\text{p}}}{n_i^2}\right) \approx \frac{k_{\text{B}}T}{e} \ln\left(\frac{N_{\text{D}}N_{\text{A}}}{n_i^2}\right). \quad (3.8)$$

The electron concentration $n_{0,\text{n}}$ in the n-doped side and the hole concentration $p_{0,\text{p}}$ in the p-doped side are replaced with the concentration of donors, N_{D} , and acceptors, N_{A} , since a complete ionization of donors and acceptors can be assumed in most cases. The band diagram in figure 3.2b illustrates the formation of this built-in voltage.

Applying an external voltage in the same direction as the built-in voltage is called reverse biasing. From either side, further majority carriers are removed and the space charge region is extended. This is shown in figure 3.3a. Solving Poisson's equation in one dimension

$$\frac{d^2V}{dx^2} = -\frac{Ne}{\epsilon_0\epsilon_{\text{Si}}}, \quad (3.9)$$

which describes the potential as a function of the externally applied voltage V (see figure 3.3d) across a silicon p-n junction with doping concentration N and relative permittivity ϵ_{Si} , allows to calculate the width of the depletion zone [110]

$$W = x_{\text{n}} + x_{\text{p}} = \sqrt{\frac{2\epsilon_0\epsilon_{\text{Si}}}{e} \left(\frac{1}{N_{\text{A}}} + \frac{1}{N_{\text{D}}}\right) (V + V_{\text{bi}})}, \quad (3.10)$$

where x_{n} and x_{p} are the part of the zone in the respective n- and p-type doped sides. The elementary charge e and the vacuum permittivity ϵ_0 are physical constants. P⁺-n junctions are usually realized by a highly doped ($N_{\text{A}} > 10^{18} \text{ cm}^{-3}$) p⁺-implant in a low-doped ($N_{\text{D}} \approx 10^{12} \text{ cm}^{-3}$) n-bulk material. The space charge region reaches much deeper into the lower doped side of the junction, as visualized in figure 3.3b. Hence, the term $1/N_{\text{A}}$ in equation 3.10 can be neglected as well as the built-in voltage V_{bi} since, in most cases, the external applied voltage V is higher by a factor $\mathcal{O}(100)$. These assumptions result in the widely used formula for calculating the depletion width:

$$W \approx x_{\text{n}} \approx \sqrt{\frac{2\epsilon_0\epsilon_{\text{Si}}}{eN_{\text{D}}} V}. \quad (3.11)$$

The maximum value of the electric field

$$E_{\text{max}} = \frac{2V}{W} \approx \sqrt{\frac{2eN_{\text{D}}}{\epsilon_0\epsilon_{\text{Si}}} V} \quad (3.12)$$

is reached at the junction as shown in figure 3.3c. The electric field decreases linearly towards the

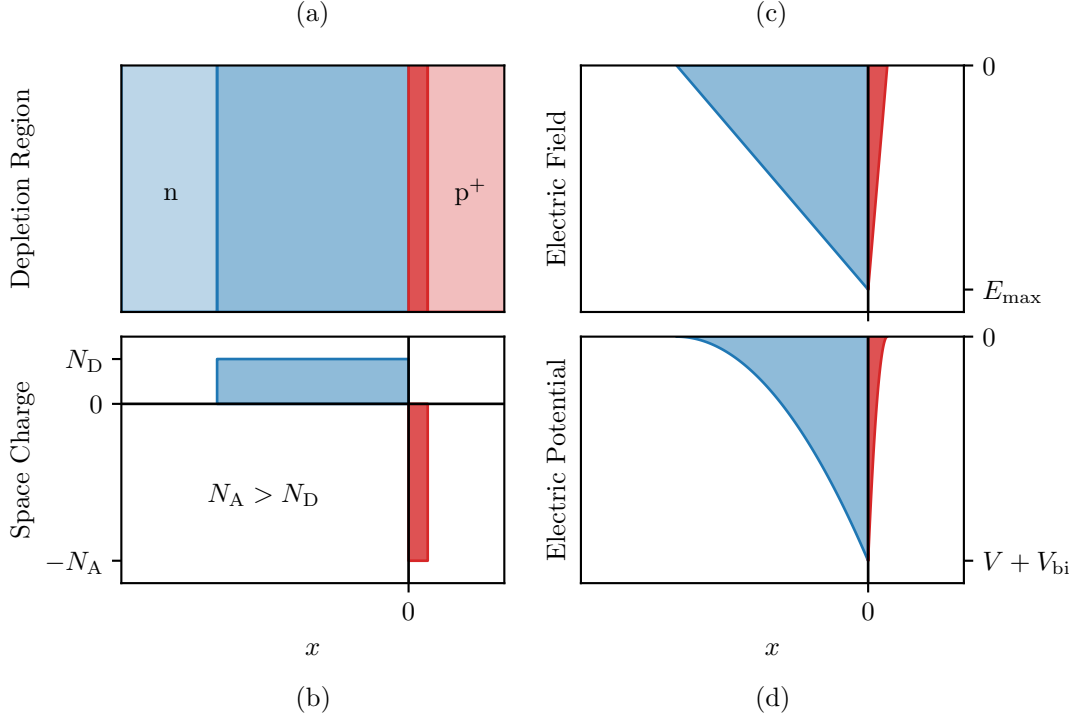


Figure 3.3: **Reverse Biasing of a p⁺-n Junction**

(a): Applying an external voltage in the same direction as the built-in voltage, i. e. connecting the negative terminal of a voltage source to the p⁺-type doped material and the positive terminal to the n-type doped material, removes further majority carriers from both materials and extends the space charge region. This region is illustrated by the darker colored areas. For low-doped n-type and high-doped p⁺-type material, the depletion zone reaches deeper into the n-type material. The total width depends on the doping concentrations and the built-in and external voltages.

(b): The space charge region of the p⁺-n junction is characterized by the different concentrations of the donor N_D and acceptor N_A dopants. P⁺-n junctions are usually realized by a highly doped p⁺ implant in a low-doped n-bulk material.

(c): The electric field across the p⁺-n junction reaches its maximum value E_{\max} directly at the junction and decreases linearly towards the end of the space charge region.

(d): The electric potential is obtained by solving Poisson's equation in one dimension. The sum of the externally applied voltage V and the built-in voltage V_{bi} define the maximum potential.

The figure is adapted from [110].

end of the space charge region and vanishes there. Transforming equation 3.11 yields the depletion voltage V_{depl} [110]

$$V_{\text{depl}} = \frac{eN_{\text{eff}}d^2}{2\epsilon_0\epsilon_{\text{Si}}}. \quad (3.13)$$

This is the voltage needed to extend the depletion zone over the entire wafer thickness $d \approx x_n$.

3.2 Working Principle of Silicon Drift Detectors

The fully depleted volume of a semiconductor can be used for particle detection. When a photon or a charged particle enters the material, valence electrons are excited into the conduction band, leaving an equal number of holes. This is called an event. The number N of electron-hole pairs inside the created charge cloud depends on the particle's energy E and the average energy w required to generate one electron-hole pair:

$$N = \frac{E}{w} \quad (3.14)$$

For silicon, the average energy is $w_{\text{Si}} = 3.62 \text{ eV}$ at $T = 300 \text{ K}$ [87]. The difference between the band gap and the average excitation energy is used to generate phonons, which are dissipated as thermal energy. In addition, the number of generated electron-hole pairs fluctuates with the fano factor F : [62]

$$\langle \Delta N^2 \rangle = FN = F \frac{E}{w}. \quad (3.15)$$

For semiconductors, F is in the order of 0.1 [22] and creates a lower limit for the best achievable energy resolution of semiconductor particle detectors used in spectroscopy. Despite the full depletion, free charge carriers are also thermally created, leading to the so-called leakage current. The probability for the thermal excitation of an electron-hole pair is described by a Boltzmann distribution: [87]

$$P(T) \propto T^{3/2} \exp\left(-\frac{E_g}{2k_B T}\right). \quad (3.16)$$

The higher the temperature T , the more leakage current is produced, preventing semiconductor detectors from being fully functional. Hence, they are usually cooled down to low temperatures. Another important property is the capacitance of the device as it determines noise of the pre-amplifier [71, 106]. The width d of the depletion zone and the surface area A determine the capacitance to the backside

$$C = \epsilon_0 \epsilon_{\text{Si}} \frac{A}{d}. \quad (3.17)$$

This is the well-known formula for a parallel plate capacitor. Further information on the readout system and its components are given in section 3.5.

All created charge carriers are subject to the influence of the electric field present in the depletion zone. Due to their opposite charge, the electrons and holes move in opposite directions towards the n- and p-doped sides, the anode and cathode, respectively. There, they can be detected and read out. This process is described in detail in section 3.4.

In 1984, Gatti and Rehak introduced the semiconductor (silicon) drift chamber and the concept of sidewards depletion, which formed the basis for today's SDD [72]. The TRISTAN detectors use the SDD

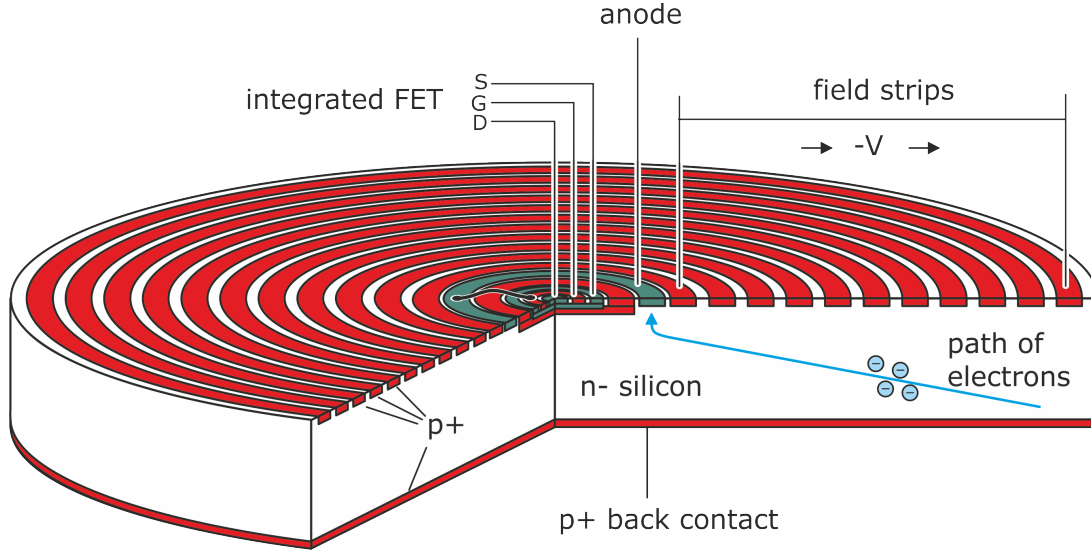


Figure 3.4: **Schematic Drawing of a TRISTAN Detector Pixel using the SDD Technology**

A monolithic n-type Si substrate (white) forms the basis for the fabrication of a TRISTAN detector. The substrate is processed with different dopants to integrate multiple different components on the device. In the pixel center, a JFET is made of n⁺-type doped material (green) and consists of the drain *D*, the gate *G*, and source *S* contacts. The JFET is shielded from the Si bulk by the p⁺-doped (red) IGR. The detector anode (green) is connected to the gate via a metal strip. The field stripes (red) form the drift rings and together with the BC (red) are responsible for the depletion of the detector. The path of the electrons created in an event is illustrated schematically.

The figure is adapted from [94].

technology to search for a keV-scale sterile neutrino. To understand the idea of SDDs, we start with the PIN diode. This diode is made from a silicon wafer, which is p⁺ doped on one side and n⁺ doped at the other. In terms of SDDs, these are called the (p⁺) Back Contact (BC) (cathode) and (n⁺) anode. For the sideways depletion, the anode is reduced in size and the additional surface volume is filled with rings of p⁺ doped field strips, the so-called drift rings. Unlike the intrinsic silicon used for PIN diodes, SDDs are made from an n⁻ substrate that forms the silicon bulk of the detector. The unique feature of SDDs is the extremely low anode capacitance of $\mathcal{O}(100 \text{ fF})$, which is almost independent of the detector area [93]. In order to take advantage of this property, a n-channel Junction-gate Field-Effect Transistor (JFET) is integrated onto the detector chip near the anode [94]. The JFET is shielded from the silicon bulk by the so-called (p⁺) Inner Guard Ring (IGR). Applying a negative voltage (with respect to the anode) to the back contact and to the field strips, fully depletes the detector. This way, an electric field parallel to the surface is created. The voltage provided to the drift rings is split by a voltage divider. Starting from the innermost ring, Ring 1 (R1), the bias voltage decreases to the outermost one, Ring X (RX), where the most negative voltage is present. Figure 3.4 depicts a schematic drawing of a TRISTAN detector pixel using the SDD technology with the mentioned components. The TRISTAN detectors themselves are described in section 3.3. The entrance window side is the side of the detector where the BC electrode

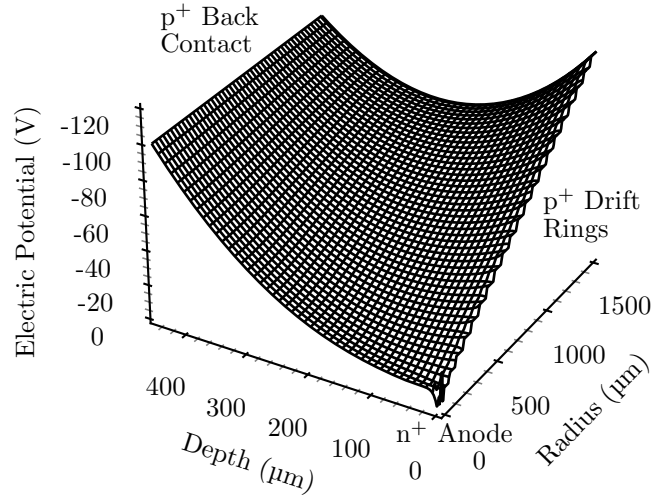


Figure 3.5: **Wireframe of the Simulated Electric Potential in a TRISTAN SDD Pixel**

When the bias voltages are applied to the detector electrodes, the detector volume is fully depleted and an electric potential is formed. Since the TRISTAN SDDs are radially symmetrical, the potential depicted here depends only on the radius and the depth of the detector pixel. The electric potential is shaped parabolically and is constrained by the constant BC voltage at a depth of 450 μm and the individual drift ring voltages at different radii. Electrons created in an event drift along this potential to the anode which marks the minimum of the electric potential.

is located. For more details on the entrance window, the reader is referred to [99]. The opposite side serves as the readout side, since the JFET interface to the front-end electronics is placed there. Due to the full depletion of the detector, its total thickness serves as the sensitive detection volume for ionizing radiation. Figure 3.5 shows the wireframe of the simulated electric potential in a TRISTAN SDD pixel. Its parabolic shape is bounded by the equipotential of the back contact and the step-like imprint of the drift rings. Chapter 6 goes into the details of the performed simulations. All charge carriers created in the depleted volume are subject to the influence of this field. Starting near the back contact, electrons fall into the transport trough of the electric potential and drift diagonally to the potential minimum, where they are collected at the anode. The drift path of the electrons is also illustrated in figure 3.4. In contrast, holes are collected at the back contact itself or the drift rings. A theoretical description of the charge carrier transport is given in section 3.4.

3.3 TRISTAN Detectors

The TRISTAN detectors are multi-pixel silicon drift detector arrays fabricated by Semiconductor Laboratory (HLL) of the Max Planck Society¹. An n-type silicon substrate with high resistivity of $4\text{ k}\Omega\text{ cm}$ and a thickness of $450\text{ }\mu\text{m}$ is employed to manufacture the SDDs [92]. The pixels are of hexagonal shape and arranged in a honeycomb pattern to avoid dead area in between. Each pixel has a diameter of 3 mm and an approximate surface area of 7 mm^2 . Besides the integrated JFET, they also feature an integrated Reset Diode (RD) and integrated feedback capacitor C_{FB} . The reset diode is designed to be operated in a pulsed-reset mode and is necessary to discharge the capacitor before saturation is reached. More details on the detector readout are given in section 3.5.

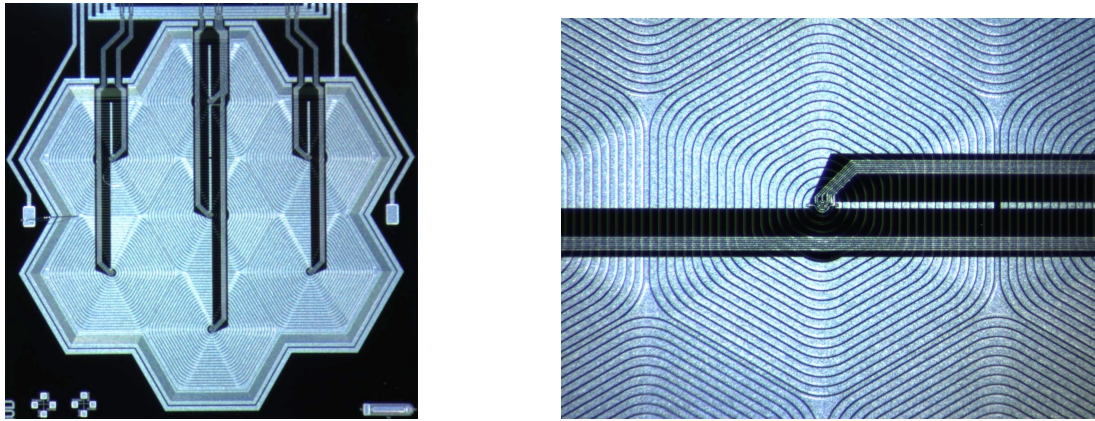
Since a staged approach is taken in the development of the TRISTAN detectors, devices with various pixel numbers (1, 7, 12, 47, and 166) were fabricated. The SDDs went through multiple iterations of design and layout modifications to minimize the detector capacitance and reduce the crosstalk between pixels. In this thesis, a TRISTAN detector with 7 pixels was chosen for characterization measurements. Figure 3.6a shows the SDD pixels of this detector on the readout side. Each pixel is formed by 20 hexagonal drift rings which are biased via a voltage divider of $5\text{ M}\Omega$ total resistance [79]. The nomenclature of the detector pixels is listed in table 3.1. The metal bus structure provides the signal and power lines for each detector pixel. The lines are connected to the bond pads at the top and are routed from there to the front-end electronics. A close up of the central pixel is given in figure 3.6b. The individual lines connect to the JFET region in the center of the pixel. The border of the pixel is defined by the outermost drift ring RX which is shared by all pixels. This area is of special interest because the effect of charge sharing occurs there. Since the detector is fabricated on a monolithic wafer, the detector pixels are not physically separated from each other. The charge carriers of a charge cloud formed near the border of a pixel can drift into

¹Halbleiterlabor (HLL) der Max-Planck-Gesellschaft, Otto-Hahn-Ring 6, 81739 Munich, Germany

Table 3.1: **Nomenclature for the 7 Pixels of a TRISTAN SDD**

The internal name scheming of the pixel numbers is assigned to the real physical arrangement of the different detector pixels.

Pixel Nr.	Abbreviation	Full Name
0	CC	Central Center
1	NN	North North
2	NE	North East
3	SE	South East
4	SS	South South
5	SW	South West
6	NW	North West



(a) Readout Side of a 7 Pixel TRISTAN SDD

(b) Close up of the Central SDD Pixel

Figure 3.6: Images of a 7 Pixel TRISTAN SDD

(a): The image taken under the microscope shows a 7 pixel TRISTAN SDD on the readout side. The individual pixels are formed by the concentric arrangement of the drift rings. The vertical metal bus structure carries the signal and power lines and provides a connection between the detector pixels and the bond pads at the top.

(b): Rotated by 90° , the photo shows a close up of the central detector pixel. The 20 hexagonal drift rings and the JFET region in the center are clearly visible. In particular, the outermost drift ring RX which is shared between all pixels, is easily recognizable. The triangular patches in the RX at the intersecting corners of the hexagonal pixels form the triple points.

the other pixel and be collected there. Therefore, this effect has an impact on the detector response and should be factored into the detector model when reconstructing single events. The areas, where the RX electrode of three adjacent pixels is in contact, are called triple points. They appear as triangular patches in figure 3.6b. There, the effect is increased even further, as the total charge can be shared by three pixels. Thus, low-pixel-count prototype detectors are studied to fully understand the physical effects inside the SDDs. Aside charge sharing [66], this includes studies of the entrance window [91], investigations of the noise performance [45], as well as the different detector responses to photons [121] and electrons [116]. This is absolutely crucial for the future operation of the full high-pixel-count TRISTAN detector in the keV-scale sterile neutrino search.

For the operation of the TRISTAN detectors, several bias voltages are required. In the following, the most important ones will be briefly introduced. The JFET drain is common to the gate and the source and is biased with the voltage V_D . V_D allows to operate the JFET with a nominal drain current of $I_D = 300 \mu\text{A}$ and a transconductance of $g_m = 300 \mu\text{S}$ which is the change of the ratio between the drain current and gate-source voltage. The inner guard ring voltage V_{IGR} is set to shield the JFET from the silicon bulk. This is necessary since the electrons drift to the minimum of the electric potential of the SDD, which would be the the JFET drain as the most positive electrode on the chip and not the anode. The electric potential itself is controlled by the back contact voltage V_{BC} and the bias voltages of the innermost and

Table 3.2: **Operating Ranges of the Detector Bias Voltages**

The bias voltage of each detector electrode can be varied independently within a certain range to find the global optimum working point for the detector. This point is usually defined by the minimum achievable energy resolution. For the most important detector electrodes, the bias voltage ranges are given.

Electrode (+Voltage)	Abbreviation	Voltage Range
JFET Drain	V_D	(5 - 10) V
Inner Guard Ring (IGR)	V_{IGR}	(-15 - -35) V
Ring 1 (R1)	V_{R1}	(-5 - -15) V
Ring X (RX)	V_{RX}	(-100 - -150) V
Back Contact (BC)	V_{BC}	(-80 - -120) V
Back Frame (BF)	V_{BF}	(-90 - -130) V

outermost drift rings, V_{R1} and V_{RX} . While V_{BC} is required to deplete the detector vertically, V_{R1} and V_{RX} are responsible for the sideways depletion of the detector and define the shape of the potential gradient and therefore the transport trough in the **SDD**. The back frame electrode surrounds the back contact to form a funnel for charge carriers generated at the border of the outer detector pixels and is biased by the voltage V_{BF} . The ranges for the individual voltages are listed in table 3.2.

3.4 Charge Motion and Signal Formation

Ionizing radiation, which enters the depleted volume of the detector, creates a charge cloud of electron-hole pairs. Since **Si** is an indirect semiconductor, a direct band-to-band recombination of electrons and holes is highly suppressed due to carrying different crystal momenta. Lattice interaction is required for a direct transmission while conserving both energy and momentum. The reader is referred to the literature of the Shockley-Read-Hall mechanism [114, 80] for a complete treatment of the process of generation and recombination of electrons and holes. Instead, this section discusses the motion and transport of these free charge carriers. In addition, the formation of the signal, which is read out at the collecting electrode, will be described.

3.4.1 Statistical Movement

In the field-free case, i. e. without additional external biasing of the detector, the electrons and holes can be considered as free particles with a mean kinetic energy of $\frac{3}{2}k_B T$, since they are not associated with a particular lattice site anymore. At room temperature, the velocity of their random motion is in the order

of 10^7 cm/s. After a mean free path of about $0.1 \mu\text{m}$, they will scatter on imperfections within the lattice, impurity atoms, and defects. This translates to a mean free time between two collisions of about 1 ps. Nevertheless, the traveled distance averaged over many charge carriers in equilibrium condition is still zero [110].

3.4.2 Self-Repulsion

Superimposed to the statistical movement of the electrons and holes is their self-repulsion. This effect occurs since charge carriers of the same electric charge repel each other. For a point charge q at a distance \vec{r} , the electric field in Si is given by

$$\vec{E} = \frac{1}{4\pi\epsilon_0\epsilon_{\text{Si}}} \frac{q}{r^2} \hat{r}, \quad (3.18)$$

where $r = |\vec{r}|$. Each charge carrier is subject to the influence of the electric field of all others. This results in a tiny displacement of all charge carriers, which slowly expands the charge clouds of electrons and holes over time. The underlying reason for this movement is the drift of the charges, as described in 3.4.3.

3.4.3 Drift

In the presence of an (external) electrical field, the charge carriers are accelerated in the time between two random collisions [110]. This process is called drift. The carriers move parallel to direction of the electric field \vec{E} . This leads to an average drift velocity [119]

$$\vec{v} = \mu \vec{E}, \quad (3.19)$$

where μ is the mobility. This equation holds for electrons and holes, but they move in opposite directions. For the linear relation between the drift velocity and the electric field, the velocity change due to the acceleration is required to be small compared to the thermal velocity of the charge carriers. It is clear, that stronger electric fields cause higher acceleration of the charges. In Si at $T = 300 \text{ K}$, the mobility at low fields is $\mu_n = (1440 \pm 15) \text{ cm}^2/(\text{Vs})$ for electrons and $\mu_p = (474 \pm 10) \text{ cm}^2/(\text{Vs})$ for holes [37]. For electric fields up to 10^4 V/cm , the mobility is constant but then reduces as the energy is used for increased phonon emission instead. At even higher fields above 10^5 V/cm , the mobility $\mu \propto 1/E$ and the increased number of random collisions will counterbalance further acceleration of the charge carriers [97]. Their drift velocity will be independent of the field and they reach a saturation velocity of 10^7 cm/s [119].

3.4.4 Diffusion

Aside drift, charge carrier transport also proceeds through diffusion. Diffusion is driven by an inhomogeneous distribution of the free charge carriers [65]. The resulting gradient of the carrier concentration is balanced by the movement of carriers from higher to lower concentration. This effect spreads out the concentration profile of the charge cloud with time t forming a Gaussian distribution with standard deviation [97]

$$\sigma = \sqrt{2Dt}. \quad (3.20)$$

The result of this process is a broadening of the charge cloud. The diffusion constant D is linked to the mobility through the Einstein relation [119]

$$D = \mu \frac{k_B T}{e}. \quad (3.21)$$

3.4.5 Signal Formation

The mentioned processes in sections 3.4.1 to 3.4.4 can be summarized as follows: Starting from the position where the initial charge cloud was generated, electrons and holes drift in opposite directions due to an external electric field, forming their individual charge clouds and experiencing diffusion and self-repulsion effects. In SDDs, the electric field is shaped so that electrons drift to the anode and holes to the back contact. The moving charges give rise to an electrical signal current on the collecting electrodes, i. e. a signal is already detectable before the charges physically arrive there. With the TRISTAN detectors, only the signal at the anode is read out. Therefore, only electrons are discussed in the following. Ramo's theorem allows to calculate the instantaneous current i induced on the anode by the infinitesimal movement of an electron with charge $-e$ and drift velocity \vec{v} [107]:

$$i = -e\vec{v}\vec{\nabla}\Phi_w, \quad (3.22)$$

where Φ_w is the weighting potential which describes the coupling of an electron to the anode at any position in the detector. Φ_w is obtained by setting the the anode to unit potential and all other electrodes to zero potential and solving Poisson's equation. The weighting potential is distinctly different from the electric potential and only depends on the detector geometry [119]. The charge Q induced on the anode by an electron drifting from position \vec{x}_1 to \vec{x}_2 in the time interval $[t_1, t_2]$ can be determined by integrating over the time of charge collection [110]:

$$Q = \int_{t_1}^{t_2} i(t) dt = -e [\Phi_w(\vec{x}_2) - \Phi_w(\vec{x}_1)]. \quad (3.23)$$

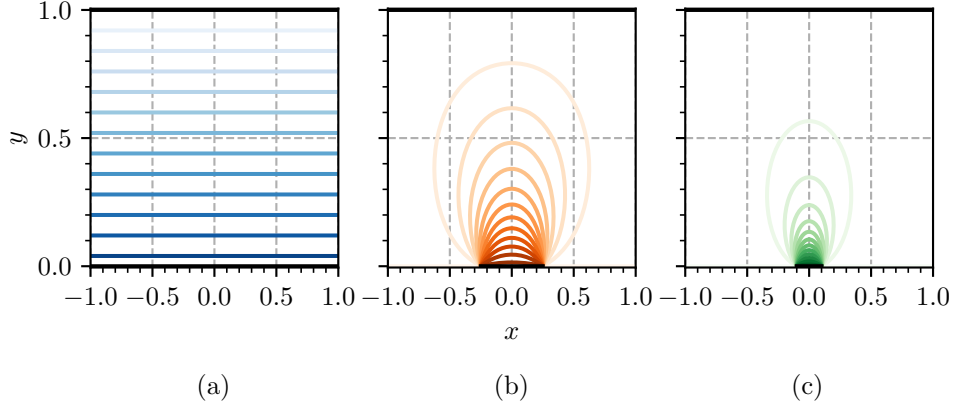


Figure 3.7: **Weighting Potential for different two Electrode Configurations**

(a): For two infinite parallel plates, the weighting potential Φ_w linearly decreases from the anode (bottom black bar) to the back contact (top black bar) electrode. The equipotential lines are equidistant which indicates that the induced charge is equal for any part in the drift path of the electrons.

(b): Reducing the size of the anode to $a = 0.5$ creates the typical shape of Φ_w present in pixel detectors. The equipotential lines of the weighting potential are most dense near the anode and gradually expand into the bulk with increasing intervals. This implies that most of the charge is induced in the last part of the drift path.

(c): Further reducing the anode size to $a = 0.2$ results in a weighting potential which is zero in most regions of the detector. Hence, only very little charge is induced while drifting in these regions.

The figure is adapted from [110].

In the following, the weighting potential for a simple two electrode configuration will be discussed. The wafer thickness y is set to $y = 1$ and the anode of size a is centered around $x = 0$ at $y = 0$. The electrodes are illustrated for different anode sizes in figure 3.7 by the black horizontal bars. The N electron-hole pairs created in this detector separate and the electrons are collected by the anode, at the bottom. In contrast, the holes drift towards the upper electrode, the back contact, and are collected there. For the calculation of the weighting potential, the anode is set to unit potential. The solution of Poisson's equation for this configuration is obtained using the Schwarz-Christoffel conformal transformation [58]. For the positive branch of the inverse tangent function, the weighting potential can be written as [110]

$$\Phi_w = \frac{1}{\pi} \arctan \left[\frac{\sin(\pi y) \sinh\left(\pi \frac{a}{2}\right)}{\cosh(\pi x) - \cos(\pi y) \cosh\left(\pi \frac{a}{2}\right)} \right]. \quad (3.24)$$

Figure 3.7 illustrates Φ_w for different anode sizes. For $a \rightarrow \infty$, figure 3.7a shows the case for two infinite parallel plates. The weighting potential linearly decreases as a function of the depth and varies only in one dimension. From the linearity follows, that the induced charge is the same for any part in the drift path. However, the induced current is not constant since the drift velocity changes due to variations in

the electric field. Furthermore, an electron-hole pair created in the middle of the detector induces the same signal on the anode when moving in opposite directions. By reducing the size of the anode, the geometry becomes more similar to that of pixel detectors and results in larger areas where the weighting potential approaches zero. This is depicted in figures 3.7b,c. While the charges drift in these regions, only very little signal is induced on the anode. The region in which the charge is induced becomes narrower the closer the electrons get to the anode. This is reflected by the increasing gradient of the weighting potential. Hence, most of the signal is induced in the last part of the drift path. In contrast, the contribution of holes, drifting towards the back contact, is insignificant [110]. Finally, when all N electrons, each of charge $-e$, have been collected, the integral of the induced signal is the sum of all charges:

$$Q = \int_{t=0}^{t=t_c} i(t) dt = \sum_{i=0}^N e = -N \cdot e. \quad (3.25)$$

Here, t_c denotes the collection time, i. e. the duration until all electrons have been collected by the anode. This is not to be confused with the drift time, which describes the time period after which the electrons arrive at the anode but have not been fully collected.

3.5 TRISTAN Readout System

In the **TRISTAN** detectors, the charge induced on the detector anode is processed in several stages to obtain an output signal at the end. The individual components of the readout chain will be discussed by following the signal step-by-step through the readout mechanism. Figure 3.8 illustrates the equivalent circuit of a single **TRISTAN** detector pixel. As discussed in section 3.4.5, the induced charge on the anode produces an instantaneous current. This current should behave like a Dirac-delta pulse $Q\delta_t$, but in reality is determined by the broadening of the charge cloud during the drift. In addition, the thermal leakage current I_{leak} is superimposed on the actual signal current. In parallel to the current sources, the capacitor C_{det} factors in the anode capacitance C_{anode} , the stray capacitance C_{stray} , and the **JFET** gate capacitance C_{gate} . The electronic noise can be minimized by making C_{anode} as small as possible [79]. The integrated **JFET** is the next step in the **CSA** chain. The **CSA** is a special circuit, that integrates the signal current into the feedback capacitance C_{FB} and converts it to a voltage step which is proportional to the charge that arrived at the anode. The integration of the leakage current leads to a linear voltage ramp with the voltage steps of the events on top. The placement of the **JFET** into the detector chip has the advantage of avoiding parasitic bond capacitances which would arise in an external readout of the anode. However, the complexity of the detector geometry and its fabrication is increased. By operating the **JFET** as follower, the anode potential is fixed. The source of the **JFET** is read out via the bond pad SC which connects the signal line to the input of the **ETTORE ASIC**. The **ETTORE ASIC** [129], named after Ettore Majorana [79], was developed by XGLab² in collaboration with Politecnico di Milano (PoliMi).

²XGLab S.R.L., Bruker Nano Analytics, Via Conte Rosso 23, 20134 Milano, Italy

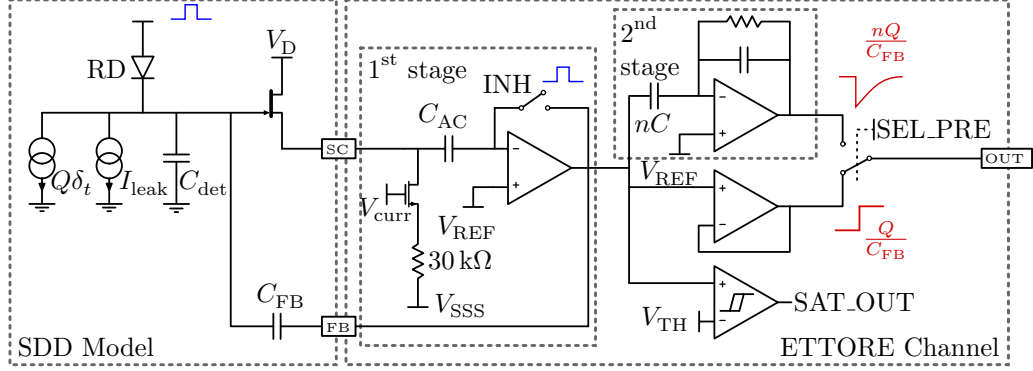


Figure 3.8: **Equivalent Circuit of the Readout Chain of a TRISTAN SDD Pixel**

The readout chain of a TRISTAN SDD pixel can be modeled by two independent systems: the SDD model and the ETTORE channel of the ASIC. Both are connected via the bond pads of the source SC and feedback FB line. The signal is routed through the CSA circuit, i. e. the anode and the JFET on the SDD chip itself and the different stages of amplification (1st and optional 2nd stage) on the ETTORE ASIC. The feedback loop is closed via the feedback capacitance C_{FB} into which the signal current is integrated to create a voltage step in the output signal. With the signal line SEL_PRE, it is possible to select between the two output stages of ETTORE.

The figure is adapted from [79].

Figure 3.9 shows a fully bonded ETTORE ASIC mounted on a TRISTAN detector. In the 1st stage of the ASIC, the capacitor C_{AC} decouples the JFET bias and signal currents by introducing a low-frequency pole. The JFET bias current can be changed by modifying the current generator voltages V_{curr} and V_{SSS} . The feedback loop of the CSA circuit is formed via the connection of the inverting input of the operational amplifier (op amp) with the feedback capacitor via the bond pad FB. C_{FB} closes the loop since it is connected the gate of the JFET. Another op amp detects the saturation of the signal. When the signal overcomes the threshold voltage V_{TH} , the SAT_OUT signal notifies an external circuit to reset the CSA. The inhibit signal INH prevents further readout of the anode and the feedback capacitance is discharged via the reset diode RD by forcing it to the reference voltage V_{REF} . The optional 2nd stage of the ASIC removes the ramp from the signal via AC-coupling. This operation introduces an exponential decay constant of 15 μ s on the signal. It is realized via a RC circuit forming a high-pass filter of first order. In addition, the signal is amplified with a gain factor n . With the signal line SEL_PRE, it is possible to select between the two output stages of ETTORE. The output line can either carry the buffered output of the 1st stage, i. e. the voltage ramp superimposed with pulses of the events, or the AC-coupled output of the 2nd stage, i. e. a constant voltage with the exponential decay pulses.

The CSA circuit was designed to handle the high event rates up to 100 kcps. For this purpose, signal rise times of less than 30 ns were targeted. The rise time t_{rise} is the time it takes for the signal pulse to rise from 10 to 90 percent of its amplitude. This requirement is fulfilled even for the presence of stray capacitances up to 40 pF on the connection lines between the SDD and the ASIC. Since the 1st

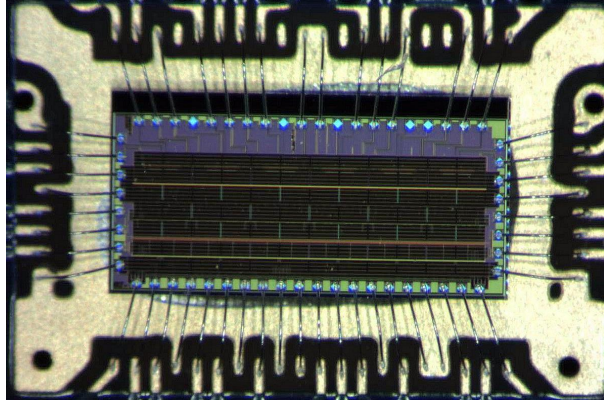


Figure 3.9: **ETTORE ASIC** mounted on a **TRISTAN Detector PCB**

ETTORE is a 12 channel front-end analog electronic ASIC developed for the TRISTAN detector and readout system. The ASIC is mounted on the PCB of a TRISTAN detector and bonded with thin wires. The chip measures $3.8 \times 1.7 \text{ mm}^2$.

More detailed information on the ETTORE ASIC can be found in [40, 129].

stage of the ETTORE ASIC acts as a first-order low-pass filter, the signal rise time is determined by the bandwidth BW of the circuit:

$$\text{BW} \simeq \frac{0.35}{t_{\text{rise}}} = \frac{0.35}{30 \text{ ns}} \approx 11.6 \text{ MHz}. \quad (3.26)$$

The most important characteristics of the detector and CSA circuit are listed in table 3.3. More detailed information on the ETTORE ASIC can be found in [40, 129].

Table 3.3: **Characteristics of the CSA Circuit**

The most important characteristics of the CSA circuit are listed. Values annotated with ^(a) are taken from [79].

Circuit Characteristics	Symbol	Value
Anode Capacitance	C_{anode}	112 fF ^(a)
JFET Gate Capacitance	C_{gate}	56 fF ^(a)
Stray Capacitance	C_{stray}	10 fF ^(a)
Total Detector Capacitance	C_{det}	178 fF ^(a)
Decoupling Capacitance	C_{AC}	10 pF ^(a)
Feedback Capacitance	C_{FB}	25 fF ^(a)
Bandwidth	BW	11.6 MHz
Rise Time	t_{rise}	30 ns

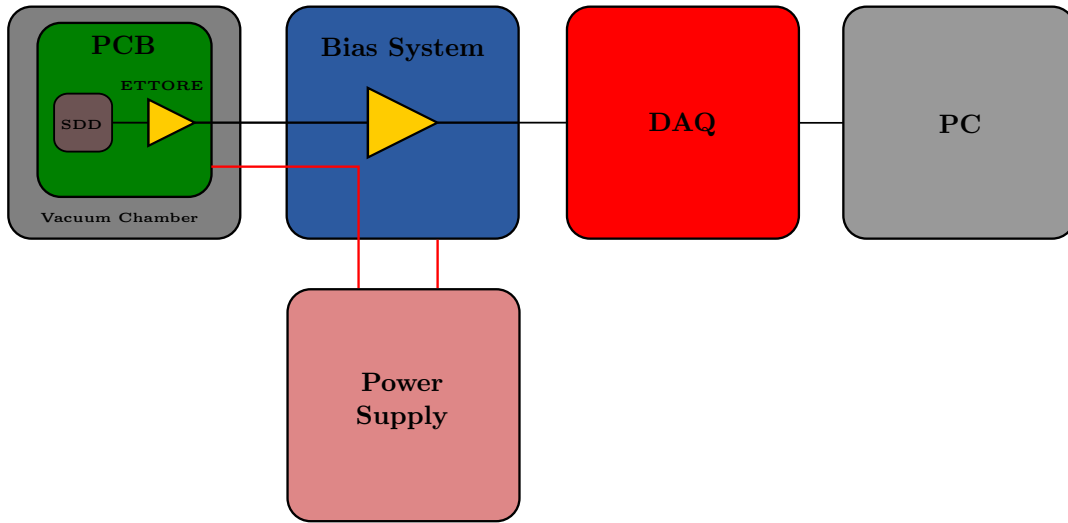


Figure 3.10: **Block Diagram of the TRISTAN Detector and Readout System**

The TRISTAN SDD and the ETTORÉ ASIC are mounted on the detector PCB and placed inside a vacuum chamber. The detector is supplied with external bias voltages from the bias system. In addition, this system transmits the signals from the detector to the DAQ. After processing by the FPGA, the digitized output is transferred to a computer, which stores the acquired data for offline analysis.

The final stage of the readout is the DAQ system. For DPPs, the signal is digitized by the ADCs and afterwards processed by the FPGA. Digital shaping filters are applied to detect events on the signal. In addition, information like the events' timestamp and energy can be extracted. For the TRISTAN detectors, currently four different formats exist: waveform mode, listwave mode, list mode, and histogram mode. In waveform mode, the pure signal output, the waveform, from the ASIC is extracted. It contains all information acquired by the detector and therefore requires extremely high data throughput of $\mathcal{O}(100 \text{ GB/s})$ for a 166 pixel detector module [78]. For this thesis, this mode was chosen for detailed studies of the signal pulses. The listwave mode reduces the amount of data. Only waveforms of events above a certain energy threshold are acquired and resets in the signal are discarded. The list mode further decreases the data volume. An energy filter evaluates the pulse height of the events and only stores the result for later offline processing. In histogram mode, these results are already processed online, by the FPGA in real time. The only output from the DAQ is the energy spectrum of the acquired events. This mode minimizes the requirements on data bandwidth and storage and will be deployed in the application of the TRISTAN detectors in the KATRIN experiment. Figure 3.10 illustrates the complete TRISTAN detector and readout system chain.

Preparatory Measurements

For the characterization of a 7 pixel [TRISTAN](#) detector with a laser system, two preparatory measurements were conducted. The experimental setups and results will be presented in this chapter. In section [4.1](#), the reference calibration of the detector with an ^{55}Fe source is demonstrated. Afterwards, in section [4.2](#), the laser system is introduced and the application of a USB-webcam as a calibration sensor is discussed.

4.1 Reference Calibration with an ^{55}Fe Source

The output signal of a [TRISTAN](#) detector is an analog voltage. The [ETTORE ASIC](#) limits this voltage to a specified range from 0 V to 3.3 V. When the signal is read out by the [DAQ](#) system, this analog voltage is digitized by the [ADC](#) of the [DPP](#). The resolution of the [ADC](#) defines the amount of bins available for the digital output values. Each bin corresponds to a certain voltage level and is represented as least significant bit (lsb).

The conversion from the [ADC](#) codes in lsb to physical energy values in eV is done in a calibration measurement. To this end, the spectrum of a well-known radioactive source is measured. Based on the distinct line positions, the conversion from lsb to eV is achieved. Since the [TRISTAN](#) detector and readout system provides an excellent [ADC](#) linearity over a wide energy range from 10 keV to 60 keV [[98](#)], a linear calibration can be conducted. For the calibration measurements performed in the scope of this thesis, an ^{55}Fe source was used. This source decays to ^{55}Mn via [EC](#) with a half-life of 2.74 yr [[84](#)]. The resulting vacancy in the K shell is filled by an electron from a higher-lying shell. During this process, the surplus energy is released in the form of Auger electrons and X-rays. The X-ray lines located at $K_\alpha = 5.89\text{ keV}$ and $K_\beta = 6.49\text{ keV}$ are used for the energy calibration [[84](#)]. Figure [4.1](#) illustrates the

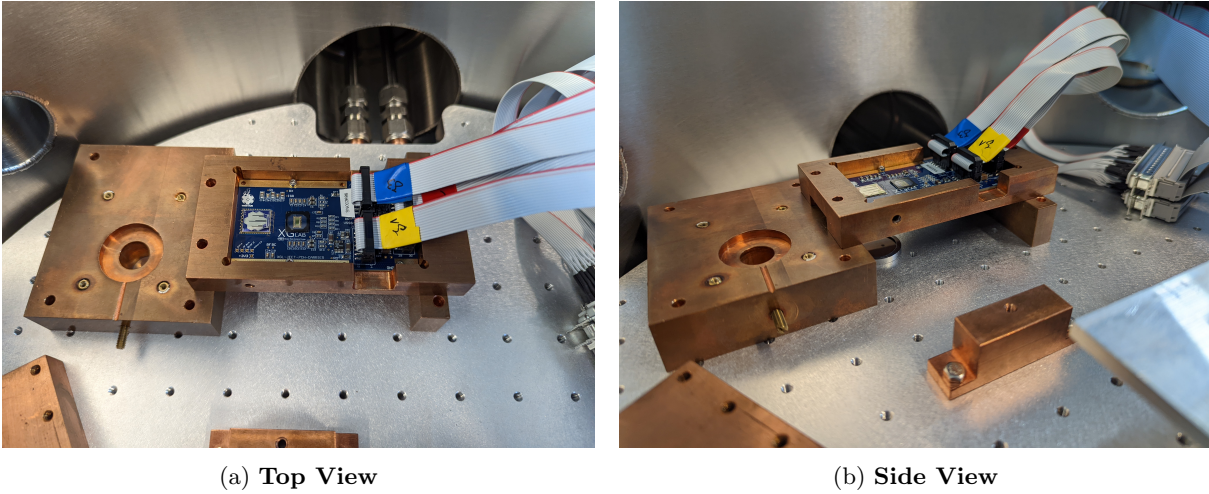


Figure 4.1: **Experimental Setup of the Detector Calibration**

(a): The **TRISTAN** detector (blue **PCB**) is mounted in a copper holding structure in a vacuum chamber. In this orientation, the readout side of the **SDD** (rectangular chip) and the **ETTORE ASIC** protected by a glass window can be seen. The ribbon cables supply the detector with the required bias voltages and transmit the signal lines via the bias system to the **DAQ**.

(b): The side perspective allows a view of the circular ^{55}Fe source. It is placed below the entrance window of the **SDD** and irradiates the detector with X-rays.

setup of this measurement. The detector S0-7-6 is mounted in a copper holding structure in a vacuum chamber. The ^{55}Fe calibration source is positioned below the entrance window of the detector. The detector is connected to a bias system which provides the bias voltages and carries the signals from the detector to the **DAQ**. The applied detector voltages are listed in table 4.1. For this measurement, the CAEN¹ DT5725S Digitizer served as the **DAQ**. This device features 8 input channels with a sampling rate of 250 MS/s. The **ADCs** have a resolution of 14 bit and provide a dynamic input range of up to $2V_{pp}$. The **DAQ** reads out the signals either in listwave mode or in waveform mode. More detailed information on the digitizer can be found in [111]. For the calibration measurement, the 1st stage output of the

¹CAEN S.p.A., CAEN Group, Via Vetraria 11, 55049 Viareggio, Italy

Table 4.1: **External Bias Voltages for the Operation of the Detector**

The relevant bias voltages applied to the detector are listed. The voltages were optimized to achieve the best possible energy resolution.

Electrode	Voltage	Electrode	Voltage
V_D	6.6 V	V_{IGR}	-19.0 V
V_{R1}	-9.0 V	V_{RX}	-120.0 V
V_{BC}	-100.0 V	V_{BF}	-110.0 V

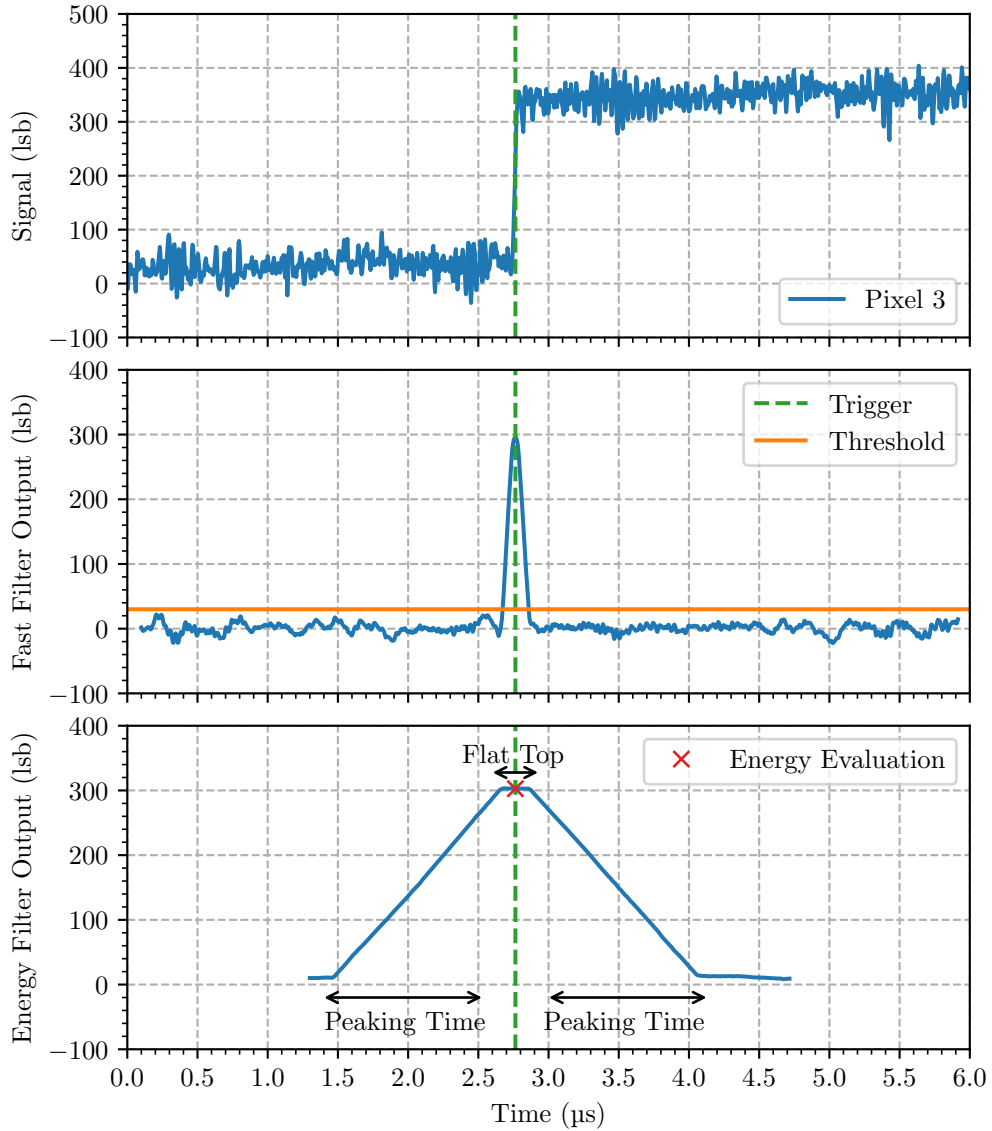


Figure 4.2: **Signal Evaluation with trapezoidal Filters**

The acquired waveform for an event in pixel 3 is displayed in the top graph. The leading edge at $\sim 2.8\mu\text{s}$ is the characteristic feature for this event. The fluctuations in the waveform is caused by electronic noise which is superimposed on the signal. The output of the trapezoidal fast filter is depicted in the center plot. For this filter, a peaking time of 80 ns and flat top window of 40 ns was chosen. Since the signal exceeds the threshold of 30 lsb, the event is triggered. Afterwards, the energy filter evaluates the signal with a larger peaking time of 1.2 μs and flat top window of 200 ns and extracts the pulse height.

readout electronics in combination with the listwave acquisition mode was chosen. In this mode, events above a certain energy threshold are recorded. To this end, a trigger algorithm based on a trapezoidal

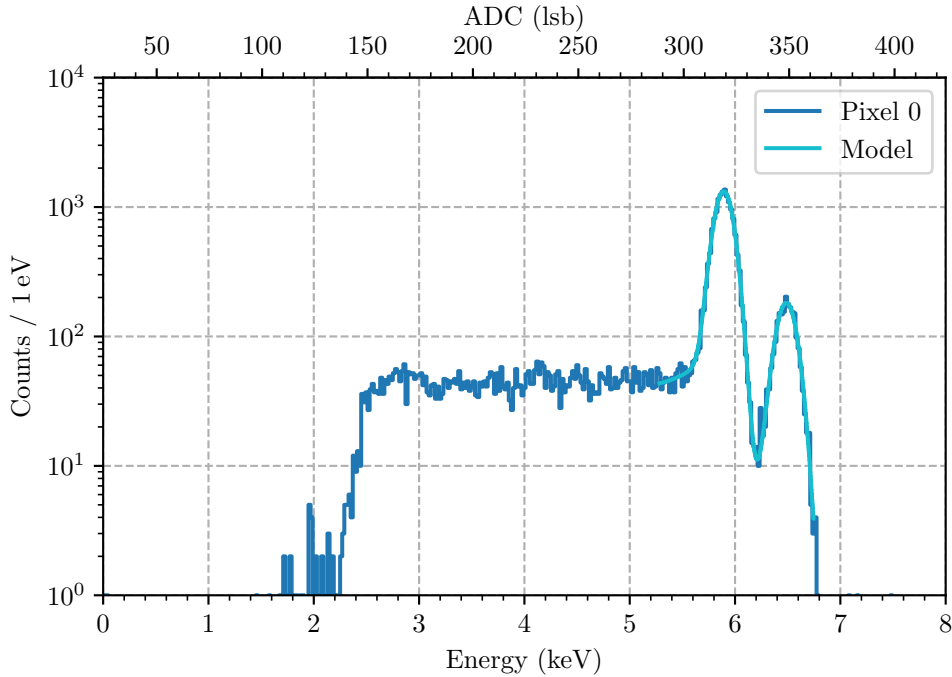


Figure 4.3: **Calibration Spectrum of the Central SDD Pixel**

The energy spectrum of central detector pixel is shown as a function of **ADC** codes and energy. For the conversion, the spectrum is fitted with a sophisticated model which consists of two Gaussian peaks each modified with an exponential tail to account for the detector entrance window as well as a sigmoid tail for the diffusion of the charge cloud. In this measurement, the energy threshold of the **DAQ** was set to ~ 2 keV.

filter is used. Events are evaluated by this trapezoidal energy filter and get a timestamp by an additional RC-CR² filter. In addition, the waveform of the corresponding event is saved for later, offline analysis. The time window for the waveform acquisition was set to a length of 6 μ s with the window divided into about one half of pre-trigger and one half of post-trigger region.

The waveform of an event of the K_{α} peak is illustrated in figure 4.2. The leading edge in the waveform at $\sim 2.8 \mu$ s is the characteristic feature of an event. Its height corresponds to the energy deposited in the detector. Two trapezoidal filters, the fast and the energy filter, are applied to the waveform. These filters average the waveform within a certain time interval, the so-called peaking time, and subtract the averaged values after and before the so-called flat top in between. The concept of the peaking time and flat top is also illustrated in figure 4.2. The fast filter averages over a much smaller amount of samples compared to the energy filter. This is necessary to handle the high signal rates and quickly distinguish between noise or a real event. The output of the filter operation is shown in the center plot of figure 4.2. The signal exceeds the selected energy threshold and is thus further processed by the energy filter. This filter evaluates the waveform signal with a larger peaking time and extracts the pulse height as illustrated

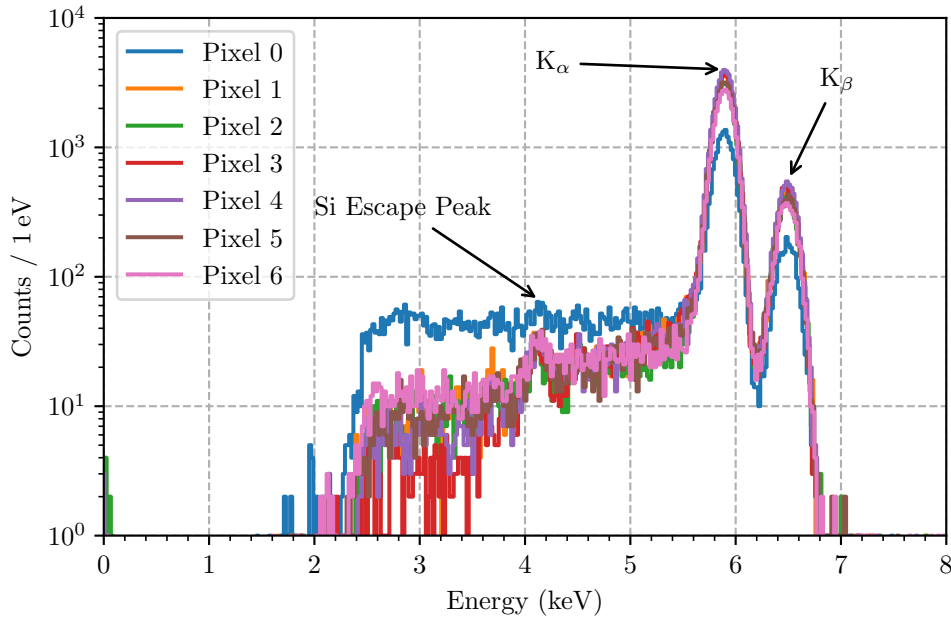


Figure 4.4: **Calibrated ^{55}Fe Spectrum of all SDD Pixels**

The energy spectrum of the ^{55}Fe decay is used to calibrate the individual detector pixels. The X-rays emitted in this decay create two distinct energy peaks, the K_α peak and the K_β peak, in the spectrum. An additional peak, the Si escape peak, arises when an electron of a Si atom is ionized by a K_α photon and a photon is emitted during the electron transition processes. When this photon leaves the detector, it carries away a fixed amount of energy which manifests itself as a shifted K_α peak. Comparing the energy spectra of the individual pixels shows that the central pixel has a slightly different shape. This behaviour is caused by the increased probability of charge sharing for this pixel. The energy of many events is not entirely deposited in one pixel, but is rather shared with the other ones. That is the reason why, there are more events with lower energy detected in the central pixel.

in the bottom plot of figure 4.2. This process is done for all events that were detected and acquired by the DAQ.

For the central pixel, figure 4.3 illustrates the calibration spectrum, which relates lsb and eV. The X-ray lines of the spectrum are fitted as Gaussian peaks modified with an exponential tail to account for the detector entrance window as well as a sigmoid tail for the diffusion of the charge cloud. The calibration is performed for all pixels, see figure 4.4. The K_α and K_β peaks used for the calibration can be clearly identified. In addition, a third peak is visible at an energy of about 4.15 keV, the so-called Si escape peak. It appears, when the K_α photon of the ^{55}Fe decay ionizes an electron from the innermost shell of a Si atom. The Si atom itself emits a K_α photon with an energy of 1.74 keV during the electron transition processes. The photon can leave the detector and take away this specific amount of energy from the total, initially deposited energy. For the K_β line of the ^{55}Fe decay, the Si escape peak is suppressed by the

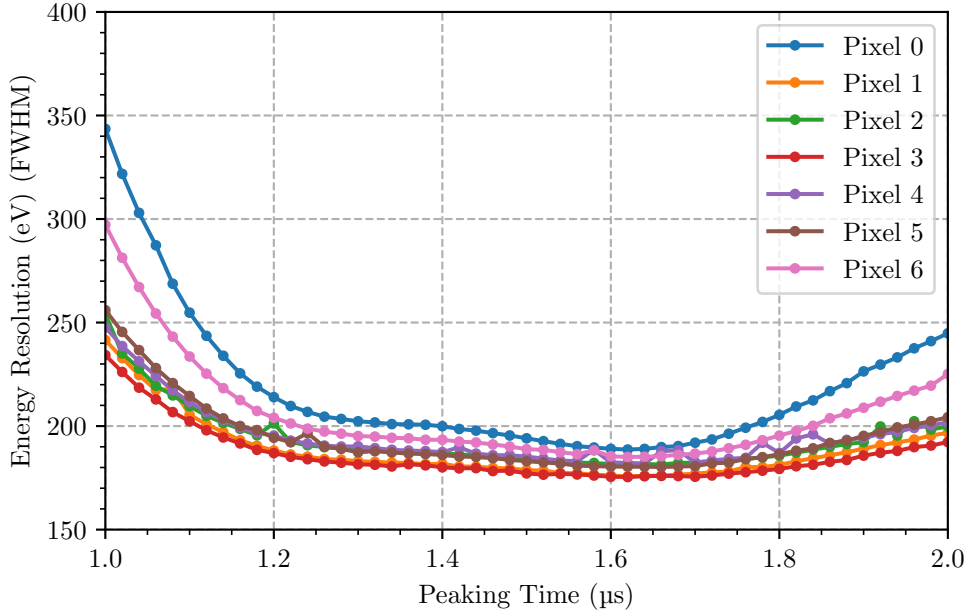


Figure 4.5: **Energy Resolution of all Detector Pixels as a Function of the Peaking Time of the Energy Filter**

By varying the peaking time of the trapezoidal energy filter while keeping the flat top window length constant, the minimum energy resolution is obtained for all detector pixels. Since the measurement was performed at room temperature, the impact of electronic noise was particularly high in the pixels 0 and 6. At a peaking time of $1.62\ \mu\text{s}$ the minimum energy resolution is reached.

same ratio as the main peaks of the spectrum. The energy spectrum of the central pixel has a slightly different shape compared to the spectra of the other pixels. While the overall number of events in the vicinity of the X-ray lines is reduced, the spectrum has a more pronounced tail towards lower energies. This behaviour can be explained by charge sharing. Since pixel 0 is the central pixel, the probability of charge sharing is strongly increased. Consequently, the energy of many events is not entirely deposited in one pixel, but is rather shared with the other ones. That is the reason why, there are more events with lower energy detected in the central pixel.

To achieve minimum energy resolution, the peaking time of the trapezoidal energy filter was varied, since the influence of noise contribution depends on the filter time. The energy resolution is defined as the **FWHM** of the K_{α} peak. Figure 4.5 depicts a sweep over the filter peaking time from $1\ \mu\text{s}$ to $2\ \mu\text{s}$. It can be observed that pixels 0 and 6 have an overall increased energy resolution compared to the other pixels. Since the measurement was performed at room temperature, the impact of electronic noise was particularly high in these pixels. Nevertheless, a minimum mean energy resolution of $(181.2 \pm 1.7)\ \text{eV}$ (**FWHM**) at a peaking time of $1.62\ \mu\text{s}$ is achieved with this detector.

4.2 Optimization of the Laser System

Prior to the actual characterization measurement of the detector, the laser system was optimized. This system consists of multiple components that will be introduced in the following paragraphs and are displayed in figure 4.7.

Laser Diode The laser itself is the Thorlabs² Nanosecond Pulsed Laser NPL64A with a wavelength $\lambda = (640 \pm 10)$ nm [126]. By external triggering, it provides pulses with a fixed width with a typical duration of (10 ± 1) ns. The delay from the external trigger input to the optical output is (35 ± 5) ns and has to be taken into account for the analysis. The elliptical laser beam is linearly polarized and collimated by an integrated aspheric collimating lens. The lens is positioned behind the shutter for a typical beam divergence of about 1 mrad.

Optical Fiber with Attenuator The beam is coupled into an optical fiber which features the integrated attenuator Thorlabs VOA630-FC. The Single Mode **Variable Optical Attenuator (VOA)** allows to manually vary the attenuation of the beam in the fiber. By adjusting the screw of the **VOA**, only the desired fraction of the beam is transmitted.

Collimating Lens Afterwards, the beam is decoupled from the fiber and collimated using the the Thorlabs CFC2-A Collimator. The collimator is equipped with a lens of 2 mm focal length. By adjusting the distance between the lens and the tip of the fiber, the collimator allows to compensate for changes of the focal length and to re-collimate and focus the beam at a certain distance.

XYZ Stage The collimating lens is mounted facing down in an L-shaped optical table, which in turn is attached to an XYZ linear translation stage. This stage can move freely in three dimensions and is controlled either manually via turning screws or motorized linear actuators. The Thorlabs Z812BV Vacuum-Compatible Motorized Actuators provide a travel range of 12 mm and a theoretical resolution of 29 nm [127]. The actuators are controlled with the Thorlabs KDC101 K-Cube DC Servo Controller via a USB connection [125].

Holding Structure The laser beam is focused onto the detector mounted in the holding structure. It is located below the collimating lens and is made of cooper for optimal heat transfer.

²Thorlabs GmbH, Münchner Weg 1, 85232 Bergkirchen, Germany

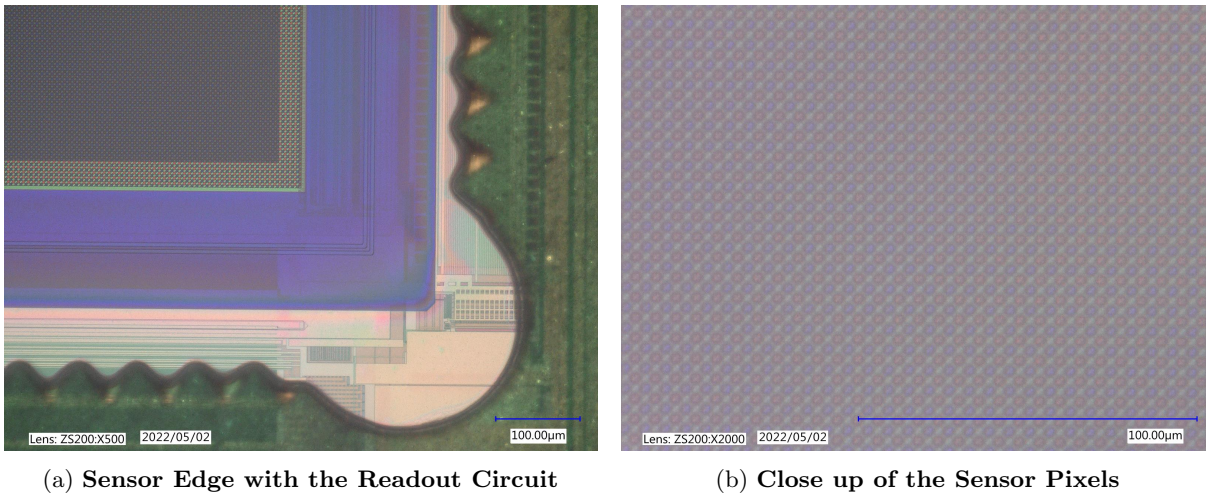


Figure 4.6: **Microscope Images of the Webcam Sensor**

A microscope was used to determine several properties of the webcam sensor like the size of the individual pixels, the sensor resolution, or its dimensions.

(a): With a magnification of $500\times$, the edge of the sensor and parts of the readout circuit are shown. The blue horizontal bar marks the size of $100\ \mu\text{m}$.

(b): With a larger magnification of $2000\times$, the individual pixels can be examined. The photosensors are covered by RGB color filters and are arranged as a Bayer filter. The reference bar also extends to $100\ \mu\text{m}$.

Vacuum Chamber The entire setup is installed in a light-tight vacuum chamber. This is necessary for multiple reasons: Due to the class 3B classification of the laser, unwanted exposure to the beam must be avoided. In addition, the **TRISTAN** detectors would immediately saturate when being illuminated by ambient light. Controlled sources such as the laser system offer the flexibility to fine-tune the amount of light reaching the detector.

The major goal of the optimization of the laser system was to find the distance between the collimating lens and the detector, that minimizes the laser beam width. Since the **TRISTAN** detectors are only capable of detecting the total energy of the incident radiation, another method of studying the beam size was required. The application of a webcam as a calibrating sensor is an easy and cost-effective solution. The laser beam can be monitored safely and changes to its shape are visible in real time. For this task, the Generalplus Technology Inc.³ GENERAL WEBCAM was deployed. Its **Complementary Metal-Oxide-Semiconductor (CMOS)** sensor features a resolution of 1280×720 pixels and a pixel diameter of $(3 \pm 1)\ \mu\text{m}$. While figure 4.6a shows the edge of the sensor area with parts of its readout circuit, figure 4.6b depicts some of the individual sensor pixels. The photosensors are covered by RGB color filters that only transmit light in the color of the respective filter. The arrangement of the color filter array is called Bayer filter, which is widely-used in color imaging [36]. This filter uses twice as many green elements as red or

³Generalplus Technology Inc., No.19, East No.4 Industry Road Hsinchu, Science Park Hsinchu City, 30077, Taiwan

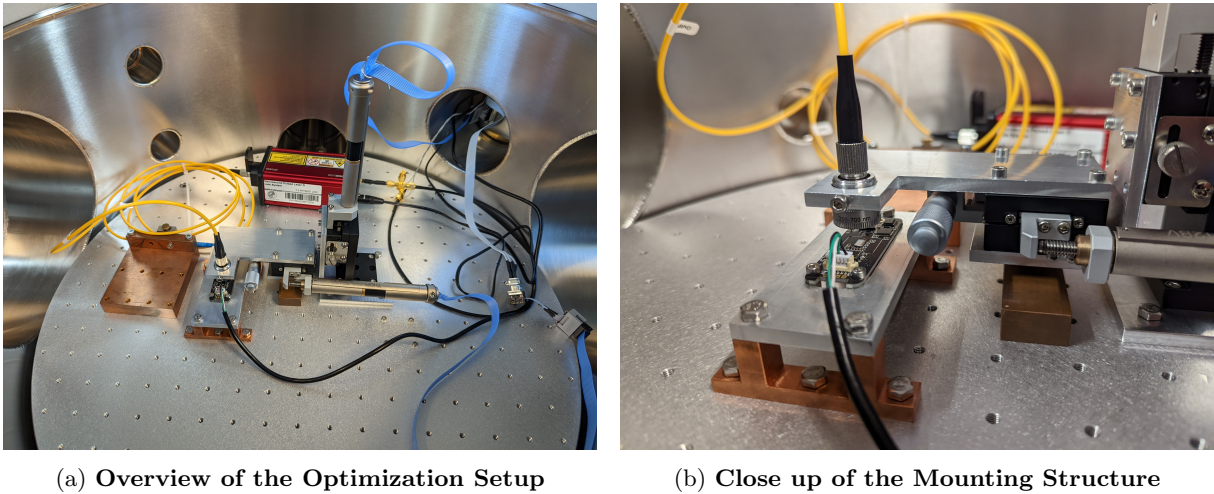


Figure 4.7: **Experimental Setup for the Optimization of the Laser System**

(a): The laser housed in the red metal box emits a Gaussian beam which is coupled into the yellow optical fiber. The VOA attached to the cooper block on the left is set to a transmission of $\sim 0.5\%$ such that most of the beam is blocked. The beam is decoupled from the fiber and collimated by the lens mounted in the L-shaped optical table. This table is attached to the XYZ linear translation stage which can move freely in three dimensions. For precise movements, motorized actuators are employed.

(b): For the laser system optimization, the collimating lens is centered above the webcam sensor mounted in the holding structure and only translations in Z direction are allowed. The copper bar below the optical stage limits the vertical movement and prevents the lens from hitting the sensor. The goal of the optimization was to find the distance between the collimating lens and the detector, that minimizes the laser beam diameter. The sensor data is read out via a USB connection.

blue ones to mimic the human eye's luminance perception, which is most sensitive to green light. The Bayer arrangement follows the structure of columns with alternating blue-green or green-red color filters. Usually, the full-color image is obtained by applying demosaicing algorithms to interpolate an entire set of red, green, and blue values for each pixel [86]. However, for our application we require the raw output of the sensor, which is read out via a USB connection. This output is called Bayer pattern image and contains the data from the independent RGB color channels. Since the laser operates in near-infrared regime, only the red channel is relevant for the analysis.

As mentioned before, the entire setup is illustrated in figure 4.7. The beam is emitted by the laser housed in a red metal box and is coupled into the yellow optical fiber. An external trigger frequency of 1 kHz was used to pulse the laser. The transmission of the attenuator is decreased to $\sim 0.5\%$, such that most of the beam is blocked. Figure 4.7b shows a close up of the webcam, which is mounted on the holding structure. The collimating lens is positioned above the webcam sensor, the X and Y positions of the XYZ stage are centered and fixed, and only translations in the Z direction are allowed. A motorized actuator is used to automate the vertical movement in steps of $10\ \mu\text{m}$. By varying the distance between the lens and the

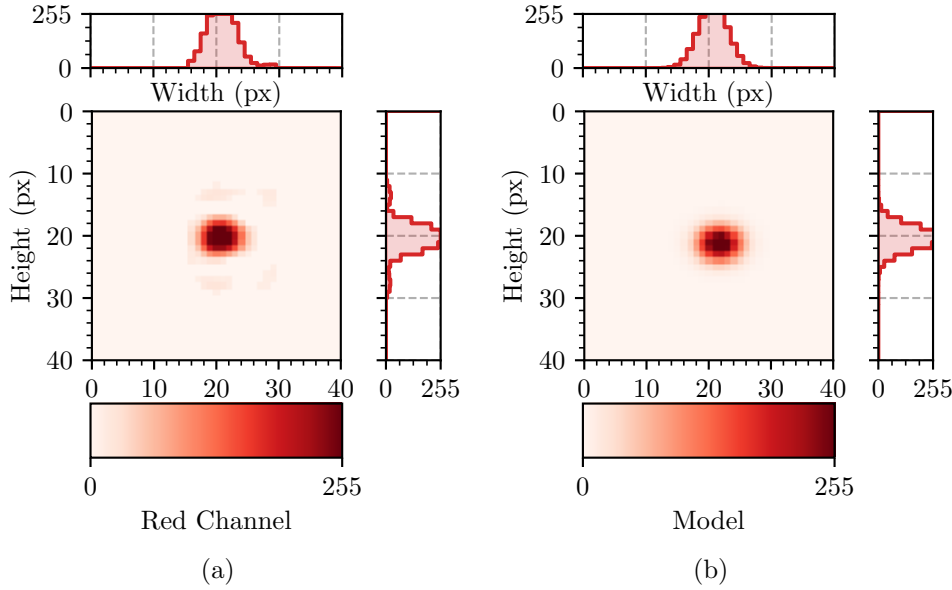


Figure 4.8: **Smallest Laser Beam Spot and Multivariate Gaussian Reconstruction**

(a): The red color channel is read from the sensor data and the region containing the laser beam spot is extracted. Due to the 8 bit resolution of the sensor, the color values range from 0 to 255. The beam maintains the profile of a two-dimensional Gaussian distribution and has its highest intensity in the center. In this configuration, the laser beam of smallest spot size is shown. The distinct patches surrounding the beam spot are compressing artifacts originating from the sensor readout algorithm and are not considered in the analysis.

(b): The sensor data of the red color channel is fitted with a multivariate Gaussian distribution to obtain the width of the laser beam. The best fit is depicted here. The one-dimensional projections in the horizontal and vertical direction display the maximum value in each dimension.

sensor, the beam size is changed and the focal point is obtained. The raw webcam sensor data is acquired using the open-source, computer-vision library OPENCV [43]. Figure 4.8a shows the red color channel for the distance of $z = (5.35 \pm 0.01)$ mm. The red spot in the center of the image is the laser beam. Since the resolution of the sensor is 8 bit, the color values range from 0 to 255. Assuming that the laser beam is described by the fundamental transverse electromagnetic (TEM_{00}) mode, it maintains the profile of a two-dimensional Gaussian distribution. Hence, in the center, the intensity of the beam is highest and the beam spot is brightest. In figure 4.8, the higher intensity of the beam is illustrated with darker colors. One-dimensional projections in the horizontal and vertical direction confirm the Gaussian shape. The bright, distinct patches surrounding the central spot are compression artifacts originating from the sensor readout algorithm. Hence, they are not taken into account for the analysis. The sensor data is fitted with a multivariate Gaussian distribution. The result of the best fit is displayed in figure 4.8b. Scaled

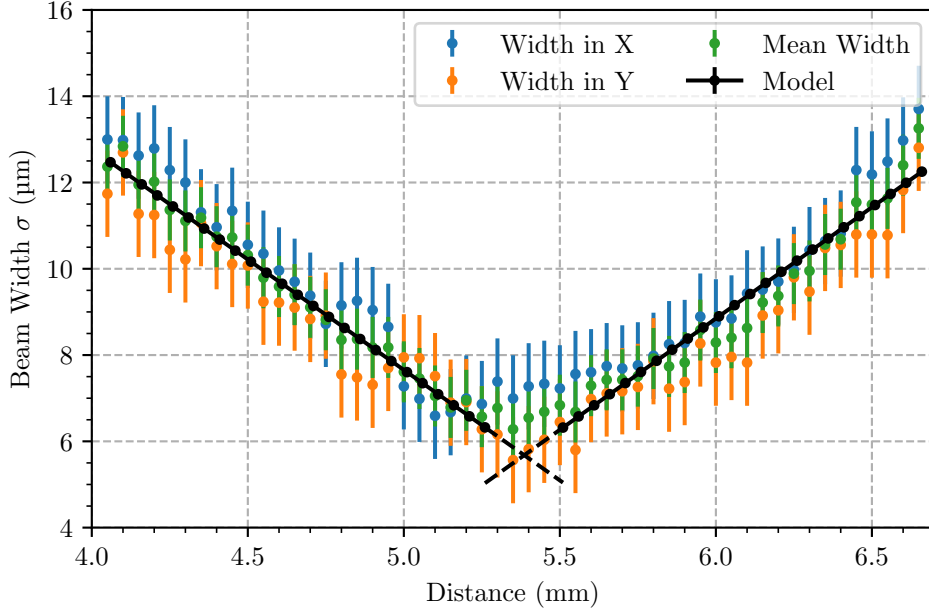


Figure 4.9: **Distribution of the Laser Beam Width for different Distances**

The laser beam width is determined for different distances between the collimating lens and the webcam sensor. By fitting a multivariate Gaussian distribution to the sensor data of the red color channel, the beam width in X and Y is obtained. Averaging the widths in both dimensions yields the mean laser beam width which follows the Gaussian formula for thin lenses. Fitting this model to the mean beam width distribution and extracting the intersection of both lines provides the theoretical minimal laser beam width. To keep the figure clear and understandable, only measured values at an interval of $50 \mu\text{m}$ are plotted.

with the diameter of the individual pixels, the mean experimental minimal laser beam width

$$\sigma_{\text{laser}}^{\text{exp, min}} \geq (6.3 \pm 0.7) \mu\text{m} \quad (4.1)$$

is obtained. The trend of the beam width for other distances is depicted in figure 4.9. The mean of the individual widths in X and Y direction follow the linear model of the well-known Gaussian formula for thin lenses [55]. Fitting the distributions with this model and determining their intersection, yields the theoretical minimal laser beam width

$$\sigma_{\text{laser}}^{\text{theo, min}} \geq (5.7 \pm 0.1) \mu\text{m} \quad (4.2)$$

for a distance of $z = (5.39 \pm 0.01) \text{mm}$, which could be achievable with this lens in the ideal case.

Detector Characterization

In this chapter, the main results of the detector characterization with the laser system are discussed. In section 5.1, the experimental setup of the detector system is introduced and the measurement methodology is described. Afterwards, the view is directed to the data analysis. The modelling of the waveform and the extraction of the relevant parameters is explained in detail in section 5.2. Concluding this chapter, the key findings will be presented and discussed in section 5.3.

5.1 Experimental Setup

For the characterization measurements of the 7 pixel **TRISTAN** detector (S0-7-6), the same laser system was employed, which was introduced in section 4.2. However, the system is adapted to meet the new requirements and changes in the setup, that are necessary for the operation of the detector. Figure 5.1a gives an overview of the experimental setup. The webcam was dismantled from the holding structure and replaced by the detector. Compared to the calibration measurement described in section 4.1, the detector is mounted with the entrance window facing upwards. Normally, this is avoided at any time to prevent damaging the detector entrance window. Damage could originate from touching the SiO_2 window or dust particles in the air being collected on. The deposition of any substance on the detector surface worsens the energy resolution or, in the worst case, could cause irreversible damage, so the affected pixels are no longer functional [44]. However, since the collimating lens is positioned directly above the detector entrance window, accidental damage is substantially reduced. A close up of the entrance window side of detector and the collimating lens is shown in figure 5.1b. Two thin aluminum bond wires are visible near the center of the image. These bond wires connect the two bond pads on the detector **PCB** to the back frame and back contact electrodes of the detector pixels. The vertical position of the lens is set based on the optimal distance between the lens and the sensor that minimized the laser beam width, see

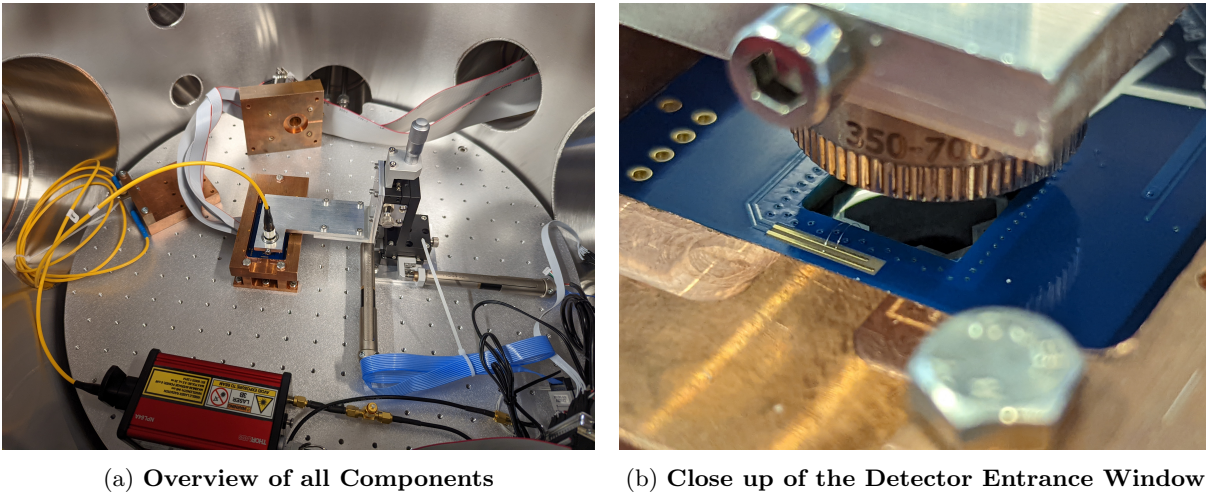


Figure 5.1: **Experimental Setup for the Detector Characterization Measurements**

(a): Compared to the setup for the optimization of the laser system (see figure 4.7), the webcam was replaced by a 7 pixel TRISTAN SDD. In addition, the XYZ linear translation stage was fixed in Z position but kept freely movable in X and Y directions. The movements were automatized using two linear motorized actuators to allow high-precision scans of the SDD.

(b): The detector was mounted facing upwards such that the entrance window was positioned directly below the collimating lens. The laser beam was focused on the SDD and moved over the detector pixels.

section 4.2. For the characterization measurements, the XYZ stage was therefore fixed in the Z position but kept freely movable in the X and Y directions. A motorized actuator was used for each of the two axes to automate the movement in high-precision steps. The laser was pulsed with an external trigger frequency of 500 kHz. This setting allowed a high repetition rate for many laser pulses in the limited measurement time window, but at the same time a large enough time interval for the detector to return to its nominal state between each pulse. To minimize the crosstalk between the laser and the detector caused by the external trigger pulses, the trigger voltage was set to $200 \text{ mV}_{\text{pp}}$. In addition, the pulse width was adjusted to 150 ns with an edge transition time of 20 ns. This way, a distinct pulse is generated and the fast rising edge served as a precise trigger for the laser as well as for the offline analysis.

The measurement procedure was as described in the following: A two-dimensional grid of X and Y coordinates is software generated that covers the surface area of the detector to be examined. Since two independent measurements with different areas of interest were performed, two distinct grids were created. For the first measurement, a grid was formed spanning across the entire detector entrance window. The goal was to investigate the homogeneity and the behavior of the individual pixels of the detector with respect to the charge collection. The grid was chosen to be a square of 350×350 points with a spacing of $25 \mu\text{m}$. This configuration provided a good compromise between the resolution of the scan and the total duration of the measurement. In the second measurement, the area in which three detector pixels are

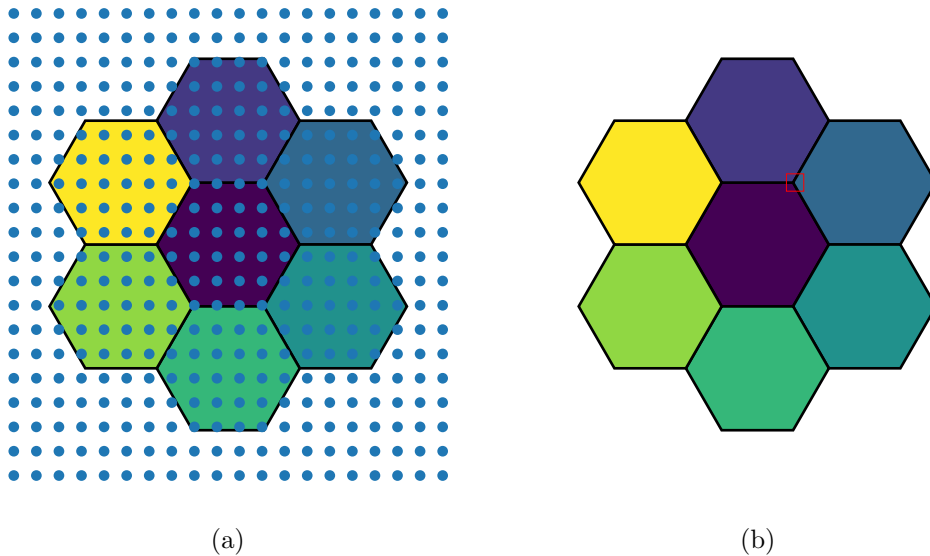


Figure 5.2: **Illustration of the Grid for the Laser Scan**

The 7 pixel **TRISTAN** detector is sketched with each pixel in a different color.

(a): A grid of 20×20 points with a spacing of 0.5 mm illustrates the grid coordinates covering the entire detector. In the measurement, a grid of 350×350 points with a spacing of $25 \mu\text{m}$ is used instead. At each position, the laser beam hits the entrance window and the photons penetrate the **SDD**.

(b): At the location where three detector pixels are in contact a scan of higher resolution was conducted. This region is called a triple point and is of special interest in the analysis. The red rectangle marks the area where a grid of 90×90 points with a spacing of $4.5 \mu\text{m}$ allowed for a more detailed scan. Since the grid points would fill the entire region, the grid is not shown.

adjacent to each other, i. e. the triple point, was studied. For this investigation, the region where pixels 0, 1, and 2 are in contact was selected. A grid of 90×90 points with a spacing of $4.5 \mu\text{m}$ was generated for a high resolution scan. Both cases are depicted in figure 5.2. The actuators steering the XYZ stage move the collimator to the specified coordinates of each XY pair. Since the actuators are controlled via **Pulse Width Modulation (PWM)**, they are powered down after having reached the intended position to prevent crosstalk with the external laser trigger pulses. The major advantage of using a laser to characterize the detector is that the detector is irradiated at the exact location defined in the grid. In addition, the laser pulses carry a fixed amount of energy. With the **VOA**, the beam is attenuated to an output energy equivalent of about 10.6 keV . For each laser pulse, more than 5000 photons penetrate the detector about $(5 - 10) \mu\text{m}$ before being completely absorbed by the silicon and creating electron-hole pairs [77].

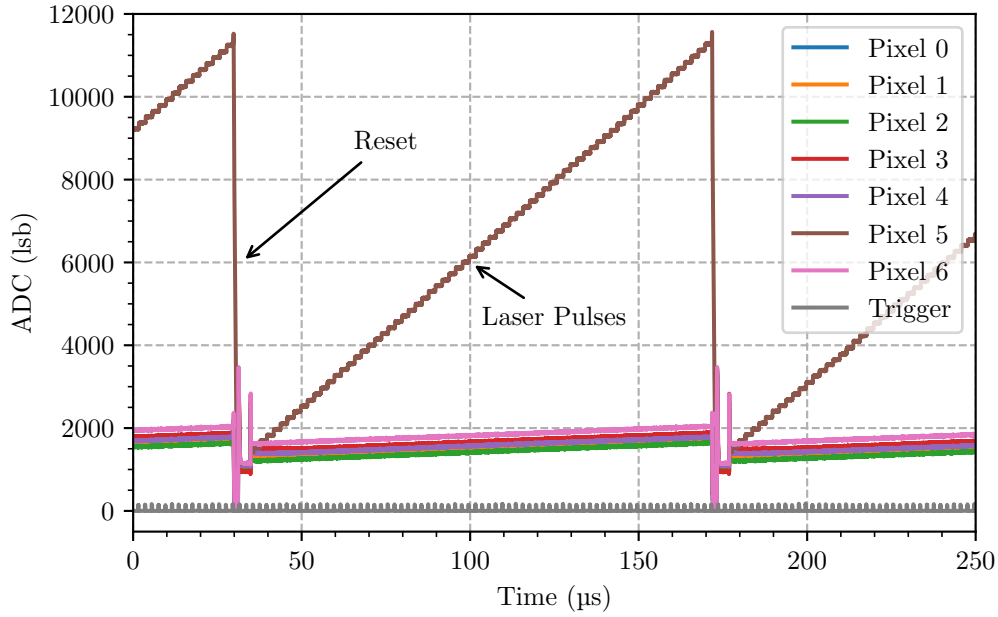


Figure 5.3: **Exemplary Waveform Output of the 7 Pixel TRISTAN SDD**

The acquired waveform signal is shown for all detector pixels. In this configuration, the collimating lens was positioned above pixel 5 during the laser scan. Each step in the waveform of this pixel corresponds to an event due to a single laser pulse. The small spikes at the bottom display the external pulses triggering the laser emissions. At the times $t \sim 30 \mu\text{s}$ and $t \sim 170 \mu\text{s}$, two resets are shown in the waveform, where the signals return to their initial value. The start and end of the inhibit signal, which prevents signals from being read out, is marked by small spikes in the waveforms.

The detector is read out in 1st stage waveform acquisition mode. For each grid position, 1 s of waveform signal is acquired using the same DAQ as for the preparatory measurement in section 4.1. Figure 5.3 shows an example of the raw waveform output for each detector pixel. Additionally, the external laser trigger pulses were recorded for timing purposes. In this configuration, the collimating lens was positioned above pixel 5. Each step in the waveform of this pixel corresponds to a single laser pulse. Since the trigger frequency was set to 500 kHz, the pulses have a period of 2 μs . The intense rate of laser pulses leads to a much faster saturation of the CSA circuit compared to the other pixels. For these, the linearly increasing waveforms are mainly caused by the leakage current which produces the ramp-like shape. At the resets, the feedback capacitors are discharged and the signals return to their initial value. Additionally, the inhibit prevents signals from being read out. The duration of this phase is set to 10 μs to ensure the full discharge of the capacitors and to eliminate non-linear waveform outputs. After the acquisition, the actuators are turned on again and the collimator is moved to the next grid position. This process is repeated for all coordinates until the scan is completed. For the measurement at a single grid position, this resulted in 65 MB of acquired data.

5.2 Modelling the Signal Shape

Studying the properties and the shape of the laser pulses is one of the main objective of this thesis. In particular it was investigated whether and how the shape of the signal can provide information about the location of the interaction in the detector. Thanks to the scanning grid, the interaction position of the incident radiation is precisely known. For the data analysis, an empirical model describing the signal pulses is introduced in the following.

We will briefly recapitulate the signal formation presented in section 3.4 and start with a generic description of a single event in a **TRISTAN** detector. When incident radiation enters the detector, it excites the **Si** atoms of the bulk material. This leads to the creation of electron-hole pairs which form two oppositely charged clouds. These clouds are subject to the electric field in the detector. During their drift, the charge carriers induce a current on the detector anode. This current appears as a pulse when reading out the detector. In the ideal case of instantaneous current, the pulse can be interpreted as a prompt transition from an initial to a final state. While the initial state describes the detector conditions prior to the event, the final state is characterized by the radiation that entered the detector and deposited its energy. The amount of deposited charge on the anode determines the height of the pulse: the higher the energy of the incident radiation, the higher the amplitude of the pulse. This condition introduces the first model parameter: the pulse height *Amplitude* A . In figure 5.4, the signal transition for different pulse heights is illustrated. Mathematically, the ideal signal transition can be described as a step function

$$h(t; A) = A \cdot \Theta(t), \quad (5.1)$$

that depends on the amplitude A and uses the Heaviside function $\Theta(t)$, where t denotes the time. Equation 5.1 represents the most simplified version of a particle detector. The deposited charge is detected and read out instantaneously. In reality, the spatial extension of the detector has to be taken into account. This extension manifests itself as a time delay between the point in time of the interaction of the incident radiation and the generation of the signal pulse. This time difference is called *Drift Time* t_{drift} . It describes the time period between the generation of the electron-hole pairs and the arrival of the electrons at the detector anode. The further away the interaction location is from the anode, the longer it takes for the charge carriers to arrive there. Equation 5.1 can be modified to include this behavior:

$$h(t; A, t_{\text{drift}}) = A \cdot \Theta(t - t_{\text{drift}}). \quad (5.2)$$

The signal is now shifted by the drift time t_{drift} . Figure 5.5 illustrates this effect for a fixed amplitude $A = 100 \text{ lsb}$ and different t_{drift} . At $t = 0 \text{ ns}$, the electrons and holes are generated and start to drift through the detector. More distant interaction positions to the anode translate to increasing drift times for the different signals. It should be noted that the drift time significantly depends on the detector geometry and the applied bias voltages. For a two electrode configuration, a fully depleted planar detector of

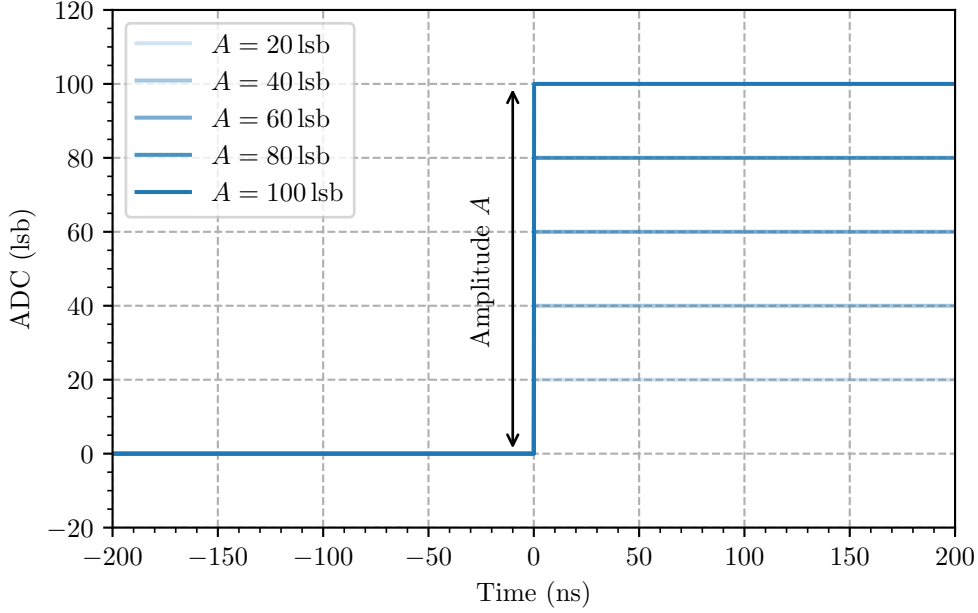


Figure 5.4: **Model Parameter: Amplitude A**

When charge carriers drift inside the detector, they induce a current on the detector anode. This current produces a step-like signal pulse when reading out the detector. The height of this pulse, i. e. the amplitude, is determined by the amount of deposited charge. In this graph, signals with different amplitudes are shown. The darker lines depict signals with higher amplitude.

thickness d , the collection time t_c can be estimated using the electric field $E = V/d$ [119]:

$$t_c \approx \frac{d}{v} = \frac{d}{\mu E} = \frac{d^2}{\mu V}, \quad (5.3)$$

where V is the externally applied bias voltage, v the drift velocity and μ the mobility of the charge carriers. The collection time extends the drift time by the duration for the collection of all charge carriers after the charge cloud arrived at the anode but was not yet fully collected. The charge collection and thus the drift can be accelerated by increasing the bias voltage. For a Si detector of $450 \mu\text{m}$ thickness, similar to a TRISTAN detector, this would result in a collection time of $t_c \approx 3 \text{ ns}$ for electrons assuming an electric field of $E = 10^4 \text{ V/cm}$. However, since the TRISTAN SDD pixels feature a radially symmetric field, the drift time increases considerably.

The longer drift period has an impact on another effect: diffusion. As explained in section 3.4.4, diffusion causes the concentration profile of the charge cloud to spread out which can be described by a Gaussian

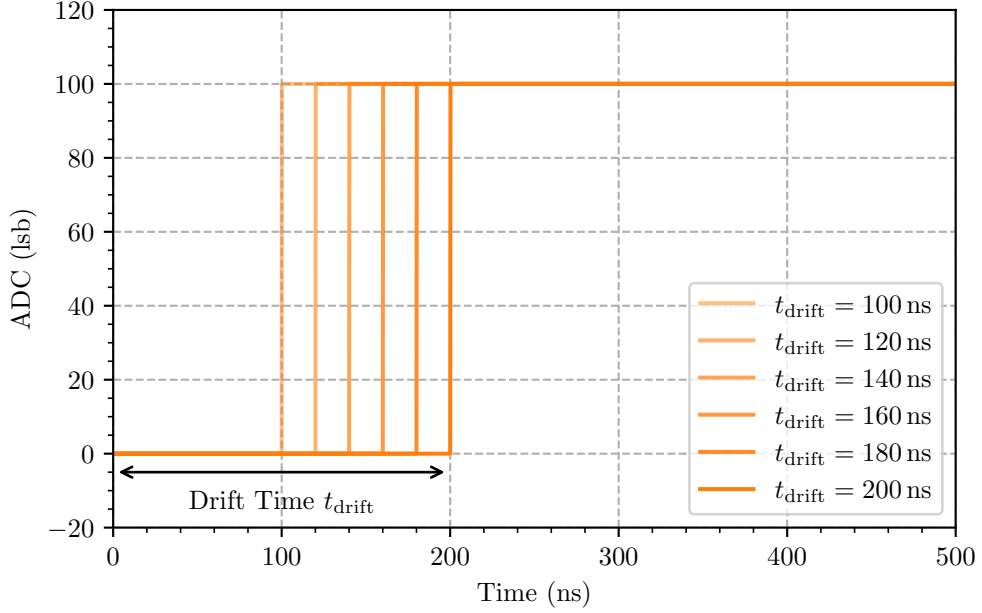


Figure 5.5: **Model Parameter: Drift Time t_{drift}**

Taking the spatial extension of the detector into account leads to a time delay between the point in time of the interaction of the incident radiation and the generation of the signal pulse. This time difference is called drift time. The further away the interaction location is from the anode, the longer it takes for the charge carriers to arrive there. For a fixed amplitude of $A = 100$ lsb, this is illustrated for different t_{drift} with darker lines indicating longer drift times.

distribution

$$g(t; \sigma) = \frac{1}{\sqrt{2\pi}\sigma} \exp\left(-\frac{t^2}{2\sigma^2}\right) \quad (5.4)$$

with standard deviation σ . Since this process is time-dependent, longer drift times will also result in a higher spread and thus larger charge clouds. Including this effect in the signal shape is illustrated in figure 5.6. For a fixed amplitude of $A = 100$ lsb and a constant drift time of $t_{\text{drift}} = 200$ ns, the signal is shown for different diffusion characteristics. Since the standard deviation is also often referred to as width, the third parameter in the model is called *Gaussian Width* σ . Mathematically, the spread can be included via a convolution of the existing model with the Gaussian distribution:

$$\begin{aligned} i(t; A, t_{\text{drift}}, \sigma) &= (h * g)(t) \\ &= \int_{-\infty}^{\infty} h(s; A, t_{\text{drift}}) h(t - s; \sigma) ds \\ &= \int_{-\infty}^{\infty} A \cdot \Theta(s - t_{\text{drift}}) \left(\frac{1}{\sqrt{2\pi}\sigma} \exp\left(-\frac{(t - s)^2}{2\sigma^2}\right) \right) ds. \end{aligned} \quad (5.5)$$

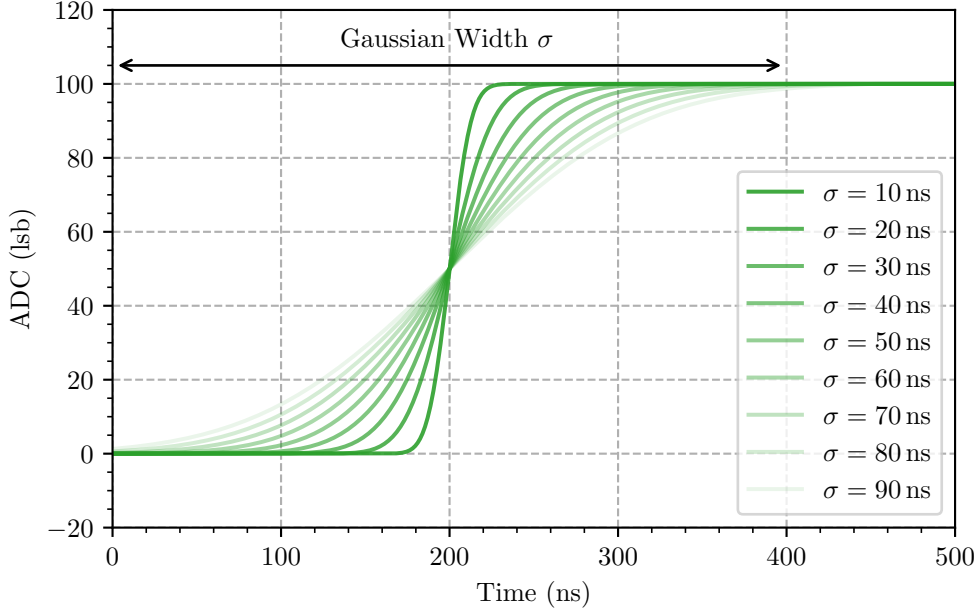


Figure 5.6: **Model Parameter: Gaussian Width σ**

The impact of diffusion on the charge cloud manifests as Gaussian smearing of the signal. For a fixed amplitude of $A = 100$ lsb and a constant drift time of $t_{\text{drift}} = 200$ ns, the width of the Gaussian distribution (i. e. the Gaussian width), that is convoluted with the existing model, is varied to illustrate the influence on the signal shape. While the darker lines represent signals that were subject to less diffusion effects, the fainter lines show signals of charge clouds that were highly diffused.

For the TRISTAN detectors, the diffusion for charge clouds and therefore the Gaussian width is expected to increase at larger radial positions, since longer times are required to drift from there to the anode.

Another model parameter is the *Exponential Rise Time* τ . This time constant accounts for the response of the charge sensitive pre-amplifier to a signal pulse. Applying a voltage step to the input of an amplifier does not result in an instant response since the feedback capacitance C_{FB} has to charge up first. In this context, the exponential rise time determines how quickly charge can be transferred from the detector to the amplifier. The response of the CSA circuit to a unit voltage step can be written as

$$j(t; t_{\text{drift}}, \tau) = 1 - \exp\left(-\frac{t - t_{\text{drift}}}{\tau}\right). \quad (5.6)$$

This function describes the discharge of the detector capacitance by the resistive input impedance R_i of the pre-amplifier with the time constant [119, 110]

$$\tau = R_i C_{\text{det}} = \frac{1}{w_0} \frac{C_{\text{det}}}{C_{\text{FB}}} = \frac{C_o}{g_m} \frac{C_{\text{det}}}{C_{\text{FB}}}, \quad (5.7)$$

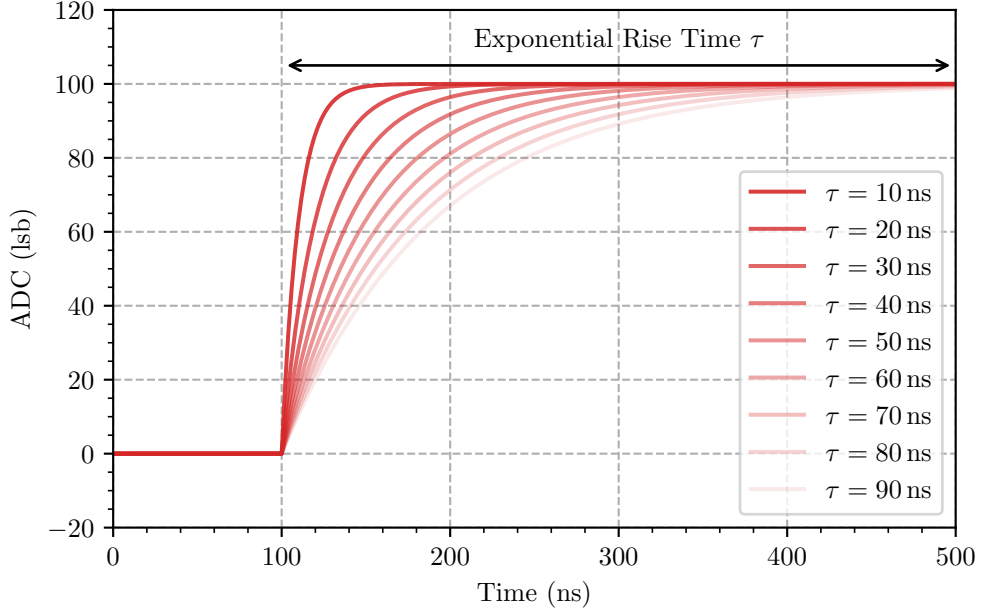


Figure 5.7: **Model Parameter: Exponential Rise Time τ**

Applying a voltage step to the input of an amplifier does not result in an instant response since the feedback capacitance has to charge up first. In this context, the response of the CSA circuit is characterized by how quickly charge can be transferred from the detector to the amplifier. The discharge of the detector capacitance by the resistive input impedance of the pre-amplifier can be described by a rising exponential function with time constant τ . For a fixed amplitude of $A = 100$ lsb and a constant drift time of $t_{\text{drift}} = 100$ ns, the exponential rise time is varied to illustrate different responses of the CSA circuit. While the darker lines demonstrate the fast transfer of charge from the detector to the amplifier, the fainter lines feature longer exponential tails due to a slower transfer.

where w_0 is the unity gain-bandwidth of the amplifier, C_o the capacitive output load, g_m the transconductance of the JFET, and $C_{\text{FB}}/C_{\text{det}}$ the closed loop feedback gain. Since the rise time of the CSA circuit increases with detector capacitance, the feedback capacitor C_{FB} is smaller than C_{det} . In reality, τ is determined by the duration and the shape of the charge cloud during charge collection. We extend the model from equation 5.2 with equation 5.6 and obtain

$$\begin{aligned} k(t; A, t_{\text{drift}}, \tau) &= h(t; A, t_{\text{drift}}) \cdot j(t; t_{\text{drift}}, \tau) \\ &= A \cdot \Theta(t - t_{\text{drift}}) \cdot \left(1 - \exp\left(-\frac{t - t_{\text{drift}}}{\tau}\right) \right). \end{aligned} \quad (5.8)$$

This function is used to illustrate the impact of the exponential rise time on the signal in figure 5.7. Since the electric field in the TRISTAN detectors is homogeneous within a single pixel, a nearly constant, low-value exponential rise time is expected. However, towards the pixel borders, τ will increase steeply as the electric fields of multiple pixels intersect.

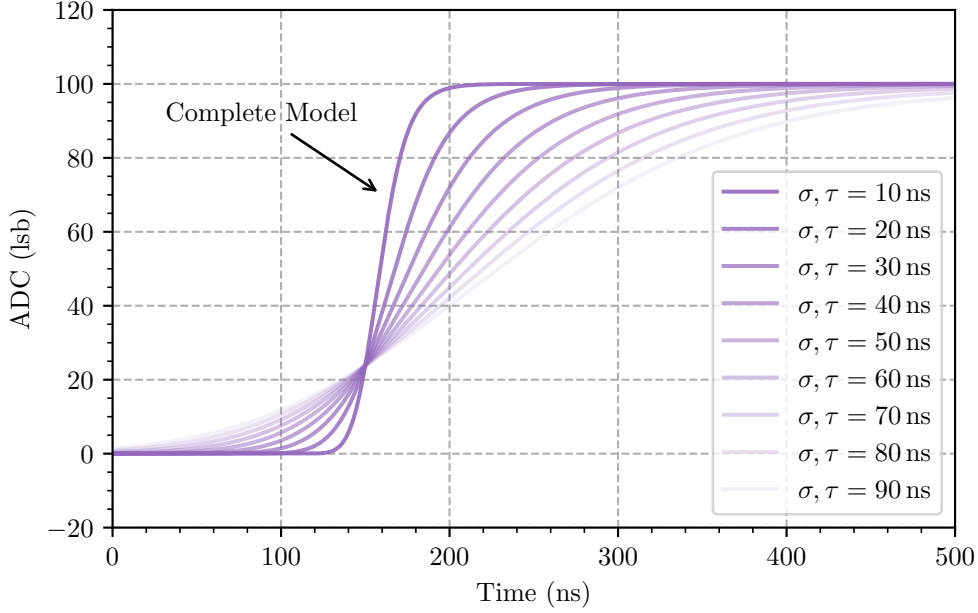


Figure 5.8: **Complete Model of the Signal Shape**

The combination of all model parameters gives the complete model of the signal shape. For a fixed amplitude of $A = 100$ lsb and a constant drift time of $t_{\text{drift}} = 150$ ns, signals are shown for various tuples of identical Gaussian widths σ and exponential rise times τ . The darker lines illustrate signals which maintain a steep shape for low-valued tuples. However, as σ and τ are increased, the pulses become shallower, as indicated by the fainter lines

Putting together equations 5.4 and 5.8, the complete model to describe the signal shape is obtained:

$$\begin{aligned}
 f(t; A, t_{\text{drift}}, \sigma, \tau) &= (k * g)(t) \\
 &= \int_{-\infty}^{\infty} k(s; A, t_{\text{drift}}, \tau) g(t - s; \sigma) ds \\
 &= \int_{-\infty}^{\infty} \left(A \cdot \Theta(t - t_{\text{drift}}) \cdot \left(1 - \exp\left(-\frac{t - t_{\text{drift}}}{\tau}\right) \right) \right) \left(\frac{1}{\sqrt{2\pi}\sigma} \exp\left(-\frac{(t - s)^2}{2\sigma^2}\right) \right) ds
 \end{aligned} \tag{5.9}$$

The convolution is evaluated numerically and displayed in figure 5.8. The impact of the Gaussian broadening as well as the exponential tail due to the response of the CSA circuit are clearly visible. As was to be expected, all curves pass through the same point at the specified drift time. This model is used to fit the measurement data.

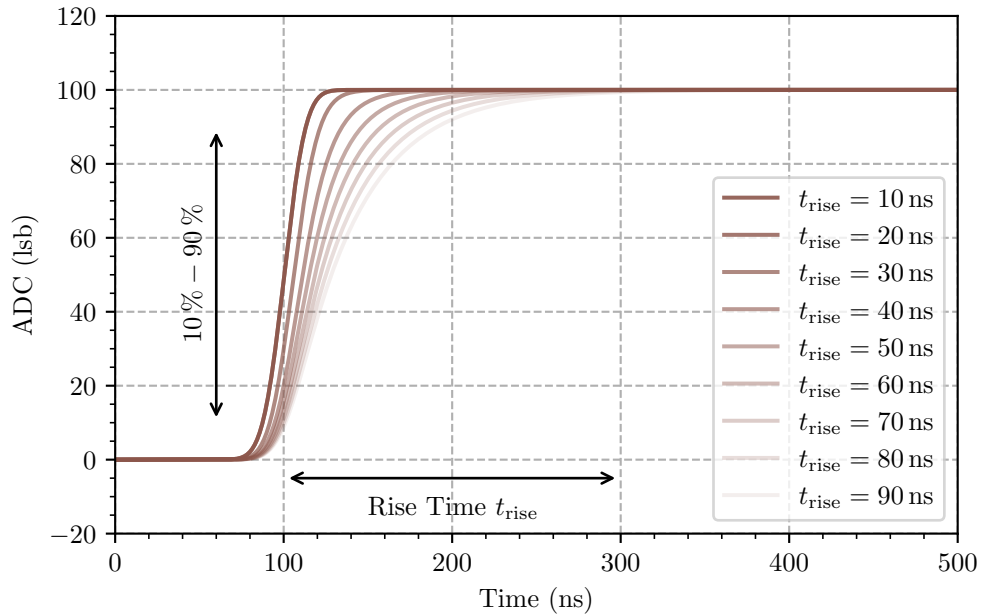


Figure 5.9: **Signal Pulses for different (10 - 90)% Rise Times**

For a fixed amplitude of $A = 100$ lsb, a constant drift time of $t_{\text{drift}} = 100$ ns and a given Gaussian width of $\sigma = 10$ ns, the exponential rise time is kept as a free parameter to illustrate the variation of the signal pulse shape for different (10 - 90) % rise times. While the darker lines represent the signals of events with short rise times, the fainter lines visualize the impact of longer rise times on the exponential tail of the signals.

Another parameter for measuring the timing of the signal is the rise time t_{rise} . The rise time is typically defined as the time period in which the signal rises from 10 % to 90 % of its amplitude. It is a combination of the Gaussian width σ and the exponential rise time τ . Compared to σ and τ , t_{rise} is a more commonly used time constant that allows for comparisons to other detectors and experiments. Figure 5.9 shows the signal shape for different rise times. In general, a shorter distance between the interaction location and the detector anode results in a lower signal rise time. Increasing the distance to the anode, extends the signal rise time as well. This is because the charge cloud increases in size during longer drifts in the electric field of the detector pixel, prolonging the collection of charge carriers at the anode.

With the well-established model, an exemplary analysis of the measured data acquired at a single grid position during one of the laser scans is conducted. The analysis is performed in multiple steps. The recorded waveforms of 1s length are convolved with a trapezoidal filter to detect the resets in the signal. This is similar to the process of identifying ^{55}Fe events as described in section 4.1 but with a much higher energy threshold. At the same time, the rising edges in the external laser trigger pulses are also identified. These define the reference timestamps for the generation of the charge carriers and therefore mark the onset of the charge cloud drift. The waveforms are then divided into small signal

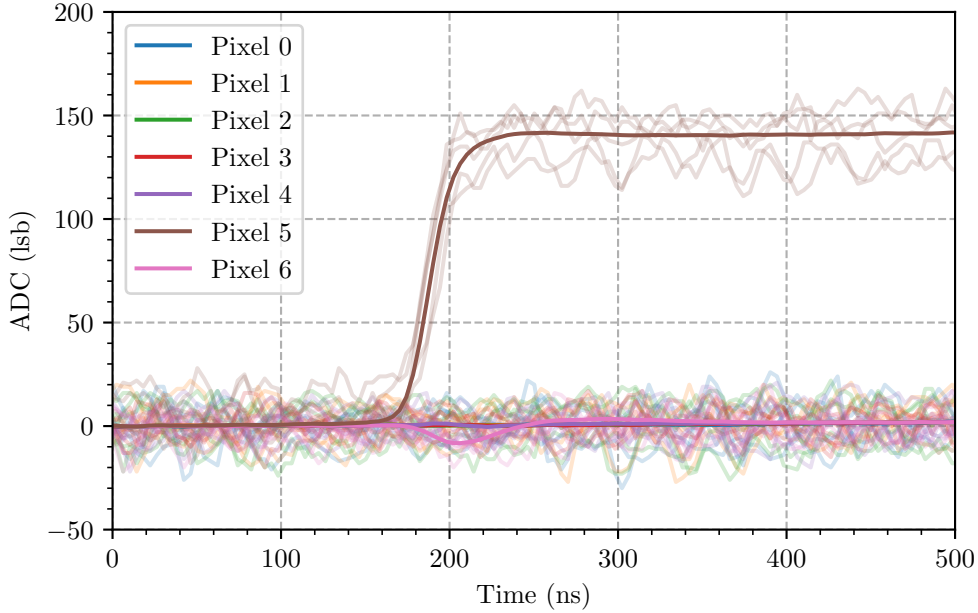


Figure 5.10: **Averaging Procedure of the Waveform Snippets**

Exemplarily, the waveform snippets obtained from figure 5.3 are shown. Since, the collimating lens was positioned above pixel 5, the signal pulses only were present in this pixel. While the fainter lines depict the individual waveform snippets event by event, the solid lines illustrate the result of averaging over all of these snippets for each pixel. This procedure is performed to eliminate fluctuations on the waveforms caused by thermal and electronic noise. In addition, it also makes the effect of crosstalk between pixels 5 and 6 clearly visible.

snippets whose start and end are defined by the trigger timestamps of the current and the next following event. For the analysis, only events that are $10\ \mu\text{s}$ before or after the resets are considered to prevent any potential impacts of the resets on the waveforms of the signals. The waveform snippets contain the laser pulses and are all $2\ \mu\text{s}$ in length, which corresponds to the period of the external laser trigger pulses. A baseline correction, which is an important pre-processing technique that moves the baseline of all signals to zero, is applied to the individual snippets. Afterwards, all digitized waveform snippets start with the identical value of 0 lsb at the time $t = 0\ \text{ns}$. Figure 5.10 visualizes this state in the analysis process. Due to the noise in the signals, all snippets of one pixel are averaged. This procedure is well-motivated since the waveforms are uncorrelated. The stability of the laser with respect to the average output power per pulse is an important requirement and is examined in section A.1. The result of the averaging procedure is indicated by the dark solid lines. These signals are now free of fluctuations caused by thermal and electronic noise. Hence, only these averaged waveforms will be used in the fitting procedure. In addition to the positive signal pulse of pixel 5, a negative dip is observed in the signal of pixel 6. This dip is caused by crosstalk between these two pixels, since both cells are read out via the same metal bus structure. This behavior can be explained by the presence of a parasitic capacitance between the feedback line of the

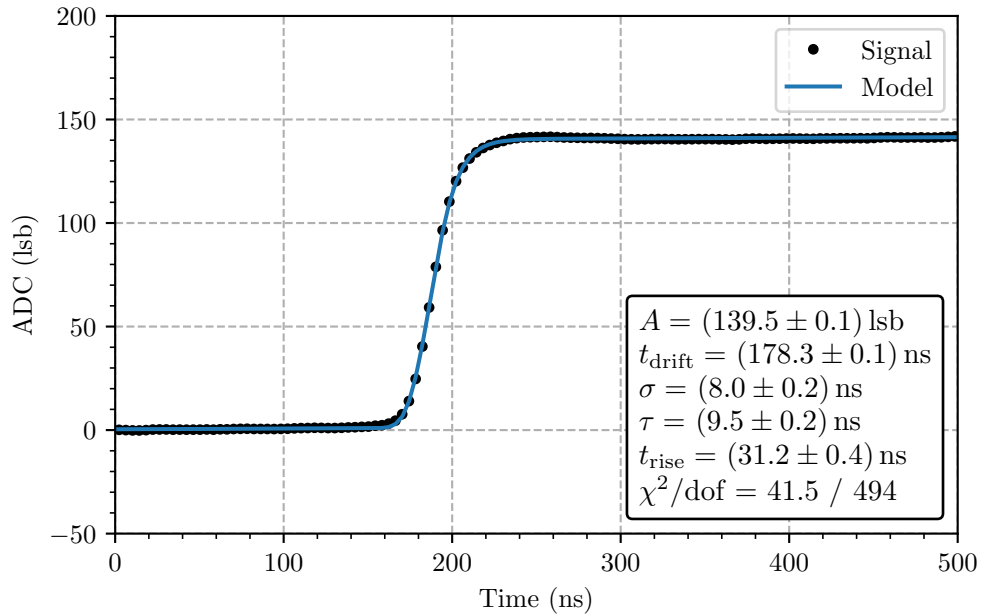


Figure 5.11: **Exemplary Fit of a Signal Pulse**

The black dots show the averaged waveform snippet of pixel 5 of figure 5.10. The blue line depicts the best fit of the signal model to the waveform data for which χ^2 is minimal. Since the other pixels were not irradiated by the laser, they are not considered here.

aggressor (pixel 5) and the source line of the victim (pixel 6). A positive voltage step in the feedback line of one pixel induces another voltage step with the same sign on the source line of the other pixel. This leads to a negative voltage step in its feedback line and results in the observed output. The same holds for the pixels (0, 1, 4) and (2, 3). A more detailed description of this phenomenon is given in [79]. Since the signal model does not account for crosstalk, it will be neglected in the following analyses. Therefore, only pixel combinations that are not affected by crosstalk are examined when studying the effects of pixel borders on the drift of the charge carriers. The entire procedure of the waveform extraction and signal averaging is repeated for each individual grid point.

Finally, figure 5.11 shows an exemplary fit of a signal pulse. The data was fitted with the model obtained in equation 5.9 using least squares minimization. The leakage current component is compensated by a linear model in addition to the signal model. Similar to the waveform averaging, the fitting procedure is done for all pixels at each grid point.

5.3 Results of the Laser Characterization

In this section, the results of the characterization of a [TRISTAN SDD](#) with a laser are discussed. The individual model parameters are covered in the upcoming subsections.

5.3.1 Amplitude

The fitted amplitude A of the signals is the first parameter that will be analyzed. For the conversion from [ADC](#) codes to energy, the calibration determined in section [4.1](#) is applied to the obtained values. Figure [5.12](#) shows a two-dimensional heat map of the measured energy as a function of X and Y positions. These positions correspond to the grid points as introduced in section [5.1](#). The individual detector pixels are clearly visible. As expected, a mostly homogeneous energy distribution for all pixels with a mean energy of $E_0 \approx 10.6$ keV is observed. The yellow vertical stripes arise from the fact that the scan was performed along the vertical direction and the output power of the laser was fluctuating. This behavior may have been caused by the laser's temperature sensor: When the temperature is too high, the laser's output power is reduced. Since this measurement was conducted over a time period of more than two weeks, the continuous operation of the laser could have resulted in this effect.

In the region of the pixel borders, the reconstructed energies are much smaller. This is due to the effect of charge sharing. This effect leads to the splitting of the charge cloud between multiple pixels. Each of the participating pixel collects a fraction of the created charge which is why each of them detects an event. Since only a single event happened in reality, summing up the energies of the individual events yields the total deposited energy of the incident radiation. In traditional analysis techniques, charge sharing events can be identified by comparing the timestamps between consecutive events. A coincidence time window of (100 - 200) ns length can be defined to find events that are within a certain interval. The multiplicity of a single event is determined by how many pixels participate in charge sharing. The higher the multiplicity, the more pixels are involved in the process of charge collection. In this thesis, however, the charge drift is investigated using the interaction point and the shape of the signal pulses directly.

In figure [5.13](#), the reconstructed energy is depicted for the region of a triple point. The plot clearly shows the boundaries of the individual pixels and the contour lines correspond to a certain energy. Approaching the pixel borders, the collected charge decreases, until no charge carriers are collected any longer. At the same time, the amount of charge collected by the adjacent pixel increases. At the triple point, i. e. the location where the three pixels are in contact with each other, equal amount of charge is shared between them and in each pixel an event is triggered. Summing up the energies of the three corresponding events indicated that all charge carriers were collected. Charge carriers of the created charge clouds are observed to reach more than $50 \mu\text{m}$ into the neighboring pixels. Therefore, knowing the actual size of

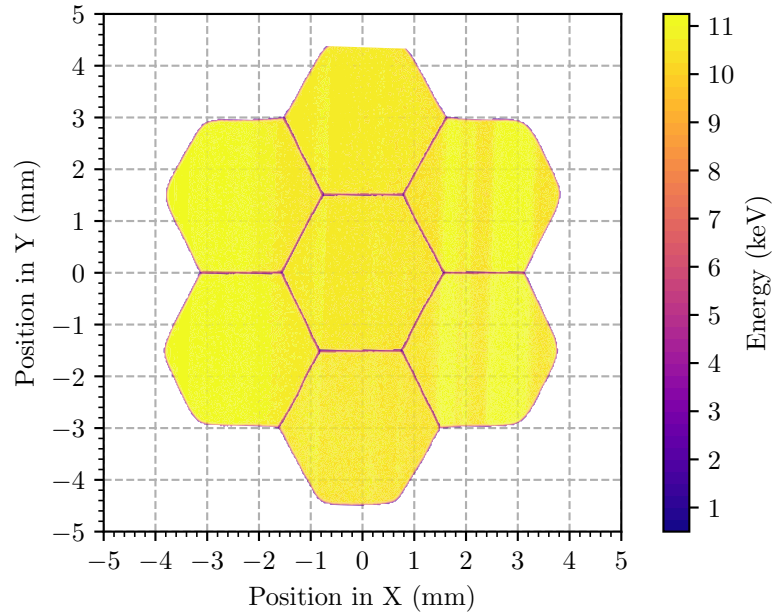


Figure 5.12: **Measured Energy Spectrum of a 7 Pixel TRISTAN SDD**

The measured energy spectrum is displayed for the 7 pixels of the detector as a function of X and Y positions. The reconstructed energies are homogeneously distributed over the SDD pixels, showing that the process of charge collection works equally in all pixels. Superimposed on the distribution are yellow vertical stripes which are the result of a fluctuating output power of the laser. The borders of the individual pixels are clearly visible. However, in the case of the top pixel, the upper border is missing because the maximum extension length of the actuator was reached.

the charge cloud is of high importance. Making use of the effects of charge sharing, this is investigated by examining the data along a certain axis X with the other axis Y kept at a constant value. The black dashed line at $Y \approx 1343 \mu\text{m}$ illustrates this as an example. In figure 5.14, the one-dimensional data along the X-axis crossing two adjacent pixels (pixels 0 and 2) is shown. During the transition from one pixel to the other, the amount of collected charge balances between the pixels. When one pixel collects less charge, the other pixel collects more. Reconstructing the total energy at each position of the charge cloud distribution yields the mean deposited energy of $\sim 10.6 \text{ keV}$. This means that all charge carriers generated near the border between adjacent pixels are fully collected at their respective anodes.

By measuring the width of the charge cloud distribution, the charge cloud size can be obtained. The size of the charge cloud determines the proportion of charge collected in one pixel relative to the charge collected in the adjacent pixel. The further the charge cloud extends into the neighboring pixel, the more charge carriers move into this pixel. Exactly at the border between the involved pixels, the same amount of energy is shared. Since the charge cloud has the shape of a Gaussian distribution, the charge cloud distribution takes the form of its integral. Therefore, the energy as a function of the X position is

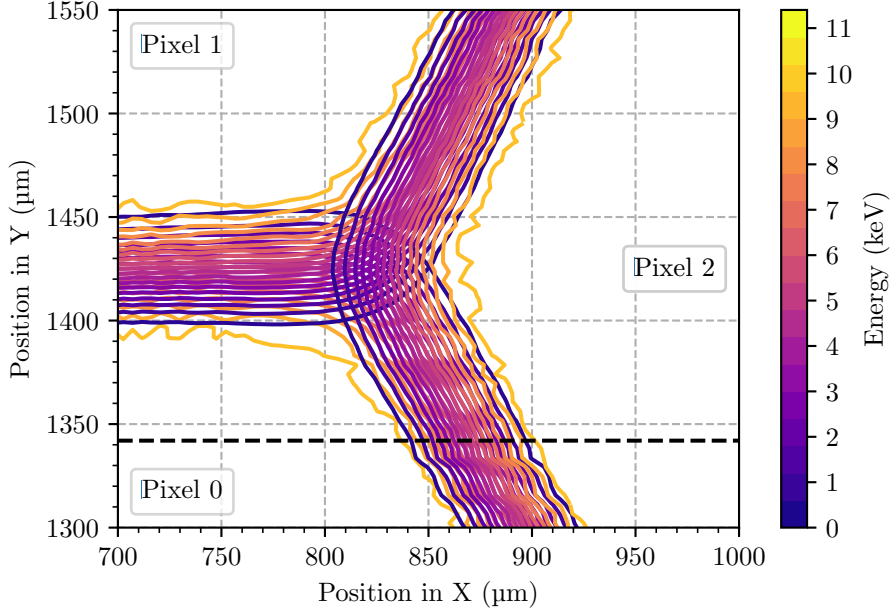


Figure 5.13: **Reconstructed Energy at the Region of a SDD Triple Point**

The reconstructed energy at the region of a detector triple point is shown for the pixels 0, 1, and 2. The contour lines enclose the areas of the pixels where the same amount of charge was collected. At the borders of the pixels, the charge clouds split due to the effect of charge sharing and the charge carriers are collected at the respective anodes. The region where the contour lines overlap is one of the triple points of the SDD. The energy of incident radiation deposited there is distributed to all three detector pixels. The black dashed line represents one of the horizontal slices used to determine the charge cloud size.

described by

$$E(X) = \frac{\langle E \rangle}{2} \left(1 + \operatorname{erf} \left(\frac{X - \mu}{\sqrt{2}\sigma} \right) \right), \quad (5.10)$$

where $\langle E \rangle$ is the mean deposited energy in the pixel, μ the location of the pixel border, and σ the width of the charge cloud distribution. Only transitions between pixels (0, 1) and (1, 2) are considered as for pixels 0 and 1 the crosstalk causes a too large distortion of the signal. In total, the data of 45 one-dimensional horizontal slices is extracted. Since the hexagonal shape of the detector pixels is achieved by corners of angles of 120° , the non-perpendicular transition between the pixels must be corrected for by 30° . Calculating the weighted average of the widths of the individual charge cloud distributions obtained from fitting the model of equation 5.10 to the examined data, yields a total experimental charge cloud distribution width of

$$\sigma_{\text{tot}}^{\text{exp}} = (17.5 \pm 0.1) \mu\text{m}. \quad (5.11)$$

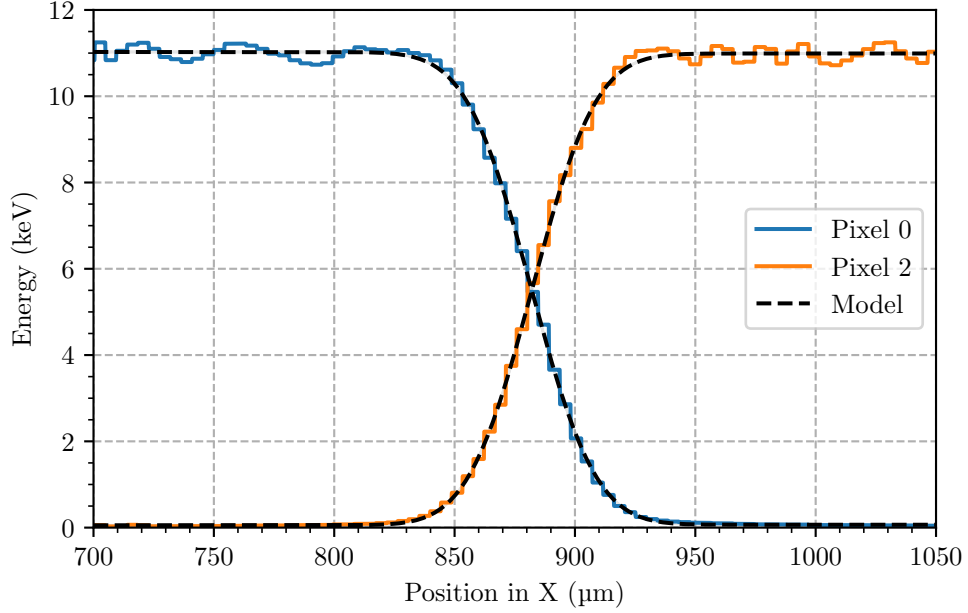


Figure 5.14: **Exemplary Charge Cloud Distribution between Pixels 0 and 2**

For a fixed position in $Y \approx 1320 \mu\text{m}$, the data along the X-axis is examined for the pixels 0 and 2. The blue curve depicts the decrease of collected charge for pixel 0, while at the same time, the orange curve shows the increase for pixel 2. The intersection of the curves corresponds to equal amounts of shared energy and marks the location of the pixel border. For both pixels, the charge cloud distribution is fitted with the model of equation 5.10 to obtain the width. The results of the best fits are displayed as black dashed lines.

This value is composed of the width of the charge cloud and the width of the laser beam:

$$(\sigma_{\text{tot}}^{\text{exp}})^2 = (\sigma_{\text{CC}}^{\text{exp}})^2 + (\sigma_{\text{laser}}^{\text{exp,min}})^2. \quad (5.12)$$

Since the components follow the shapes of Gaussian distributions, summing in quadrature is allowed. Transforming equation 5.12 and using $\sigma_{\text{laser}}^{\text{exp,min}} \geq (6.3 \pm 0.7) \mu\text{m}$ as discussed in section 4.2, an upper limit on the experimental charge cloud width of

$$\sigma_{\text{CC}}^{\text{exp}} \leq (16.3 \pm 0.2) \mu\text{m} \quad (5.13)$$

is obtained. This is one of the major results of this thesis. For the keV-scale sterile neutrino search with the TRISTAN detectors, the precise understanding of the detector response to incident radiation is essential. This is necessary since the impact of the charge cloud size on the detector response increases as the energy range studied becomes larger. In the reconstruction of the deposited energy by the incident radiation a minimum energy threshold must be defined to discriminate the signal produced by electrons

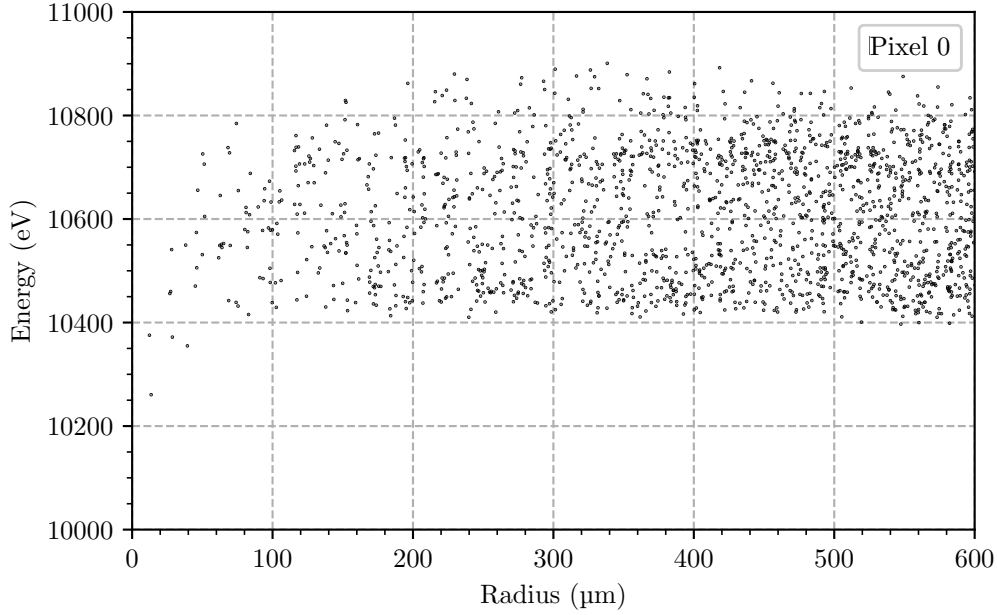


Figure 5.15: **Reconstructed Energy in the Central SDD Pixel**

For the central detector pixel, the energy reconstructed from the amplitude of the signal pulses is shown as a function of the radius. The distribution is centered around its mean at $E_0 \approx 10.6$ keV and has a spread of approximately 400 eV. While the energy is constant above a radius of 100 μm , the reconstructed energy is reduced by about 4% at $r \approx 0$ μm . This behavior is explained by the presence of the integrated **JFET** in the center of the pixel, which influences the process of charge collection.

and holes created in an event from the thermal and electronic noise also present in the signal. For charge sharing events, this can lead to the effect that a fraction of the deposited energy is not fully reconstructed when the amount of collected charge was below this threshold. This results in the affected pixels not being triggered, leading to an underestimation of the energy of the incident radiation in the data analysis. This issue is particularly prominent when the energy of the incident particle is very small, i. e. < 1 keV. Hence, the energy threshold is usually set as low as possible. The sensitivity studies conducted for the keV-scale sterile neutrino search investigate a.o. how low the energy threshold can be set. Currently, the model of the detector response factors in a charge cloud size of (15 ± 3) μm obtained in previous measurements [130]. Now, the model is given an upper limit on σ_{CC}^{exp} , which is independent of the definition of a coincidence window, but determined in a more direct way based on the location of the interaction of the incident radiation.

The entire two-dimensional data of central detector pixel is projected down to one dimension. Figure 5.15 shows the inner region of this pixel. The scatter plot illustrates the reconstructed energy as a function of the pixel radius. The distribution is centered around its mean and has a spread of approximately 400 eV.

For radii above $100\ \mu\text{m}$, the energy is constant. However, for smaller radii, the energy decreases and a significant drop of about 4% is visible at $r \approx 0\ \mu\text{m}$. This behavior can be explained by the presence of the integrated **JFET** in the center of the pixel, c.f. section 3.2. Although the anode should form the actual minimum of the electric potential, the drain contact of the **JFET** is the most positive electrode inside the **SDD** pixel. To prevent electrons from drifting to the transistor instead of the anode, the **IGR** is placed between **JFET** source contact and the anode. It acts as a barrier to shield the **JFET** from the silicon bulk. As it turned out in the analysis of the measurement data, the **IGR** electrode was set to a too positive voltage. Electrons could surpass the potential barrier formed by the **IGR** and were collected by the drain electrode of the transistor. This resulted in the effect of charge loss. Electrons are lost during the collection process and the measured energy no longer corresponds to the deposited energy. This leads to distortions in the energy spectrum and must be avoided. Decreasing the voltage V_{IGR} applied to the **IGR** contact to more negative voltages will increase the barrier strength and restore the conditions for complete charge collection.

5.3.2 Drift Time

The drift time t_{drift} is the second model parameter to be discussed. Just as for the energy distribution, figure 5.16 shows a two-dimensional contour plot of the values obtained in the fitting procedure of the measured data. It can be observed that due to the drift ring geometry, the drift time distribution forms isochrones. As expected, the isochrones are of identical shape for all detector pixels. Since the electric potential of the pixels of the **SDD** is radially symmetric, c.f. chapter 6, the drift time of the charge cloud is a well-suited parameter to describe the radial dependence of the charge cloud drift.

As it turns out, the drift ring geometry inherent to the design of the **SDD** leads to different t_{drift} regimes. Figure 5.17 shows the two-dimensional drift time distribution of the central detector pixel projected down to one dimension as a function of the pixel radius. In the range of $r = (500 - 1000)\ \mu\text{m}$, where the transport trough in the electric potential is of linear shape, the distribution of the drift times can be fitted with a linear model. We obtain the description for the minimum, mean, and maximum drift time as a function of the radius r :

$$t_{\text{drift}}^{\text{min}}(r) = (137.0 \pm 0.5) \frac{\text{ns}}{\text{mm}} \cdot r + (1.1 \pm 0.4) \text{ ns}, \quad (5.14)$$

$$t_{\text{drift}}^{\text{mean}}(r) = (149.2 \pm 0.6) \frac{\text{ns}}{\text{mm}} \cdot r + (0.3 \pm 0.4) \text{ ns}, \quad (5.15)$$

$$t_{\text{drift}}^{\text{max}}(r) = (157.7 \pm 0.4) \frac{\text{ns}}{\text{mm}} \cdot r + (2.7 \pm 0.3) \text{ ns}. \quad (5.16)$$

A close look on figure 5.16 can explain the different drift time regimes: As noted before, the drift time distribution resembles the actual drift ring structure (compare to figure 3.6b, note the rotation by 90°). While the drift rings are straight on the vertical axis (i. e. parallel to the signal bus structure), they have

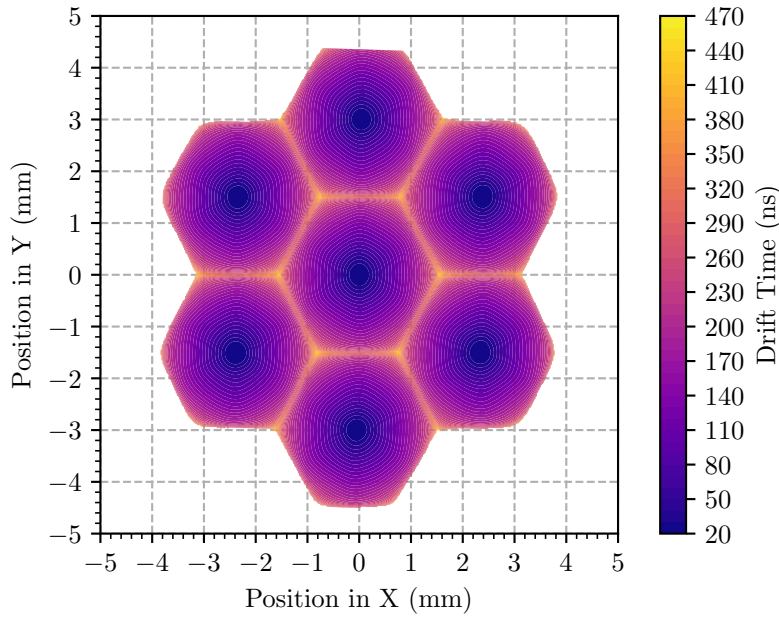


Figure 5.16: **Measured Drift Time Distribution of a 7 Pixel TRISTAN SDD**

The distribution of the measured drift times of the generated charge clouds is shown for the 7 pixels of the detector as a function of X and Y positions. The distribution forms isochrones which are of identical shape for all pixels. This is expected as the structure of these lines resembles the drift ring geometry. Charge clouds generated close to the pixel center are characterized by drift times of about 20 ns. For larger radii, the drift times increase to about 280 ns due to longer distances to the anode. Even larger drift times are the consequence of the impact of the pixel borders on the distribution of the electric potential.

a curved shape on the horizontal axis. Hence, charge clouds, which are created at the same distance to the center but one on the vertical axis and the other on the horizontal axis, experience different electric fields. The detector regions in which the drift rings are not of curved shape feature more stable and stronger field gradients. Hence, the overall drift characteristics of the charge clouds are improved and the drift times are reduced.

The change of the shape of the drift time distribution outside this linear regime is caused by multiple aspects: Towards smaller radii, the charge carriers are closer to the detector anode. Therefore, less drift rings are available to guide these charges in the transport trough and the impact on the drift time decreases. Instead, the drift time is now determined by other field components. This can be seen in particular at the pixel center. There, the charge clouds either drift directly to the anode resulting in shorter drift times or they have to be guided around the **JFET**, which in turn leads to slightly increased drift times. Both effects can be observed in figure 5.17. At larger radial positions, the impact of the drift rings on the charge drift also reduces. Here, the shape of the electric potential at the pixel borders is responsible for the increase of the drift time.

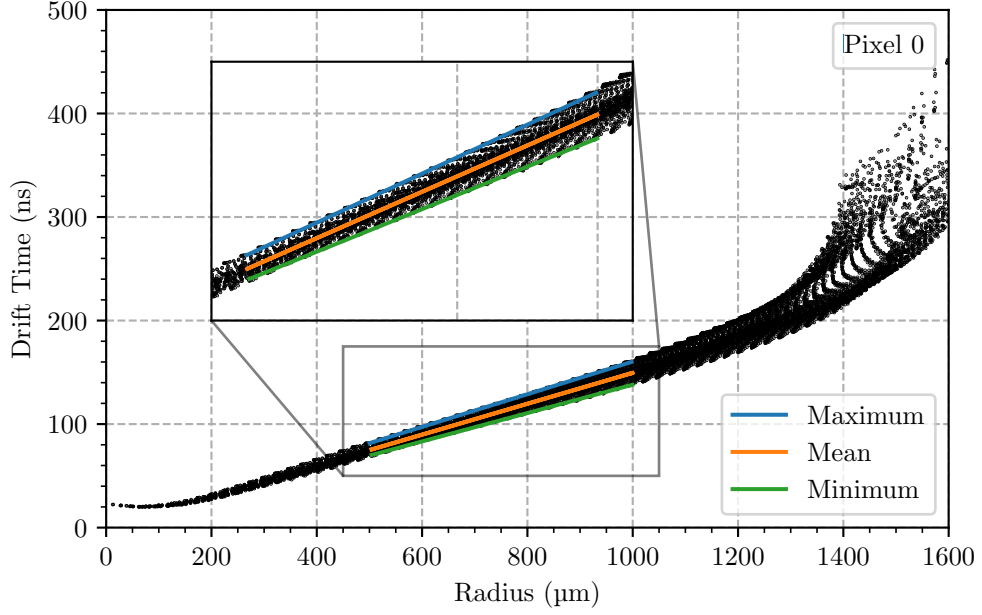


Figure 5.17: **Drift Time of Charge Clouds in the Central SDD Pixel**

The distribution of the drift times of charge clouds generated in the central detector pixel is shown as a function of the radius. The drift time increases towards larger radial positions due to longer drift distances to the detector anode. In the linear regime of the transport trough of the electric potential a linear model describes the drift time distribution. The different slopes of the best fits (illustrated by the blue, orange, and green lines) to the drift time distribution in this regime are a consequence of the drift ring geometry. The increase of the drift time at small radii results from the influence of the integrated JFET on the drift of the charge clouds. The shape of the electric potential at the pixel border is responsible for the increase of t_{drift} at large radii.

Figure 5.18 shows a histogram of the drift time distribution of the central SDD pixel. A distinct peak at 20 ns defines the minimum drift time for all charge clouds. The histogram follows the shape of an exponentially modified Gaussian distribution

$$g_{\text{exp}}^{\text{mod}}(t_{\text{drift}}; T, \mu, \xi, \gamma) = T \cdot \frac{\gamma}{2} \cdot \exp\left(\gamma(\mu + \gamma\xi^2 - t_{\text{drift}})\right) \cdot \left(1 - \text{erf}\left(\frac{\mu + \gamma\xi^2 - t_{\text{drift}}}{\sqrt{2}\xi}\right)\right), \quad (5.17)$$

where T is the scaling amplitude, μ the mean and ξ the standard deviation of the Gaussian component, and γ the rate of the exponential. The Gaussian component represents the distribution of the drift time of charge clouds whose energy was completely collected at the anode of this SDD pixel and the exponential tail that of the clouds involved in charge sharing. The mean

$$\eta_{\text{exp}}^{\text{mod}} = \mu + \frac{1}{\gamma} = (161.6 \pm 1.9) \text{ ns} \quad (5.18)$$

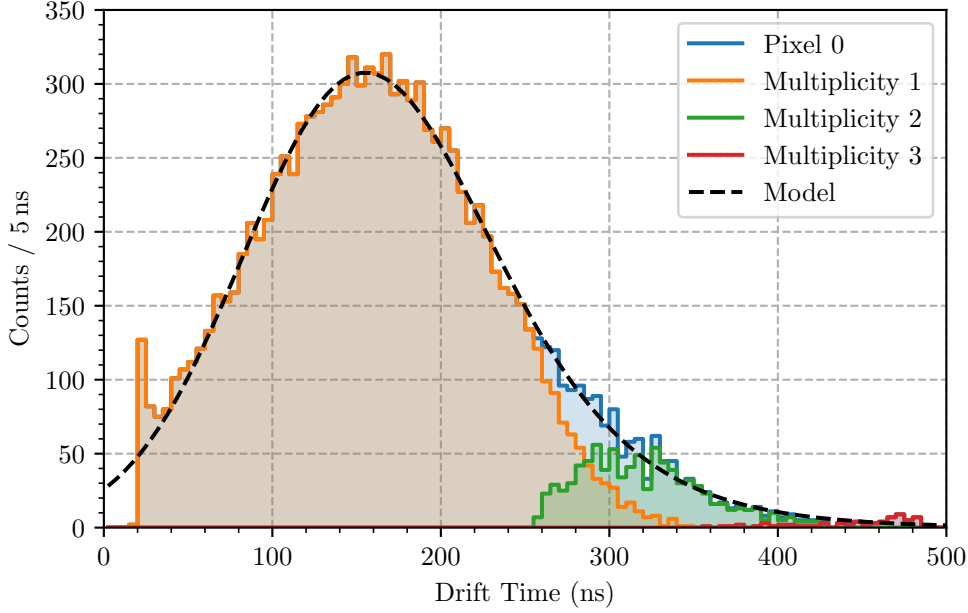


Figure 5.18: **Distribution of the Drift Time of Charge Clouds in the Central SDD Pixel**

The histogram shows the distribution of the drift time of the central detector pixel. Events of multiplicity 1 whose entire charge was collected in this pixel are Gaussian distributed. The peak at 20 ns defines the minimum drift time for all charge clouds. The exponential tail towards larger drift times is the result of charge clouds being affected by the configuration of the electric potential at the pixel borders. Charge clouds formed at the detector triple points are characterized by the longest drift times since there the shape the electric potential has an even more pronounced effect on the drift of the charge carriers. The best fit of an exponentially modified Gaussian distribution to the histogram data is illustrated by the black dashed line. For the histogram, a width of 5 ns was chosen to compute the bins.

and the standard deviation

$$\kappa_{\text{exp}}^{\text{mod}} = \sqrt{\xi^2 + \frac{1}{\gamma^2}} = (77.0 \pm 2.2) \text{ ns} \quad (5.19)$$

of the distribution are obtained as averaged values across all pixels. Most events, in particular those of multiplicity 1, are characterized by drift times of approximately (80 - 240) ns. This is consistent with geometrical considerations: The larger the radius from the pixel center, the more surface area is available for particles to be detected. In contrast, a small radius only covers a small area and therefore fewer events are detectable. The decreasing number of counts in the exponential tail of the distribution follows the same argumentation, since going closer to the boundary of the pixel also decreases the available detection surface.

Charge clouds generated near the pixel borders feature drift times of above 300 ns. This behaviour is visible in both figures 5.16 and 5.18. Starting at $t_{\text{drift}} \approx 260$ ns, charge clouds with drift times of (280 -

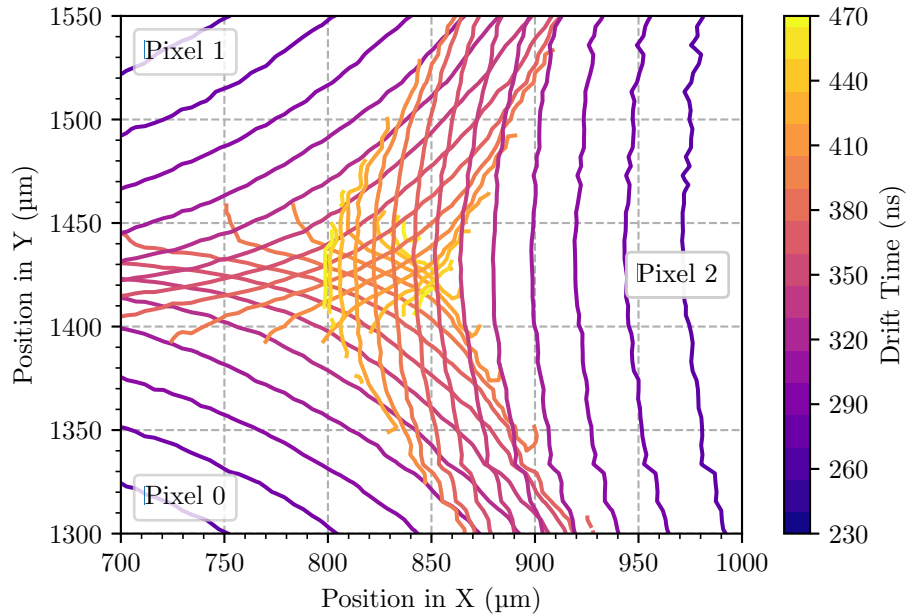


Figure 5.19: **Measured Drift Time Distribution at a Triple Point Region**

The distribution of the drift times is shown for charge clouds created in the region where the pixels 0, 1, and 2 are in contact. Isochrones illustrate charge clouds of equal drift time. The lines are equidistant within the individual pixels and form concentric rings around the pixel centers following the drift ring geometry. At the pixel borders, the drift times increase considerably. Since the outermost drift ring R_X is shared between all pixels of the SDD , a saddle point forms in the electric potential at the boundaries. This is particularly pronounced where the three pixels are in contact with each other. This effect leads to a distortion of the field gradient and results in slower and longer drifts.

430) ns are most likely to be shared between two adjacent pixels and are therefore of multiplicity 2. These events are responsible for the exponential tail in figure 5.18. The longer drift times are caused by the influence of the pixel boundaries on the shape of the electric potential. Since the individual pixels of the $TRISTAN$ $SDDs$ are physically not separated and also share the outermost drift ring R_X , the field at the pixel borders differs significantly from that in the inner region of the pixels. The electric potential forms a saddle point at the boundary between the adjacent pixels which distorts the field gradient and leads to slower and longer drifts. This effect is even more pronounced at the triple points. To demonstrate this, figure 5.19 shows the drift time distribution at a triple point region. Isochrones illustrate charge clouds of equal drift time by concentric lines following the drift ring geometry. The regions in which the isochrones cross each other indicate the pixel boundaries. In particular, the triple point is easy to identify. For charge clouds generated there, the drift takes almost 500 ns before they reach the anode. These events can also be identified at the upper end of the histogram in figure 5.18. They are characterized by drift times above 430 ns and the peak at $t_{\text{drift}} \sim 470$ ns marks charge clouds exactly created at the triple point. Since the charge is shared between three pixels, these events are of multiplicity 3.

The standard deviation $\kappa_{\text{exp}}^{\text{mod}}$ of the histogram is an indicator for the **Intrinsic Time Resolution (ITR)** of the detector. When two particles enter the same pixel within a short time period of $\mathcal{O}(10 \text{ ns})$ and the difference of the drift times of the created charge clouds is much less than 80 ns, it is likely that these two events cannot be clearly distinguished. Since the targeted count rate for the keV-scale sterile neutrino search with the **TRISTAN SDDs** is $\mathcal{O}(10^{-4} \text{ cpns/pixel})$, the **ITR** and the minimum resolution time of the timing filter will be the limiting factors for precise timing. If the signal pulses of two events overlap, pile-up events are created and the energies of the individual events cannot be clearly reconstructed. Further information on the topic of timing filters is given in [54]. For future measurements it is planned to increase the repetition rate of the laser to higher frequencies above 500 kHz to find the minimal time difference, i. e. the **ITR**, for which two consecutive events in the same detector pixel can still be distinguished.

5.3.3 Gaussian Width

The Gaussian width σ is the third model parameter that is studied in the following. Like for the reconstructed energy and drift time distributions, the values obtained in the fitting procedure of the signal pulses are shown in figure 5.20. Within the individual pixels, hexagonal ring structures are observed. These structures indicate an increase of σ from the pixel center to the border while maintaining a distinct hexagonal shape. This behavior can be explained using figure 5.21 which illustrates the correlation of the drift time and the Gaussian width. Both model parameters are linearly correlated over a range of $t_{\text{drift}} \approx (20 - 240) \text{ ns}$ and for $\sigma \leq 10 \text{ ns}$. We recall, that the Gaussian width describes the impact of the diffusion on the signal shape. Equation 3.20 reminds that the effect of diffusion is a function of the duration of the drift of the charge cloud. Hence, the Gaussian width depends directly on the drift time and figures 5.16 and 5.20 feature the identical hexagonal structures due to the alignment of the drift rings.

In figure 5.20, in the center of each pixel two distinct circles are visible inside the innermost ring structure. While this ring is characterized by the overall lowest Gaussian width of the complete pixel, the circles indicate larger σ compared to their direct surroundings. This effect is also visible in figure 5.22 which shows the two-dimensional data of the central **SDD** pixel projected down to one dimension to picture the radial dependence of the Gaussian width. The overall shape of the graph confirms the direct connection to the drift time of the charge clouds. The drift of the charge clouds generated in the range of $r \approx (400 - 1200) \mu\text{m}$ is primarily determined by the transport trough of the electric potential which guides the charge carriers through the detector and maintains a linear shape due to the potential gradient of the drift ring electrodes. Therefore, the Gaussian width of the signal pulses also increases linearly. At small radial positions, the transport trough changes from a linear to a curved shape pointing to the anode. This field configuration can be interpreted as a funnel which changes the drift properties for charge clouds generated in this region. In addition, the weighting potential of the anode is of larger magnitude and thus leads to faster charge collection. The increase towards $r \approx 0 \mu\text{m}$ is caused by the integrated **JFET**.

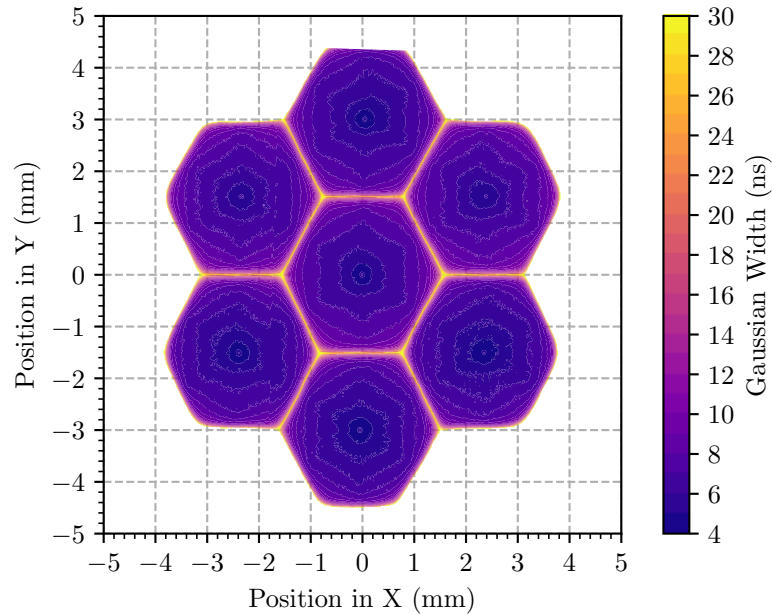


Figure 5.20: **Distribution of the Gaussian Width of the Signal Pulses of a 7 Pixel TRISTAN SDD**

The distribution of the Gaussian width of the signal pulses obtained in the fitting procedure of the measured data is shown for the 7 pixels of the detector as a function of X and Y positions. Within the individual pixels, concentric ring structures are observed. These structures are identical to those of the drift time distribution of figure 5.16. This is explained by the fact that the Gaussian width describes the impact of diffusion on the signal shape and that diffusion is a time dependent process. Hence, the Gaussian width depends directly on the drift time of the charge cloud.

Charge clouds created directly above the transistor have to be guided away from the center to the anode by the IGR. This extends the drift time and tears the clouds apart, further increasing the broadening. Moreover, the observed charge loss distorts the shape of the charge cloud and thus the shape of the signals as well. Adjusting V_{IGR} to regain complete charge collection will however reduce this effect.

The increase of the Gaussian width to values above 10 ns indicates the influence of the pixel borders on the drift of the charge clouds. Figure 5.21 shows that the correlation between t_{drift} and σ loses its linear form. Instead, the distribution spreads for large radii as also depicted in figure 5.22. This can be explained by the following two reasons: On the one hand, the effect of charge sharing comes into play. Due to the splitting of the charges, the charge clouds naturally enlarge in size due to an increased concentration gradient in the charge distribution. On the other hand, the field distribution at the boundaries between adjacent pixels also has an influence on the expansion of the charge cloud and the drift of the charge carriers. Since a saddle point forms in the electric potential, the charge carriers remain at the same position and are subject to diffusion processes over a considerably longer period than usual. This results

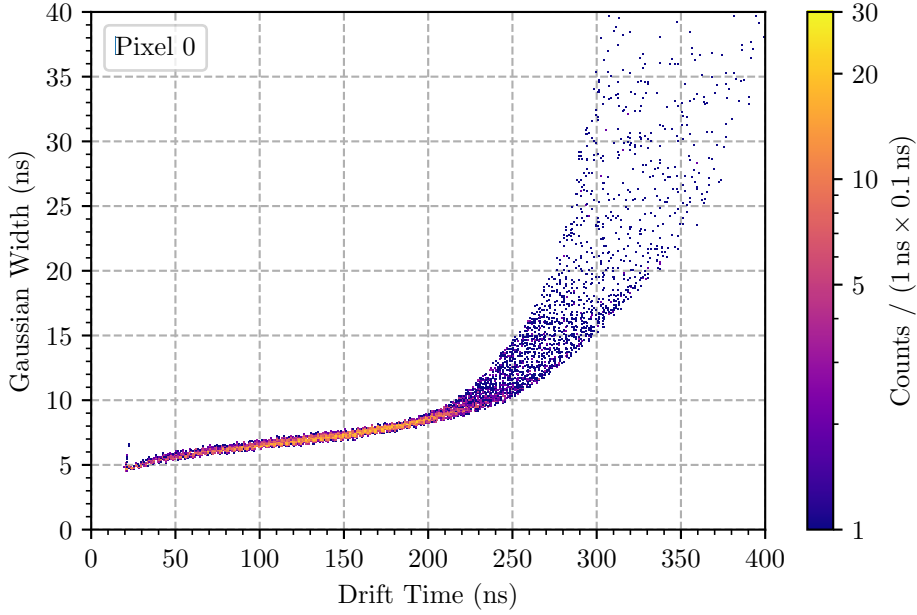


Figure 5.21: **Correlation of the Drift Time and the Gaussian Width in the Central SDD Pixel**

For the central detector pixel, the correlation between the drift time of the charge clouds and the Gaussian width of the signal pulses is shown. Both model parameters are linearly correlated for $t_{\text{drift}} \approx (20 - 240) \mu\text{m}$. The drift of the charge clouds generated in this range is primarily determined by the transport trough of the electric potential which maintains a linear shape following the potential gradient of the drift ring electrodes. For larger radial positions and therefore longer drift times, the impact of the drift rings on the drift of the charge clouds reduces as the influence of the pixel borders takes effect and the parameters lose their linear relation. In the innermost region of the pixel, i. e. for drift times below 50 ns, the correlation changes slightly since there the drift of the charge clouds is determined by the field distribution of the **JFET** region.

in an increased spreading of the charge cloud and is superimposed on the effect of the saddle point on the exponential rise time of the signal pulses, which is discussed in section 5.3.4.

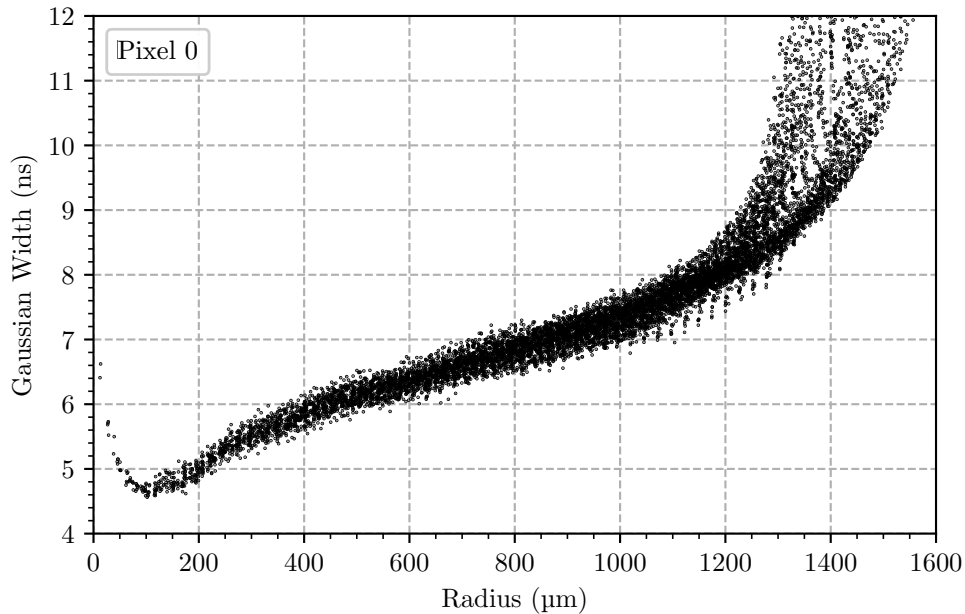


Figure 5.22: **Gaussian Width of the Signal Pulses in the Central SDD Pixel**

The radial dependence of the Gaussian width of the signal pulses is shown for the central detector pixel. As expected, the distribution follows the same shape as that of the drift time of the charge clouds. The drift of the charge clouds in the linear regime between $r \approx (400 - 1200) \mu\text{m}$ is determined by the transport trough of the electric potential. For larger radial positions, the pixel borders influence the distribution of the electric potential as well as the effect of charge sharing lead to larger σ of the signal pulses. In contrast, for smaller radii the drift of the charge clouds is determined by the field distribution of the **JFET** region.

5.3.4 Exponential Rise Time

The exponential rise time τ is the final model parameter to be discussed. Figure 5.23 displays the values obtained in the fitting procedure of the signal pulses just as for the model parameters A , t_{drift} , and σ . In contrast to the other parameters, a significant difference between the individual pixels is observed. While the upper half of the pixels is characterized by exponential rise times of $\tau \lesssim 11$ ns, the lower half takes values of $\tau \gtrsim 12$ ns. In particular, the top pixel (pixel 1) features the lowest exponential rise time of $\tau \lesssim 9$ ns. For each pixel, the overall spread of τ is in the order of 1 ns.

To understand this behavior, remember that this time constant accounts for the response of the **CSA** circuit to the induced charge of a signal pulse. From equation 5.7, recall that the only free parameter is the capacitive output load C_o . To match the observed exponential rise times of $\mathcal{O}(10$ ns), this capacitance must be in the order of $C_o \sim 0.4$ pF. The differences between the pixels hence has to originate from

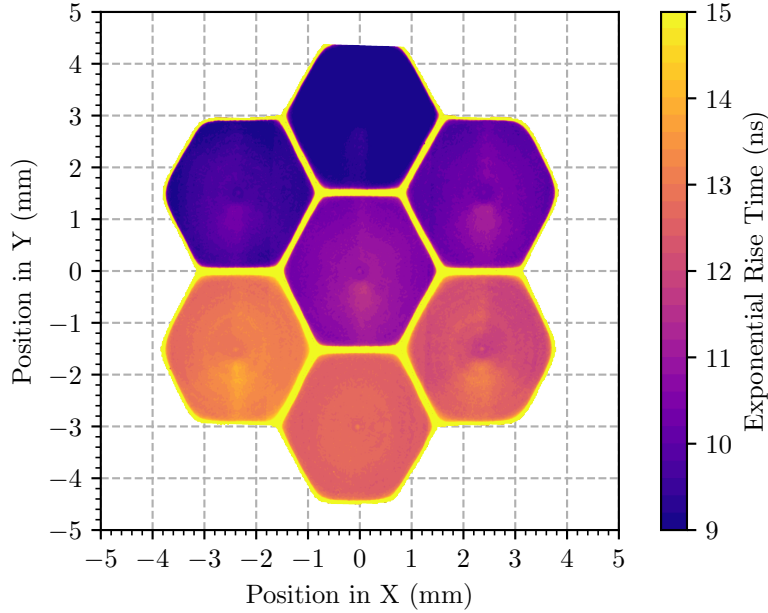


Figure 5.23: **Distribution of the Exponential Rise Time of the Signal Pulses of a 7 Pixel TRISTAN SDD**

The exponential rise time of the signal pulses obtained in the fitting procedure is shown for the 7 pixels of the detector as a function of X and Y positions. The upper half of the pixels is characterized by exponential rise times of $\tau \lesssim 11$ ns, while the lower half takes values of $\tau \gtrsim 12$ ns. This difference results from the capacitive coupling of the signal and biasing lines of the metal bus structure with the detector pixels. Since the lines to the lower pixels are longer, the amount of stray capacitance is higher, leading to longer exponential rise times. The distinct increase of τ at the pixel borders is caused by the saddle point in the electric potential. While parts of the charge cloud already drift to the detector anode, other parts remain at the saddle point and follow only gradually. This causes the charge cloud to stretch in the radial direction and results in very long exponential rise times.

variations of this capacitive load. It was found that the positioning of the signal and biasing lines of the bus structure on the readout side of the detector resulted in capacitive coupling between these lines and the pixels of the SDD. The amount of coupling depends on the length and the size of these lines. Since the bus structure branches from the top to the bottom, the metal strips connecting the lower pixels couple to more stray capacitance. This resulted in the higher exponential rise times observed for these pixels. In this iteration of SDDs, the metal strips have already been reduced in width and spaced more widely to minimize the coupling between the lines. In the subsequent detector iteration, this process was repeated to reduce the coupling even further. Since the SDDs of the TRISTAN detector modules feature longer signal and biasing lines compared to a 7 pixel TRISTAN SDD, the capacitive coupling of the lines to the detector pixels is even more pronounced and must be taken into account when studying the signal shapes.

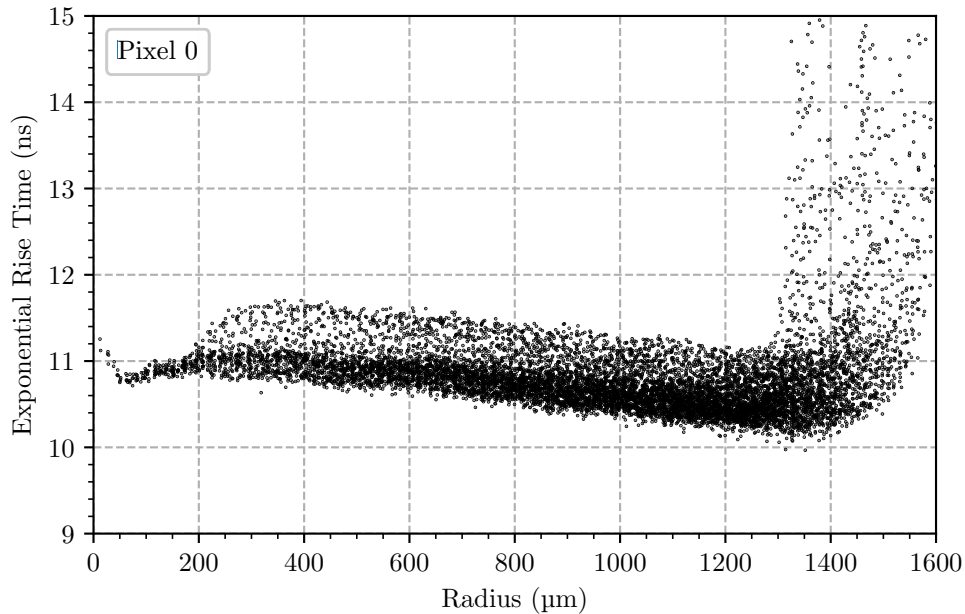


Figure 5.24: **Exponential Rise Time of the Signal Pulses in the Central SDD Pixel**

The exponential rise time of the signal pulses is shown for the central detector pixel as a function of the radius. Over the complete pixel, τ is almost constant since it is determined by the capacitive output load of the CSA circuit. However, the reason for the tendency to decrease toward larger radial positions is unclear and requires further investigations. The dip and the increase towards the center of the pixel can be explained by the same reasons mentioned for the Gaussian width. The shape of the electric potential at the pixel borders leads to longer exponential rise times as can be seen for large radial positions.

The two-dimensional data of the central SDD pixel of figure 5.23 is projected down to one dimension to illustrate the radial dependence of the exponential rise time in figure 5.24. The plot confirms the shallow distribution of τ across the complete pixel. The dip and the increase towards the center of the pixel can be explained by the same reasons mentioned for the Gaussian width in section 5.3.3. The increase of τ for larger radial positions marks the pixel borders which are also clearly visible in figure 5.23. Charge clouds created there, are characterized by exponential rise times $\tau \geq 20$ ns. Since the individual pixels of the TRISTAN detectors are physically not separated and also share the outermost drift ring RX, a saddle point forms in the electric potential at the boundary between the adjacent pixels. This effect is even more pronounced in a triple point region. At the saddle point, the influence of the electric field on the charge carriers is very weak. The charges remain at the same location for a significantly long period and are subject to diffusion processes. Eventually, parts of the charge cloud drift towards the potential minimum at the anode, while other parts remain at the saddle point and follow only gradually. This causes the charge cloud to stretch in the radial direction. In contrast, diffusion expands the charge cloud isotropically. When the charge carriers arrive at the anode, this effect imprints itself as an extended exponential tail in the signal and thus a very long exponential rise time.

5.3.5 Rise Time

Since the time constants σ and τ of the signal model can be compared with other experiments only to a limited extent, the much more widely used (10 - 90) % signal rise time t_{rise} was determined as well. Figure 5.25 displays t_{rise} like the model parameters in the previous sections. Since the signal rise time is not a parameter of the signal model, the acquired waveform data was interpolated by a factor of 10 to calculate the time difference between the rise from 10 % to 90 % of the obtained signal amplitude more precisely. As the rise time is a combination of the Gaussian width σ and the exponential rise time τ , the different characteristics of both components can be recognized. In all pixels, the distribution of t_{rise} is found to behave like that of σ . It features the same pattern and increases at a similar rate from the pixel center to the pixel borders. This pattern is superimposed by the distribution of τ . The higher signal rise times of the lower pixels indicate the higher capacitive coupling due to the longer connection lines of the metal bus structure which resulted in higher exponential rise times as observed in section 5.3.4. Nevertheless, at the center of each pixel a small circular area of higher rise times compared to the direct surrounding is visible. These depict the presence of the integrated JFETs and their impact on the drift

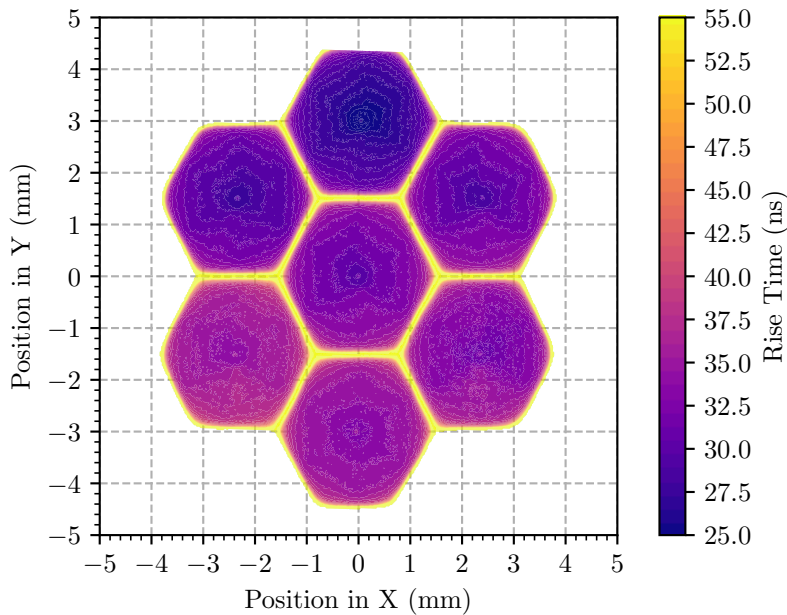


Figure 5.25: **Distribution of the Signal Rise Time of a 7 Pixel TRISTAN SDD**

The (10 - 90) % signal rise time is shown for the 7 pixels of the detector as a function of X and Y positions. The distribution is a superposition of the Gaussian width and the exponential rise time of the signal pulses. It features the same pattern for σ and the higher signal rise times of the lower half of the pixels result from the slower exponential rise times due to the longer connection lines of the metal bus structure. The distinct increase of t_{rise} above 50 ns at the pixel borders allows for event discrimination of regular and charge sharing events.

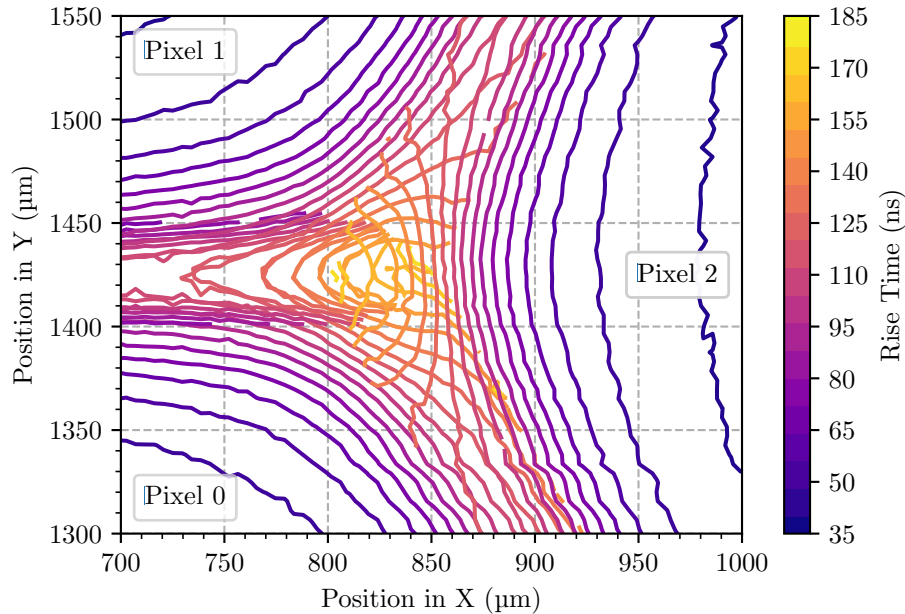


Figure 5.26: **Distribution of the Signal Rise Time at a Triple Point Region**

The distribution of the signal rise times is shown for charge clouds created in the region where the pixels 0, 1, and 2 are in contact. Isochrones illustrate charge clouds which generate signal pulses of equal rise times. Due to the shape of the electric potential at the pixel borders t_{rise} increases substantially and takes its maximum value at the triple point. While the distribution of the rise time for the boundary regions between the pixels (0, 2) and (1, 2) looks as expected, it is dominated by crosstalk in the region between the pixels 0 and 1.

of charge clouds created there. Probing the regions at the pixel borders shows a significant increase of t_{rise} above 50 ns. This major difference compared to regular rise times of (30 - 40) ns (depending on the pixel), allows for event discrimination as already shown in other studies [66].

At the triple points, the signal pulses are characterized by the longest rise times. To demonstrate this, figure 5.26 shows the rise time distribution at a triple point region. Charge clouds that produce signals with the same rise times are represented by isochrone lines. These lines emanate from the center of the pixels where rise times of $\lesssim 35$ ns are observed. When approaching the pixel borders t_{rise} increases to ~ 80 ns before the isochrones intersect with those of the other pixels. This area marks the boundary region of the pixels which features signal rise times of ~ 100 ns directly at the borders. As observed in section 5.3.4, the electric potential at the pixel borders forms a saddle point from where the charge carriers gradually drift to the anode. This results in extended exponential tails in the signal pulses, increased exponential rise times and therefore also higher signal rise times. At the triple point this effect is most prominent and t_{rise} takes its maximum value of approximately 185 ns.

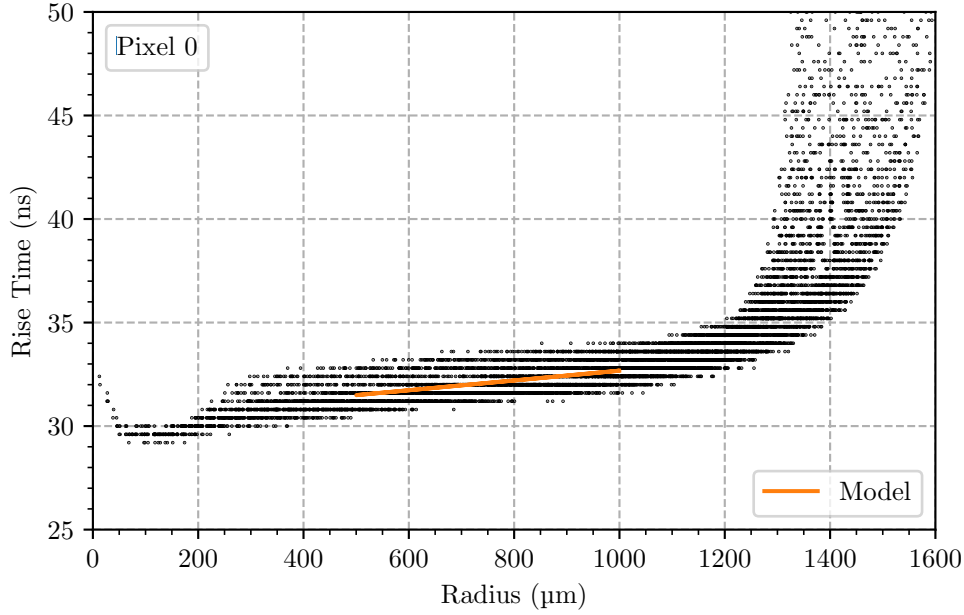


Figure 5.27: **Rise Time of the Signal Pulses in the Central SDD Pixel**

The rise time of the signal pulses is shown for the central detector pixel as a function of the radius. The signal rise time is determined by the combination of the Gaussian width σ and the exponential rise time τ . While the distribution follows σ over almost the complete pixel, the increase of t_{rise} at the pixel borders is the result of high τ values. In the linear regime, the signal rise time is fitted with a linear model to obtain a description of the rise time as a function of the radial position. The best fit result is shown by the orange line.

The two-dimensional data of the central SDD pixel is projected down to one dimension to illustrate the radial dependence of the signal rise time. At small radii, the influence of the transistor on the field distribution is evident. Charge carriers created there are influenced by the saddle point in the electric potential and drift gradually from the JFET to the anode guided by the IGR. This results in longer signal rise times compared to the region where the charges can drift directly to the anode and the weighting potential is dominant. In the regime, in which the drift of the charge clouds is dominated by the transport in the trough of the electric potential, the signal rise times increase linearly towards larger radii. By fitting the experimental data in the range of $r = (500 - 1000) \mu\text{m}$, a linear model is obtained that describes the rise times of signal pulses as a function of the pixel radius r :

$$t_{\text{rise}}(r) = (2.4 \pm 0.1) \frac{\text{ns}}{\text{mm}} \cdot r + (30.3 \pm 0.1) \text{ ns}. \quad (5.20)$$

The shallow slope is primarily determined by the impact of diffusion on the charge cloud and therefore the Gaussian width of the signal pulses. Since the distribution spans only over a range of 5 ns, the rise time is an excellent parameter to distinguish events in the regular region of the SDD from those at the pixel border.

Simulations

Simulations were performed to verify the obtained experimental results. In section 6.1 of this chapter, the method to simulate the electric potential inside the [TRISTAN SDD](#) is introduced. Afterwards, in section 6.2 the charge drift in the simulated field is presented. The actual comparison of the experimental and simulated data is conducted in section 6.3. Section 6.4 concludes this chapter with the discussion of the impact of the variation of simulation parameters on the charge cloud drift.

6.1 Simulation of the Field Configuration in a TRISTAN SDD Pixel

This chapter focuses on the simulation of a single [TRISTAN](#) detector pixel¹. The results are valid universally and applicable to other pixels as well since all feature the same field configuration. In the [TRISTAN SDDs](#), a pixel is formed by applying a bias voltage to the electrode structure of the device. This depletes the [Si](#) semiconductor and creates an electric potential Φ . Electrons and holes generated in an event are guided by this electric potential through the detector pixel. Similar to the one-dimensional p-n junction (see equation 3.9), the electric potential in the [SDD](#) pixel can be obtained by solving the three-dimensional Poisson's equation

$$\nabla^2 \Phi = -\frac{Ne}{\epsilon_0 \epsilon_{\text{Si}}}, \quad (6.1)$$

where N is the effective doping concentration of the bulk material, e the elementary charge, ϵ_0 the vacuum permittivity, and ϵ_{Si} the relative permittivity of [Si](#). Although the [TRISTAN SDD](#) pixels are of hexagonal shape, they are considered to be radially symmetric in first order approximation. Thus, the Laplace

¹The simulations are based on the preparatory work of K. Urban.

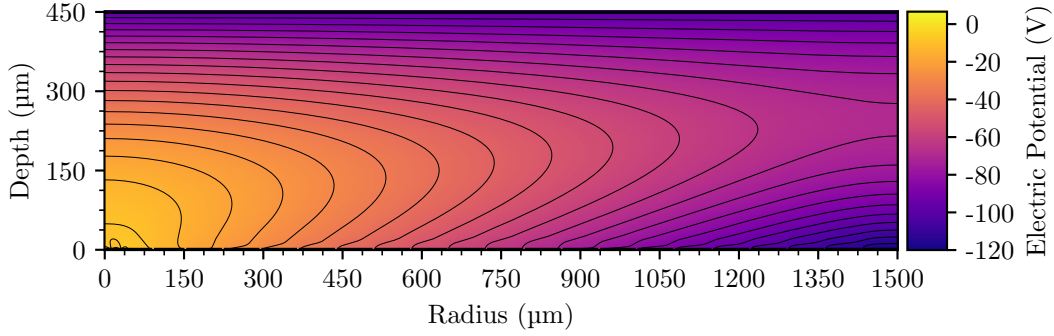


Figure 6.1: **Simulation of the Electric Potential in a TRISTAN SDD Pixel**

The radially symmetric electric potential of a TRISTAN SDD pixel is obtained by solving Poisson's equation and is shown as a function of the radius r and the depth z . The equipotential lines drawn over the electric potential have a spacing of 5 V. The pixel electrodes placed on the entrance window side ($z = 450 \mu\text{m}$) and the readout side ($z = 0 \mu\text{m}$) are shown in black.

operator is written in cylindrical coordinates and equation 6.1 reduces to:

$$\frac{1}{r} \frac{\partial}{\partial r} \left(r \frac{\partial \Phi}{\partial r} \right) + \frac{\partial^2 \Phi}{\partial z^2} = - \frac{Ne}{\epsilon_0 \epsilon_{\text{Si}}} . \quad (6.2)$$

Here, r denotes the radial and z the axial component of the electric potential. The solution of this Partial Differential Equation (PDE) is obtained numerically using the software SFEPY which implements the Finite Element Method (FEM) [48]. The pixel geometry and the applied bias voltages constrain the solution of this PDE. This is called a boundary value problem. In particular, equation 6.2 describes a Dirichlet problem. The solution has to satisfy the specified Boundary Conditions (BCs) on the boundary of a given region, the so-called domain Ω . The domain of the simulation is defined as a two dimensional mesh grid in r and z . A single TRISTAN SDD pixel extends $1500 \mu\text{m}$ in radial and $450 \mu\text{m}$ in axial direction. Hence, for a simulation resolution of $1 \mu\text{m}$, the grid consists of 1501×451 coordinates.

The individual pixel electrodes are placed on this grid. The back contact electrode is positioned at $z = 450 \mu\text{m}$ on the entrance window side. On the readout side, the JFET components (i.e. the drain, gate, and source contacts), the IGR, the anode, and the drift rings are arranged at larger radial positions at $z = 0 \mu\text{m}$. The exact dimensions and extensions of the electrodes are listed in table 6.1. This table also provides an overview of the applied bias voltages and all other relevant boundary conditions. Integrating the PDE over Ω respecting all BCs using Newton's method yields the electric potential Φ . Figure 6.1 illustrates Φ as a two-dimensional slice through the three dimensional SDD pixel (compare to figure 3.4). The concept of sidewards depletion can nicely be seen as all field lines form a potential minimum towards the pixel anode. To realize this, the back contact electrode is supplied with $V_{\text{BC}} = -100.0 \text{ V}$, the innermost drift ring R1 with $V_{\text{R1}} = -9.0 \text{ V}$ and the outermost drift ring RX with $V_{\text{RX}} = -120.0 \text{ V}$. Due

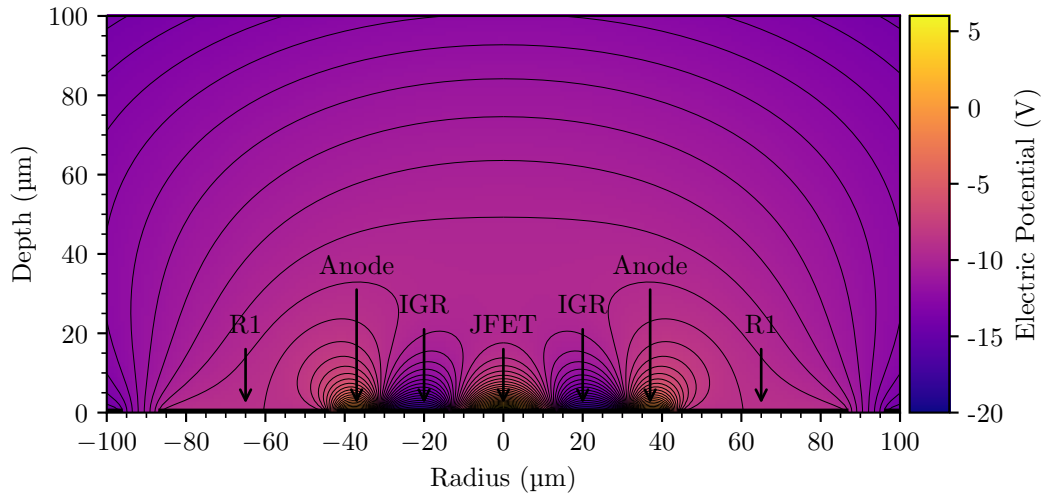


Figure 6.2: **Electric Potential in the Center Region of a TRISTAN SDD Pixel**

The electric potential in the center region of the detector pixel is mainly determined by the voltages applied to the components of the integrated **JFET**, the **IGR**, the anode, and the innermost drift ring **R1** and is shown as a function of the radius and the depth of the detector pixel. Since the pixel is considered to be radially symmetric, the electrodes are annular. The colorbar is readjusted to reflect the potential distribution in this region. The distance of the equipotential lines is set to 0.5 V. Above the **JFET**, the shallow lines indicate the saddle point in the electric potential.

to the integrated voltage divider, that splits the voltages applied to the **R1** and **RX** electrodes to the other drift rings in between, a transport trough in the electric potential is formed. This depletes the detector pixel from the top and bottom while at the same time creates a radial component in the field as the electric potential increases towards smaller radii.

The pixel region near the integrated **JFET** is characterized by the highest voltages. Figure 6.2 shows a close up of the center region of the pixel. Since the **SDD** pixel is radially symmetric, all electrodes on the readout side are annular. The individual components of the **JFET** are located in the range of $r = (0 - 12) \mu\text{m}$. With $V_{\text{drain}} = 6.6 \text{ V}$, the drain contact in the center of the pixel is the most positive electrode in the device. Therefore, electrons would rather drift to the **JFET** instead of the anode placed at $r_{\text{anode}} = (33 - 41) \mu\text{m}$. Hence, the **IGR** is installed around the transistor in the range of $r_{\text{IGR}} = (15 - 30) \mu\text{m}$ to shield it from the **Si** bulk. The equipotential lines of the **JFET** and **IGR** in figure 6.2 illustrate this quite well. The **IGR** surrounds the **JFET** and is biased at $V_{\text{IGR}} = -19.0 \text{ V}$. The high negative voltage acts as a potential barrier and prevents the electrons from getting lost during the charge collection. The anode is the designed potential minimum and is placed between the **IGR** and the innermost drift ring **R1**. When the electrons deposit their charge, the potential of the anode fluctuates. However, the integration of the charge on the feedback capacitor brings the potential back to its operating voltage of $V_{\text{anode}} = 2.0 \text{ V}$. Therefore, a constant anode voltage is assumed in the simulations. Since the

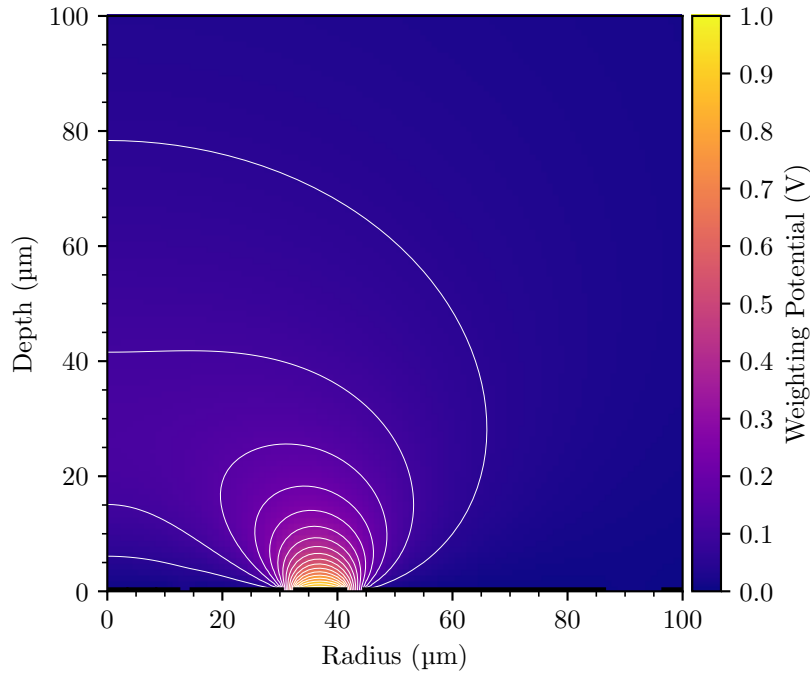


Figure 6.3: **Simulation of the Weighting Potential in a TRISTAN SDD Pixel**

The weighting potential is obtained by applying unit potential to the anode and zero potential to all other electrodes. The solution of Poisson's equation for this configuration is shown for the region near the anode as a function of the radius and the depth. From its maximum value at the anode, the weighting potential decreases the further it extends into the bulk. The equipotential lines are set to a spacing of 50 mV.

anode and the gate electrode of the JFET are connected via a metal strip, the same voltage is applied there as well.

A completely different kind of potential is the weighting potential Φ_w as introduced in section 3.4.5. Φ_w describes the coupling of the charge carriers to the pixel anode. During the drift, the charges induce a current on the anode and are already detected before they physically arrive there. The weighting potential is obtained by setting the anode to the unit potential of 1 V and all other electrodes to 0 V. Solving equation 6.2 for this configuration yields Φ_w . Figure 6.3 illustrates the distribution of the weighting potential near the anode. The weighting potential is maximal at the anode with $\Phi_w = 1$ V and decreases continuously the further it extends into the bulk. The equipotential lines indicates that Φ_w approaches 0 V for most parts of the pixel. The curvature of the lines towards the center implies the presence of a saddle point in the electric potential above the JFET.

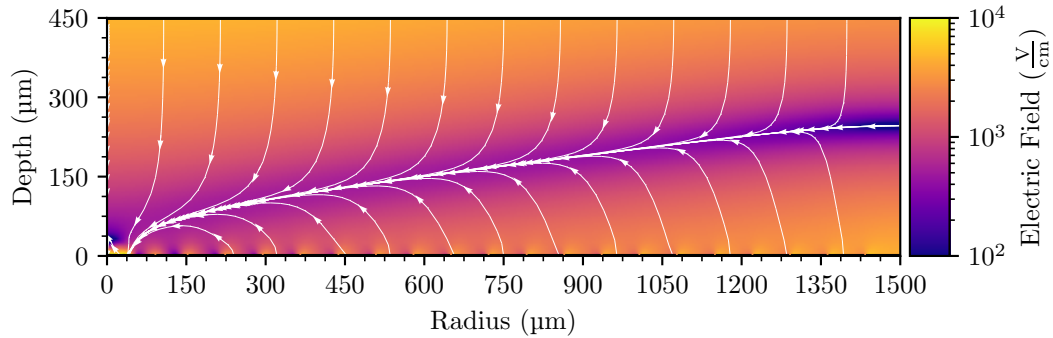


Figure 6.4: **Simulation of the Electric Field in a TRISTAN SDD Pixel**

The electric field is obtained as the gradient of the electric potential and illustrated as a function of the radius and the depth of the detector pixel. The range of the colorbar is limited to $(10^2 - 10^4)$ V/cm for visualization purposes. While the strength of the electric field is almost 10^4 V/cm at the back contact and the drift ring electrodes, it decreases substantially towards the middle to below 10^3 V/cm where the transport trough of the electric potential is located. Electrons drift along the electric field lines to the pixel anode. These are represented by the white lines and the arrows indicate the drift direction.

While the horizontal equipotential lines in figure 6.2 give a first hint towards the existence of this saddle point, its impact is much more visible in the distribution of the electric field \vec{E} . The electric field is obtained as the gradient of the electric potential

$$\vec{E} = -\vec{\nabla}\Phi \quad (6.3)$$

and is shown in figure 6.4. As can be seen, the magnitude of the electric field changes significantly throughout the pixel. While the field strength is almost 10^4 V/cm at the back contact and the drift ring electrodes, it decreases substantially towards the middle to below 10^3 V/cm. This reduction results from the presence of the transport trough of the electric potential. Its purpose is to channel the charges towards the center of the pixel. From the entrance window side as well as the readout side the electric field lines converge into this transport trough. Charge carriers generated in the SDD pixel drift along these field lines and are guided towards the anode. Along the electric field lines, the charge carriers change their drift velocity. Following equation 3.19, the velocity is directly proportional to the magnitude of the electric field. Therefore, charges drift faster in vertical direction before slowing down when they reach the transport trough. The overall shape of the trough is determined by ratio of the voltages V_{R1} and V_{RX} applied to the innermost ring R1 and outermost ring RX. The larger the difference between V_{R1} and V_{RX} , the steeper is the gradient of the electric potential. This leads to stronger electric fields, higher drift velocities and shorter drift times. At $r = 1500 \mu\text{m}$, the saddle point which is formed between adjacent pixels, is clearly visible. There, the electric field is minimal. This results in the effects observed in section 5.3. The vertical position of the saddle point is specified by the ratio of V_{RX} and V_{BC} . The saddle point is shifted closer to the drift rings if the back contact voltage is increased and vice versa.

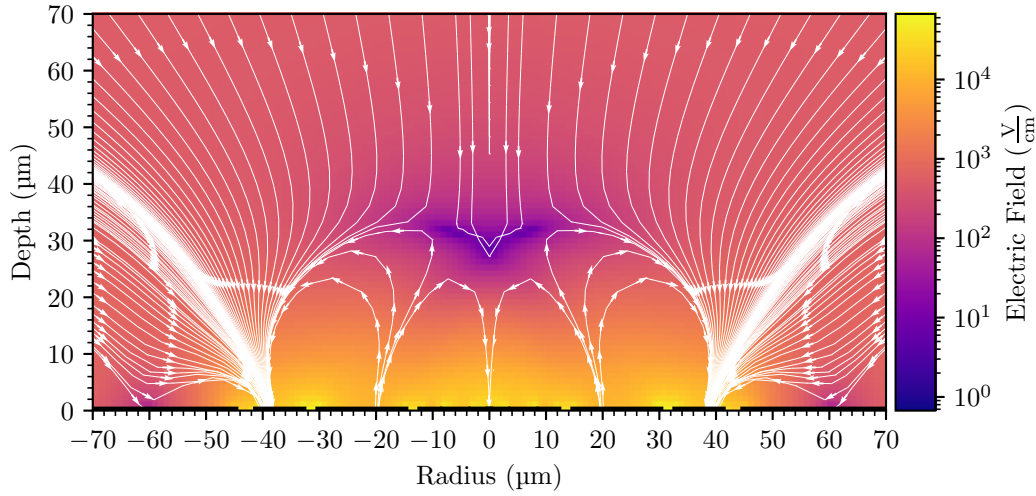


Figure 6.5: **Electric Field in the Center Region of a TRISTAN SDD Pixel**

The electric field is highest in the center region of the detector pixel. The **JFET**, the **IGR**, and the anode create fields which extend into the bulk up to $z = 30 \mu\text{m}$. For the **JFET**, the guarding effect is illustrated by the field lines emanating from the **IGR**. Electrons are guided from the inner region above the transistor to larger radii. Just as the electrons that drift along the field lines in the transport trough, these also end up at the anode. The minimum in the electric field formed in the region above the **JFET** is depicted in blue.

When the influence of the drift rings declines towards the center of the pixel, the electric field lines in the transport trough lose their linear shape. The presence of the transistor modifies the field even more. A detailed view of the electric field at the center of the pixel is given in figure 6.5. Three different regions can be identified in which the field strength differs significantly. The **JFET**, the **IGR**, and the anode create fields which extend into the bulk up to a depth of approximately $30 \mu\text{m}$. For several micrometers, the field magnitude is larger than 10^4 V/cm before gradually decreasing. For the **JFET**, the guarding effect is illustrated by the field lines emanating from the **IGR**. Electrons are guided from the inner region above the transistor to larger radii. Just as the electrons that drift along the field lines in the transport trough, these also end up at the anode. In this field configuration, however, a minimum in the electric field is formed in the region above the **JFET**. This is a consequence of V_{IGR} being too positive and thus not fully shielding the **JFET** from the bulk. Charges drifting into this region are most likely to settle in this minimum and subsequently are lost at the **JFET** drain electrode. The field lines pointing downwards to the drain electrode illustrate the path of these electrons. Nevertheless, all other field lines from the bulk, except those facing the **JFET** directly, converge on the anode and guide the electrons properly.

Table 6.1: **Boundary Conditions for the Simulation of the Electric Potential**

The boundary conditions used for the simulation of the electric potential in a [TRISTAN SDD](#) pixel are listed. The table is separated into the general simulation settings used to solve Poisson's equation, the configuration of the electrode geometry, and the bias voltages applied to the pixel electrodes.

Courtesy to P. Lechner.

Boundary Condition	Symbol	Value
Doping Concentration	N	$0.9 \times 10^{12} \text{ cm}^{-3}$
Relative Permittivity Si	ϵ_{Si}	11.68
Radius	r	1500 μm
Depth	z	450 μm
Drain Electrode	r_{drain}	(0 - 3) μm
Gate Electrode	r_{gate}	(4 - 8) μm
Source Electrode	r_{source}	(9 - 12) μm
IGR Electrode	r_{IGR}	(15 - 30) μm
Anode Electrode	r_{anode}	(33 - 41) μm
R1 Electrode	r_{R1}	45 μm
Rings	N_{rings}	21
Ring Gap	g_{rings}	10.2 μm
Width of R1	w_{R1}	41 μm
Width of R2	w_{R2}	51 μm
Width of RX	w_{RX}	61 μm
Drain Voltage	V_{drain}	6.6 V
Gate Voltage	V_{gate}	2.0 V
Source Voltage	V_{source}	-6.0 V
IGR Voltage	V_{IGR}	-19.0 V
Anode Voltage	V_{anode}	2.0 V
R1 Voltage	V_{R1}	-9.0 V
RX Voltage	V_{RX}	-120.0 V
BC Voltage	V_{BC}	-100.0 V

6.2 Simulation of the Drift of the Charge Carriers

The electric potential obtained in section 6.1 is used for the simulation of the drift of charge carriers in the detector pixel. Exactly as in the field simulation before, the drift is simulated at a temperature of $T = 300\text{ K}$ in Si with a relative permittivity of $\epsilon_{\text{Si}} = 11.68$ [12]. Incident radiation with an energy of 10 keV is assumed to enter the detector pixel at different initial radii in a range of $r_0 = (0 - 1600)\text{ }\mu\text{m}$. Extending the radial range from $1500\text{ }\mu\text{m}$ to $1600\text{ }\mu\text{m}$ allows to investigate the effect of charge sharing at the pixel boundary. To simplify the simulation, the mechanism of the generation and the recombination of the electron-hole pairs is not considered. Instead, the charge clouds of the electrons and the holes are simulated to be created at a fixed depth of the detector pixel of $z_0 = 440\text{ }\mu\text{m}$. This is equivalent to a distance of $10\text{ }\mu\text{m}$ below the entrance window and is in experimental agreement with the penetration depth of $(5 - 10)\text{ }\mu\text{m}$ for photons of $\lambda = 640\text{ nm}$ [77] and electrons with energies up to 60 keV . Hence, all charge carriers are located at the same position at the start of the simulation at the time $t_0 = 0\text{ ns}$.

The drift of the charge carriers is simulated following equation 3.19. The influence of the electric field on each charge is calculated at any position in the detector. Together with the respective mobilities for electrons, $\mu_n = 1440\text{ cm}^2/(\text{Vs})$, and holes, $\mu_p = 474\text{ cm}^2/(\text{Vs})$, this yields the drift velocity for each charge carrier [37]. The change in position is subsequently computed as the product of the velocity and the time for a single step in the simulation. The time step, i. e. the time difference between the current and next simulation iteration, is determined by the mean free path between two collisions. The resolution of the mesh on which the field distribution was calculated limits this distance to $1\text{ }\mu\text{m}$. Therefore, a simulation time step of $\Delta t = 10\text{ ps}$ was chosen. In total, the drift is simulated in a time period of $t_{\text{sim}} = 1\text{ }\mu\text{s}$. A summary of all parameters used for the drift simulation can be found in table 6.2. By convention, the drift velocity vector was defined in the positive direction for electrons and in the negative direction for holes. Thus, the charge carriers separate and form two charge clouds moving into opposite directions. Since the charge clouds are created right below the entrance window, the collection time for holes is less than 1 ns . Due to this and the fact that electrons are responsible for the signal generation at the anode, the focus was solely on them.

As discussed in section 3.4.4, charge carrier transport also happens through diffusion. The spreading of the charge cloud follows equation 3.20 and creates a Gaussian distribution with standard deviation σ . This effect was implemented in the drift simulation taking into account the respective diffusion constants for electrons, $D_n = 37.23\text{ cm}^2/\text{s}$, and holes, $D_p = 12.25\text{ cm}^2/\text{s}$, which were calculated using equation 3.21. Figure 6.6 shows the evolution of the standard deviation of the electron cloud size placed inside a field-free volume. The simulated effect of the diffusion on the expansion of the cloud follows the model given in equation 3.20 and is compared to the theoretical prediction [65]. The diffusion constant extracted by fitting the simulated data to the model, is in $> 99\%$ agreement with the theoretical value. Therefore, it is assumed that the diffusion of the charge cloud during the simulated drift is correctly represented.

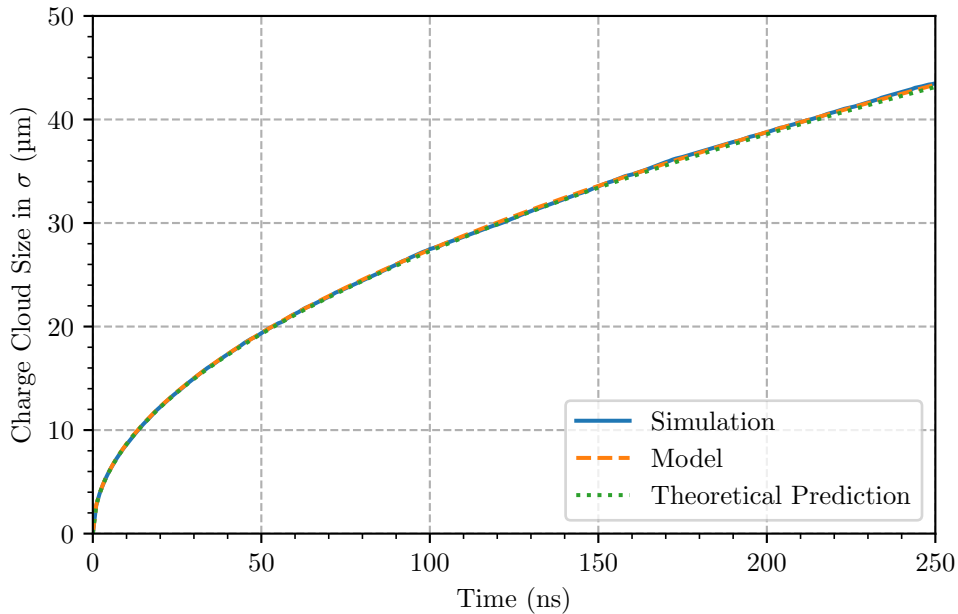


Figure 6.6: **Spreading of the Electron Charge Cloud due to Diffusion**

Placed inside a field-free volume, the spreading of the electron charge cloud over time due to diffusion is illustrated as the standard deviation σ of the size of the cloud. The simulated effect of the diffusion on the expansion of the cloud follows the model given in equation 3.20 and is compared to the theoretical prediction. Since the diffusion constant extracted by fitting the simulated data to the model is in $> 99\%$ agreement with the theoretical value, it is assumed that the diffusion of the charge cloud during the simulated drift is correctly represented.

Another effect, that was introduced earlier in section 3.4.2, is the self-repulsion of the charge carriers. According to Coulomb's law, point charges, i. e. electrons and holes, create an electric field. Stated in equation 3.18, this field leads to the interaction of two charged particles over a certain distance. Since electron-hole interaction, recombination, or similar processes are not considered, both charge clouds drift independently. Assuming a field-free volume, a single charge within a charge cloud is therefore subject only to the influence of the electric field generated by all other charges in that cloud. Since all charge carriers within the cloud carry the same charge, the field acts repelling. This leads to an expansion of the charge cloud over time. Figure 6.7 illustrates the mode displacement of the charge carriers due to this self-repulsive electric fields. It has to be noted, that diffusion was also enabled in this simulated drift. This is necessary because the interaction of charge carriers located at the same position is not physical and therefore not taken into account. Instead, the charges first have to spread due to diffusion processes before self-repulsion can be factored in. The displacement due to self-repulsion almost vanishes within 1 ns of simulation time. As the effect is in the order of $\mathcal{O}(\text{pm})$, the impact on the charge cloud drift is negligible. Since the computation of the repulsive interaction for all charge carriers in each iteration is quite time-consuming, neglecting this effect significantly reduces the time required for the simulation of

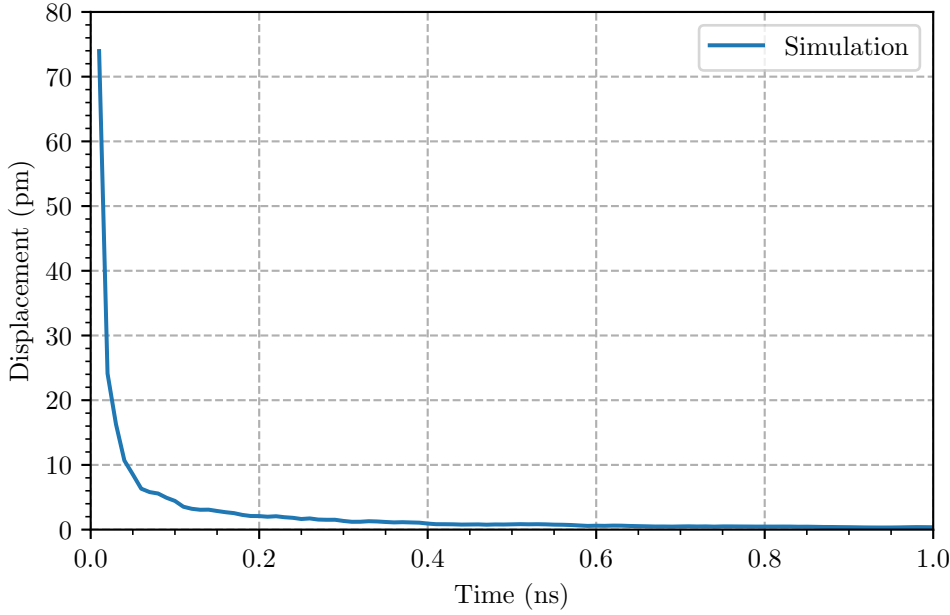


Figure 6.7: **Expansion of the Electron Charge Cloud due to Self-Repulsion**

The mode displacement of the electrons inside the electron charge cloud caused by the self-repulsion is shown as a function of the simulation time. Since the interaction of charge carriers located at the same position at $t = 0$ ns is not physical, the charges first have to spread due to diffusion processes before self-repulsion can be factored in. This is the reason why the graph starts after the first simulation time step. The displacement due to self-repulsion almost vanishes within 1 ns of simulation time. As the effect is in the order of $\mathcal{O}(\text{pm})$, the impact on the charge cloud drift is negligible.

the drift. Therefore, only the impact of diffusion on the charge cloud is simulated in the drift simulations.

The drift of the electron cloud starting at the radius $r_0 = 1000 \mu\text{m}$ is illustrated in figure 6.8. The figure shows the transport of the electron charge cloud in the electric potential of the detector pixel as a series of frames of 10 ns intervals. The vertical drift downwards and the increase of the size of the charge cloud are particularly visible in the range of (1 - 20) ns. The subsequent drift in the transport trough is depicted in the frames of (30 - 120) ns. Due to the exposure to the radial field component, the cloud expands in radial direction. At $t = 130$ ns, the charge cloud leaves the trough and enters the field distribution at the center of the pixel. The electrons arrive at the anode 10 ns later, resulting in a drift time of ~ 140 ns. Within the next 30 ns, the electrons are collected and produce a signal pulse.

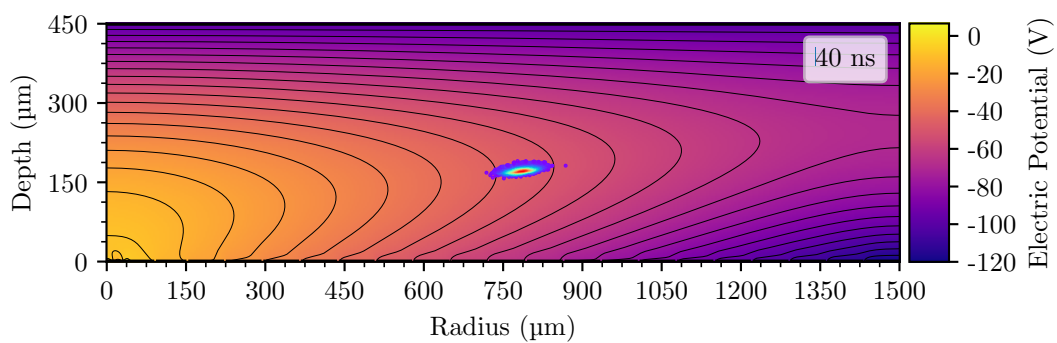
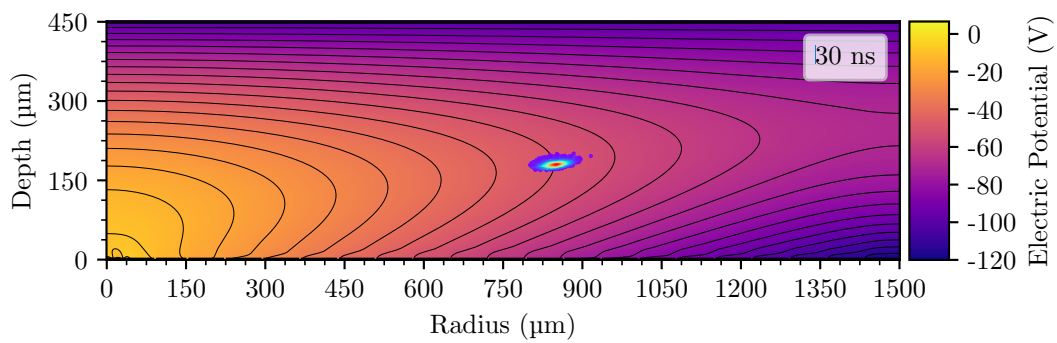
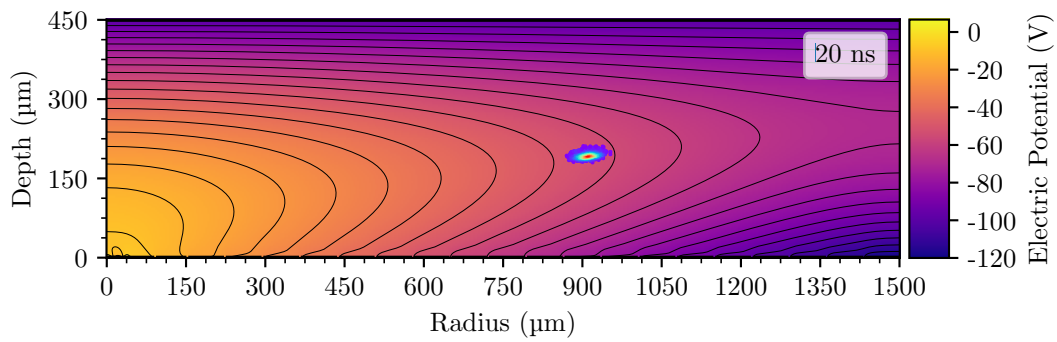
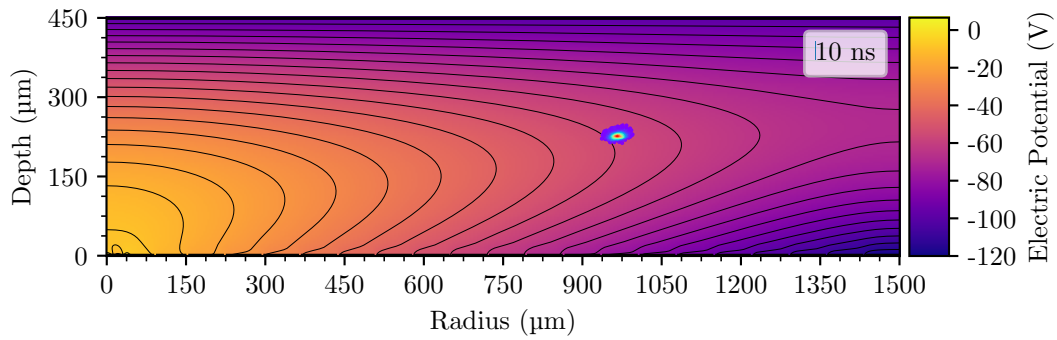
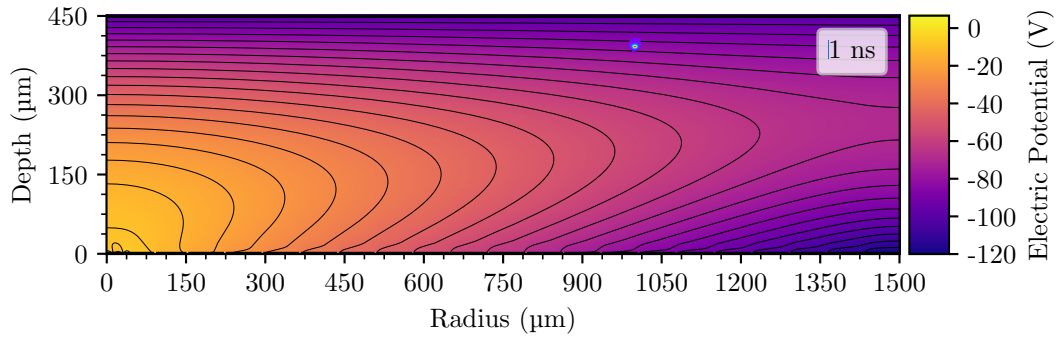
Figure 6.9 illustrates the output signal for different initial radii r_0 . From the top to the bottom, r_0 increases from $0 \mu\text{m}$ to $1500 \mu\text{m}$. It can be observed that the impact of the induced charge on the total output signal is highest at the center of the pixel and decreases towards larger radii. The reason for this is that the magnitude of the weighting potential is maximal at the anode and reduces with increasing

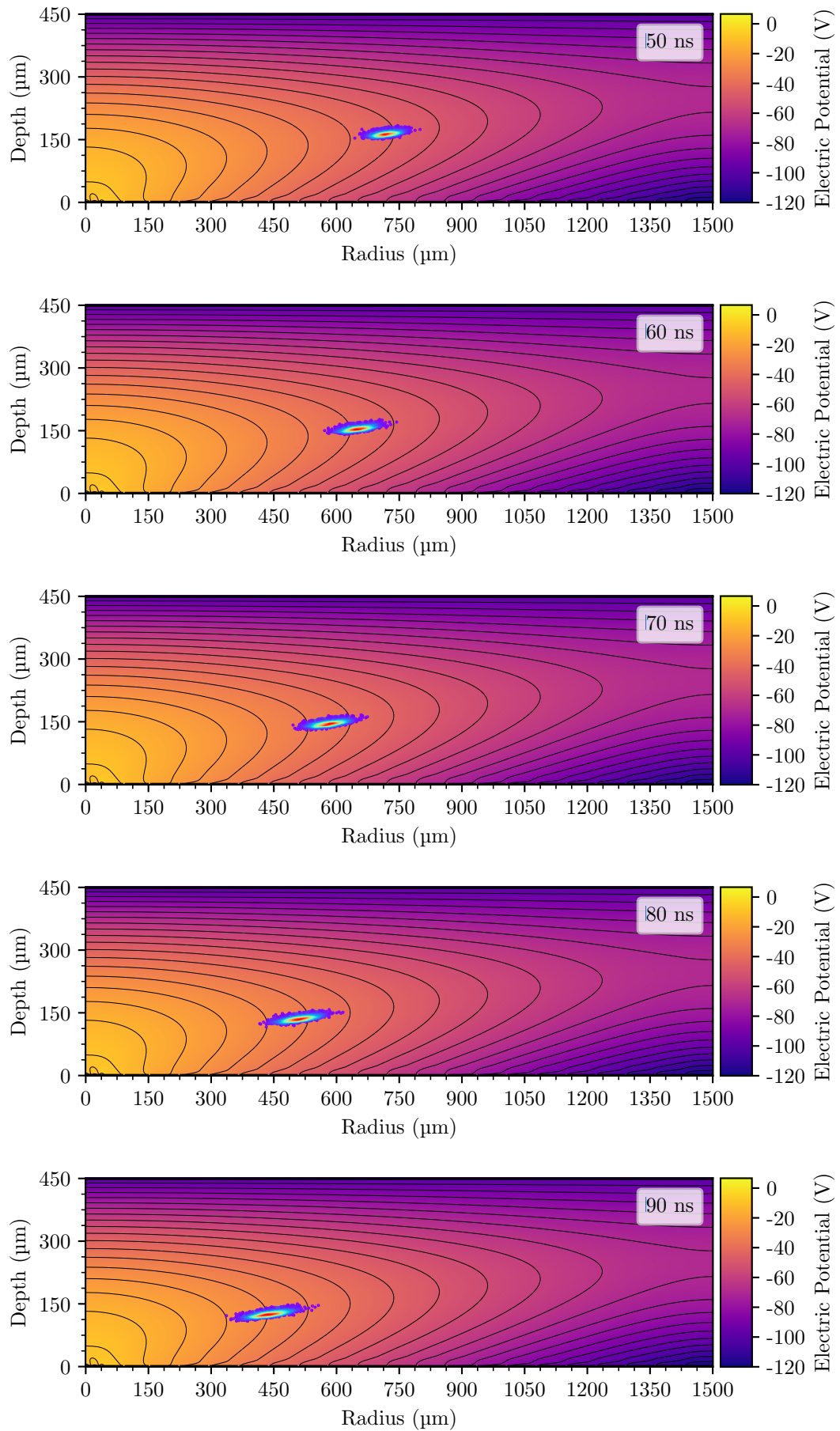
distance. Therefore, charge clouds generated near the center are subject to the influence of a much stronger weighting potential and consequently induce a higher amount of charge on the anode as they drift. This effect decreases for larger radial positions because the charge carriers gradually approach the anode rather than being seen as a complete charge cloud at once. The first figure shows the signal for a charge cloud formed directly at the center of the pixel at $r_0 = 0 \mu\text{m}$. Since the JFET is located there and V_{IGR} was set too positive, the charge loss can be noticed the simulations as well. Starting at $r_0 = 100 \mu\text{m}$, all charge carriers are collected again as they are not longer under the influence of the fields at the transistor. For $r_0 = 1000 \mu\text{m}$, the signal created by the charge cloud whose drift is illustrated in figure 6.8 is shown. As expected, the signal pulse starts later because of the longer drift time for the electrons. Moreover, the shape of the signal pulse changes slightly due to the impact of diffusion. This effect increases further up to $r_0 = 1425 \mu\text{m}$ where the effect of charge sharing begins. At $r_0 = 1500 \mu\text{m}$, the charge is equally shared between both pixels. The field distribution at the pixel border leads to a significant change of the signal shape. The exponential tail and the higher rise time are caused by electrons being trapped at the saddle point and gradually being released. This increases the collection time to above 600 ns. The individual properties of the simulated and experimental signal pulses will be compared in section 6.3.

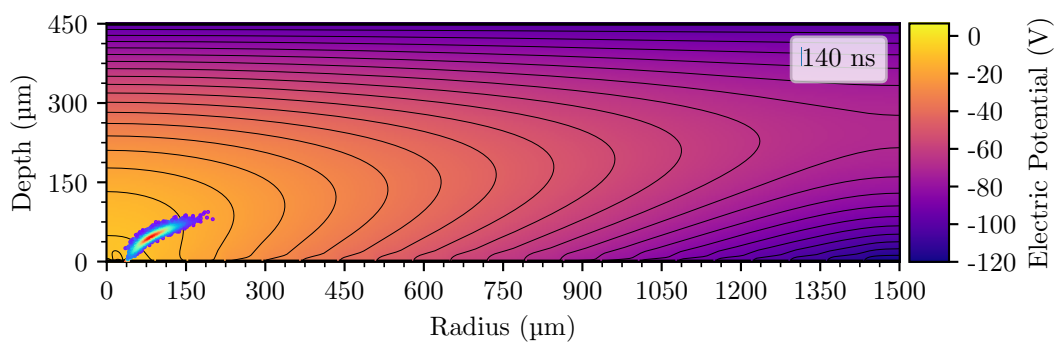
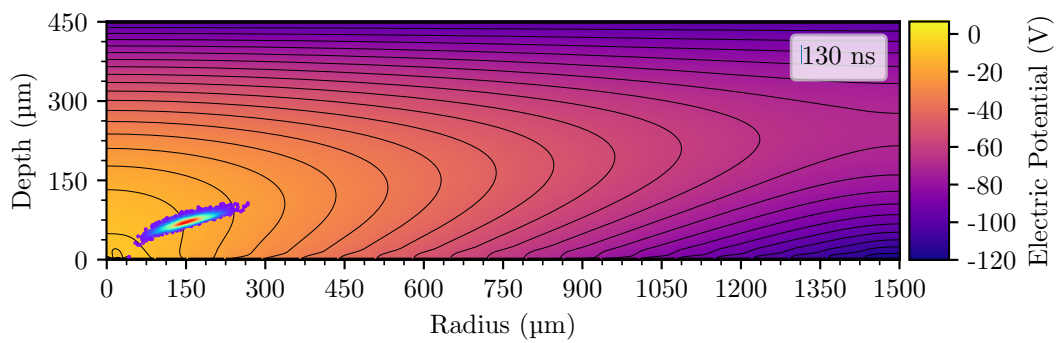
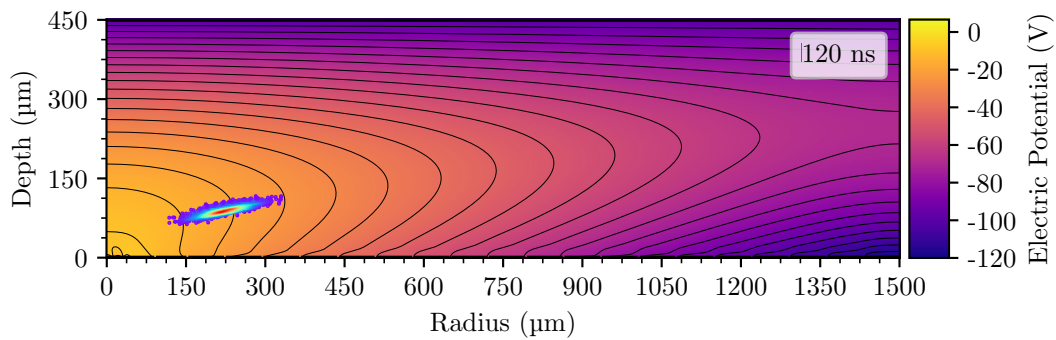
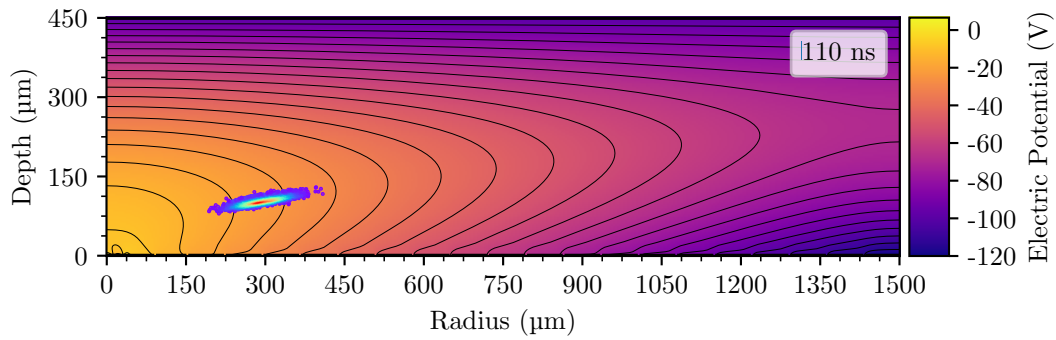
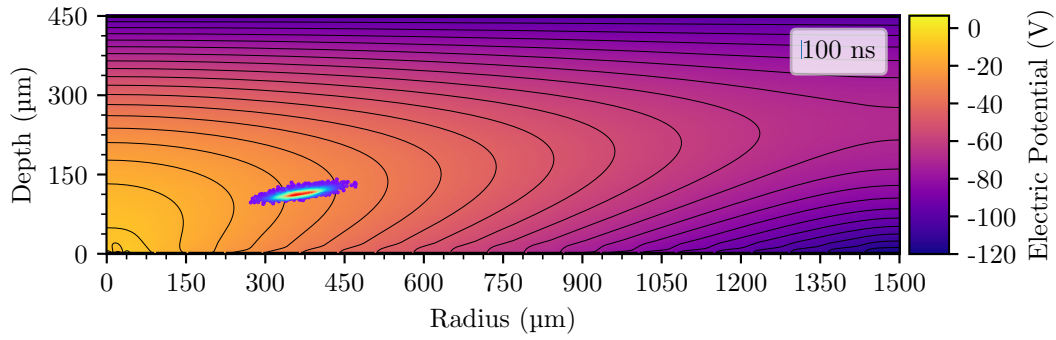
Table 6.2: **Parameters for the Simulation of the Drift of the Charge Carriers**

The parameters used for the simulation of the drift of the charge carriers in the electric potential are listed.

Simulation Parameter		Symbol	Value
Energy of Incident Radiation		E_0	10 keV
Temperature		T	300 K
Electron-Hole Pair Creation Energy Si		w_{Si}	3.62 eV
Relative Permittivity Si		ϵ_{Si}	11.68
Simulation Time		t_{sim}	1 μs
Time Step		Δt	10 ps
Mobility	Electrons	μ_n	1440 $\frac{\text{cm}^2}{\text{Vs}}$
	Holes	μ_p	474 $\frac{\text{cm}^2}{\text{Vs}}$
Diffusion Constant	Electrons	D_n	37.23 $\frac{\text{cm}^2}{\text{s}}$
	Holes	D_p	12.25 $\frac{\text{cm}^2}{\text{s}}$
Interaction Point	Radius	r_0	(0 - 1600) μm
	Depth	z_0	440 μm







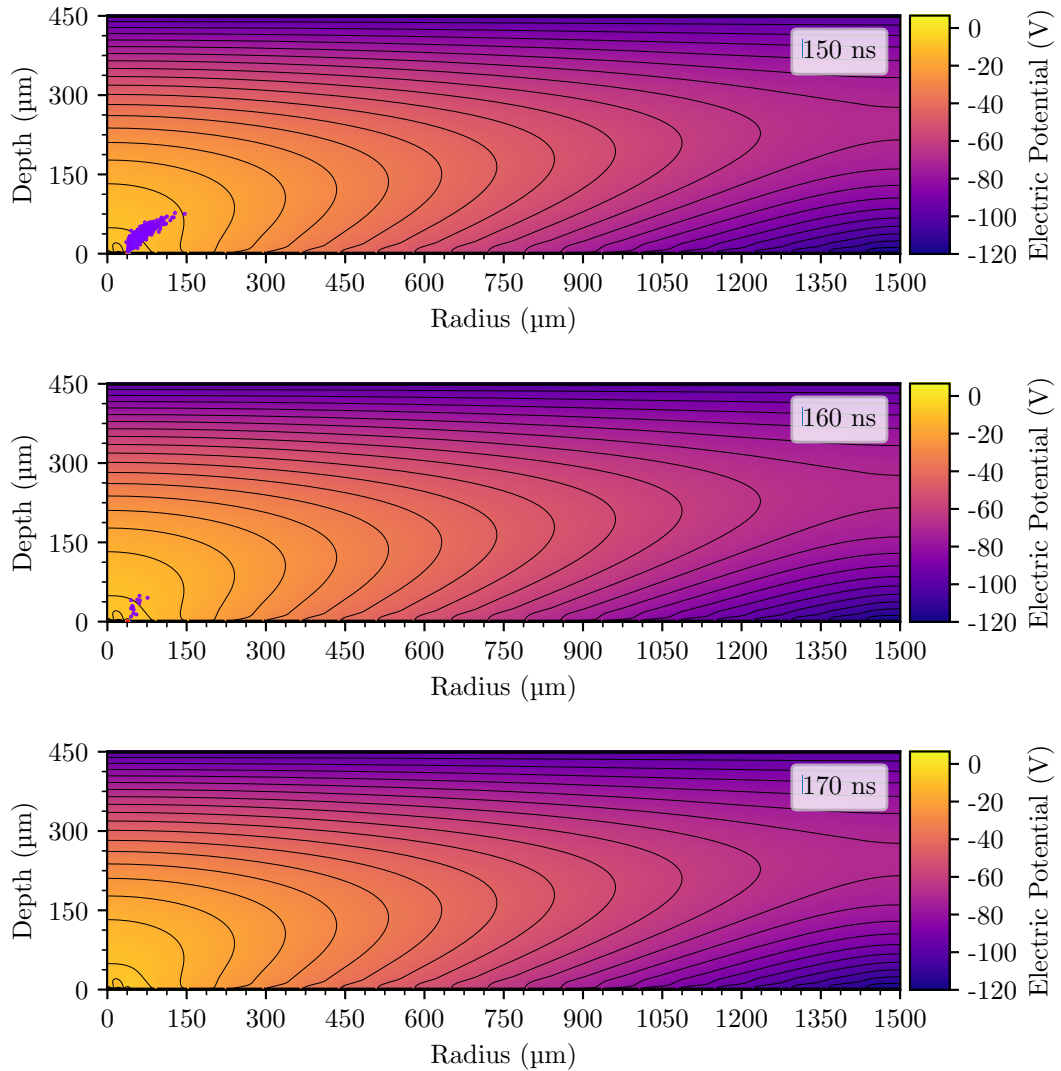


Figure 6.8: **Simulated Drift of the Electron Charge Cloud in a TRISTAN SDD Pixel**

The figure shows the drift of the electron charge cloud in the electric potential of the detector pixel starting at $r_0 = 1000 \mu\text{m}$ and $z_0 = 440 \mu\text{m}$ as a series of frames of 10 ns intervals. The cloud is color-coded following a Gaussian distribution. The high electron density in the center of the cloud is indicated by the red color and decreases for larger distances to the center of the cloud. In the range of (1 - 20) ns, the vertical drift downwards and the increase of the size of the charge cloud are particularly visible. The subsequent drift in the transport trough is depicted in the frames of (30 - 120) ns. Due to the exposure to the radial field component, the cloud expands in radial direction. At $t = 130$ ns, the charge cloud leaves the trough and enters the field distribution at the center of the pixel. The electrons arrive at the anode 10 ns later, resulting in a drift time of ~ 140 ns. Within the next 30 ns, the electrons are collected and produce a signal pulse. Thus, it takes 170 ns from the creation of the cloud to the complete collection of all electrons.

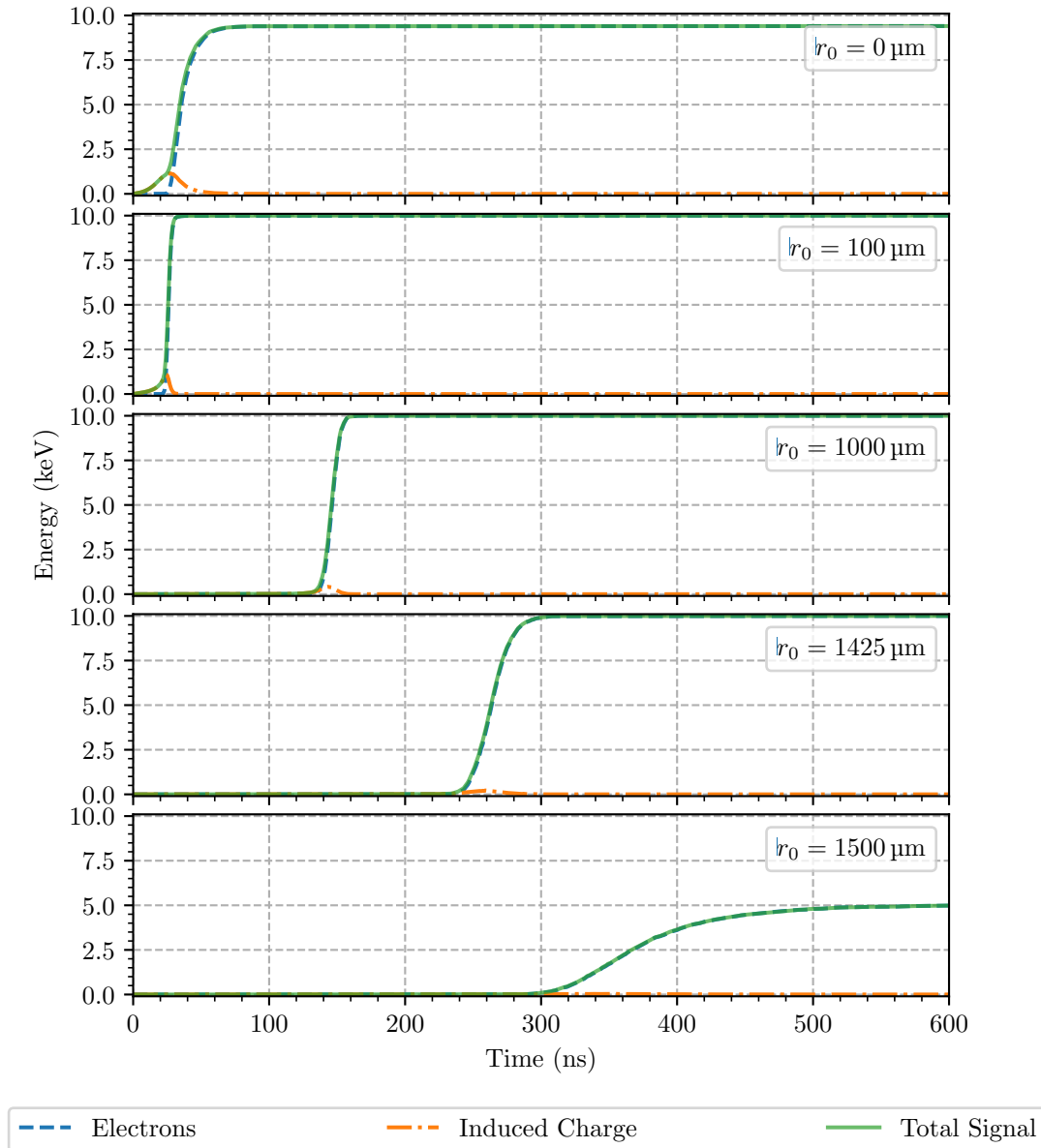


Figure 6.9: **Produced Signal Pulses in the Simulation of the Charge Cloud Drift**

The signal pulses produced in the simulation of the charge cloud drift are shown for different initial radii r_0 . For each plot, three different lines are shown. While the blue line illustrates the signal generated by electrons that have physically arrived at the anode, the orange line depicts the signal created by the induced charge on the anode from electrons drifting in the weighting potential. The resulting total signal is displayed in green. It can be observed that the impact of the induced charge on the total output signal is highest at the center of the pixel and decreases towards larger radial positions. In addition, the shape of the signal pulse changes as the impact of diffusion increases due to the longer drift time. The field distribution at the pixel border leads to the pronounced exponential tail in the signal as electrons trapped at the saddle point are gradually being released.

6.3 Comparison of Experiment and Simulation

In this section, the experimental results will be compared to the simulations. For each interaction radius r_0 , the drift of the charge cloud is simulated and the total output signal is saved and fitted with the model introduced in section 5.2. Since this signal is the pure response of the anode alone, a direct comparison with the experimental signals is not possible yet. For a proper comparison, both the shape of the laser pulse as well as the response of the CSA circuit must be accounted for.

First, the impact of the laser pulse on the signal shape is discussed. By design, the laser emits a bunch of photons (35 ± 5) ns after receiving an external trigger signal. In the ideal case, the distribution of photons would correspond to a rectangular pulse. For an external trigger signal at the time $t = 0$ ns, figure 6.10 illustrates this ideal pulse. In reality, however, the laser is not capable of delivering the full output power instantaneously. Instead, the limited switching times of the laser diode cause a Gaussian spreading of the laser pulse. Figure 6.10 visualizes this spreading for different standard deviations σ_{laser} of the Gaussian distribution (see equation 5.4). While for $\sigma_{\text{laser}} = 1$ ns the pulse maintains the overall shape of the ideal pulse, both the leading and the trailing edge of the pulse smear more and more as σ_{laser} increases. The effect of this non-ideal laser pulse can be seen in the Gaussian width of the signal pulses (compare to section 5.2). Figure 6.11 depicts the Gaussian width as a function of the radius of the experimental and the simulated signal pulses for different laser pulse shapes. For an ideal rectangular laser pulse the simulation does not match the experimental data. Only increasing the Gaussian spreading of the laser pulse up to $\sigma_{\text{laser}} = 4$ ns leads to the desired agreement. However, this only holds for radial positions above 400 μm . Below, the simulation overestimates the Gaussian width significantly.

Therefore, the effect of the effect of the laser pulse spreading can be interpreted as follows: A laser pulse of constant output power deposits its energy uniformly throughout the entire pulse duration. This creates a homogeneous charge cloud in the detector. But for a pulse with changing output power, the generated charge cloud follows the form of this pulse. Together with the overall longer pulse, this naturally enlarges the charge cloud already during its creation and can be seen as temporal broadening. As was observed later, a defocused and therefore enlarged laser beam could have enhanced this effect, as it would also have increased the size of the cloud during its formation. The cloud takes the form of a Gaussian distribution and is spread further by the diffusion during the drift. While this explains the behavior for large radii, the discrepancy towards the pixel center has to be explained differently. Charge clouds created there are under a much higher influence of the weighting potential. It could be that the drift of a charge cloud in the weighting field and induction of charge on the anode, masks the larger spread of the cloud as it actually is. Another, more likely explanation is that the high complexity of the field distribution in the detector near the pixel center is simply not represented precisely enough in the field simulation. Therefore, the simulated drift of the charge carriers created there differs from the experimental data for this and all other model parameters as well.

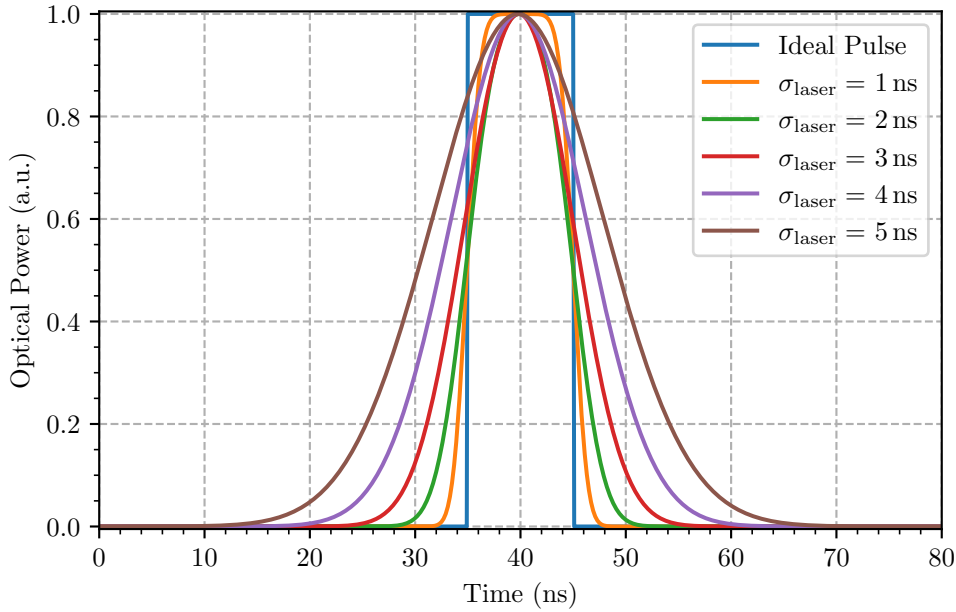


Figure 6.10: **Simulation of the Laser Pulse**

The laser is triggered by an external trigger signal at $t = 0$ ns and emits a bunch of photons after (35 ± 5) ns. In the ideal case, a pulse of rectangular shape would be emitted. However, due to limited switching times of the laser diode the laser pulse is spread following a Gaussian distribution of standard deviation σ_{laser} . For σ_{laser} in the range of (1 - 5) ns the corresponding laser pulses are shown.

As mentioned before, the second aspect for the comparison of the experimental and simulated signals is to consider the response of the CSA circuit. The response of the CSA circuit to a unit voltage step is given by equation 5.6, which contains the exponential rise time parameter τ . Following equation 3.26, the bandwidth BW and therefore the rise time of the CSA circuit limits the rise time of the signal pulses. As stated previously, the 1st stage of the ETTORÉ ASIC acts as a first-order low-pass filter on the signal. This filter is characterized by its cutoff frequency which is defined as the frequency for which the output of the circuit is attenuated by 3 dB compared to its nominal value. To account for this behavior in the simulated signals, first-order low-pass Bessel filters are used to model this effect. These filters provide a maximally linear phase response which preserves the signal shape in the passband [124]. Figure 6.12 illustrates the magnitude-normalized Bessel filter frequency response for different Bessel filter rise times $t_{\text{rise}}^{\text{bessel}}$. The filter rise time defines the frequency at which the magnitude of the signal has decreased by 3 dB, which corresponds approximately to half the signal power. As expected, for higher $t_{\text{rise}}^{\text{bessel}}$ the cutoff frequency is lower. This results in a smaller bandwidth of the CSA circuit and a higher signal rise time. This trend is confirmed in figure 6.13 which shows the rise time of the experimental and simulated signal pulses for different Bessel filter rise times as a function of the radius. The influence of the different filter rise times on the simulated signals is clearly visible. Although the simulation follows

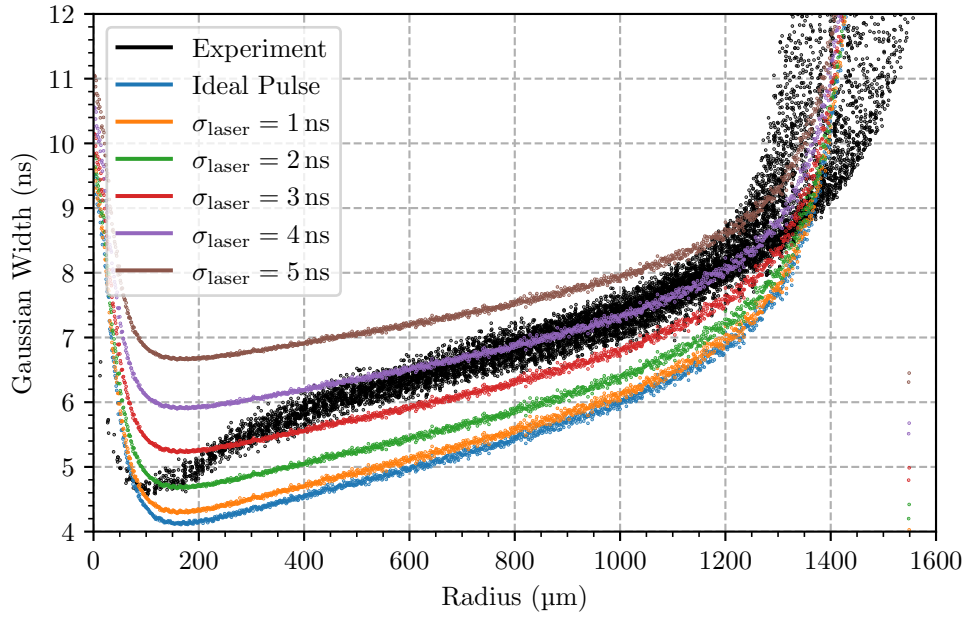


Figure 6.11: **Comparison of the Gaussian Width of the Experimental and Simulated Signal Pulses**

The Gaussian width of the experimental and simulated signal pulses is shown as a function of the radius. The influence of a non-ideal laser pulse on the shape of the simulated signals is illustrated by the variation of the standard deviation σ_{laser} of the Gaussian spread laser pulse. For a laser pulse of $\sigma_{\text{laser}} = 4$ ns, the simulation is in agreement with the experimental data for radial positions above $400 \mu\text{m}$. Below, the simulation overestimates the Gaussian width which. This is likely due to the fact that the high complexity of the field distribution near the pixel center is simply not represented precisely enough in the field simulation.

the same overall shape as the experiment, the different Bessel filters acting on the simulated signals lead to better representation of the experimental data in some regions and worse in others. The simulation with a Bessel filter rise time of $t_{\text{rise}}^{\text{bessel}} = 25$ ns fits best to the experimental data at large radial positions above $1300 \mu\text{m}$. However, while in the range of $r \approx (900 - 1300) \mu\text{m}$ the simulation with $t_{\text{rise}}^{\text{bessel}} = 26$ ns is in agreement with the experimental data, for $r \approx (500 - 900) \mu\text{m}$ the simulation with a filter rise time of $t_{\text{rise}}^{\text{bessel}} = 27$ ns represents the experiment in a superior way. In contrast, for $r < 500 \mu\text{m}$ the simulation with $t_{\text{rise}}^{\text{bessel}} = 26$ ns and eventually $t_{\text{rise}}^{\text{bessel}} = 25$ ns is found to reproduce the experimental data more accurately. The disagreement of the simulation and the experiment at the pixel center is explained as before: The highly complex electric fields due to the integrated JFET are not correctly represented in the field simulation.

Taking a look at figure 6.14 reveals further limitations of the simulations. This figure displays the exponential rise time of the experimental and the simulated signal pulses for different Bessel filter rise times as a function of the radius. In contrast to the signal rise times in figure 6.13, the simulation shows a

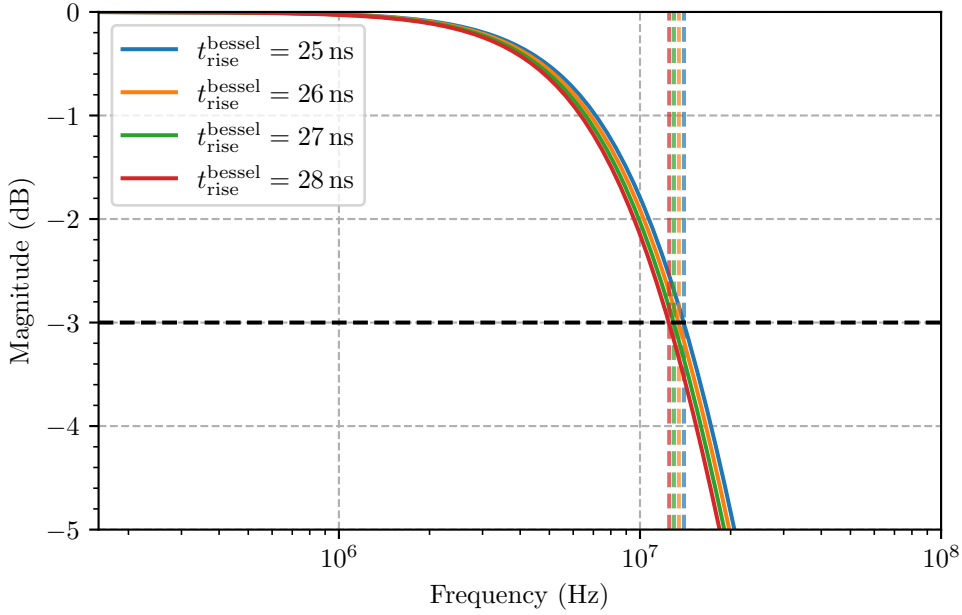


Figure 6.12: **Magnitude-Normalized Bessel Filter Frequency Response for different Bessel Filter Rise Times**

First-order low-pass Bessel filters are used to model the response of the CSA circuit to a unit voltage step resulting by the deposition of charge on the anode. The rise time of the bessel filter $t_{\text{rise}}^{\text{bessel}}$ defines the cutoff frequency at which the magnitude of the signal has decreased by 3 dB. The position of this frequency for different $t_{\text{rise}}^{\text{bessel}}$ is represented by the intersection of the vertical dashed lines in the respective color of the filter response and the horizontal dashed line in black, which indicates the reduction of the magnitude to -3 dB.

clear disagreement for Bessel filter rise times of $t_{\text{rise}}^{\text{bessel}} \geq 26$ ns. Only simulated signals with $t_{\text{rise}}^{\text{bessel}} = 25$ ns are in the same order of magnitude as the experimental data. However, unlike the simulated signals, which follow the same radial dependence of signal rise time as the experimental data, this is not the case for the exponential rise time. While the experimental distribution tends to decrease slightly towards larger radii, the simulation is almost constant at $\tau \sim 11.2$ ns for $r = (100 - 1300)$ μm . Although this agrees with the measurement for small radii, it is above the expectation for large radial positions. The overestimation at the pixel center can be explained by the same arguments as before. It is apparent that the parameterization of the CSA circuit response by a simple first-order low-pass Bessel filter is suitable as a rough approximation. However, it does not factor in effects like stray capacitive coupling or the impact of the changing phase of the CSA loop at frequencies close above the cutoff frequency. In future simulations, this should be considered since these effects have already been studied in detail [40].

For the simulated drift of the electron charge cloud depicted in figure 6.8, figure 6.15 shows the generated output signal. The raw, unprocessed total signal from the simulation illustrates the deposited charge of the electron cloud on the anode over time in the ideal case. In this case, all charge carriers are created

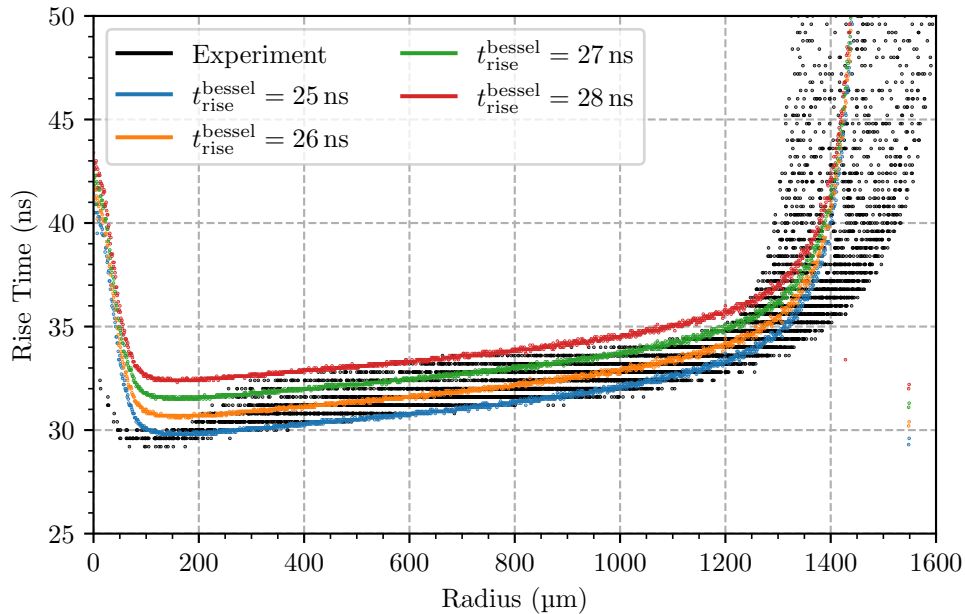


Figure 6.13: **Comparison of the Rise Time of the Experimental and Simulated Signal Pulses** The rise time of the experimental and simulated signal pulses is shown as a function of the radius. For the simulated signal pulses, the variation of the rise time $t_{\text{rise}}^{\text{bessel}}$ of the first-order low-pass Bessel filter is demonstrated, which is used to illustrate the influence of the limited rise time of the CSA circuit. Although the simulation follows the same overall shape as the experiment, the different Bessel filters acting on the simulated signals lead to better representation of the experimental data in some regions and worse in others.

at a single point in the detector and the cloud forms over time, as described in section 6.2. To account for the influence of the laser pulse on the formation of the charge cloud, the signal is convoluted with a Gaussian distribution. The standard deviation is set to $\sigma_{\text{laser}} = 4$ ns to match the experimental results. This process flattens the signal pulse which is completely absorbed by the Gaussian width parameter of the signal model as discussed in section 5.2. The response of the CSA circuit is factored in by applying the first-order low-pass Bessel filter illustrated earlier. The filter is chosen to provide a rise time of $t_{\text{rise}}^{\text{bessel}} = 25$ ns, since the simulations agree best with the experimental results for this value. The impact of this filter manifests itself as an exponential tail which is absorbed by the exponential rise time parameter as observed before. The obtained signal is very similar to the real signal of the detector. By fitting this signal with the model introduced in section 5.2, the simulation and experiment can be compared. Since the Gaussian width σ and exponential rise time τ have already been addressed, only the amplitude A and the drift time t_{drift} remain for discussion. As shown in figure 6.15, the obtained amplitude has already been converted to energy. Although the energy E_0 of the simulated incident radiation was 10 keV, the energy extracted by fitting differs by approximately 2 eV. This is the result of integer division performed for the calculation of the number of charge carriers produced by E_0 (see equation 3.14). Since the drift

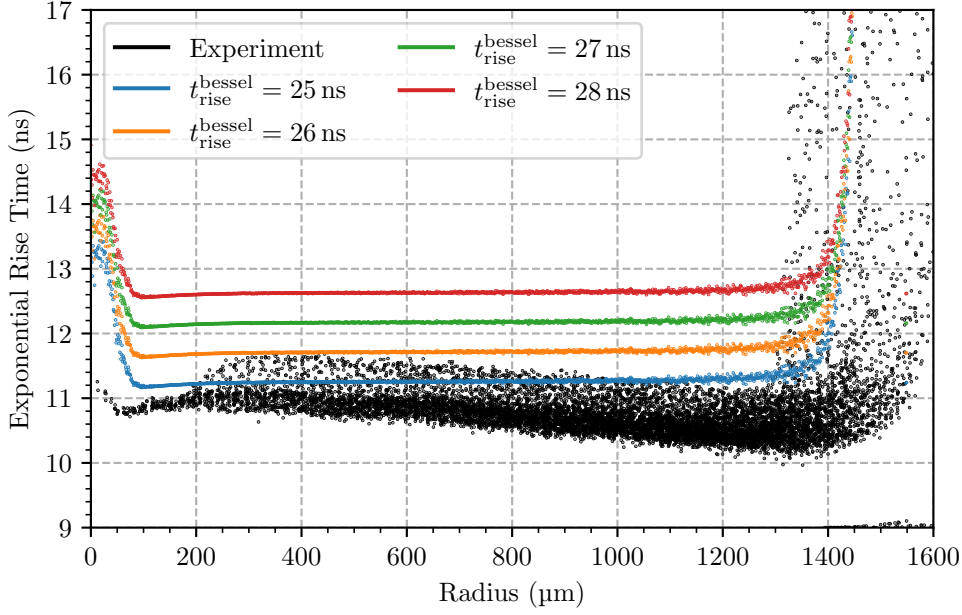


Figure 6.14: **Comparison of the Exponential Rise Time of the Experimental and Simulated Signal Pulses**

The exponential rise time of the experimental and simulated signal pulses is shown as a function of the radius. Just as for the signal rise time, the rise time $t_{\text{rise}}^{\text{bessel}}$ of the first-order low-pass Bessel filter is varied to illustrate the influence on the exponential rise time of the simulated signal pulses. For a Bessel filter rise time of $t_{\text{rise}}^{\text{bessel}} = 25$ ns, the simulation is in the same order of magnitude as the experimental data. However, unlike the simulated signals, which follow the same radial dependence of signal rise time as the experimental data, this is not the case for the exponential rise time. Nevertheless, the parameterization of the CSA circuit response by a simple first-order low-pass Bessel filter is suitable as a rough approximation.

is simulated for every charge, only integers are allowed.

Normalizing the collected charge to the mean/incident energy allows to compare the experimental and simulated charge collection. Figure 6.16 illustrates the normalized reconstructed energy of the experimental and the simulated signal pulses as a function of the radius. The **Quantum Efficiency (QE)** describes the ratio of generated electron-hole pairs per incident energy. In the simulation, QE is limited by the integer division constraint to

$$\text{QE} = \frac{N}{E_0} = (99.8 \pm 0.1) \% . \quad (6.4)$$

This agrees to literature values for SDDs of 450 μm thickness [112]. Both distributions are subject to the same radial dependence. For radial positions of $r \geq 100$ μm , the entire charge is collected in the experiment and the simulation. Charge loss was observed at smaller radii, with the maximum at $r = 0$ μm . There, the charge loss in the experiment was determined to be $\sim 4\%$. In the simulation, $\sim 6\%$ of the charge

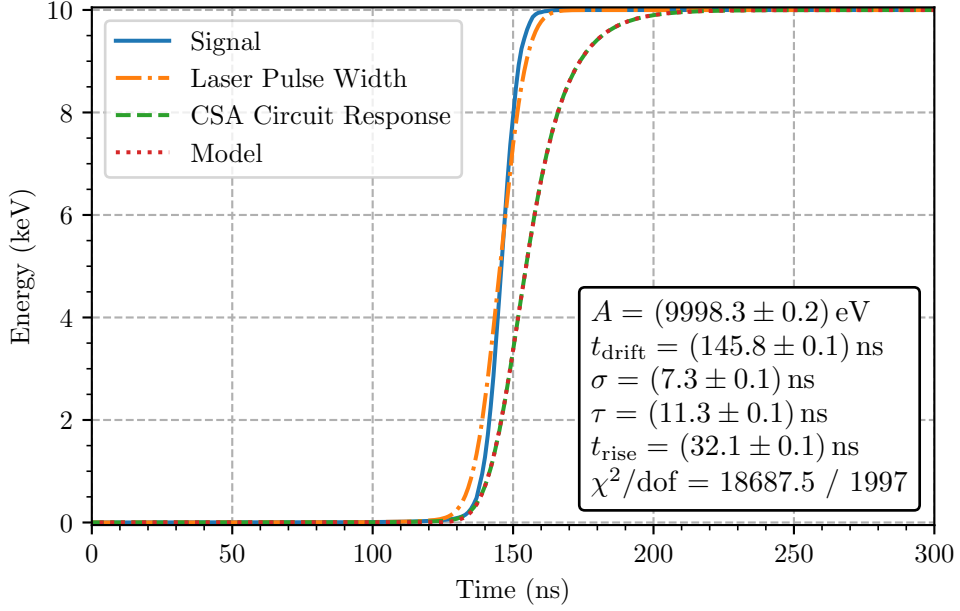


Figure 6.15: **Exemplary Processing of the Simulated Signal Pulses**

The raw, unprocessed total signal from the simulation of the charge cloud drift for an initial radius of $r_0 = 1000 \mu\text{m}$ is shown in blue. To account for the influence of the laser pulse on the formation of the charge cloud, the signal is convoluted with a Gaussian distribution of standard deviation $\sigma_{\text{laser}} = 4 \text{ ns}$. The resulting signal is represented by the orange dash-dotted line. Afterwards, the response of the CSA circuit is factored in by applying a first-order low-pass Bessel filter with a rise time of $t_{\text{rise}}^{\text{bessel}} = 25 \text{ ns}$ to the Gaussian convoluted signal. The signal obtained after this process is depicted by the green dashed line and is very similar to the real signal of the detector. By fitting this signal with the model introduced in section 5.2, the simulation and experiment can be compared. The best fit of the model to the processed signal pulse is represented by the red dotted line.

was lost. Although the complex fields at the transistor were not be absolute precisely represented in the field simulation, the results for the charge collection are almost identical. The limited amount of data available at the JFET region and the fluctuations in the experimental results could indicate that even less charge was collected than observed. Therefore, a detailed study of the pixel center region should be conducted. At large radii, the effects of charge sharing are observed in the simulation, too. Figure 6.17 illustrates the collected charge at the border between two adjacent pixels. Both distributions are fitted with the model described by equation 5.10 to directly obtain the simulated charge cloud size of

$$\sigma_{\text{CC}}^{\text{sim}} = (15.1 \pm 0.1) \mu\text{m}. \quad (6.5)$$

The deviation from the measured charge cloud size in the experiment $\sigma_{\text{CC}}^{\text{exp}} \leq (16.3 \pm 0.2) \mu\text{m}$ is calculated to

$$\Delta\sigma_{\text{CC}} = \sigma_{\text{CC}}^{\text{exp}} - \sigma_{\text{CC}}^{\text{sim}} \leq (1.2 \pm 0.3) \mu\text{m}. \quad (6.6)$$

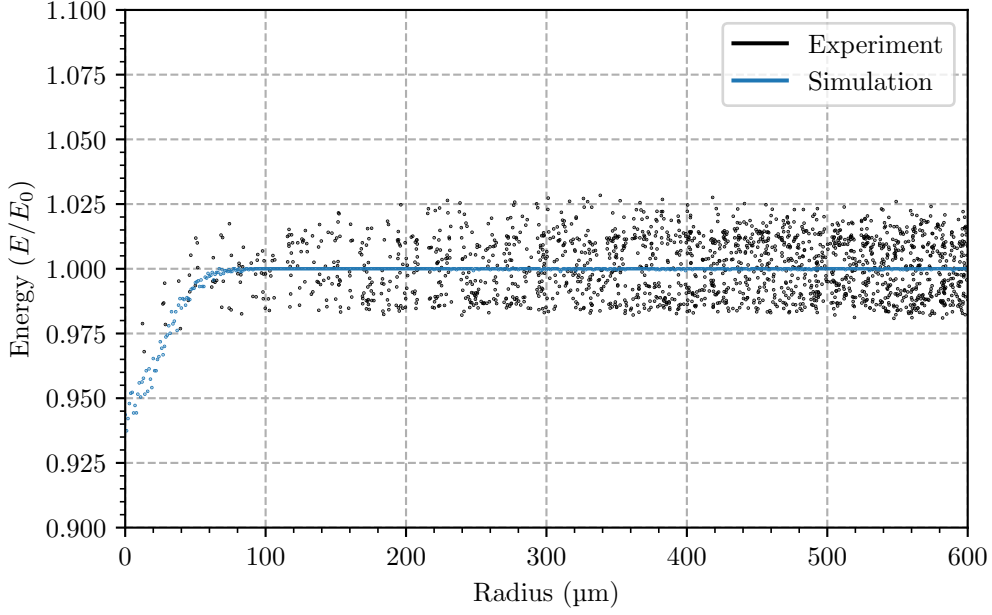


Figure 6.16: **Normalized Reconstructed Energy of the Experimental and Simulated Signal Pulses**

The normalized energy reconstructed from the amplitude of the experimental and simulated signal pulses is shown as a function of the radius. Both distributions share the same radial dependence. For radial positions of $r \geq 100 \mu\text{m}$, the entire charge is collected in the experiment and the simulation. Charge loss was observed at smaller radii, with the maximum at $r = 0 \mu\text{m}$, and was determined to be $\sim 4\%$ in the experiment and $\sim 6\%$ in the simulation. Although the complex fields at the transistor were not be absolute precisely represented in the field simulation, the results for the charge collection are almost identical.

Since σ_{CC}^{exp} is an upper limit, a possible explanation for the larger experimental charge cloud is, that the laser beam width determined during the preparatory measurement with the webcam sensor in section 4.2 did not correspond to the laser beam width in the detector measurement in section 5.3.1. During the setup modifications, a change in Z position would have resulted in a defocused and therefore enlarged laser beam. Consequently, this shift would have affected the calculation of σ_{CC}^{exp} . Based on the charge cloud size σ_{CC}^{sim} determined in the simulation, the minimal theoretical total experimental width of the charge cloud distribution would have been

$$\sigma_{\text{tot,theo}}^{\text{exp,min}} \geq (16.4 \pm 0.2) \mu\text{m} \quad (6.7)$$

assuming the laser beam width of $\sigma_{\text{laser}}^{\text{exp,min}} \geq (6.3 \pm 0.7) \mu\text{m}$ obtained in section 4.2. Hence, a displacement of $\Delta z \leq (0.61 \pm 0.02) \text{mm}$ in the Z position would have resulted in an enlarged laser beam of a width of $\sigma_{\text{laser}}^{\text{exp,max}} \leq (8.8 \pm 0.2) \mu\text{m}$.

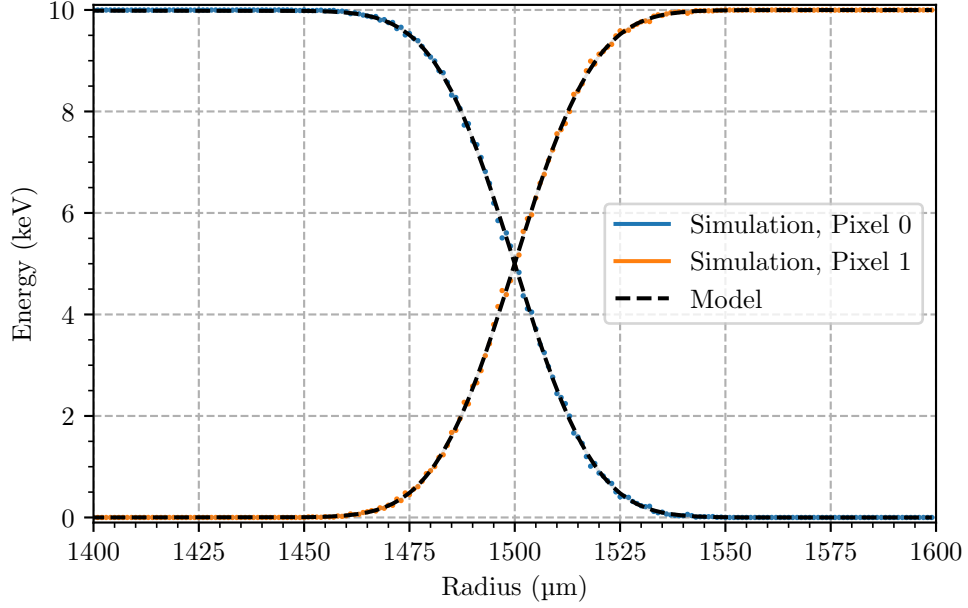


Figure 6.17: **Simulated Charge Cloud Distribution between adjacent Pixels**

The collected charge at the border between two adjacent pixels is shown as a function of the radius. While the blue line represents the decrease in collected charge for pixel 0, at the same time the orange line displays the increase for pixel 1. As expected, at the pixel border at $r = 1500 \mu\text{m}$ exactly half the energy is shared between both pixels. The distributions are fitted with the model described by equation 5.10 to directly obtain the charge cloud size. The black dashed lines represent the best fit results for both pixels.

Finally, the drift time of the charge clouds in the experiment and the simulation is compared as a function of the radius. Figure 6.18 displays the drift time distribution of the experiment in black and the simulation. The overall shape of the drift time of the simulated charge clouds clearly follows the experimental distribution and agrees for almost the entire pixel. While the simulation overestimates the drift time for charge cloud generated at the pixel center, it slightly underestimates t_{drift} in the range of $r \approx (400 - 1100) \mu\text{m}$. Nevertheless, the drift time is still within the lower boundaries determined in section 5.3.2. In the linear regime of $r = (500 - 1000) \mu\text{m}$, the drift time in dependence of the radius is obtained:

$$t_{\text{drift}}^{\text{sim}}(r) = (151.3 \pm 0.2) \frac{\text{ns}}{\text{mm}} \cdot r + (-7.1 \pm 0.2) \text{ns}. \quad (6.8)$$

Compared to the mean experimental drift time in equation 5.15, the simulation yields a slightly steeper slope, i. e. longer drift at the same radius, but also a negative intercept. This shows that the simulated drift of the charge carriers is very similar to the experiment, but not identical. The difference at small radii is probably due to the deviation of the simulated from the real fields in the transistor region.

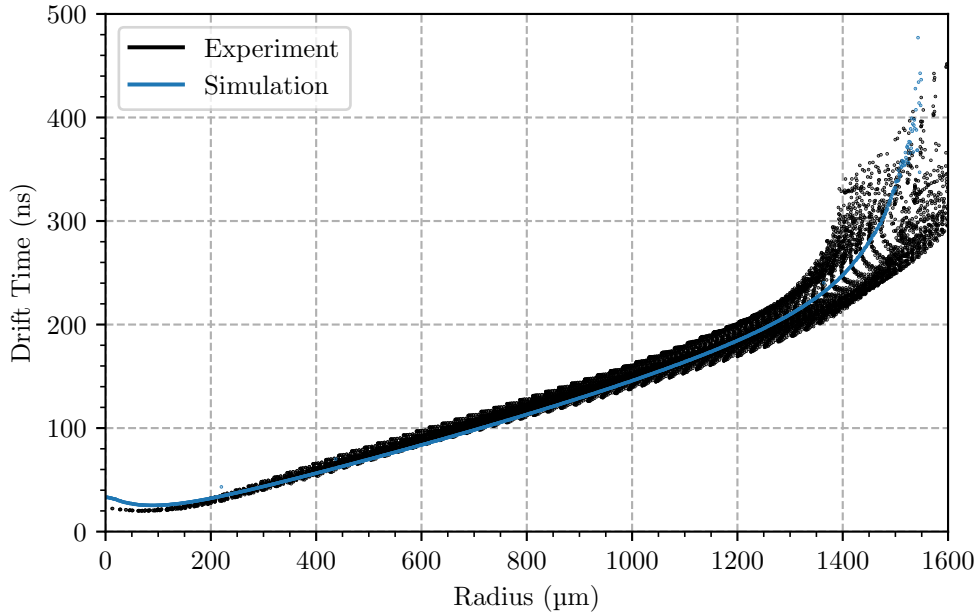


Figure 6.18: **Comparison of the Drift Time of Charge Clouds in the Experiment and Simulation**

The drift time of charge clouds is shown as a function of the radius for the experimental data and results obtained in the simulation. While the simulation overestimates the drift time for charge cloud generated at the pixel center, it slightly underestimates t_{drift} in the range of $r \approx (400 - 1100) \mu\text{m}$. Nevertheless, the overall shape of the drift time of the simulated charge clouds clearly follows the experimental distribution and agrees for almost the entire pixel.

In conclusion, the simulation of the field and the charge cloud drift is in good agreement with the experimental results. Factoring in the laser pulse shape and a simple first-order low-pass filter to simulate the response of the CSA circuit, leads to consistent signal shapes of the simulation and the experiment. The observed charge loss in the transistor region could be reproduced and matches almost completely. The obtained size of the charge cloud in the experiment and simulation differs slightly but is probably the consequence of a defocused laser beam. Furthermore, the charge clouds showed the same drift time distribution in both the experiment and the simulation.

6.4 Variation of Simulation Parameters

The field simulation was performed with the identical bias voltages applied to the detector in the experiment and provided good agreement with the experimental results as shown in section 6.3. The impact of varying these voltages will now be investigated with regards to the drift of the charge carriers. In each section, the potential of one of the selected electrodes (i. e. V_{BC} , V_{IGR} , V_{R1} , and V_{RX}) is varied and the effects on the signal shape is studied. Before that, however, the effects of changing the energy of the incident radiation on the drift of the charge cloud are discussed.

6.4.1 Variation of the Energy of the Incident Radiation

In the drift simulation, the energy of the incident radiation E_0 was set to 10 keV to correspond approximately to the energy deposited by the laser beam. Since the [TRISTAN SDDs](#) are operated also in other energy regimes [98], the question arose whether E_0 has an influence on the drift of the charge cloud and thus on the signal shape. For the keV-scale sterile neutrino search, the [PAE](#) boosts the electrons with additional (10 - 20) keV to total energies up to 60 keV. Hence, the simulation of the drift of the charge carriers was repeated with different incident energies to test if the outcomes of this thesis are also valid for the entire operating energy range of the detector. The results of the simulation presented in section 6.3 were defined as the reference for all parameter variations throughout this entire section 6.4. Figure 6.19 shows the combined results for the variation of E_0 for all model parameters as a function of the radius. In each image, the absolute difference between the extracted and the reference model parameter is plotted. Expressed in equations this is

$$\Delta A = \frac{A(E_0 = E_0^{\text{var}})}{E_0^{\text{var}}} - \frac{A(E_0 = 10 \text{ keV})}{E_0}, \quad (6.9)$$

$$\Delta t_{\text{drift}} = t_{\text{drift}}(E_0 = E_0^{\text{var}}) - t_{\text{drift}}(E_0 = 10 \text{ keV}), \quad (6.10)$$

$$\Delta \sigma = \sigma(E_0 = E_0^{\text{var}}) - \sigma(E_0 = 10 \text{ keV}), \quad (6.11)$$

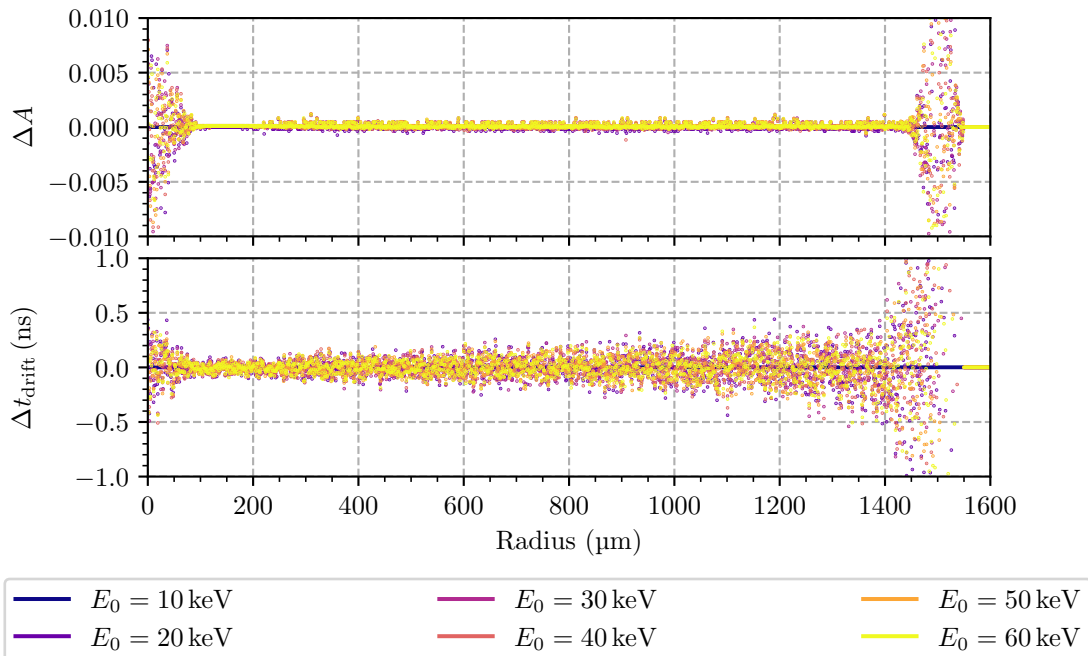
$$\Delta \tau = \tau(E_0 = E_0^{\text{var}}) - \tau(E_0 = 10 \text{ keV}), \quad (6.12)$$

$$\Delta t_{\text{rise}} = t_{\text{rise}}(E_0 = E_0^{\text{var}}) - t_{\text{rise}}(E_0 = 10 \text{ keV}), \quad (6.13)$$

where the energy of incident radiation E_0^{var} is varied in the range of (20 - 60) keV in intervals of 10 keV and the difference in amplitude is normalized to the energy of the incident radiation. Within the limits of numerical accuracy, all model parameters yield the identical results for each variation of E_0 as in the reference simulation. The tendency for the deviations to increase with larger radial positions is due to numerical reasons. The longer the charge cloud drifts, the more the numerical inaccuracies add up. Although the charge cloud consists of more charges, charge sharing affects the cloud in the same way.

The size of the charge cloud increases by about $0.1\ \mu\text{m}$ at $60\ \text{keV}$ compared to at $10\ \text{keV}$. The spread near the pixel border is an effect of the random movement of the charge carriers caused by diffusion at the saddle point in the electric potential. This slightly changes the distribution of the charges and results in a modified signal shape. At the pixel center, the fluctuations arise from the increased probability of incomplete charge collection due to the higher number of charge carriers. More charges are likely to get trapped in the minimum of the electric field above the **JFET** even longer enhancing this effect further before reaching the anode. This also impacts the signal shape in terms of increased diffusion and a more pronounced exponential tail.

In summary, charge clouds of different energies created by photons of a single wavelength at a fixed interaction point are subject to the same drift properties. The increased number of charge carriers can lead to deviating results in case of charge sharing due to their random movement. However, apart from the effects at the pixel borders, the electric field guides charge clouds of any energy in the same way as intended by design. Since electrons are charged particles, they interact with the detector differently than photons. While photons with an energy of $10\ \text{keV}$ can penetrate the detector up to $100\ \mu\text{m}$, the detector of $450\ \mu\text{m}$ thickness is transparent to them above $20\ \text{keV}$, as determined in **GEANT4** [13, 24, 25] simulations. In contrast, electrons in the energy range of $(10 - 60)\ \text{keV}$ share the same penetration depth of up to $10\ \mu\text{m}$ as photons of $\lambda = 640\ \text{nm}$. However, while the detector entrance window is transparent to photons, it is not to electrons. Therefore, further studies should investigate whether the drift of charge clouds generated by electrons is different, since the effect of the detector entrance window was not considered in the simulation.



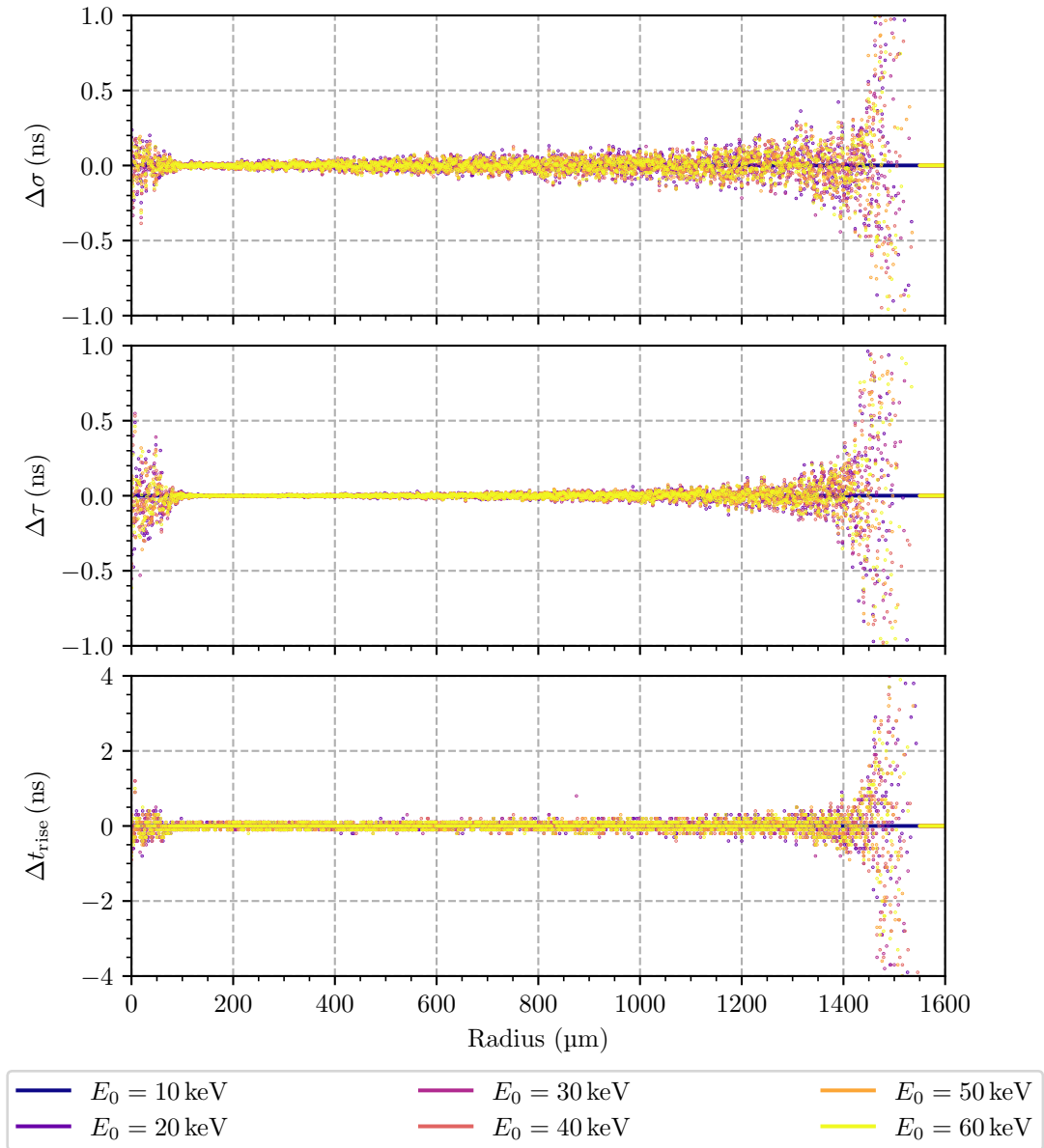


Figure 6.19: **Change of the Signal Pulses due to the Variation of the Energy of the Incident Radiation**

The signal pulses generated in the simulated drift of the charge carriers were compared for different energies E_0 deposited by the incident radiation in the range of (10 - 60) keV. Within the limits of numerical accuracy, all parameters of the model introduced in section 5.2 yield the identical values for each variation of E_0 as the reference simulation of section 6.3. Charge clouds of different energies created by photons of a single wavelength of $\lambda = 640$ nm at a fixed interaction point are subject to the same drift properties. Although electrons in the energy range of (10 - 60) keV share the same penetration depth of up to $10 \mu\text{m}$ as photons of $\lambda = 640$ nm, further studies should investigate whether the drift of charge clouds generated by electrons is different, since the effect of the detector entrance window was not considered in the simulation.

6.4.2 Variation of the Back Contact (BC) Voltage

The back contact voltage V_{BC} is the first to be modified in the field simulation. Since the back contact electrode is responsible for the vertical depletion of the detector, the drift of the charge cloud is prone to the effects of under- or over-biasing. This affects the signal shape as well. Similar to section 6.4.1, the signal pulses generated in the simulated drift of the charge carriers in the different field configurations are fitted with the model introduced in section 5.2 and compared with the reference simulation of section 6.3. In terms of equations, this can be written as

$$\Delta A = \frac{A(V_{\text{BC}} = V_{\text{BC}}^{\text{var}})}{E_0} - \frac{A(V_{\text{BC}} = -100 \text{ V})}{E_0}, \quad (6.14)$$

$$\Delta t_{\text{drift}} = t_{\text{drift}}(V_{\text{BC}} = V_{\text{BC}}^{\text{var}}) - t_{\text{drift}}(V_{\text{BC}} = -100 \text{ V}), \quad (6.15)$$

$$\Delta \sigma = \sigma(V_{\text{BC}} = V_{\text{BC}}^{\text{var}}) - \sigma(V_{\text{BC}} = -100 \text{ V}), \quad (6.16)$$

$$\Delta \tau = \tau(V_{\text{BC}} = V_{\text{BC}}^{\text{var}}) - \tau(V_{\text{BC}} = -100 \text{ V}), \quad (6.17)$$

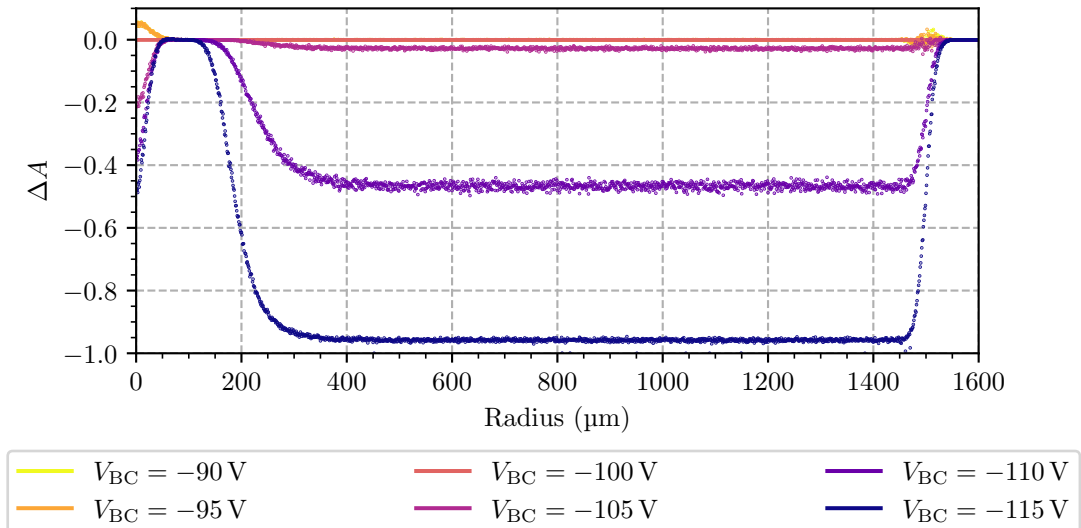
$$\Delta t_{\text{rise}} = t_{\text{rise}}(V_{\text{BC}} = V_{\text{BC}}^{\text{var}}) - t_{\text{rise}}(V_{\text{BC}} = -100 \text{ V}), \quad (6.18)$$

where the difference in amplitude is normalized to the energy of the incident radiation of $E_0 = 10 \text{ keV}$ and the variation of the back contact voltage $V_{\text{BC}}^{\text{var}}$ is in the range of $(-90 - -115) \text{ V}$ in intervals of 5 V . Figure 6.20 presents the results as a function of the radius for each model parameter. Decreasing the back contact potential to more negative voltages leads to the mentioned effects of over-depletion. While for $V_{\text{BC}} = -110 \text{ V}$ about 50 % of the charges are still collected, for $V_{\text{BC}} = -115 \text{ V}$ almost 100 % are lost in the process of charge collection for almost all radial positions. This also holds for $V_{\text{BC}} = -105 \text{ V}$ for which about 3 % of the charge carriers are lost. Only charge clouds created in the region, in which the weighting potential is dominant, are collected properly. This behavior is a consequence of shifting the transport trough in the electric potential towards the drift rings making the concept of sideways depletion less effective. The trough does not guide the electrons to the anode, but to the innermost drift ring **R1** and are consequently lost. The remaining charges feature a shorter drift time because the lower V_{BC} increases the electric field in the vertical direction which results in higher drift velocities towards the readout side of the detector. The timing constants σ , τ , and t_{rise} of the signals are almost identical for all radii. The deviation at $V_{\text{BC}} = -115 \text{ V}$ is however caused by a distorted signal shape due to the incomplete charge collection. The over-biasing also leads to an increased charge loss in the center region of the pixel. The saddle point in the electric potential above the **JFET** is removed but the **IGR** is not capable of shielding the transistor from the bulk anymore. The electrons drift directly to the drain electrode and are lost. At $V_{\text{BC}} = -115 \text{ V}$, approximately only half of all charge carriers are collected compared to at $V_{\text{BC}} = -100 \text{ V}$.

In contrast, increasing V_{BC} to more positive voltages increases the effectiveness of the inner guard ring. The charge missing at $V_{\text{BC}} = -100 \text{ V}$ is fully collected at $V_{\text{BC}} = -90 \text{ V}$ and $V_{\text{BC}} = -95 \text{ V}$. At the same time, however, the drift time of the charge clouds increases overall because the lower back contact voltage

leads to a reduced strength of the electric field in vertical direction. This also leads to an increase of the Gaussian width as the charge cloud undergoes diffusion for longer time. At $V_{BC} = -90$ V, the impact of the transport trough shifted towards the entrance window side of the detector on the drift of the charge carriers is even more pronounced in the signal shape. While at the reference back contact voltage the trough guides the electrons to the anode directly, the charges accumulate above the anode and then fall into the potential minimum. At the same time, however, parts of the charge cloud are subject to the influence of the saddle point in the electric potential above the **JFET**. The **IGR** has to guide these charge carriers away from the center of the pixel to the anode which increases both τ and t_{rise} . This effect is particularly prominent for charge clouds created at small radial positions. There, the rise time of the signals is about 5 times higher compared to the average.

Concluding the observations, yields the following results: By decreasing the back contact voltage, the effects of over-depletion start to appear. Charge is lost for almost all radii except in the regime where the weighting potential is most effective. At the same time, decreasing the potential of the **IGR** to more negative voltages can prevent the effect of incomplete charge collection in the **JFET** region. The drift times of the charge clouds are shorter due to the increased field strength in the vertical direction guiding the charge carriers faster to the respective electrodes and thereby slightly reducing the effects diffusion. Since τ and t_{rise} are dominated by the response of the **CSA** circuit, they are almost identical to the reference simulation. In contrast, increasing V_{BC} naturally results in longer drift times and improves charge collection in the transistor region. However, the extended period of drifting in the detector also results in increased diffusion. In addition, the collection is slowed down due to the larger impact of the saddle point in the electric potential. As the **IGR** guides the charge carriers away from the center of the pixel, their gradual drift towards the anode eventually leads to longer rise times.



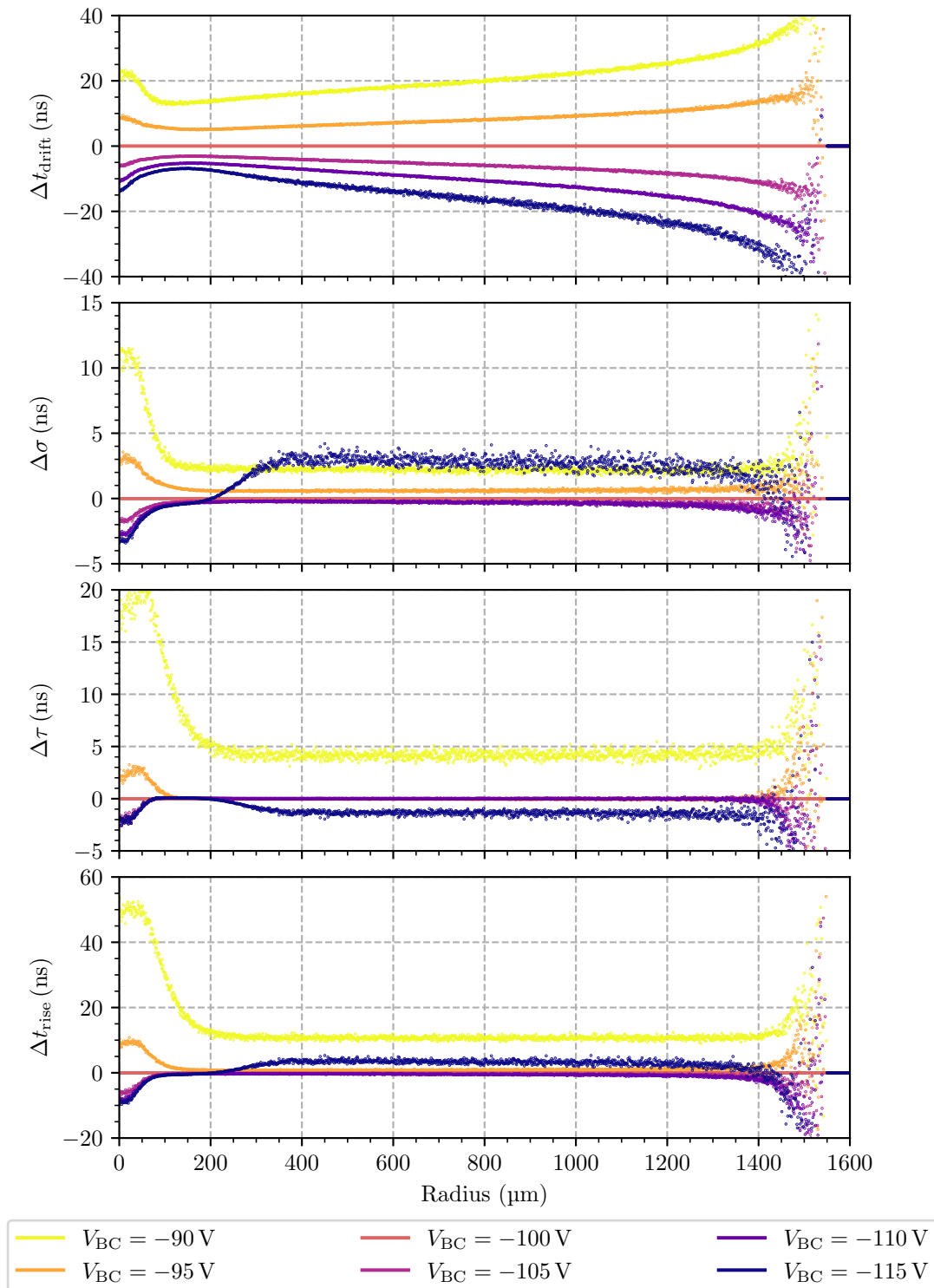


Figure 6.20: **Change of the Signal Pulses due to the Variation of the Back Contact Voltage**
 The signal pulses generated in the simulated drift of the charge carriers were compared for different field configurations in which the back contact voltage V_{BC} was varied. For more negative BC voltages, the over-depletion resulted in higher drift velocity and therefore reduced drift times but also charge loss in most parts of the pixel. In contrast, more positive V_{BC} led to complete charge collection at the center region of the pixel but also longer drift times and increased signal rise times.

6.4.3 Variation of the Inner Guard Ring (IGR) Voltage

The inner guard ring voltage V_{IGR} is the second to be modified in the field simulation. As previously discussed, the main purpose of the **IGR** is to shield the transistor components from the **Si** bulk. Changing this bias voltage therefore modifies the capability to effectively prevent charge carriers from getting lost and not reaching the anode. Like before, the signals pulses generated in the simulated drift of the charge carriers in the different field configurations are fitted with the model introduced in section 5.2 and compared with the reference simulation of section 6.3. This writes in the following equations:

$$\Delta A = \frac{A(V_{\text{IGR}} = V_{\text{IGR}}^{\text{var}})}{E_0} - \frac{A(V_{\text{IGR}} = -19 \text{ V})}{E_0}, \quad (6.19)$$

$$\Delta t_{\text{drift}} = t_{\text{drift}}(V_{\text{IGR}} = V_{\text{IGR}}^{\text{var}}) - t_{\text{drift}}(V_{\text{IGR}} = -19 \text{ V}), \quad (6.20)$$

$$\Delta \sigma = \sigma(V_{\text{IGR}} = V_{\text{IGR}}^{\text{var}}) - \sigma(V_{\text{IGR}} = -19 \text{ V}), \quad (6.21)$$

$$\Delta \tau = \tau(V_{\text{IGR}} = V_{\text{IGR}}^{\text{var}}) - \tau(V_{\text{IGR}} = -19 \text{ V}), \quad (6.22)$$

$$\Delta t_{\text{rise}} = t_{\text{rise}}(V_{\text{IGR}} = V_{\text{IGR}}^{\text{var}}) - t_{\text{rise}}(V_{\text{IGR}} = -19 \text{ V}), \quad (6.23)$$

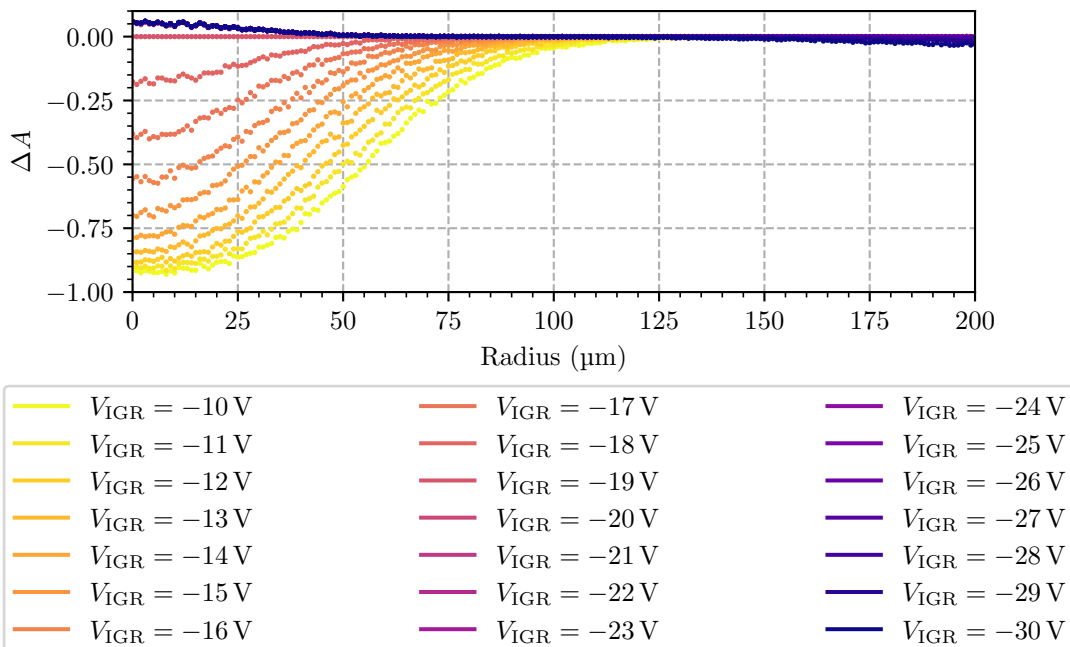
where the difference in amplitude is normalized to the energy of the incident radiation of $E_0 = 10 \text{ keV}$ and the inner guard ring voltage $V_{\text{IGR}}^{\text{var}}$ is varied in the range of $(-10 - -30) \text{ V}$ in steps of 1 V . The obtained results are depicted in figure 6.21. Since the impact of the **IGR** is maximal on the drift of charge clouds generated in the center region of the pixel, the plots are limited to $r = (0 - 150) \mu\text{m}$. Above, the results are identical within numerical accuracy.

Decreasing the inner guard ring voltage below $V_{\text{IGR}}^{\text{ref}} = -19 \text{ V}$, increases the strength of the potential barrier surrounding the transistor. Electrons are protected from the potential of the drain electrode and properly guided to the detector anode. The charge loss previously caused by the **JFET** has been eliminated. As the **IGR** potential extends further into the bulk, the electrons are subject to longer drift paths. Compared to at $V_{\text{IGR}} = -19 \text{ V}$, where the saddle point in the electric potential is located at $z \approx 30 \mu\text{m}$, it is shifted approximately $25 \mu\text{m}$ deeper into the bulk at $V_{\text{IGR}} = -30 \text{ V}$. The charges have to be guided around this potential, which increases the drift time and also the Gaussian width due to the prolonged effect of diffusion on the charge cloud. The exponential rise time decreases slightly since the enhanced potential creates a steeper electric field to the anode which leads to a faster charge collection when the cloud has arrived in the region above the anode. Therefore, the signal rise time remains approximately the same within numerical accuracy. However, a side effect of the larger expansion of the **IGR** potential is the incomplete charge collection of charge clouds generated at larger radial positions. At the end of the transport trough in the electric potential, a fraction of the charge carriers is misguided to the **R1** electrode instead of to the anode and is lost. Hence, a good compromise for the complete collection of all charges created at any position is achieved at $V_{\text{IGR}} \approx (-20 - -21) \text{ V}$, respecting the experimental results of section 5.3. Additional studies are required to confirm this set point is consistent

with the detector conditions for complete charge collection.

In contrast, increasing V_{IGR} to more positive voltages weakens the potential barrier surrounding the transistor. Changing the inner guard ring voltage exemplarily by 1 V to $V_{\text{IGR}} = -18$ V, increases the charge loss at the center of the pixel by 20%. For even higher voltages, this behavior intensifies approaching a state in which the signal is too distorted to be fitted properly. This state is reached above $V_{\text{IGR}} = -14$ V. The induced current of the drifting charge carriers on the anode leads to a rising signal pulse. However, since most of the electrons are collected by the drain electrode of the **JFET**, the current vanishes abruptly, leaving a spike in the signal. Only a small fraction of the charge carriers contributes to the actual deposition of the electric charge on the anode, leading to a constant signal after the spike. Since the **IGR** potential does not extend so far into the bulk, charge carriers are less deflected and can reach the anode more directly. This leads to lower drift times and therefore less impact due to diffusion. The reduced signal rise times are a direct consequence of the increased charge loss. The smaller number of charge carriers physically arriving at the anode take less time to get collected compared to the expectation from the induced current. The rather abrupt transition of the signal from a rising pulse to a constant voltage leads to a shortened exponential tail and thus to lower rise times.

In summary, the correct biasing of the inner guard ring is essential for the **TRISTAN SDDs**. If the voltage deviates by (1 - 2) V from the optimum operating point, charge losses occur, which are caused either by the transistor or the innermost drift ring **R1**. This affects the drift of the charge clouds and distorts the signal pulses and the energy spectrum, but can be avoided by applying the correct detector voltages.



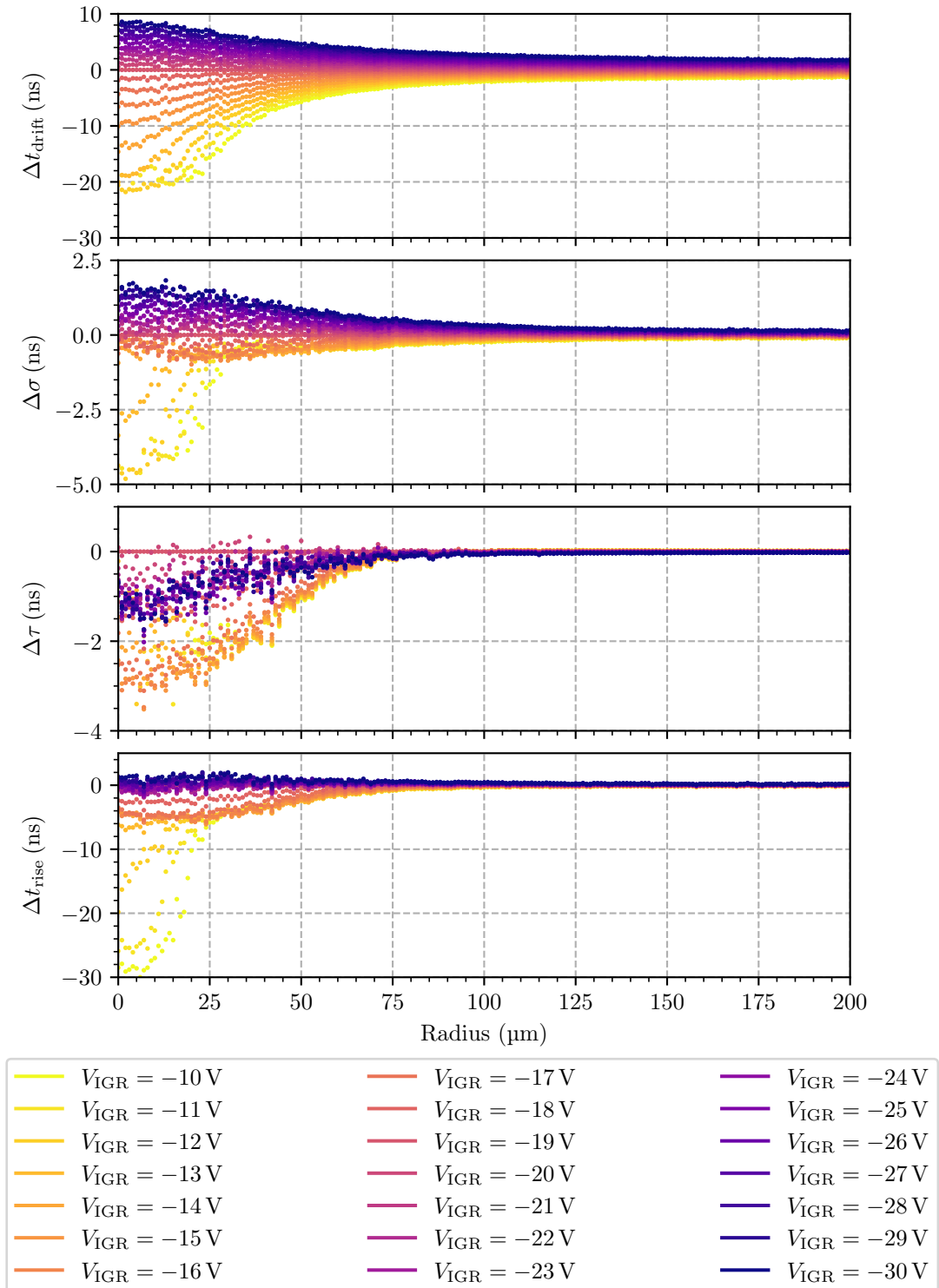


Figure 6.21: **Change of the Signal Pulses due to the Variation of the Inner Guard Ring Voltage**

The signal pulses generated in the simulated drift of the charge carriers were compared for different field configurations in which the inner guard ring voltage V_{IGR} was varied. In summary, the correct biasing of the inner guard ring is essential for the [TRISTAN SDDs](#). If the voltage deviates by (1 - 2) V from the optimum operating point, charge losses occur, which are caused either by the transistor or the innermost drift ring [R1](#).

6.4.4 Variation of the Innermost Drift Ring (R1) Voltage

The voltage V_{R1} applied to the innermost drift ring **R1** is one of the two key elements in the effectiveness of the sideways depletion of the **SDD**. Since the voltages of the drift rings **R1** and **RX** determine the potential of all other rings in between via the integrated voltage divider, changing V_{R1} will affect the shape of the electric potential substantially. Therefore, the impact of different V_{R1} on the drift of the charge clouds is studied in this section. The variation of the **R1** voltage V_{R1}^{var} is performed in the range of $(-5 - -13)$ V in steps of 1 V. The signal pulses generated in the simulated drift of the charge carriers are fitted with the model introduced in section 5.2 and compared for the different field configurations with the reference simulation of section 6.3. The absolute difference is calculated for each parameter and writes

$$\Delta A = \frac{A(V_{R1} = V_{R1}^{\text{var}})}{E_0} - \frac{A(V_{R1} = -9 \text{ V})}{E_0}, \quad (6.24)$$

$$\Delta t_{\text{drift}} = t_{\text{drift}}(V_{R1} = V_{R1}^{\text{var}}) - t_{\text{drift}}(V_{R1} = -9 \text{ V}), \quad (6.25)$$

$$\Delta \sigma = \sigma(V_{R1} = V_{R1}^{\text{var}}) - \sigma(V_{R1} = -9 \text{ V}), \quad (6.26)$$

$$\Delta \tau = \tau(V_{R1} = V_{R1}^{\text{var}}) - \tau(V_{R1} = -9 \text{ V}), \quad (6.27)$$

$$\Delta t_{\text{rise}} = t_{\text{rise}}(V_{R1} = V_{R1}^{\text{var}}) - t_{\text{rise}}(V_{R1} = -9 \text{ V}), \quad (6.28)$$

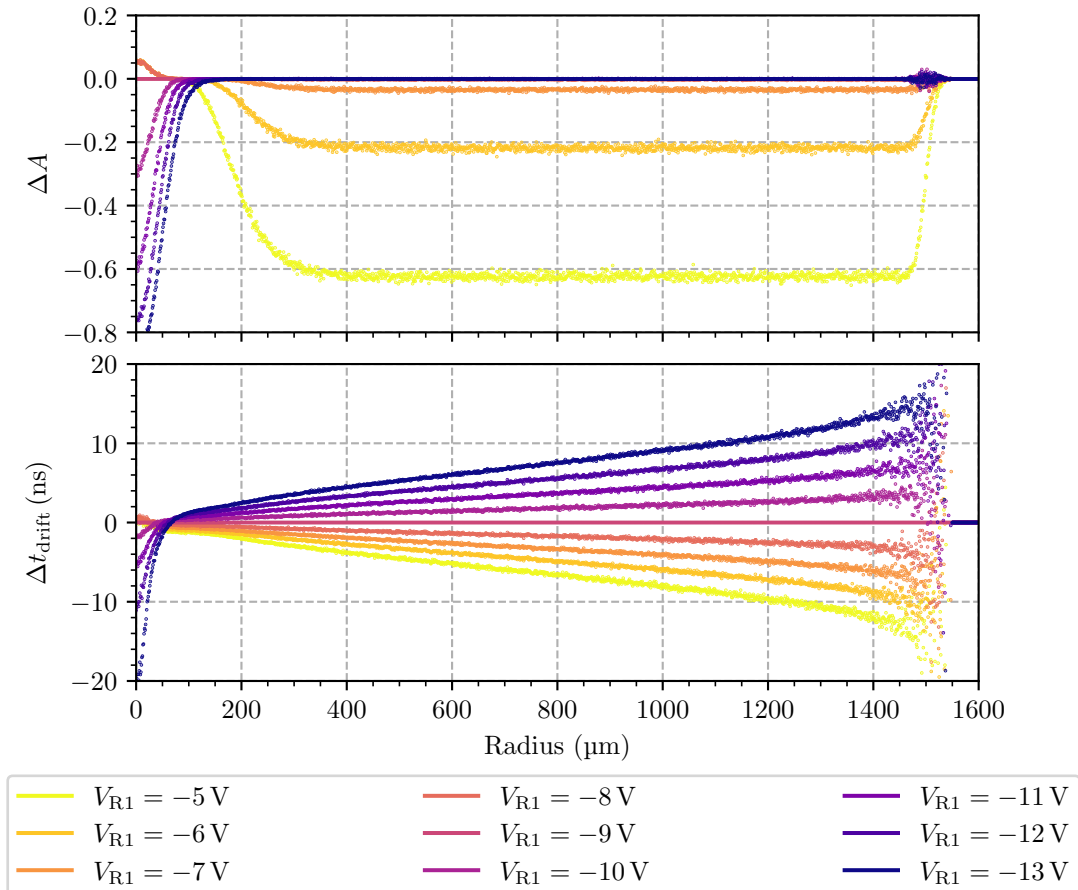
where the difference in amplitude is normalized to the energy of the incident radiation of $E_0 = 10$ keV. The results are presented in figure 6.22.

When V_{R1} is increased to more positive voltages, the gradient between the drift ring **R1** and the drift ring **RX** becomes larger. This makes the transport trough in the electric potential steeper and leads to a stronger electric field. Consequently, this results in an overall reduced drift time for all charge clouds. The absolute difference of the drift times shows that this behavior is linearly proportional to the radius, as expected due to the voltage divider. Since the diffusion processes are time dependent, the reduced drift time also leads to a slight decrease in the Gaussian width. However, when the potential generated by the **R1** electrode is too positive, the field distribution is dominated by the **IGR** in the center region of the pixel. Although, this resolves the charge loss caused by the transistor, the potential trough is not capable of guiding the entire charge cloud to the anode anymore. The **IGR** affects the field distribution at the anode, so that the charges drift to the **R1** electrode instead and are lost.

In contrast, decreasing V_{R1} to more negative voltages, reduces the potential gradient between the drift rings **R1** and **RX**. Consequently, the drift time increases and so does the influence of diffusion on the charge clouds. However, charge carriers are now lost in the center region of the pixel, instead of at large radial positions as before. When the potential of the **R1** electrode is in the same order of magnitude as that of the **IGR** electrode, the effective field distribution is not able to create a potential barrier which completely shields the transistor. Hence, charge carriers generated in the center region of the pixel drift

to the drain electrode of the **JFET** and are lost. The created signals share the same features as discussed for too positive inner guard ring voltages in section 6.4.3. Therefore, they cannot be fitted properly anymore to obtain the required parameters. This is particularly visible in distribution of the signal rise times. While the time constants of the signal pulses are almost constant for all variations of V_{R1} , despite a slight tendency of following the drift time towards larger radial position, the distorted signal pulses cause the pronounced drop in the center of the pixel.

From the simulations, it can be concluded that for the successful operation of the **TRISTAN SDDs**, a balance between V_{IGR} and V_{R1} needs to be found. The impact on the charge collection was shown for too low and too high voltages applied to the **R1** electrode. In addition, the dependency of the drift time on the potential gradient between the drift rings **R1** and **RX** was illustrated. The influence on the signal rise times is almost negligible although the distributions slightly follow the drift times towards larger radial positions.



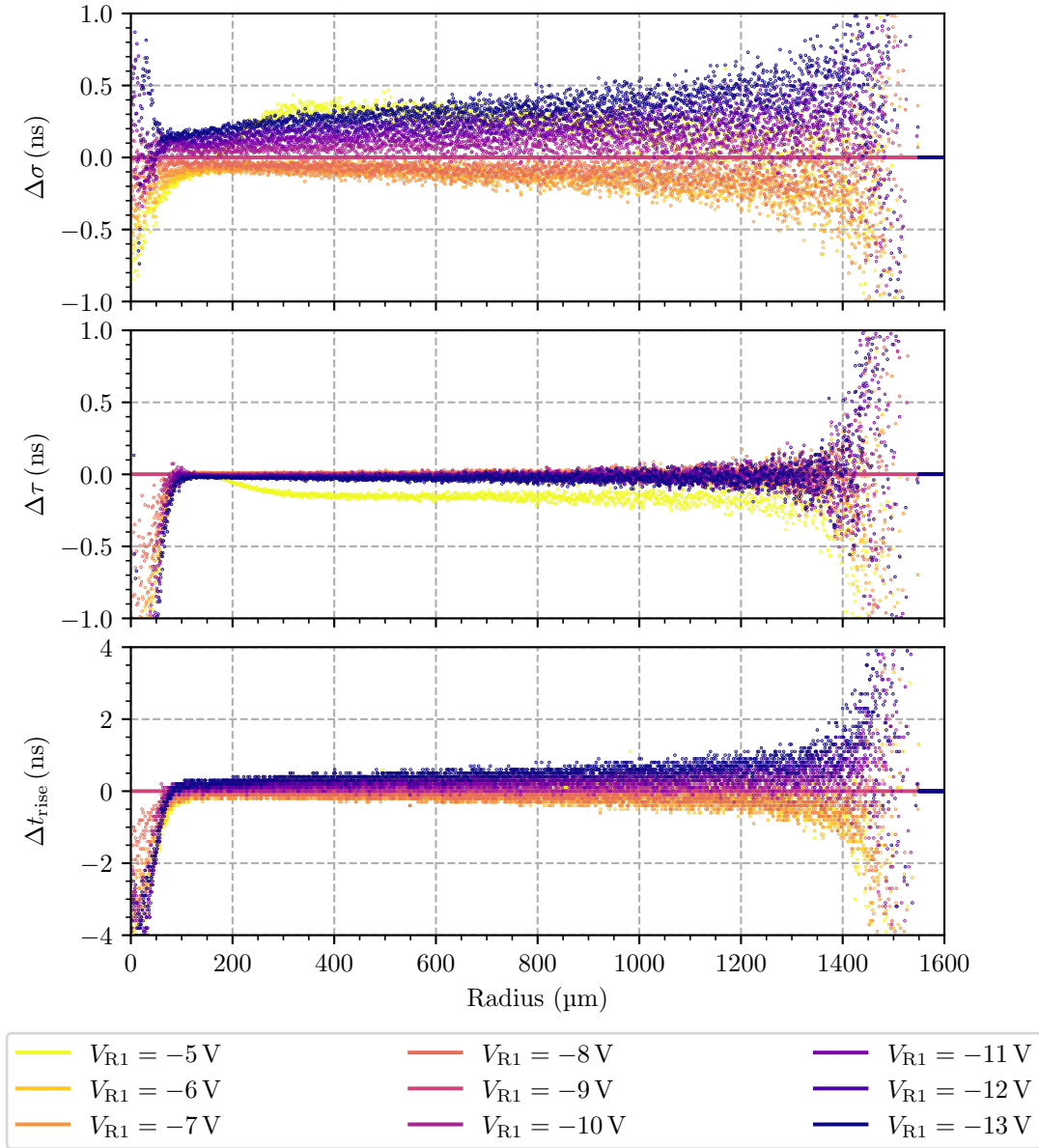


Figure 6.22: **Change of the Signal Pulses due to the Variation of the Innermost Drift Ring (R1) Voltage**

The signal pulses generated in the simulated drift of the charge carriers were compared for different field configurations in which the innermost drift ring **R1** voltage V_{R1} was varied. When V_{R1} is increased to more positive voltages, the gradient between the drift ring **R1** and the drift ring **RX** becomes larger and the charge carriers drift faster to the center region of the pixel. However, when the potential generated by the **R1** electrode is too positive, the field distribution is dominated by the **IGR** in the center region of the pixel and the charges drift to the **R1** electrode instead and are lost. In contrast, more negative voltages lead to a more shallow gradient and therefore longer charge cloud drifts. When the potential of the **R1** electrode is in the same order of magnitude as that of the **IGR** electrode, the effective field distribution is not able to create a potential barrier which completely shields the transistor. Hence, charge carriers generated in the center region of the pixel drift to the drain electrode of the **JFET** and are lost.

6.4.5 Variation of the Outermost Drift Ring (RX) Voltage

The second key element for the effective sideways depletion is the voltage V_{RX} applied to the outermost drift ring **RX**. Since the ratio of V_{BC} to V_{RX} determines the origin of the transport trough in the electric potential, applying different voltages to the **RX** electrode will substantially influence the charge carrier transport through the bulk. Hence, different field configurations are simulated in a range $V_{\text{RX}}^{\text{var}} = (-100 - -140) \text{ V}$ in intervals of 5 V . The signal pulses generated in the simulated drift of the charge carriers in these fields are fitted with the model introduced in section 5.2 and compared to the signals of the charge carriers of the reference simulation of section 6.3. The deviations are obtained from the absolute differences of the relevant parameters and are described by the following equations:

$$\Delta A = \frac{A(V_{\text{RX}} = V_{\text{RX}}^{\text{var}})}{E_0} - \frac{A(V_{\text{RX}} = -120 \text{ V})}{E_0}, \quad (6.29)$$

$$\Delta t_{\text{drift}} = t_{\text{drift}}(V_{\text{RX}} = V_{\text{RX}}^{\text{var}}) - t_{\text{drift}}(V_{\text{RX}} = -120 \text{ V}), \quad (6.30)$$

$$\Delta \sigma = \sigma(V_{\text{RX}} = V_{\text{RX}}^{\text{var}}) - \sigma(V_{\text{RX}} = -120 \text{ V}), \quad (6.31)$$

$$\Delta \tau = \tau(V_{\text{RX}} = V_{\text{RX}}^{\text{var}}) - \tau(V_{\text{RX}} = -120 \text{ V}), \quad (6.32)$$

$$\Delta t_{\text{rise}} = t_{\text{rise}}(V_{\text{RX}} = V_{\text{RX}}^{\text{var}}) - t_{\text{rise}}(V_{\text{RX}} = -120 \text{ V}), \quad (6.33)$$

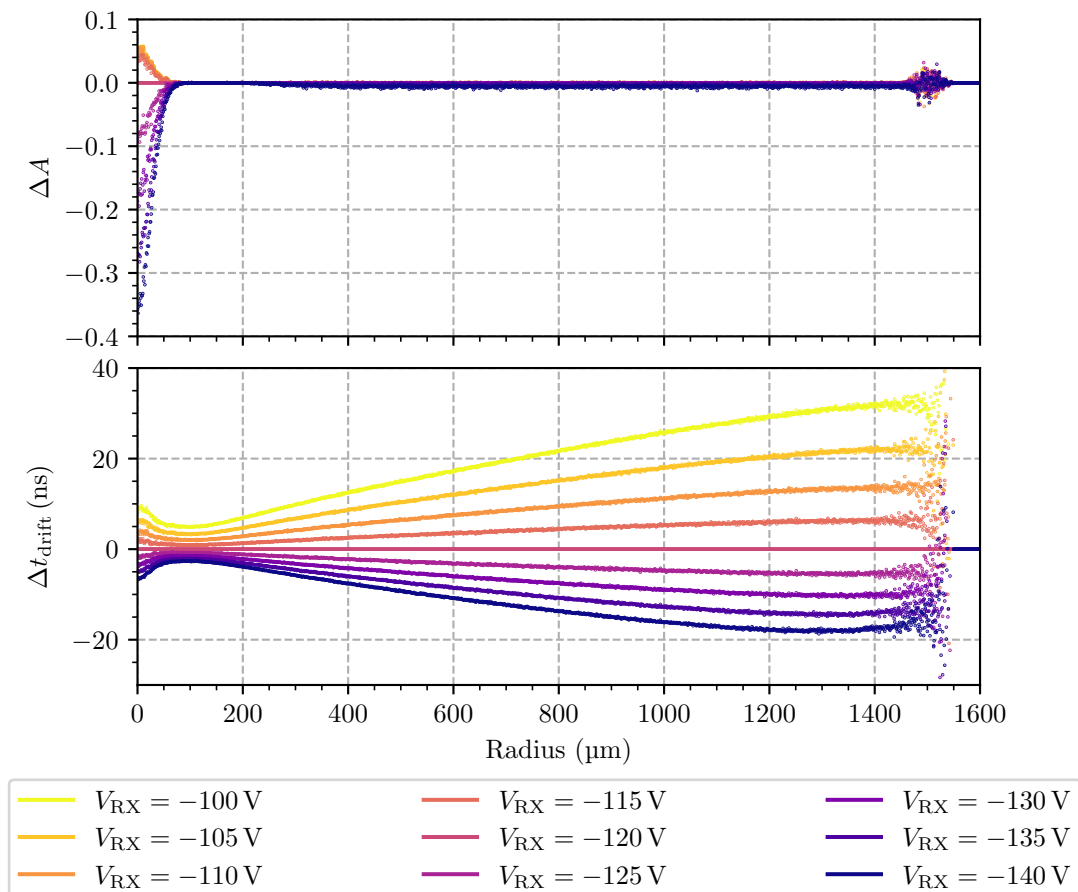
where the difference in amplitude is normalized to the energy of the incident radiation of $E_0 = 10 \text{ keV}$. Figure 6.23 shows the results for the different voltages applied to the **RX** electrode.

Decreasing V_{RX} to more negative voltages, shifts the origin of the transport trough nearer towards the back contact electrode. The origin determines the position of the saddle point in the electric potential at the pixel border. Since the voltage of the **R1** electrode is kept constant, this results in a steeper gradient between the drift rings **R1** and **RX**. Just as before in section 6.4.4, this reduces the drift time for all charge clouds. However, the deviation from the reference simulation is not following the radius linearly but rather converges to a maximum value. The faster drift also leads to a reduced influence of diffusion on the charge cloud as well as lower signal rise times. Nevertheless, the over-depletion results in a substantial charge loss at the pixel center. The **IGR** is not capable of providing a strong enough potential barrier around the the transistor. Therefore, the charges drift to the drain electrode of the **JFET** and are lost.

If V_{RX} is increased to more positive voltages, the saddle point is positioned closer to the drift ring structure on the readout side of the detector pixel. This leads to a shallower gradient between the drift rings **R1** and the **RX** and thus to longer drift times. However, in contrast to more negative voltages applied to the **RX** electrode, the non-linear deviation from the reference simulation converges to larger values. Starting from $V_{\text{RX}} = V_{\text{BC}}$, when the saddle point is located exactly at half the thickness of the wafer, the potential of the **RX** electrode can be varied in positive and negative direction until some voltage limit is reached where the drift of the charge carriers does not change anymore. Hence, a voltage window exists

in which V_{RX} can move the origin of the transport trough in the electric potential in vertical direction while maintaining the sideways depletion. The increased drift times naturally result in larger influence of diffusion on the charge cloud and also longer signal rise times. Nonetheless, since the working conditions of the IGR are restored, all charge carriers are collected properly.

In summary, V_{RX} has a more significant influence on the drift of the charges than is apparent at first glance. Although the influence on the shape of the transport trough in the electric potential suggests that the voltage applied to the RX electrode has a major effect on the drift times of the charge carriers and the diffusion processes of the charge clouds, the impact on the overall field distribution is rather unexpected as different bias voltages result in different levels of effectiveness of the sideways depletion. This changes the signal rise times as well as the capability of complete charge collection in the center region of the pixel.



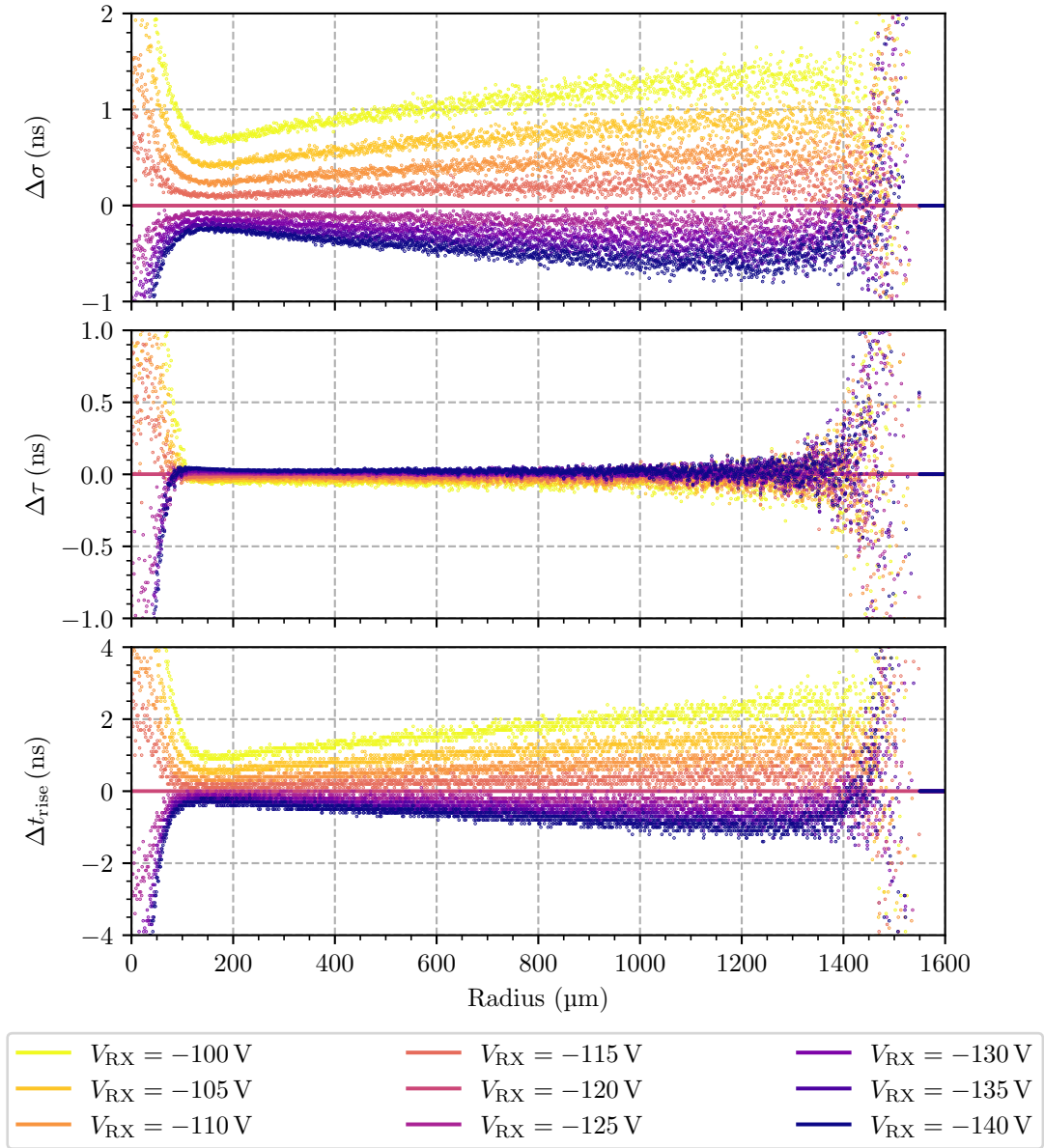


Figure 6.23: **Change of the Signal Pulses due to the Variation of the Outermost Drift Ring (RX) Voltage**

The signal pulses generated in the simulated drift of the charge carriers were compared for different field configurations in which the outermost drift ring **RX** voltage V_{RX} was varied. Decreasing V_{RX} to more negative voltages, shifts the origin of the transport trough nearer towards the back contact electrode which results in a steeper gradient between the drift rings **R1** and **RX**. This over-depletion reduces the drift time for all charge clouds but also leads to charge loss in the center region of the pixel. If V_{RX} is increased to more positive voltages, the saddle point is positioned closer to the drift ring structure on the readout side of the detector pixel. This leads to a shallower gradient between the drift rings **R1** and the **RX** and thus to longer drift times. Moreover, the time constants follow the distribution of the drift time for all variations of V_{RX} in the complete pixel.

Conclusions

The [Karlsruhe Tritium Neutrino \(KATRIN\)](#) experiment is designed to measure the effective electron antineutrino mass using the tritium β -decay with an unprecedented precision. After the neutrino mass measurements have been completed, the [KATRIN](#) experiment will be modified to search for sterile neutrinos on the keV-mass scale. These particles are a minimal extension to the [Standard Model \(SM\)](#) of particle physics and are a promising [Dark Matter \(DM\)](#) candidate. In particular, since the detector currently installed in the experiment is not capable of handling the expected high rates, a novel detector and readout system is currently being developed, the [TRISTAN](#) detector. It features an excellent energy resolution and has the capability of handling high count rates. The detectors make use of the [Silicon Drift Detector \(SDD\)](#) technology whose unique feature is the extremely low anode capacitance which allows for high-precision electron spectroscopy. The ultimate noise performance is achieved with a [Junction-gate Field-Effect Transistor \(JFET\)](#) that is directly integrated into every detector pixel.

The precise understanding of the detector response to incident radiation, particularly electrons, is one of the key elements to search for sterile neutrinos. To this end, the main goal of this thesis was to investigate the effects of detector timing with respect to the drift of the electron charge cloud in the [SDD](#), the influence of the integrated [JFET](#) on the charge collection properties, and the impact of charge sharing at the boundary between adjacent pixels. A dedicated experimental setup consisting of a laser and corresponding optics was designed to scan the surface of a 7 pixel [TRISTAN SDD](#) with a monochromatic photon beam. To extract the parameters of interest, an empirical model was developed to compare the signals generated at each position of the detector in the scans.

In a first step, timing effects of the incident radiation in the detector were investigated. The analysis revealed that the geometry of the detector pixels has a substantial influence on the drift of the charge carriers. By reconstructing the drift times of the electron charge clouds, it was found that the drift of the charge carriers is determined by the arrangement of the drift rings of the individual detector pixels.

Due to the hexagonal structure of the drift rings, differences in the duration of the charge cloud drift were observed. Since a linear relation could be obtained between the drift time and the distance to the detector anode, the drift time is a well-suited parameter to describe the radial dependence of the charge cloud drift in the **TRISTAN SDD** pixels. Moreover, the influence of diffusion on the charge cloud was reflected in the broadening of the signals, which correlated with the drift time of the cloud. Consequently, the signals could provide information about the location of a particle's interaction in the detector.

As a second effect, the charge collection in the region of the integrated **JFET** was studied. To prevent electrons from drifting to the most positive electrode of the **SDD**, the drain electrode of the transistor, the **Inner Guard Ring (IGR)** is placed between the **JFET** and the anode to create a potential barrier that shields the **JFET** from the bulk. Prior to the investigations in the scope of this thesis, a too positive voltage applied to the **IGR** electrode caused electrons to surpass this barrier and be collected by the drain electrode. This resulted in a charge loss of $\sim 4\%$ in the center region of the pixels. This caused the measured energy to no longer correspond to the deposited energy and led to distortions in the energy spectrum. One of the main results of this thesis was the definition of a new operating point for the **IGR** voltage. By decreasing the voltage applied to the **IGR** contact to more negative values, the barrier strength will be increased and the conditions for complete charge collection restored.

In the third step, the effect of charge sharing at the boundary of three adjacent pixels was analyzed. Energy deposited there is shared between these three **SDD** pixels which are in contact with each other. This effect was utilized to obtain an upper limit on the size of the electron charge cloud of $(16.3 \pm 0.2) \mu\text{m}$ which will be used as an input parameter in the tritium model. In addition, the comparison of signals of regular and charge sharing events has shown that the presence of a saddle point in the electric potential results in significantly longer signal rise times. While the signal rise times of the regular events were consistent with the expectation of $\mathcal{O}(30 \text{ ns})$, an increase to $\mathcal{O}(100 \text{ ns})$ was observed for charge sharing events directly at the boundaries.

The experimental results were verified in simulations of the electric potential and the drift of the charge carriers in a **TRISTAN SDD** pixel. It was shown that the simulation of the field and the charge cloud drift is in good agreement with the experimental results. The observed charge loss in the transistor region could be reproduced with high accuracy. The simulated size of the charge cloud of $(15.1 \pm 0.1) \mu\text{m}$ was slightly lower than the measured value. This can be most likely attributed to the laser beam which was not perfectly focused. Moreover, the charge clouds showed the same drift time distribution in both, the experiment and the simulation. Furthermore, the effects of applying different bias voltages to the detector on the drift of the charge carriers was investigated. It was demonstrated that the combination of the correct bias voltages is mandatory to ensure optimal working conditions for the **TRISTAN SDDs**. In particular, it was shown that a proper balance between the voltages applied to the **IGR** and the **R1** electrodes is required for complete charge collection.

In conclusion, scanning the surface of a [TRISTAN SDD](#) with a laser system allowed for a detailed investigation of the drift of the charge carriers in the detector pixels and at their boundaries. For the first time, the properties of the [IGR](#) to shield the integrated [JFET](#) were studied and its effectiveness was presented. The experimental results were verified by simulations of the field distribution and the drift of the charge carriers in a [TRISTAN](#) detector pixel. As a result, this thesis lays the foundation for the event discrimination based on precise signal timing as well as provide an upper limit on the charge cloud size for the model of the detector response in the keV-scale sterile neutrino search.

Appendix

A.1 Laser Stability

As discussed in section 5.2, the stability of the laser with respect to the average output power per pulse is an important requirement for the averaging procedure of the waveform snippets. Figure A.1 shows the reconstructed energy for each laser pulse at a single exemplary grid position. It can be seen that the laser power fluctuates around the weighted mean of the distribution and is spread with the standard deviation σ . Assuming the energy of the laser pulses is Poisson distributed, the expected standard deviation σ_{expected} can be calculated as

$$\sigma_{\text{expected}} = w_{\text{Si}} \cdot \sqrt{\langle N \rangle}, \quad (\text{A.1})$$

where w_{Si} is the electron-hole pair creation energy in Si and $\langle N \rangle$ is the average number of created electron-hole pairs determined using equation 3.14. The observed and expected standard deviation were found to differ by $\sim 2\%$. Therefore, the procedure of waveform averaging is well-motivated and yields consistent results.

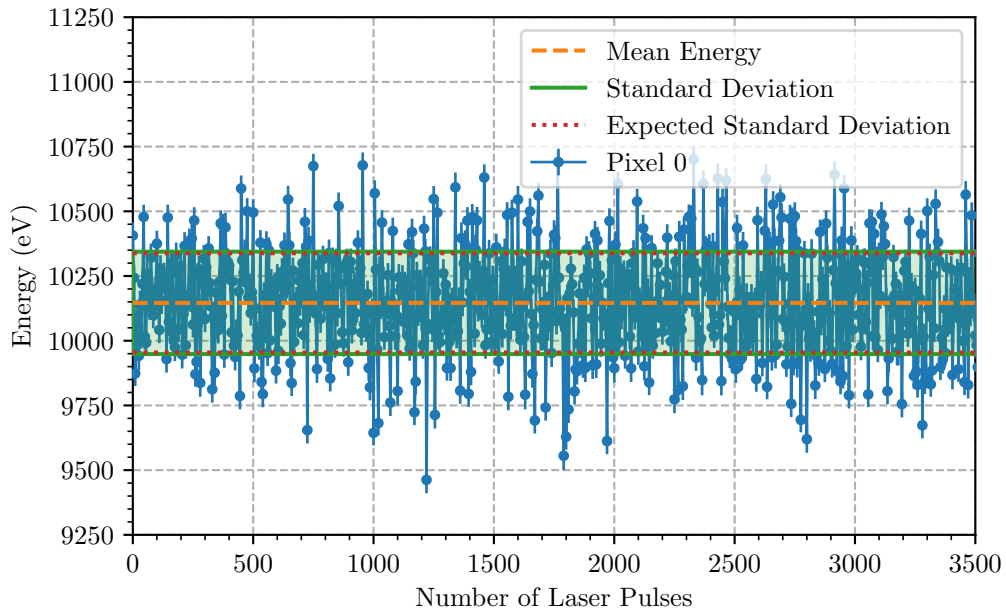


Figure A.1: **Exemplary Reconstructed Energy per Laser Pulse**

The reconstructed energy is shown for each laser pulse at a single exemplary grid position. In this configuration, the laser was positioned above the central [SDD](#) pixel. The energy of the pulses fluctuates around the weighted mean indicated by the orange dashed line. The standard deviation of the distribution depicted by the green band and the expected standard deviation illustrated by the red dotted lines were found to differ by $\sim 2\%$. Therefore, the procedure of waveform averaging is well-motivated and yields consistent results.

Acronyms

$0\nu\beta\beta$	neutrinoless double β -decay
$2\nu\beta\beta$	two-neutrino double β -decay
ν MSM	Neutrino Minimal Standard Model
LHe	Liquid Helium
LN ₂	Liquid Nitrogen
LNe	Liquid Neon
Si	Silicon
ADC	Analog-to-Digital Converter
AGS	Alternating Gradient Synchrotron
ASIC	Application-Specific Integrated Circuit
BAO	Baryonic Acoustic Oscillations
BBN	Big Bang Nucleosynthesis
BC	Back Contact
BCs	Boundary Conditions
BEST	Baksan Experiment on Sterile Transitions
BF	Back Frame
Borexino	Borexino Experiment
BW	Bandwidth
CDM	Cold Dark Matter
CMB	Cosmic Microwave Background
CMOS	Complementary Metal-Oxide-Semiconductor
CMS	Calibration and Monitoring System
CP	Charge conjugation Parity
CPS	Cryogenic Pumping Section
CRES	Cyclotron Radiation Emission Spectroscopy
CSA	Charge Sensitive Pre-Amplifier
DAQ	Data Acquisition System

DM	Dark Matter
DONUT	Direct observation of the nu tau
DPP	Digital Pulse Processor
DPS	Differential Pumping Section
e-gun	Electron Gun
EC	Electron Capture
ECHo	Electron Capture in ^{163}Ho Experiment
EMI	Electromagnetic Interference
FBM	Forward Beam Monitor
FEM	Finite Element Method
FPD	Focal Plane Detector
FPGA	Field-Programmable Gate Array
FWHM	Full Width at Half Maximum
GALLEX	Gallium Experiment
GERDA	Germanium Detector Array
GNO	Gallium Neutrino Observatory
GUT	Grand Unified Theory
HDM	Hot Dark Matter
HLL	Halbleiterlabor
HOLMES	The Electron Capture Decay of ^{163}Ho Experiment
HV	High Voltage
IBD	Inverse Beta Decay
IGR	Inner Guard Ring
IO	Inverted Ordering
IPE	Institute for Data Processing and Electronics
ITR	Intrinsic Time Resolution
JFET	Junction-gate Field-Effect Transistor
KATRIN	Karlsruhe Tritium Neutrino
KIT	Karlsruhe Institute of Technology
LARA	Laser Raman
LEGEND	Large Enriched Germanium Experiment for Neutrinoless $\beta\beta$ Decay
LEP	Large Electron-Positron
LNGS	Laboratori Nazionali del Gran Sasso
LSND	Liquid Scintillator Neutrino Detector
MAC-E	Magnetic Adiabatic Collimation combined with an Electrostatic filter
MAJORANA	MAJORANA Neutrinoless Double-beta Decay Experiment
MiniBooNE	Mini Booster Neutrino Experiment
MMC	Metallic Magnetic Calorimeter

MoS	Monitor Spectrometer
NO	Normal Ordering
op amp	operational amplifier
PAE	Post Acceleration Electrode
PCB	Printed Circuit Board
PDE	Partial Differential Equation
PIN	Positive-Intrinsic-Negative
PMNS	Pontecorvo-Maki-Nakagawa-Sakata
PMT	Photo Multiplier Tube
PWM	Pulse Width Modulation
QE	Quantum Efficiency
R1	Ring 1
RD	Reset Diode
RS	Rear Section
RW	Rear Wall
RX	Ring X
SAGE	Soviet–American Gallium Experiment
SDD	Silicon Drift Detector
SM	Standard Model
SNO	Sudbury Neutrino Observatory
SSM	Standard Solar Model
TES	Transition-Edge Sensor
TLK	Tritium Laboratory Karlsruhe
TMP	Turbo Molecular Pump
TRISTAN	Tritium Investigations on Sterile to Active Neutrino mixing
UHV	Ultra-High Vacuum
VEV	Vacuum Expectation Value
VOA	Variable Optical Attenuator
WDM	Warm Dark Matter
WGTS	Windowless Gaseous Tritium Source
WIMPS	Weakly Interacting Massive Particles
XHV	Extreme-High Vacuum
XMM	X-ray Multi-Mirror

List of Figures

1.1	Three Generations of Matter in the ν MSM	6
1.2	Comparison of the Fermion Masses	8
2.1	Tritium β -Decay Spectrum and Endpoint Region	14
2.2	Schematic Drawing of the KATRIN Main Spectrometer	15
2.3	Experimental Setup of the KATRIN Experiment	17
2.4	Tritium β -decay Spectrum with Sterile Neutrino Admixture	21
2.5	TRISTAN Detector Module with 166 Pixels	22
2.6	Experimental Setup of the TRISTAN Detector for Phase 1	23
3.1	Concept of Valence and Conduction Band in Semiconductors	26
3.2	Processes at a p-n Junction	28
3.3	Reverse Biasing of a p ⁺ -n Junction	30
3.4	Schematic Drawing of a TRISTAN Detector Pixel using the SDD Technology	32
3.5	Wireframe of the Simulated Electric Potential in a TRISTAN SDD Pixel	33
3.6	Images of a 7 Pixel TRISTAN SDD	35
3.7	Weighting Potential for different two Electrode Configurations	39
3.8	Equivalent Circuit of the Readout Chain of a TRISTAN SDD Pixel	41
3.9	ETTORE ASIC mounted on a TRISTAN Detector PCB	42
3.10	Block Diagram of the TRISTAN Detector and Readout System	43
4.1	Experimental Setup of the Detector Calibration	46
4.2	Signal Evaluation with trapezoidal Filters	47
4.3	Calibration Spectrum of the Central SDD Pixel	48
4.4	Calibrated ⁵⁵ Fe Spectrum of all SDD Pixels	49
4.5	Energy Resolution of all Detector Pixels as a Function of the Peaking Time of the Energy Filter	50
4.6	Microscope Images of the Webcam Sensor	52
4.7	Experimental Setup for the Optimization of the Laser System	53
4.8	Smallest Laser Beam Spot and Multivariate Gaussian Reconstruction	54
4.9	Distribution of the Laser Beam Width for different Distances	55

5.1	Experimental Setup for the Detector Characterization Measurements	58
5.2	Illustration of the Grid for the Laser Scan	59
5.3	Exemplary Waveform Output of the 7 Pixel TRISTAN SDD	60
5.4	Model Parameter: Amplitude A	62
5.5	Model Parameter: Drift Time t_{drift}	63
5.6	Model Parameter: Gaussian Width σ	64
5.7	Model Parameter: Exponential Rise Time τ	65
5.8	Complete Model of the Signal Shape	66
5.9	Signal Pulses for different (10 - 90)% Rise Times	67
5.10	Averaging Procedure of the Waveform Snippets	68
5.11	Exemplary Fit of a Signal Pulse	69
5.12	Measured Energy Spectrum of a 7 Pixel TRISTAN SDD	71
5.13	Reconstructed Energy at the Region of a SDD Triple Point	72
5.14	Exemplary Charge Cloud Distribution between Pixels 0 and 2	73
5.15	Reconstructed Energy in the Central SDD Pixel	74
5.16	Measured Drift Time Distribution of a 7 Pixel TRISTAN SDD	76
5.17	Drift Time of Charge Clouds in the Central SDD Pixel	77
5.18	Distribution of the Drift Time of Charge Clouds in the Central SDD Pixel	78
5.19	Measured Drift Time Distribution at a Triple Point Region	79
5.20	Distribution of the Gaussian Width of the Signal Pulses of a 7 Pixel TRISTAN SDD	81
5.21	Correlation of the Drift Time and the Gaussian Width in the Central SDD Pixel	82
5.22	Gaussian Width of the Signal Pulses in the Central SDD Pixel	83
5.23	Distribution of the Exponential Rise Time of the Signal Pulses of a 7 Pixel TRISTAN SDD	84
5.24	Exponential Rise Time of the Signal Pulses in the Central SDD Pixel	85
5.25	Distribution of the Signal Rise Time of a 7 Pixel TRISTAN SDD	86
5.26	Distribution of the Signal Rise Time at a Triple Point Region	87
5.27	Rise Time of the Signal Pulses in the Central SDD Pixel	88
6.1	Simulation of the Electric Potential in a TRISTAN SDD Pixel	90
6.2	Electric Potential in the Center Region of a TRISTAN SDD Pixel	91
6.3	Simulation of the Weighting Potential in a TRISTAN SDD Pixel	92
6.4	Simulation of the Electric Field in a TRISTAN SDD Pixel	93
6.5	Electric Field in the Center Region of a TRISTAN SDD Pixel	94
6.6	Spreading of the Electron Charge Cloud due to Diffusion	97
6.7	Expansion of the Electron Charge Cloud due to Self-Repulsion	98
6.8	Simulated Drift of the Electron Charge Cloud in a TRISTAN SDD Pixel	103
6.9	Produced Signal Pulses in the Simulation of the Charge Cloud Drift	104
6.10	Simulation of the Laser Pulse	106
6.11	Comparison of the Gaussian Width of the Experimental and Simulated Signal Pulses	107

6.12	Magnitude-Normalized Bessel Filter Frequency Response for different Bessel Filter Rise Times	108
6.13	Comparison of the Rise Time of the Experimental and Simulated Signal Pulses	109
6.14	Comparison of the Exponential Rise Time of the Experimental and Simulated Signal Pulses	110
6.15	Exemplary Processing of the Simulated Signal Pulses	111
6.16	Normalized Reconstructed Energy of the Experimental and Simulated Signal Pulses	112
6.17	Simulated Charge Cloud Distribution between adjacent Pixels	113
6.18	Comparison of the Drift Time of Charge Clouds in the Experiment and Simulation	114
6.19	Change of the Signal Pulses due to the Variation of the Energy of the Incident Radiation	117
6.20	Change of the Signal Pulses due to the Variation of the Back Contact Voltage	120
6.21	Change of the Signal Pulses due to the Variation of the Inner Guard Ring Voltage	123
6.22	Change of the Signal Pulses due to the Variation of the Innermost Drift Ring (R1) Voltage	126
6.23	Change of the Signal Pulses due to the Variation of the Outermost Drift Ring (RX) Voltage	129
A.1	Exemplary Reconstructed Energy per Laser Pulse	136

List of Tables

1.1	Overview of Neutrino Oscillation Parameters	5
3.1	Nomenclature for the 7 Pixels of a TRISTAN SDD	34
3.2	Operating Ranges of the Detector Bias Voltages	36
3.3	Characteristics of the CSA Circuit	42
4.1	External Bias Voltages for the Operation of the Detector	46
6.1	Boundary Conditions for the Simulation of the Electric Potential	95
6.2	Parameters for the Simulation of the Drift of the Charge Carriers	99

Bibliography

- [1] M. G. Aartsen et al. “Combined sensitivity to the neutrino mass ordering with JUNO, the IceCube Upgrade, and PINGU”. In: *Phys. Rev. D* 101 (3 Feb. 2020), p. 032006. DOI: [10.1103/PhysRevD.101.032006](https://doi.org/10.1103/PhysRevD.101.032006).
- [2] M. G. Aartsen et al. “Determining neutrino oscillation parameters from atmospheric muon neutrino disappearance with three years of IceCube DeepCore data”. In: *Phys. Rev. D* 91 (7 Apr. 2015), p. 072004. DOI: [10.1103/PhysRevD.91.072004](https://doi.org/10.1103/PhysRevD.91.072004).
- [3] K. N. Abazajian et al. *Light Sterile Neutrinos: A White Paper*. 2012. DOI: [10.48550/ARXIV.1204.5379](https://doi.org/10.48550/ARXIV.1204.5379).
- [4] A. I. Abazov et al. “Search for neutrinos from the Sun using the reaction $^{71}\text{Ga}(\nu_e, e^-)^{71}\text{Ge}$ ”. In: *Phys. Rev. Lett.* 67 (24 Dec. 1991), pp. 3332–3335. DOI: [10.1103/PhysRevLett.67.3332](https://doi.org/10.1103/PhysRevLett.67.3332).
- [5] J. N. Abdurashitov. “Solar neutrino flux measurements by the Soviet-American gallium experiment (SAGE) for half the 22-year solar cycle”. In: *Journal of Experimental and Theoretical Physics* 95.2 (Aug. 2002), pp. 181–193. ISSN: 1090-6509. DOI: [10.1134/1.1506424](https://doi.org/10.1134/1.1506424).
- [6] J. N. Abdurashitov et al. “The Russian-American Gallium Experiment (SAGE) Cr Neutrino Source Measurement”. In: *Phys. Rev. Lett.* 77 (23 Dec. 1996), pp. 4708–4711. DOI: [10.1103/PhysRevLett.77.4708](https://doi.org/10.1103/PhysRevLett.77.4708).
- [7] K. Abe et al. “Solar neutrino results in Super-Kamiokande-III”. In: *Phys. Rev. D* 83 (5 Mar. 2011), p. 052010. DOI: [10.1103/PhysRevD.83.052010](https://doi.org/10.1103/PhysRevD.83.052010).
- [8] K. Abe et al. “Constraint on the matter–antimatter symmetry-violating phase in neutrino oscillations”. In: *Nature* 580.7803 (Apr. 2020), pp. 339–344. ISSN: 1476-4687. DOI: [10.1038/s41586-020-2177-0](https://doi.org/10.1038/s41586-020-2177-0).
- [9] N. Abgrall et al. “The large enriched germanium experiment for neutrinoless double beta decay (LEGEND)”. In: *AIP Conference Proceedings* 1894.1 (2017), p. 020027. DOI: [10.1063/1.5007652](https://doi.org/10.1063/1.5007652).
- [10] P. A. R. Ade et al. “Planck 2015 results - XIII. Cosmological parameters”. In: *Astronomy & Astrophysics* 594 (2016), A13. DOI: [10.1051/0004-6361/201525830](https://doi.org/10.1051/0004-6361/201525830).

- [11] R. Adhikari et al. “A White Paper on keV sterile neutrino Dark Matter”. In: *Journal of Cosmology and Astroparticle Physics* 2017.01 (Jan. 2017), pp. 025–025. DOI: [10.1088/1475-7516/2017/01/025](https://doi.org/10.1088/1475-7516/2017/01/025).
- [12] M. N. Afsar and K. J. Button. “Precise Millimeter-Wave Measurements of Complex Refractive Index, Complex Dielectric Permittivity and Loss Tangent of GaAs, Si, SiO₂, Al₂O₃, BeO, Macor, and Glass”. In: *IEEE Transactions on Microwave Theory and Techniques* 31.2 (1983), pp. 217–223. DOI: [10.1109/TMTT.1983.1131460](https://doi.org/10.1109/TMTT.1983.1131460).
- [13] S. Agostinelli et al. “Geant4—a simulation toolkit”. In: *Nuclear Instruments and Methods in Physics Research Section A: Accelerators, Spectrometers, Detectors and Associated Equipment* 506.3 (2003), pp. 250–303. ISSN: 0168-9002. DOI: [10.1016/S0168-9002\(03\)01368-8](https://doi.org/10.1016/S0168-9002(03)01368-8).
- [14] M. Agostini et al. “Final Results of GERDA on the Search for Neutrinoless Double- β Decay”. In: *Phys. Rev. Lett.* 125 (25 Dec. 2020), p. 252502. DOI: [10.1103/PhysRevLett.125.252502](https://doi.org/10.1103/PhysRevLett.125.252502).
- [15] A. Aguilar et al. “Evidence for neutrino oscillations from the observation of $\bar{\nu}_e$ appearance in a $\bar{\nu}_\mu$ beam”. In: *Phys. Rev. D* 64 (11 Nov. 2001), p. 112007. DOI: [10.1103/PhysRevD.64.112007](https://doi.org/10.1103/PhysRevD.64.112007).
- [16] A. A. Aguilar-Arevalo et al. “Significant Excess of Electronlike Events in the MiniBooNE Short-Baseline Neutrino Experiment”. In: *Phys. Rev. Lett.* 121 (22 Nov. 2018), p. 221801. DOI: [10.1103/PhysRevLett.121.221801](https://doi.org/10.1103/PhysRevLett.121.221801).
- [17] Q. R. Ahmad et al. “Measurement of the Rate of $\nu_e + d \rightarrow p + p + e^-$ Interactions Produced by ^8B Solar Neutrinos at the Sudbury Neutrino Observatory”. In: *Phys. Rev. Lett.* 87 (7 July 2001), p. 071301. DOI: [10.1103/PhysRevLett.87.071301](https://doi.org/10.1103/PhysRevLett.87.071301).
- [18] M. Aker. “Improved Upper Limit on the Neutrino Mass from a Direct Kinematic Method by KATRIN”. In: *Phys. Rev. Lett.* 123 (22 Nov. 2019), p. 221802. DOI: [10.1103/PhysRevLett.123.221802](https://doi.org/10.1103/PhysRevLett.123.221802).
- [19] M. Aker et al. “Direct neutrino-mass measurement with sub-electronvolt sensitivity”. In: *Nature Physics* 18.2 (Feb. 2022), pp. 160–166. ISSN: 1745-2481. DOI: [10.1038/s41567-021-01463-1](https://doi.org/10.1038/s41567-021-01463-1).
- [20] M. Aker et al. “First operation of the KATRIN experiment with tritium”. In: *The European Physical Journal C* 80.3 (Mar. 2020), p. 264. ISSN: 1434-6052. DOI: [10.1140/epjc/s10052-020-7718-z](https://doi.org/10.1140/epjc/s10052-020-7718-z).
- [21] M. Aker et al. “Improved eV-scale sterile-neutrino constraints from the second KATRIN measurement campaign”. In: *Phys. Rev. D* 105 (7 Apr. 2022), p. 072004. DOI: [10.1103/PhysRevD.105.072004](https://doi.org/10.1103/PhysRevD.105.072004).
- [22] R. C. Alig et al. “Scattering by ionization and phonon emission in semiconductors”. In: *Phys. Rev. B* 22 (12 Dec. 1980), pp. 5565–5582. DOI: [10.1103/PhysRevB.22.5565](https://doi.org/10.1103/PhysRevB.22.5565).
- [23] G. Alimonti et al. “The Borexino detector at the Laboratori Nazionali del Gran Sasso”. In: *Nuclear Instruments and Methods in Physics Research Section A: Accelerators, Spectrometers, Detectors and Associated Equipment* 600.3 (2009), pp. 568–593. ISSN: 0168-9002. DOI: [10.1016/j.nima.2008.11.076](https://doi.org/10.1016/j.nima.2008.11.076).

- [24] J. Allison et al. “Geant4 developments and applications”. In: *IEEE Transactions on Nuclear Science* 53.1 (2006), pp. 270–278. DOI: [10.1109/TNS.2006.869826](https://doi.org/10.1109/TNS.2006.869826).
- [25] J. Allison et al. “Recent developments in Geant4”. In: *Nuclear Instruments and Methods in Physics Research Section A: Accelerators, Spectrometers, Detectors and Associated Equipment* 835 (2016), pp. 186–225. ISSN: 0168-9002. DOI: [10.1016/j.nima.2016.06.125](https://doi.org/10.1016/j.nima.2016.06.125).
- [26] M. Altmann et al. “Complete results for five years of GNO solar neutrino observations”. In: *Physics Letters B* 616.3 (2005), pp. 174–190. ISSN: 0370-2693. DOI: [10.1016/j.physletb.2005.04.068](https://doi.org/10.1016/j.physletb.2005.04.068).
- [27] J.F. Amsbaugh et al. “Focal-plane detector system for the KATRIN experiment”. In: *Nuclear Instruments and Methods in Physics Research Section A: Accelerators, Spectrometers, Detectors and Associated Equipment* 778 (2015), pp. 40–60. ISSN: 0168-9002. DOI: [10.1016/j.nima.2014.12.116](https://doi.org/10.1016/j.nima.2014.12.116).
- [28] P. Anselmann et al. “GALLEX solar neutrino observations: complete results for GALLEX II”. In: *Physics Letters B* 357.1 (1995), pp. 237–247. ISSN: 0370-2693. DOI: [10.1016/0370-2693\(95\)00897-T](https://doi.org/10.1016/0370-2693(95)00897-T).
- [29] M. Arenz et al. “First transmission of electrons and ions through the KATRIN beamline”. In: *Journal of Instrumentation* 13.04 (Apr. 2018), P04020. DOI: [10.1088/1748-0221/13/04/P04020](https://doi.org/10.1088/1748-0221/13/04/P04020).
- [30] C. Arpesella et al. “First real time detection of ^7Be solar neutrinos by Borexino”. In: *Physics Letters B* 658.4 (2008), pp. 101–108. ISSN: 0370-2693. DOI: [10.1016/j.physletb.2007.09.054](https://doi.org/10.1016/j.physletb.2007.09.054).
- [31] T. Asaka and M. Shaposhnikov. “The νMSM , dark matter and baryon asymmetry of the universe”. In: *Physics Letters B* 620.1 (2005), pp. 17–26. ISSN: 0370-2693. DOI: [10.1016/j.physletb.2005.06.020](https://doi.org/10.1016/j.physletb.2005.06.020).
- [32] V. N. Aseev et al. “Upper limit on the electron antineutrino mass from the Troitsk experiment”. In: *Phys. Rev. D* 84 (11 Dec. 2011), p. 112003. DOI: [10.1103/PhysRevD.84.112003](https://doi.org/10.1103/PhysRevD.84.112003).
- [33] J. N. Bahcall et al. “Present Status of the Theoretical Predictions for the ^{37}Cl Solar-Neutrino Experiment”. In: *Phys. Rev. Lett.* 20 (21 May 1968), pp. 1209–1212. DOI: [10.1103/PhysRevLett.20.1209](https://doi.org/10.1103/PhysRevLett.20.1209).
- [34] V. V. Barinov et al. “Search for electron-neutrino transitions to sterile states in the BEST experiment”. In: *Phys. Rev. C* 105 (6 June 2022), p. 065502. DOI: [10.1103/PhysRevC.105.065502](https://doi.org/10.1103/PhysRevC.105.065502).
- [35] M. Bauer and T. Plehn. *Yet Another Introduction to Dark Matter*. Springer, 2019. DOI: [10.1007/978-3-030-16234-4](https://doi.org/10.1007/978-3-030-16234-4).
- [36] B. E. Bayer. “Color imaging array”. US3971065A. Mar. 1975. URL: <https://patents.google.com/patent/US3971065A>.
- [37] J. Becker et al. “Measurements of charge carrier mobilities and drift velocity saturation in bulk silicon of $\langle 111 \rangle$ and $\langle 100 \rangle$ crystal orientation at high electric fields”. In: *Solid-State Electronics* 56.1 (2011), pp. 104–110. ISSN: 0038-1101. DOI: [10.1016/j.sse.2010.10.009](https://doi.org/10.1016/j.sse.2010.10.009).

- [38] G Bellini et al. “Precision Measurement of the ^7Be Solar Neutrino Interaction Rate in Borexino”. In: *Phys. Rev. Lett.* 107 (14 Sept. 2011), p. 141302. DOI: [10.1103/PhysRevLett.107.141302](https://doi.org/10.1103/PhysRevLett.107.141302).
- [39] F. Bezrukov. “ νMSM and its experimental tests”. In: *Journal of Physics: Conference Series* 110.8 (May 2008), p. 082002. DOI: [10.1088/1742-6596/110/8/082002](https://doi.org/10.1088/1742-6596/110/8/082002).
- [40] R. Bisognin. “Caratterizzazione sperimentale dell’elettronica di front-end per l’esperimento TRISTAN”. MA thesis. Politecnico di Milano, 2018. URL: <http://hdl.handle.net/10589/141721>.
- [41] A. Boyarsky et al. “Unidentified Line in X-Ray Spectra of the Andromeda Galaxy and Perseus Galaxy Cluster”. In: *Phys. Rev. Lett.* 113 (25 Dec. 2014), p. 251301. DOI: [10.1103/PhysRevLett.113.251301](https://doi.org/10.1103/PhysRevLett.113.251301).
- [42] S. Boyd. *Neutrino Mass and Direct Measurements*. The University of Warwick, Mar. 2004. URL: https://warwick.ac.uk/fac/sci/physics/staff/academic/boyd/stuff/neutrinolectures/lec_neutrinomass_writeup.pdf.
- [43] G. Bradski. “The OpenCV Library”. In: *Dr. Dobb’s Journal of Software Tools* 25 (11 Nov. 2000), pp. 120–123. URL: <https://drdobbs.com/open-source/the-opencv-library/184404319>.
- [44] C. Bruch. “Characterisation of a 166-Pixel TRISTAN Detector Module in the KATRIN Monitor Spectrometer”. MA thesis. Technische Universität München, 2023. URL: https://www.ph.nat.tum.de/fileadmin/w00bya/neutrinos/Thesis/Master/TRISTAN_Bruch_Christina_23.pdf.
- [45] C. Bruch. “Investigation of the noise performance of silicon drift detectors for the TRISTAN project”. Technische Universität München, 2020. URL: https://www.ph.nat.tum.de/fileadmin/w00bya/neutrinos/Thesis/Bachelor/TRISTAN_Bruch_Christina_20.pdf.
- [46] E. Bulbul et al. “Detection of an unidentified emission line in the stacked x-ray spectrum of galaxy clusters”. In: *The Astrophysical Journal* 789.1 (June 2014), p. 13. DOI: [10.1088/0004-637X/789/1/13](https://doi.org/10.1088/0004-637X/789/1/13).
- [47] J. Chadwick. “Intensitätsverteilung im magnetischen Spectrum der β -Strahlen von Radium B + C”. In: *Verhandl. Dtsch. Phys. Ges.* 16 (1914), p. 383. URL: <http://cds.cern.ch/record/262756>.
- [48] Robert Cimrman, Vladimír Lukeš, and Eduard Rohan. “Multiscale finite element calculations in Python using SfePy”. In: *Advances in Computational Mathematics* (2019). ISSN: 1572-9044. DOI: [10.1007/s10444-019-09666-0](https://doi.org/10.1007/s10444-019-09666-0).
- [49] KATRIN Collaboration. *KATRIN design report 2004*. Tech. rep. 51.54.01; LK 01. Forschungszentrum Jülich, 2005. 245 pp. DOI: [10.5445/IR/270060419](https://doi.org/10.5445/IR/270060419).
- [50] LEP Collaborations. “Precision electroweak measurements on the Z resonance”. In: *Physics Reports* 427.5 (2006), pp. 257–454. ISSN: 0370-1573. DOI: [10.1016/j.physrep.2005.12.006](https://doi.org/10.1016/j.physrep.2005.12.006).
- [51] C. L. Cowan et al. “Detection of the Free Neutrino: a Confirmation”. In: *Science* 124.3212 (1956), pp. 103–104. ISSN: 0036-8075. DOI: [10.1126/science.124.3212.103](https://doi.org/10.1126/science.124.3212.103).
- [52] G. Danby et al. “Observation of High-Energy Neutrino Reactions and the Existence of Two Kinds of Neutrinos”. In: *Phys. Rev. Lett.* 9 (1 July 1962), pp. 36–44. DOI: [10.1103/PhysRevLett.9.36](https://doi.org/10.1103/PhysRevLett.9.36).

- [53] R. Davis et al. “Search for Neutrinos from the Sun”. In: *Phys. Rev. Lett.* 20 (21 May 1968), pp. 1205–1209. DOI: [10.1103/PhysRevLett.20.1205](https://doi.org/10.1103/PhysRevLett.20.1205).
- [54] M. Descher. “High rate systematic effects for keV sterile neutrino searches at KATRIN”. MA thesis. Karlsruhe Institute of Technology, June 2019. URL: <https://www.katrin.kit.edu/publikationen/mth-descher.pdf>.
- [55] F. J. Dijksterhuis. *Lenses and Waves*. Springer, 2004. ISBN: 978-1-4020-2698-0. DOI: [10.1007/1-4020-2698-8](https://doi.org/10.1007/1-4020-2698-8).
- [56] K. Dolde et al. “Impact of ADC non-linearities on the sensitivity to sterile keV neutrinos with a KATRIN-like experiment”. In: *Nuclear Instruments and Methods in Physics Research Section A: Accelerators, Spectrometers, Detectors and Associated Equipment* 848 (2017), pp. 127–136. ISSN: 0168-9002. DOI: [10.1016/j.nima.2016.12.015](https://doi.org/10.1016/j.nima.2016.12.015).
- [57] O. Dragoun and V. Drahoslav. “Constraints on the Active and Sterile Neutrino Masses from Beta-Ray Spectra: Past, Present and Future”. In: *Open Physics Journal* 3 (Sept. 2016), pp. 73–113. DOI: [10.2174/1874843001603010073](https://doi.org/10.2174/1874843001603010073).
- [58] E. Durand. *Electrostatique*. Masson, 1964. URL: https://archive.org/details/electrostatique0000dura_u0w3.
- [59] E. Ellinger et al. “Monitoring the KATRIN source properties within the beamline”. In: *Journal of Physics: Conference Series* 888.1 (Sept. 2017), p. 012229. DOI: [10.1088/1742-6596/888/1/012229](https://doi.org/10.1088/1742-6596/888/1/012229).
- [60] A. A. Esfahani et al. *The Project 8 Neutrino Mass Experiment*. 2022. DOI: [10.48550/ARXIV.2203.07349](https://doi.org/10.48550/ARXIV.2203.07349).
- [61] I. Esteban et al. “The fate of hints: updated global analysis of three-flavor neutrino oscillations”. In: *Journal of High Energy Physics* 2020.9 (Sept. 2020), p. 178. ISSN: 1029-8479. DOI: [10.1007/JHEP09\(2020\)178](https://doi.org/10.1007/JHEP09(2020)178).
- [62] U. Fano. “Ionization Yield of Radiations. II. The Fluctuations of the Number of Ions”. In: *Phys. Rev.* 72 (1 July 1947), pp. 26–29. DOI: [10.1103/PhysRev.72.26](https://doi.org/10.1103/PhysRev.72.26).
- [63] M. Faverzani et al. “Status of the HOLMES Experiment”. In: *Journal of Low Temperature Physics* 199.3 (May 2020), pp. 1098–1106. ISSN: 1573-7357. DOI: [10.1007/s10909-020-02385-7](https://doi.org/10.1007/s10909-020-02385-7).
- [64] E. Fermi. “Versuch einer Theorie der β -Strahlen. I”. In: *Zeitschrift für Physik* 88.3 (Mar. 1934), pp. 161–177. DOI: [10.1007/BF01351864](https://doi.org/10.1007/BF01351864).
- [65] A. Fick. “Über Diffusion”. In: *Annalen der Physik* 170.1 (1855), pp. 59–86. DOI: [10.1002/andp.18551700105](https://doi.org/10.1002/andp.18551700105).
- [66] C. Forstner. “Pulse Shape Analysis with the TRISTAN Silicon Drift Detector”. Technische Universität München, 2020. URL: https://www.ph.nat.tum.de/fileadmin/w00bya/neutrinos/Thesis/Bachelor/TRISTAN_Forstner_Christian_20.pdf.

- [67] Y. Fukuda et al. “Evidence for Oscillation of Atmospheric Neutrinos”. In: *Phys. Rev. Lett.* 81 (8 Aug. 1998), pp. 1562–1567. DOI: [10.1103/PhysRevLett.81.1562](https://doi.org/10.1103/PhysRevLett.81.1562).
- [68] W. H. Furry. “On Transition Probabilities in Double Beta-Disintegration”. In: *Phys. Rev.* 56 (12 Dec. 1939), pp. 1184–1193. DOI: [10.1103/PhysRev.56.1184](https://doi.org/10.1103/PhysRev.56.1184).
- [69] A. Gando et al. “Reactor on-off antineutrino measurement with KamLAND”. In: *Phys. Rev. D* 88 (3 Aug. 2013), p. 033001. DOI: [10.1103/PhysRevD.88.033001](https://doi.org/10.1103/PhysRevD.88.033001).
- [70] L. Gastaldo et al. “The electron capture in ^{163}Ho experiment - ECHO”. In: *The European Physical Journal Special Topics* 226.8 (June 2017), pp. 1623–1694. ISSN: 1951-6401. DOI: [10.1140/epjst/e2017-70071-y](https://doi.org/10.1140/epjst/e2017-70071-y).
- [71] E. Gatti and P. F. Manfredi. “Processing the signals from solid-state detectors in elementary-particle physics”. In: *La Rivista del Nuovo Cimento (1978-1999)* 9.1 (Jan. 1986), pp. 1–146. ISSN: 1826-9850. DOI: [10.1007/BF02822156](https://doi.org/10.1007/BF02822156).
- [72] E. Gatti and P. Rehak. “Semiconductor drift chamber - An application of a novel charge transport scheme”. In: *Nuclear Instruments and Methods in Physics Research* 225.3 (1984), pp. 608–614. ISSN: 0167-5087. DOI: [10.1016/0167-5087\(84\)90113-3](https://doi.org/10.1016/0167-5087(84)90113-3).
- [73] F. Glück et al. “Electromagnetic design of the large-volume air coil system of the KATRIN experiment”. In: *New Journal of Physics* 15.8 (Aug. 2013), p. 083025. DOI: [10.1088/1367-2630/15/8/083025](https://doi.org/10.1088/1367-2630/15/8/083025).
- [74] S. N. Gninenko et al. “Search for GeV-Scale Sterile Neutrinos Responsible for Active Neutrino Oscillations and Baryon Asymmetry of the Universe”. In: *Advances in High Energy Physics* 2012 (Dec. 2012), p. 718259. ISSN: 1687-7357. DOI: [10.1155/2012/718259](https://doi.org/10.1155/2012/718259).
- [75] M. Goepfert-Mayer. “Double Beta-Disintegration”. In: *Phys. Rev.* 48 (6 Sept. 1935), pp. 512–516. DOI: [10.1103/PhysRev.48.512](https://doi.org/10.1103/PhysRev.48.512).
- [76] M. Goldhaber et al. “Helicity of Neutrinos”. In: *Phys. Rev.* 109 (3 Feb. 1958), pp. 1015–1017. DOI: [10.1103/PhysRev.109.1015](https://doi.org/10.1103/PhysRev.109.1015).
- [77] M. A. Green and M. J. Keevers. “Optical properties of intrinsic silicon at 300 K”. In: *Progress in Photovoltaics: Research and Applications* 3.3 (1995), pp. 189–192. DOI: [10.1002/pip.4670030303](https://doi.org/10.1002/pip.4670030303).
- [78] TRISTAN group. *Conceptual Design Report: KATRIN with TRISTAN modules*. Tech. rep. Sept. 2021. URL: [https://www.katrin.kit.edu/downloads/TRISTAN__Technical_Design_Report%20\(10\).pdf](https://www.katrin.kit.edu/downloads/TRISTAN__Technical_Design_Report%20(10).pdf).
- [79] M. Gugiatti. “Development of a large-matrix SDD-based Radiation Detector for beta-Decay Spectroscopy in Neutrino Physics”. PhD thesis. Politecnico di Milano, 2022. URL: <https://hdl.handle.net/10589/189406>.
- [80] R. N. Hall. “Electron-Hole Recombination in Germanium”. In: *Phys. Rev.* 87 (2 July 1952), pp. 387–387. DOI: [10.1103/PhysRev.87.387](https://doi.org/10.1103/PhysRev.87.387).

- [81] W. Hampel et al. “Final results of the ^{51}Cr neutrino source experiments in GALLEX”. In: *Physics Letters B* 420.1 (1998), pp. 114–126. ISSN: 0370-2693. DOI: [10.1016/S0370-2693\(97\)01562-1](https://doi.org/10.1016/S0370-2693(97)01562-1).
- [82] K. Hugenberg. “Design of the electrode system for the KATRIN main spectrometer”. Westfälische Wilhelms-Universität Münster, Jan. 2008. URL: https://www.uni-muenster.de/Physik.KP/AGWeinheimer/theses/Diplom_Karen_Hugenberg.pdf.
- [83] T. Jeltema and S. Profumo. “Discovery of a 3.5 keV line in the Galactic Centre and a critical look at the origin of the line across astronomical targets”. In: *Monthly Notices of the Royal Astronomical Society* 450.2 (Apr. 2015), pp. 2143–2152. ISSN: 0035-8711. DOI: [10.1093/mnras/stv768](https://doi.org/10.1093/mnras/stv768).
- [84] H. Junde. “Nuclear Data Sheets for $A = 55$ ”. In: *Nuclear Data Sheets* 109.4 (2008), pp. 787–942. ISSN: 0090-3752. DOI: [10.1016/j.nds.2008.03.001](https://doi.org/10.1016/j.nds.2008.03.001).
- [85] K. Y. Kamal. “The Silicon Age: Trends in Semiconductor Devices Industry”. In: *Journal of Engineering Science and Technology Review* 15 (Oct. 2022), pp. 110–115. DOI: [10.25103/jestr.151.14](https://doi.org/10.25103/jestr.151.14).
- [86] R. Kimmel. “Demosaicing: image reconstruction from color CCD samples”. In: *IEEE Transactions on Image Processing* 8.9 (1999), pp. 1221–1228. DOI: [10.1109/83.784434](https://doi.org/10.1109/83.784434).
- [87] G. F. Knoll. *Radiation Detection and Measurement*. Wiley, 2010. ISBN: 9780470131480. URL: <https://www.wiley.com/en-us/Radiation+Detection+and+Measurement%2C+4th+Edition-p-9780470131480>.
- [88] K. Kodama et al. “Observation of tau neutrino interactions”. In: *Physics Letters B* 504.3 (2001), pp. 218–224. ISSN: 0370-2693. DOI: [10.1016/S0370-2693\(01\)00307-0](https://doi.org/10.1016/S0370-2693(01)00307-0).
- [89] C. Kraus et al. “Final results from phase II of the Mainz neutrino mass search in tritium β -decay”. In: *The European Physical Journal C - Particles and Fields* 40.4 (Apr. 2005), pp. 447–468. ISSN: 1434-6052. DOI: [10.1140/epjc/s2005-02139-7](https://doi.org/10.1140/epjc/s2005-02139-7).
- [90] P. Kruit and F. H. Read. “Magnetic field paralleliser for 2π electron-spectrometer and electron-image magnifier”. In: *Journal of Physics E: Scientific Instruments* 16.4 (Apr. 1983), p. 313. DOI: [10.1088/0022-3735/16/4/016](https://doi.org/10.1088/0022-3735/16/4/016).
- [91] M. Lebert. “Characterization of the Detector Response to Electrons and Test of a New Entrance Window Technology of Silicon Drift Detectors for the TRISTAN Project”. MA thesis. Technische Universität München, 2019. URL: https://www.ph.nat.tum.de/fileadmin/w00bya/neutrinos/Thesis/Master/TRISTAN_Lebert_Manuel_19.pdf.
- [92] P. Lechner. *TRISTAN SDD Simulation Plots*. Internal Discussion. Nov. 2022.
- [93] P. Lechner et al. “Silicon drift detectors for high count rate X-ray spectroscopy at room temperature”. In: *Nuclear Instruments and Methods in Physics Research Section A: Accelerators, Spectrometers, Detectors and Associated Equipment* 458.1 (2001). Proc. 11th Inbt. Workshop on Room Temperature Semiconductor X- and Gamma-Ray Detectors and Associated Electronics, pp. 281–287. ISSN: 0168-9002. DOI: [10.1016/S0168-9002\(00\)00872-X](https://doi.org/10.1016/S0168-9002(00)00872-X).

- [94] P. Lechner et al. “Silicon drift detectors for high resolution room temperature X-ray spectroscopy”. In: *Nuclear Instruments and Methods in Physics Research Section A: Accelerators, Spectrometers, Detectors and Associated Equipment* 377.2 (1996). Proceedings of the Seventh European Symposium on Semiconductor, pp. 346–351. ISSN: 0168-9002. DOI: [10.1016/0168-9002\(96\)00210-0](https://doi.org/10.1016/0168-9002(96)00210-0).
- [95] V.M. Lobashev and P.E. Spivak. “A method for measuring the electron antineutrino rest mass”. In: *Nuclear Instruments and Methods in Physics Research Section A: Accelerators, Spectrometers, Detectors and Associated Equipment* 240.2 (1985), pp. 305–310. ISSN: 0168-9002. DOI: [10.1016/0168-9002\(85\)90640-0](https://doi.org/10.1016/0168-9002(85)90640-0).
- [96] M. R. Lovell. “The haloes of bright satellite galaxies in a warm dark matter universe”. In: *Monthly Notices of the Royal Astronomical Society* 420.3 (Feb. 2012), pp. 2318–2324. ISSN: 0035-8711. DOI: [10.1111/j.1365-2966.2011.20200.x](https://doi.org/10.1111/j.1365-2966.2011.20200.x).
- [97] G. Lutz. *Semiconductor Radiation Detectors*. Springer, 2007. DOI: [10.1007/978-3-540-71679-2](https://doi.org/10.1007/978-3-540-71679-2).
- [98] S. Mertens et al. “A novel detector system for KATRIN to search for keV-scale sterile neutrinos”. In: *Journal of Physics G: Nuclear and Particle Physics* 46.6 (May 2019), p. 065203. DOI: [10.1088/1361-6471/ab12fe](https://doi.org/10.1088/1361-6471/ab12fe).
- [99] S. Mertens et al. “Characterization of silicon drift detectors with electrons for the TRISTAN project”. In: *Journal of Physics G: Nuclear and Particle Physics* 48.1 (Dec. 2020), p. 015008. DOI: [10.1088/1361-6471/abc2dc](https://doi.org/10.1088/1361-6471/abc2dc).
- [100] R. N. Mohapatra et al. “Neutrino Mass and Spontaneous Parity Nonconservation”. In: *Phys. Rev. Lett.* 44 (14 Apr. 1980), pp. 912–915. DOI: [10.1103/PhysRevLett.44.912](https://doi.org/10.1103/PhysRevLett.44.912).
- [101] E. W. Otten and C. Weinheimer. “Neutrino mass limit from tritium β decay”. In: *Reports on Progress in Physics* 71.8 (July 2008), p. 086201. DOI: [10.1088/0034-4885/71/8/086201](https://doi.org/10.1088/0034-4885/71/8/086201).
- [102] N. Palanque-Delabrouille et al. “Neutrino masses and cosmology with Lyman-alpha forest power spectrum”. In: *Journal of Cosmology and Astroparticle Physics* 2015.11 (Nov. 2015), p. 11. DOI: [10.1088/1475-7516/2015/11/011](https://doi.org/10.1088/1475-7516/2015/11/011).
- [103] M. L. Perl et al. “Evidence for Anomalous Lepton Production in $e^+ - e^-$ Annihilation”. In: *Phys. Rev. Lett.* 35 (22 Dec. 1975), pp. 1489–1492. DOI: [10.1103/PhysRevLett.35.1489](https://doi.org/10.1103/PhysRevLett.35.1489).
- [104] B. Pontecorvo. “Mesonium and Antimesonium”. In: *J. Exptl. Theoret. Phys.* 33 (Aug. 1957), pp. 549–551. URL: http://jetp.ras.ru/cgi-bin/dn/e_006_02_0429.pdf.
- [105] F. Priester et al. “Commissioning and detailed results of KATRIN inner loop tritium processing system at Tritium Laboratory Karlsruhe”. In: *Vacuum* 116 (2015), pp. 42–47. ISSN: 0042-207X. DOI: [10.1016/j.vacuum.2015.02.030](https://doi.org/10.1016/j.vacuum.2015.02.030).
- [106] V. Radeka. “Low-Noise Techniques in Detectors”. In: *Annual Review of Nuclear and Particle Science* 38.1 (1988), pp. 217–277. DOI: [10.1146/annurev.ns.38.120188.001245](https://doi.org/10.1146/annurev.ns.38.120188.001245).
- [107] S. Ramo. “Currents Induced by Electron Motion”. In: *Proceedings of the IRE* 27.9 (1939), pp. 584–585. DOI: [10.1109/JRPROC.1939.228757](https://doi.org/10.1109/JRPROC.1939.228757).

- [108] A. G. Riess et al. “A 3% solution: Determination of the Hubble constant with the Hubble Space Telescope and wide field camera”. In: *The Astrophysical Journal* 730.2 (Mar. 2011), p. 119. DOI: [10.1088/0004-637X/730/2/119](https://doi.org/10.1088/0004-637X/730/2/119).
- [109] M. Riordan and L. Hoddeson. “The origins of the pn junction”. In: *IEEE Spectrum* 34.6 (June 1997), pp. 46–51. ISSN: 0018-9235. DOI: [10.1109/6.591664](https://doi.org/10.1109/6.591664).
- [110] L. Rossi et al. *Pixel Detectors - From Fundamentals to Applications*. 1st ed. Springer, 2006. DOI: [10.1007/3-540-28333-1](https://doi.org/10.1007/3-540-28333-1).
- [111] CAEN S.p.A. *DT5730 & DT5725 Digitizer User Manual*. Sept. 2021. URL: <https://www.caen.it/?downloadfile=6019>.
- [112] D.M. Schlosser et al. “Expanding the detection efficiency of silicon drift detectors”. In: *Nuclear Instruments and Methods in Physics Research Section A: Accelerators, Spectrometers, Detectors and Associated Equipment* 624.2 (2010). New Developments in Radiation Detectors, pp. 270–276. ISSN: 0168-9002. DOI: [10.1016/j.nima.2010.04.038](https://doi.org/10.1016/j.nima.2010.04.038).
- [113] M. Schlösser et al. “Accurate calibration of the laser Raman system for the Karlsruhe Tritium Neutrino Experiment”. In: *Journal of Molecular Structure* 1044 (2013), pp. 61–66. ISSN: 0022-2860. DOI: [10.1016/j.molstruc.2012.11.022](https://doi.org/10.1016/j.molstruc.2012.11.022).
- [114] W. Shockley and W. T. Read. “Statistics of the Recombinations of Holes and Electrons”. In: *Phys. Rev.* 87 (5 Sept. 1952), pp. 835–842. DOI: [10.1103/PhysRev.87.835](https://doi.org/10.1103/PhysRev.87.835).
- [115] R.E. Shrock. “New tests for and bounds on neutrino masses and lepton mixing”. In: *Physics Letters B* 96.1 (1980), pp. 159–164. ISSN: 0370-2693. DOI: [10.1016/0370-2693\(80\)90235-X](https://doi.org/10.1016/0370-2693(80)90235-X).
- [116] D. Siegmann. “Investigation of the Detector Response to Electrons of the TRISTAN Prototype Detectors”. MA thesis. Technische Universität München, 2019. URL: https://www.ph.nat.tum.de/fileadmin/w00bya/neutrinos/Thesis/Master/TRISTAN_Siegmann_Daniel_19.pdf.
- [117] J. J. Simpson. “Measurement of the β -energy spectrum of ${}^3\text{H}$ to determine the antineutrino mass”. In: *Phys. Rev. D* 23 (3 Feb. 1981), pp. 649–662. DOI: [10.1103/PhysRevD.23.649](https://doi.org/10.1103/PhysRevD.23.649).
- [118] M. Slezak. “Monitoring of the energy scale in the KATRIN neutrino experiment”. PhD thesis. Charles University, Prague, Nov. 2015. URL: https://www.katrin.kit.edu/publikationen/phd-Martin_Slezak.pdf.
- [119] H. Spieler. *Semiconductor Detector Systems*. Oxford University Press, 2005. ISBN: 9780198527848. URL: <https://global.oup.com/academic/product/semiconductor-detector-systems-9780198527848>.
- [120] D. Spreng. “Electron backscattering on Silicon Drift Detectors and its impact on a sterile neutrino search with KATRIN”. MA thesis. Technische Universität München, 2023. URL: https://www.ph.nat.tum.de/fileadmin/w00bya/neutrinos/Thesis/Master/TRISTAN_Spreng_Daniela_23.pdf.

- [121] D. Spreng. “Energy Calibration of the TRISTAN Silicon Drift Detectors”. Technische Universität München, 2020. URL: https://www.ph.nat.tum.de/fileadmin/w00bya/neutrinos/Thesis/Bachelor/TRISTAN_Spreng_Daniela_20.pdf.
- [122] S. M. Sze and K. Ng Kwok. *Physics of Semiconductor Devices*. Wiley, 2006. DOI: [10.1002/0470068329](https://doi.org/10.1002/0470068329).
- [123] S. M. Sze and M. K. Lee. *Semiconductor Devices: Physics and Technology*. Wiley, 2012. ISBN: 9780470537947. URL: <https://www.wiley.com/en-us/Semiconductor+Devices:+Physics+and+Technology,+3rd+Edition-p-9780470537947>.
- [124] W. E. Thomson. “Delay networks having maximally flat frequency characteristics”. In: *Proceedings of the IEE - Part III: Radio and Communication Engineering* 96 (44 Nov. 1949), 487–490(3). ISSN: 0369-8947. DOI: [10.1049/pi-3.1949.0101](https://doi.org/10.1049/pi-3.1949.0101).
- [125] Thorlabs. *KDC101 DC Servo Motor Driver Kinesis User Guide*. Aug. 2022. URL: https://www.thorlabs.com/_sd.cfm?fileName=ETN017655-D03.pdf&partNumber=KDC101.
- [126] Thorlabs. *NPL Series of Nanosecond Pulsed Lasers User Guide*. Oct. 2019. URL: https://www.thorlabs.com/_sd.cfm?fileName=TTN122959-D02.pdf&partNumber=NPL64A.
- [127] Thorlabs. *Z800 Series Vacuum Compatible Motorized DC Servo Actuator*. Aug. 2022. URL: https://www.thorlabs.de/_sd.cfm?fileName=19741-D02.pdf&partNumber=Z812BV.
- [128] V. I. Tretyak and Y. G. Zdesenko. “Tables of double beta decay data - an update”. In: *Atomic Data and Nuclear Data Tables* 80.1 (2002), pp. 83–116. ISSN: 0092-640X. DOI: [10.1006/adnd.2001.0873](https://doi.org/10.1006/adnd.2001.0873).
- [129] P. Trigilio et al. “ETTORE: a 12-Channel Front-End ASIC for SDDs with Integrated JFET”. In: *2018 IEEE Nuclear Science Symposium and Medical Imaging Conference Proceedings (NSS/MIC)*. 2018, pp. 1–4. DOI: [10.1109/NSSMIC.2018.8824675](https://doi.org/10.1109/NSSMIC.2018.8824675).
- [130] K. Urban. “Application of a TRISTAN Silicon Drift Detector as Forward Beam Monitor in KATRIN”. MA thesis. Technische Universität München, 2019. URL: https://www.ph.nat.tum.de/fileadmin/w00bya/neutrinos/Thesis/Master/TRISTAN_Urban_Korbinian_19.pdf.
- [131] K. Valerius. “The wire electrode system for the KATRIN main spectrometer”. In: *Progress in Particle and Nuclear Physics* 64.2 (2010). Neutrinos in Cosmology, in Astro, Particle and Nuclear Physics, pp. 291–293. ISSN: 0146-6410. DOI: [10.1016/j.pnpnp.2009.12.032](https://doi.org/10.1016/j.pnpnp.2009.12.032).
- [132] R. L. Workman et al. “Review of Particle Physics”. In: *Progress of Theoretical and Experimental Physics* 2022 (2022), p. 083C01. DOI: [10.1093/ptep/ptac097](https://doi.org/10.1093/ptep/ptac097).
- [133] T. Yanagida. “Horizontal Symmetry and Masses of Neutrinos”. In: *Progress of Theoretical Physics* 64.3 (Sept. 1980), pp. 1103–1105. ISSN: 0033-068X. DOI: [10.1143/PTP.64.1103](https://doi.org/10.1143/PTP.64.1103).

Acknowledgments

I want to thank everyone who supported me in writing this thesis, especially:

I am very grateful to PROF. DR. SUSANNE MERTENS for giving me the opportunity to be member of your group and working with you. Your expertise in chairing this group is outstanding as well as the advice and guidance you gave in my work.

I also want to thank KORBINIAN URBAN for your great support as my supervisor. Your skills on hardware, electronics, and data analysis are superb. I will always remember the journey where we became laser experts, since you know, with great (laser) power comes great responsibility.

I would like to thank DR. FRANK EDZARDS for your relentless effort in proofreading this thesis and providing feedback, whether during the day, night, or weekend. This not only benefited my work, but also improved my writing skills in general.

I am thankful to DANIEL SIEGMANN for supporting me ever since I joined the group as a student assistant back in 2019.

I am particularly grateful to DANIELA SPRENG and CHRISTINA BRUCH for being true friends and also sharing the office with you. Although our sense of temperature may differ, you are always sympathetic and up for any fun.

I want to thank DR. CHRISTOPH WIESINGER and ALESSANDRO SCHWEMMER for sharing your detailed knowledge on statistics and your input on data processing.

I am also thankful to XAVER STRIBL, PIA VOIGT, and FLORIAN HENKES for always being fun around and having good times.

Finally, I would like to thank all the members of the E47 group for being amazing colleagues and friends.

Erklärung der Urheberschaft

Ich erkläre hiermit, dass ich die von mir eingereichte Arbeit zur Erlangung des Grades Master of Science unabhängig und selbstständig verfasst habe. Keine anderen Hilfsmittel, als die angegebenen Quellen, wurden zum Verfassen dieser Arbeit verwendet.

Declaration of Authorship

I hereby declare that the submitted thesis to receive the degree in Master of Science, has been written independently and by myself. No other resources than the quoted references have been used to write this thesis.

Christian Georg Anton Forstner
Munich, 14 March 2023